

**INVESTIGATING THE ROLE OF METAL-LIGAND BONDING ON BIOLOGICAL ACTIVITY OF
METALLOTHERAPEUTICS**

by

Thamayanthy Sriskandakumar

B.Sc., The University of Peradeniya, 2001

M.Sc., The University of Connecticut, 2007

A THESIS SUBMITTED IN PARTIAL FULFILLMENT OF
THE REQUIREMENTS FOR THE DEGREE OF

DOCTOR OF PHILOSOPHY

in

THE FACULTY OF GRADUATE STUDIES

(Chemistry)

THE UNIVERSITY OF BRITISH COLUMBIA

(Vancouver)

July 2013

© Thamayanthy Sriskandakumar, 2013

ABSTRACT

Defining and understanding the structure activity relationship and mechanisms of action of pharmaceutical agents in a biological environment is vital for their faster and successful clinical development. The mode of activation is often complicated for metalloanticancer drugs due to their wide spectrum of activity and interactions with biomolecules, during and after transport to cancer cells. The research herein describes the investigation of thiolate ligand oxygenation and its potential role in the mechanism of action for a family of “half-sandwich Ru^{II} arene” anticancer complexes. X-ray absorption spectroscopy (XAS), in concert with density functional theory (DFT) calculations, has been used to describe the influence of thiolato oxygenation on the nature of the Ru-S bond with the effect on ancillary ligands modifications in the parent thiolato (M-SR) and oxidized sulfenato (M-SOR) and sulfinato (M-SO₂R) species respectively. This study suggests that the sulfenato species are most susceptible to ligand exchange, but only via activation by protonation of the terminal oxo group. Perturbations of the sulfenato and sulfinato species can be achieved via either protonation or Lewis acid interaction; however the effect is greater in the sulfenato compared to that of sulfinato. DFT calculations are in agreement with the experimental data. Further studies of the electronic structure of a broader series of Os^{II} and Ru^{II} arene complexes have been performed using a similar combined spectroscopic and computational approach. Results from these studies provide important new insights into the chemical and biochemical properties of these complexes. Finally, these studies uncover the correlation between the electronic structure and reactivity that is important and must be considered when investigating the transition metal complexes in medicinal chemistry.

PREFACE

The research described in this dissertation is a collaborative work with Prof. Peter J. Sadler, medicinal inorganic group from University of Warwick, Coventry, UK. Ruthenium and Osmium arene complexes investigated here were prepared by Holm Petzold, Pieter C. A. Bruijninx, Abraha Habtemariam, Nicolas P. E. Barry, Anna Louisa Noffke and Khatija Bhayat from the Sadler group. I and my group members collected the X-ray absorption spectroscopic (XAS) data at Stanford Synchrotron Radiation Lightsource (SSRL) and Canadian Light Source (CLS). XAS data was processed and analysed by myself using SIXpack and BluePrintXAS. I performed all the density functional theory (DFT) calculations under the direct guidance from Pierre Kennepohl using Amsterdam density functional (ADF) and ORCA computational programs.

A version of chapter 3 has been published in Sriskandakumar, T.; Petzold, H.; Bruijninx, P. C. A.; Habtemariam, A; Sadler, P.; and Kennepohl, P. "Influence of Oxygenation on the Reactivity of Ruthenium-Thiolato Bonds in Arene Anticancer Complexes: Insights from XAS and DFT". *J. Am. Chem. Soc.* **2009**, 131, 13355-13361. I did the experimental and theoretical work for this manuscript. The first draft was written by me and then modified with input from co-authors. I wrote all the chapters herein with feedback from Prof. Pierre Kennepohl.

TABLE OF CONTENTS

ABSTRACT	ii
PREFACE	iii
TABLE OF CONTENTS.....	iv
LIST OF TABLES	vi
LIST OF FIGURES	vii
LIST OF SCHEMES.....	xii
LIST OF EQUATIONS	xiii
LIST OF SYMBOLS AND ABBREVIATIONS	xiv
ACKNOWLEDGEMENT.....	xvii
Chapter 1. INTRODUCTION	1
1.1 Scope of the Thesis.....	1
1.2 Metal Complexes as Anticancer Drugs.....	2
1.2.1 Platinum Drugs with Anticancer Properties.....	2
1.2.2 Ruthenium Complexes with Anticancer Activities	4
1.2.3 Os ^{II} Arene Complexes with Anticancer Properties.....	19
1.3 Cytotoxicity of Ruthenium and Osmium Arene Complexes.....	23
1.4 Activation Mechanisms of Organometallic Anticancer Complexes	23
1.4.1 Mode of Action: Platinum Anticancer Drugs.....	24
1.4.2 Mode of Action: Ruthenium Complexes	26
1.4.3 Mode of Action: Ru ^{II} -arene Complexes (RAPTA and RM175)	28
1.4.4 Mode of Action: Os ^{II} -arene Complexes	31
1.5 Applied Approach.....	33
Chapter 2. METHODOLOGY.....	35
2.1 X-ray Absorption Spectroscopy (XAS)	35
2.1.1 Basic Principles of X-ray Absorption Spectroscopy	35
2.1.2 Metal K-edge X-ray Absorption Near Edge Structure	38
2.1.3 Ligand K-edge X-ray Absorption Near Edge Structure	41
2.1.4 Instrumentation and Experimental Setup.....	47
2.2 Density Functional Theory (DFT).....	56
2.2.1 Fundamentals of DFT	57
2.2.2 Utilized DFT Calculations.....	60
Chapter 3. EFFECT OF OXYGENATION ON THE REACTIVITY OF RUTHENIUM (II) ARENE THIOLATO COMPLEXES	65
3.1 Introduction	65
3.2 Experimental and Computational Aspects.....	68
3.2.1 Sample Preparation.....	68
3.2.2 XAS Data Collection.....	69
3.2.3 Data Processing and Analysis	70
3.2.4 DFT Calculations	71
3.3 Results and Analysis	72
3.3.1 Effect of Oxygenation on Ru Metal Center	73
3.3.2 Effect of Oxygenation on S-Ligand	74

3.3.3	DFT Analysis.....	77
3.3.4	Ancillary Ligand Effects	81
3.4	Discussion.....	84
3.5	Conclusions	88
Chapter 4. ACTIVATION OF OXIDIZED SULFUR LIGANDS AND ITS IMPACT ON THE REACTIVITY OF RUTHENIUM (II) ARENE COMPLEXES		91
4.1	Introduction	91
4.2	Experimental and Computational Aspects.....	94
4.2.1	Sample Preparation.....	95
4.2.2	XAS Data Collection.....	96
4.2.3	Data Processing and Analysis	96
4.2.4	DFT Calculations.....	97
4.3	Results and Analysis	98
4.3.1	Lewis acid Interaction and Brønsted Acid Protonation on Sulfinato	99
4.3.2	Lewis Acid Interaction and Brønsted Acid Protonation on Sulfenato.....	104
4.4	Discussion.....	109
4.5	Conclusions	110
Chapter 5. SPECTROSCOPIC INVESTIGATION OF RUTHENIUM (II) AND OSMIUM (II) ARENE THIOSEMICARBAZONE COMPLEXES.....		112
5.1	Introduction	112
5.2	Experimental and Computational Aspects.....	115
5.2.1	Experimental Aspects.....	115
5.2.2	DFT Calculations.....	115
5.3	Results and Analysis	116
5.3.1	Effect of TSC Ligand Modification	116
5.3.2	Effect of the Monodentate Ligand.....	121
5.3.3	Effect of Metal (Ru vs Os) in Dimeric Complexes.....	122
5.3.4	Monomer to Dimer formation using UV-Vis Spectroscopy and DFT	123
5.4	Discussion.....	126
5.5	Conclusions	127
Chapter 6. CONCLUSIONS AND FUTURE DIRECTIONS		129
REFERENCES		133
APPENDIX A: BLUEPRINT XAS FITTINGS AND tddft ANALYSIS.....		146
APPENDIX B: MOLECULAR ORBITAL DESCRIPTION AND INPUT FILES.....		161
APPENDIX C: XAS AND DFT ANALYSIS OF RU^{II}/OS^{II}-ARENE (S-S-) LIGATED COMPLEXES		171

LIST OF TABLES

Table 1.1: Cytotoxicity (IC_{50}) of Ru ^{II} and Os ^{II} complexes toward human ovarian cancer cells, A2780..	23
Table 2.1: Electron binding energies of the elements investigated in this thesis	36
Table 3.1: Experimental peak energies and transition assignments and experimentally determined S_{3p} character in the acceptor orbital as estimated from normalized fit intensities*	75
Table 3.2: Selected bond lengths DFT optimized structures of 3b with (structure 1) and without (structure 2) scalar ZORA relativistic effect are compared with parameters derived from the X-ray structure	78
Table 3.3: Selected bond lengths of DFT optimized structure of 2a with scalar relativistic effect and solvent (structure 1) and without solvent (structure 2)	79
Table 4.1: Selected bond length (Å) of 3a, 3aZn ²⁺ and 3aH ⁺ from the DFT analysis	99
Table 4.2: Experimentally determined S_{3p} character* and calculated charge distribution of acceptor ($Ru_{4d\sigma^*} \leftarrow S_{3p}$) orbital in sulfinato complexes.....	100
Table 4.3: Selected bond length (Å) of 2a, 2a _{aq} , 2a-Zn ²⁺ and 2aH ⁺ from the DFT analysis	105
Table 4.4: DFT-calculated S_{3p} contribution* ($Ru_{4d\sigma^*} \leftarrow S_{3p}$) and the total charge distribution of Kohn-Sham acceptor orbital, $Ru_{4d\sigma^*}$ of 2a, 2aZn ²⁺ and 2aH ⁺ complexes	105
Table 5.1: S K-edge XAS peak energies and transition assignments with experimentally estimated S_{3p} character in the acceptor orbitals from normalized fit intensities compared with calculated DFT value	120

LIST OF FIGURES

Figure 1.1:	Structure of globally approved Pt ^{II} anticancer drugs in clinical use (a); Pt ^{IV} prodrug undergoing Phase III clinical evaluation (b)	3
Figure 1.2:	Chemical structures of first reported ruthenium complex fac-[RuCl ₃ (NH ₃) ₃] with anticancer activity (a) and other Ru ^{III} complexes currently in clinical evaluation NAMI-A and KP1019(b)	6
Figure 1.3:	General structure of some important Ru ^{II} arene complexes with anticancer property	7
Figure 1.4:	The general structure of half-sandwich Ru ^{II} arene complexes with monodentate ligand (a), bidentate chelating ligand (b) and tethered ligand (c). Reprinted from Bruijninx <i>et. al.</i> , <i>Adv. Inorg. Chem.</i> 2009, 61, 1–62., Copyright (2009), with permission from Elsevier.....	9
Figure 1.5:	Arene ligands substituted with Ru ^{II} -arene complexes developed by Sadler and Dyson.	10
Figure 1.6:	Biologically active ethacrynic acid tagged to RAPTA complexes via arene (a) and imidazole (b) ligands (next generation RAPTA complexes).....	11
Figure 1.7:	Ru ^{II} -arene complexes with monodentate ligands (a) and tethered arene ligand (b) developed by Sadler	12
Figure 1.8:	Systematic chelate variation in Ru ^{II} -arene complexes developed by Sadler. R denotes to arene	13
Figure 1.9:	Ru ^{II} -arene complexes developed by Keppler with biologically active chelating ligands..	15
Figure 1.10:	Novel Ru ^{II} -arene anticancer complexes under investigation	16

Figure 1.11:	Ru ^{II} -arene complex [(η ⁶ -hmb)Ru(en)Z] ⁺ studied for monodentate ligand (Z) substitution reactions.	17
Figure 1.12:	Most potent Os ^{II} -arene anticancer complexes reported to date by Sadler.....	20
Figure 1.13:	Systematic chelating ligand variation in Os ^{II} -arene complexes prepared by Sadler....	21
Figure 1.14:	Novel Os ^{II} -arene complex presently under investigation	22
Figure 2.1:	Energy transition and resulting spectrum of typical K-edge XAS experiment. Spectrum illustrating the key features (pre-edge, edge-jump and ionization edge)	35
Figure 2.2:	Mn K-edge XAS of rac-[Mn ^{III} (EHPG)]Na, (where EHPG - ethylenebis[(o-hydroxyphenyl)glycine]), illustrating XANES, EXAFS regions and other spectroscopic features	37
Figure 2.3:	Ru K-edge XAS of Ru carbene complexes illustrating the pre-edge intensity decreases with increased centrosymmetry of the complexes. Reprinted from Getty <i>et al.</i> , <i>Inorg. Chim. Acta</i> 2008, 361, 1059–1065. Copyright 2008, with permission from Elsevier. ¹⁷⁸	39
Figure 2.4:	Mn K-edge XAS of Mn-transferrin complex showing the edge-jump shifts with Z _{eff} during the photoreduction of the sample with multiple scans.	40
Figure 2.5:	S K-edge XAS of series of sulfur redox species. Reprinted from Pickering <i>et al.</i> <i>FEBS Lett.</i> 1998, 441, 11–14, Copyright (1998) with permission from Elsevier.....	43
Figure 2.6:	Extracting the pre-edge intensity involved in each features of S K-edge XAS obtained from [(η ⁶ -hmb)Ru(en)(SO <i>i</i> Pr)] ⁺ complex (where hmb – hexamethyl benzene, <i>i</i> Pr – isopropyl).....	44
Figure 2.7:	A series of S-ligands illustrating a linear relationship between dipole integral factor and S _{3p} ←S _{1s} transition energy. Adapted with permission from Sarangi <i>et al.</i> <i>J. Am. Chem. Soc.</i> 2007, 129, 2316-2326. Copyright 2007 American Chemical Society.....	46

Figure 2.8:	A schematic of the most important components of a 3 rd generation synchrotron source. Adapted from reference 198 with permission from John Wiley and Sons, Copyright © 2011, John Wiley and Sons. ²⁰⁶	49
Figure 2.9:	Schematic layout of beamlines configuration at SSRL	50
Figure 2.10:	A schematic layout of the XAFS station of the SXRMB beamline at CLS ²¹¹	52
Figure 2.11:	Schematic diagram for the detection methods used in this thesis work.....	53
Figure 3.1:	Molecular structures of [(η^6 -ar)Ru(en)(SO _n R)] ⁺ complexes investigated using XAS and DFT. Complexes 1, 2 and 3 are thiolates, sulfenates and sulfinates respectively. In series a ar = <i>p</i> -cymene and in series b ar = hmb. In 3a, 3b and 1c R = Ph; in 3a'' R = cyclohexyl; Complexes 3a' and 3b' are <i>in silico</i> models only.	67
Figure 3.2:	Normalized Ru K-edge XANES spectra of complexes of 1a,b - 3a,b. Inset shows the 1st derivative spectra indicating the edge jump position.....	73
Figure 3.3:	S K-edge spectra of Ru ^{II} arene A - thiolato 1a and 1b, B - sulfenato 2a and 2b, and C - sulfinato 3a and 3b complexes. An asterisk (*) denotes features due to thiolato-based impurities in the sulfenato/sulfinato complexes (>5%).....	74
Figure 3.4:	Natural bond orbital (NBO) picture of Ru-S _σ * in complexes 1a, 2a and 3a.	76
Figure 3.5:	Geometry optimized structure of 3b with (structure 1) and without (structure 2) scalar ZORA relativistic effects included during optimization.....	78
Figure 3.6:	Geometry optimized structure of 2a with relativistic effect and solvent MeOH (structure 1) and without solvent (structure 2)	78
Figure 3.7:	Breakdown of SO _n R ligand donor contributions to Ru _{4d_σ*} orbital (in %) for 1a→2a→3a' and for 1b→2b→3b' (open symbols) including the total ligand charge donation (blue squares) as well as specific contributions from sulfur (green circles),	

	oxygen (per atom, red circles), and isopropyl (black circles). Lines are used to indicate general trends only.	80
Figure 3.8:	Normalized S K-edge XAS spectra of 1a (black) and 1c (red). Inset shows second derivative spectra indicating presence of a shoulder at 2472.7 eV in 1c due to a low-lying ϕ_{π^*} orbital from the aryl moiety.....	82
Figure 3.9:	Illustration of hyperconjugation in complex 1c due to S_{3p} character mixing into aryl π^* orbitals (ϕ_{π^*}).....	83
Figure 3.10:	S K-edge XAS spectra of 3a'' (R = cyclo hexyl, black) and 3a (R = Ph, red). Presence of a shoulder at ~2477.5 eV in 3a indicating a low-lying ϕ_{π^*} orbital from the aryl moiety.	84
Figure 3.11:	Graphical representation of the $Ru_{4d\sigma^*}$ Kohn Sham orbital from 2a.	85
Figure 3.12:	Comparison of S-O bond distance and orbital mixing in Ru^{II} vs Cd^{II}	86
Figure 4.1:	Natural bond orbital (NBO) picture of $Ru-S_{\sigma^*}$ in complexes 3a, 3a _{aq} , 3aZn ²⁺ and 3aH ⁺	101
Figure 4.2:	Frontier MO diagram of complexes 3a, 3a _{aq} , 3aZn ²⁺ and 3aH ⁺ . Only α orbitals are shown but α and β orbitals are identical. Red and green arrows indicate the energy change in the SO_{σ^*} and $Ru-S_{\sigma^*}$ with protonation respectively. Orbitals are normalized to LUMO in each molecule.....	102
Figure 4.3:	(A) Normalized S K-edge XAS of complexes 3a, 3aZn ²⁺ , 3aCo ²⁺ and 3aCr ³⁺ , (B) XAS and simulated TDDFT of complex 3aZn ²⁺	103
Figure 4.4:	The $Ru-S_{\sigma^*}$ orbital of 3aCo ²⁺ and 3aCr ³⁺ showing the interaction of metal 3d with S 3p and Ru 4d orbitals	103
Figure 4.5:	Natural bond orbital (NBO) picture of $Ru-S_{\sigma^*}$ in complexes 2a, 2a _{aq} , 2aZn ²⁺ and 2aH ⁺	106

Figure 4.6:	Frontier MO diagrams for complexes 2a, 2a _{aq} , 2aZn ²⁺ and 2aH ⁺ . Only α orbitals are shown but α and β orbitals are identical. Red and green arrows indicate the energy change in the SO _{σ} * and Ru-S _{σ} * with protonation respectively. Orbitals are normalized to LUMO in each molecule.....	107
Figure 4.7:	(A) S K-edge XAS of 2b and the first scan of 2b solutions at pH 2.5 and pH 7.4; (B) simulated TDDFT of 2b, 2b _{aq} and 2bH ⁺ . An energy shift of 60.0 eV applied to simulated spectra to calibrate them with experimental data.	107
Figure 5.1:	Ru ^{II} /Os ^{II} -arene thiosemicarbazone complexes investigated in this Chapter.....	113
Figure 5.2:	Normalized S K-edge XAS of unmodified (4a) and modified (4b) TSC ligands (a) and complexes 5a-c (b). * denotes the thiolate based impurities. TDDFT spectra of these complexes are provided in Appendix A.3.1.....	116
Figure 5.3:	MO diagram of the π -systems of Thiosemicarbazone molecule described using model complex [CH ₂ =NH-CS-NH-N=CH ₂] ⁺	118
Figure 5.4:	Frontier MO diagram of complexes 5a-c. Only α orbitals are shown (α and β are identical). Red arrow indicates the energy shift from 5a→5b. Orbitals are normalized to LUMO in each complex.	119
Figure 5.5:	S K-edge XAS of complexes 6a and 6b. Os M ₃ -edge background is not subtracted from the spectrum 6b.	122
Figure 5.6:	S K-edge XAS of 5b and 6a.....	123
Figure 5.7:	(a) UV-vis spectra of complexes 5b and 6a. (b) simulated spectra of 5b with functionals BP86 and B3LYP. (c) simulated spectra of 6a with functionals BP86 and B3LYP. (d) simulated UV-vis spectra of 5baq compared with 5a spectrum.....	124
Figure 5.8:	MO orbital 324 showing the S-S interaction in 6a.	125

LIST OF SCHEMES

Scheme 1.1:	Direct Synthesis of sulfenato (2) and sulfinato (3) complexes from thiolato (1) complex, where R' = <i>p</i> -cym or hmb; R = <i>i</i> Pr or Ph.....	18
Scheme 1.2:	Oxidation of Ru ^{II} -arene thiolato complex in the presence of GSH and O ₂ , where R = <i>p</i> -cym or hmb; R' = <i>i</i> Pr or Ph.....	18
Scheme 1.3:	Activation mechanism of cisplatin	25
Scheme 1.4:	Hydrolysis mechanism of RAPTA-C complexes in pure water, where R is <i>p</i> -cym	29
Scheme 1.5:	M-Cl bond activation mechanism of Ru ^{II} /Os ^{II} – arene bidentate complexes, where R denotes arene	29
Scheme 1.6:	Proposed mechanism for Ru ^{II} -arene azopyridine, [(η^6 -ar)Ru(azpy-R)(X)] ⁺ , complexes	30
Scheme 1.7:	Proposed mechanism for the oxidation of NADH to NAD ⁺ catalysed by Os ^{II} -arene iminopyridine complex.....	32
Scheme 1.8:	Systematic approach used to investigate the research problems described in this thesis	33
Scheme 3.1:	Proposed pathway for DNA binding by Ru ^{II} arene Thiolate, 1, [(η^6 -ar)Ru(en)(SR)] ⁺ complexes	87
Scheme 3.2:	Postulated global model for biological mechanism of primary Ru ^{II} arene, [(η^6 -ar)Ru(en)(X)] ⁺ complexes	88
Scheme 4.1:	Protonation of complex 2 followed by hydrolysis under acidic condition (HCl). ⁷⁶	91
Scheme 4.2:	Brønsted acid protonation (a) ⁷⁶ and Lewis acid interaction (b) of Ru ^{II} arene sulfenato (2) complex, where R = <i>p</i> -cym, R' = <i>i</i> Pr.....	94
Scheme 4.3:	Brønsted acid protonation (a) and Lewis acid interaction (b) of Ru ^{II} arene sulfinato (3) complex, where R = <i>p</i> -cym, R' = Ph	94
Scheme 5.1:	Conversion of 6a from 5b in methanol or water.....	123

LIST OF EQUATIONS

Equation 2.1:	Ground state wave function of metal-sulfur ligand LUMO orbital, $Ru_{4d\sigma^*}$	44
Equation 2.2:	Intensity of $Ru_{4d\sigma^*} \leftarrow S_{1s}$ transition.....	45
Equation 2.3:	Relationship between dipole integral ($S3p r S1s$), S_{3p} character (β) and pre-edge intensity.....	46
Equation 2.4:	Beer-Lambert law	54
Equation 2.5:	Schrödinger equation	57
Equation 2.6:	Electron correlation functional, $E(\rho)$, describing the electron density of a system.	58
Equation 3.1:	Approximate Voigt lineshape	71

LIST OF SYMBOLS AND ABBREVIATIONS

%	Percent
←	To (indicates transition)
~	Approximately
=	Equal; Double bond
±	Plus or minus, Error bar
-	Minus; Covalent bond
≈	Almost equal
η^2	Two-fold hapticity
η^6	C ₆ six-fold hapticity
A	Ampere (units)
Å	Angstrom
β	Amount of S _{3p} character in the acceptor orbital
acac	Acetylacetonate
ar	Arene
atm	Atmosphere (101 kPa)
Azpy	Azopyridine
bip	Biphenyl
bipy	Bipyridine
bz	Benzene
dach	1,2- diaminocyclohexane
dha	Dihydroanthracene
en	Ethylenediamine
E_0	Ionisation (threshold) energy
eV	Electron volt(s)
G	Giga (units)
g	Gram (units)
gly	Glycine
hmb	Hexamethylbenzene
hrs	hours
I	Intensity
I_0	Incident X-ray intensity
I_1	Sample absorption
I_2	Reference absorption
Im	Imidazole
Impy	Iminopyridine
Ind	Indole
<i>i</i> Pr	Iso-propyl
K	Kelvin/
k	Kilo (units)
k	Photoelectron wavenumber
log P	log [Partition coefficient] or measure of hydrophobicity/lipophilicity

m	Milli (units)
<i>p</i> -cym	<i>p</i> -cymene
Ph	Phenyl
Pico	Picolinate
pKa	-log of the acid dissociation constant
pm	Pico meter
tha	Tetrahydroanthracene
Z _{eff}	Effective nuclear charge
ζ	Zeta
π, π*	Pi (bonding and anti-bonding interaction)
σ, σ*	Sigma (bonding and anti-bonding interaction)
ADF	Amsterdam density functional (Software package)
ADIT	6-amino-2,3-dimethyl-4-azahex-3-ene-2-thiolate
BL	Beamline
BluePrint XAS	Matlab-based toolbox for the fitting and analysis of XAS data
BN	Boron nitride
BNCT	Boron neutron capture therapy
BP86	Becke and Perdew exchange correlation functional
BSA	Bovin serum albumin
cGMP	Guanosine-3',5'-cyclic monophosphate
CIF	Crystallographic information file
CLS	Canadian light source, Inc.
COSMO	Conductor-like screening model
DCM	Double crystal monochromator
DFT	Density functional theory
DNA	Deoxyribonucleic acid
EPR	Electron paramagnetic resonance
ESI-MS	Electron spray ionization mass spectrometry
EXAFS	Extended X-ray absorption fine structure
GGA	generalized gradient approximation
GSH	Glutathione
GSSG	Glutathione disulfide
GTO	Gaussian type orbital
HK	Hohenberg-Kohn
HOMO	Highest occupied molecular orbital
IR	Infrared
KS	Kohn-Sham
LDA	Local density approximation
LMCT	Ligand to metal charge transfer
LUMO	Lowest unoccupied molecular orbital
MLCT	Metal-to-ligand charge transfer
MO	Molecular orbital
MOAnalyzer	Matlab-based toolbox tailored for ADF & ORCA output file

MOLDEN	Pre- and post-processing program of molecular and electronic structure
NADH	β -Nicotinamide adenine dinucleotide
NAMI-A	New anti-tumour metastasis inhibitor-A
NBO	Natural bond orbitals
NHase	Nitrile hydratase
NMR	Nuclear magnetic resonance
ORCA	An Ab initio, DFT and semiempirical electronic structure package
PBS	Phosphate-buffered saline
PIM-1	Proto-oncogene of the serine-threonine kinase family
PTA	1,3,5-triaza-7-phosphadamantane
RAPTA	Ruthenium-arene-PTA
RF	Radio frequency
RDC	Ruthenium derived compound
RNA	Ribonucleic acid
ROS	Reactive oxygen species
SCF	Self consistent field
SIXpack	Graphical user interface for XAS data processing and analysis
SSRL	Stanford synchrotron radiation lightsource
STOs	Slater-type orbitals
STXM	Scanning Transmission X-ray Microscopy
SVP	Split valence polarization
SXRMB	Soft X-ray micro-characterization beamline
TDDFT	Time-dependent density functional theory
TEY	Total electron yield
TSC	Thiosemicarbazone
TZP	Triple zeta with polarisation basis set
TZVP	Triple zeta valence polarization
UKS	Unrestricted Kohn-Sham
UV-vis	Ultraviolet-visible
XAFS	X-ray absorption fine structure
XANES	X-ray absorption near edge structure
XAS	X-ray absorption spectroscopy
XPS	X-ray photoelectron spectroscopy
XRD	X-ray diffraction
ZORA	Zeroth order regular (relativistic) approximation

ACKNOWLEDGEMENT

Apart from the efforts of myself, the success of this thesis would not have been possible without the encouragement, guidance and support of many others. I would like to take this opportunity to express my gratitude to the people who have been contributed in the successful completion of this dissertation.

First and foremost, I would like to express my greatest appreciation to Pierre for being an inspired supervisor. I can't say thank you enough for his excellent guidance, flexibility, freedom, patience and caring which provided me with an excellent atmosphere for doing research. I feel motivated, encouraged and educated every time I attend his meeting, without his encouragement and enthusiastic approach this research would not have materialized. Above all, Pierre is very understanding and excellent human being which made me feel comfortable for balancing my personal and academic life throughout the years.

Besides my advisor, I would like to extent my gratitude to the rest of my examining as well as supervisory committee: Prof. Craig Grapperhaus, Prof. Chris Orvig, Prof. Suzana Straus, Prof. Hongbin Li, Prof. Mark MacLachlan and Prof. Andrew MacFarlane for spending their valuable time to review my thesis, giving insightful comments and encouragement.

I am very fortunate to be a part of the Kennepohl group and I really appreciate the support, help, encouragement and friendship I received from past and present group members: Anusha, Mario, Vlad, Kendra, Danielle, Wei, Tulin, Insun, Shirin and Chantal. I am very grateful to Mario, who wrote the Matlab based programs BluePrint XAS and MOAnalyzer which extensively used in this thesis. Mario was always willing to discuss, help and give his best suggestions. I really appreciate his help in my research and in preparation of this thesis. I also want to thank Anusha for being my best friend and companion in the lab until she left, which made my grad school experience more memorable and enjoyable. I was able to mentor a RISE student Joey and other two summer students Caroline and Cynthia. It was my pleasure to guide and help them with experimental and computational work involved in their projects.

It was an amazing experience to work with our collaborators Prof. Peter Sadler and his coworkers Drs. Abraha Habtemariam, Holm Petzold, Pieter C. A. Bruijninx, and Nicolas P. E. Barry, as well as graduate students Anna Louisa Noffke and Khatija Bhayat from University of

Edinburgh and University of Warwick, UK. They provided with all the complexes studied in this thesis and I am extremely grateful for their collaboration. I am most grateful to the staff at the Stanford Synchrotron Radiation Lightsource (SSRL): Drs. Serena DeBeer, Mathew Latimer and Erik Nelson and Allyson Aranda; and Canadian Light Source (CLS): Dr. Yongfeng Hu; for their technical and scientific assistance in experimental setup and data collection.

I would also like to express my gratitude to Tulin and Insun for reading my thesis and giving feedback to improve on grammar and format of this document. In addition, I am very grateful to Dr. Jacqueline Cawthray and Anna Louisa Noffke, who expressed interest in reading my thesis and giving valuable comments and suggestions on my scientific writings.

I would like to extend my acknowledgement to the staff of UBC Chemistry department; first to the teaching instructors Dana Zendrowski and Sophia Nussbaum for having me as a teaching assistant, which provided me an opportunity to improve my teaching skills while being a graduate student; next to the graduate program secretary Sheri Harbour for her guidance and taking care of all the paper work throughout my graduate life and especially during my maternity leave. Other important person, I owe thanks is Jane Cua for her wonderful support with network and computers in the Chemistry department; following that to Pat Olsthoorn for his help with sample shipments to SSRL and University of Warwick, UK.

Last, but by no means least, I thank my husband Kumar and my little daughter Swathi for their personal support and great patience at all times. Kumar and Swathi were always there cheering me up and stood by me through the good times and bad. I would also like to thank my parents and brothers for their support, encouragement and best wishes.

The research work described in this thesis was funded by NSERC (Canada). Furthermore, academic, technical and infrastructure support were provided by UBC and University of Warwick. Most of the experimental work was carried out at SSRL, a national user facility operated by Stanford University on behalf of the United States Department of Energy and CLS, a national user facility supported by NSERC Canada, NRC Canada, CIHR, the Province of Saskatchewan, Western Economic Diversification Canada and the University of Saskatchewan. Additionally, the computational studies were performed through the Center for Higher Order Structure Elucidation (CHORSE) of the UBC Chemistry Department.

CHAPTER 1. INTRODUCTION

1.1 Scope of the Thesis

This thesis provides an account of investigations into the electronic structure of a series of Group 8-arene complexes with anticancer properties. A series of ruthenium (Ru^{II}) and osmium (Os^{II}) arene complexes have been studied using a combination of X-ray absorption spectroscopy (XAS) and density functional theory (DFT) calculations. Obtaining a detailed understanding of the mechanism of action of metallo-pharmaceuticals continues to be an ongoing challenge that limits broader development. X-ray absorption spectroscopy (XAS) is an element-specific probe of electronic structure that provides a unique perspective on metal-ligand bonding. This thesis utilizes XAS to provide the first in-depth investigations of Ru^{II}-arene anticancer drugs and provides novel insights into the mechanism of action of these complexes. This approach should be more generally applicable in the study of metallodrugs.

The first chapter presents a historical perspective on metallo anticancer complexes followed by their present status in human clinical studies. It further describes the ancillary ligand modifications of Ru^{II} (section 1.2.2.2) and Os^{II} arene (section 1.2.3) anticancer drugs followed by the currently accepted biological mechanisms of these complexes (section 1.3). Chapter 2 describes the basics of the experimental methodology, data analysis, and computational modelling used to interpret the experimental results.

Chapters 3 and 4 lead through the XAS and DFT analysis of a series of Ru^{II}-arene thiolato, sulfenato and sulfinato complexes and conclude with a proposal for the biological mechanism of anticancer activity of Ru^{II}-arene thiolato complexes. Chapter 5 focuses on spectroscopic studies of Ru^{II}-arene complexes with chelating thiosemicarbazone ligands. Finally, the

conclusions and key findings of the thesis work are highlighted in Chapter 6. Some recommendations for future efforts in this research area are also presented therein.

1.2 Metal Complexes as Anticancer Drugs

Medicinal inorganic chemistry is a relatively young and rapidly developing interdisciplinary research area. While the use of metals as pharmaceuticals has been identified in ancient ayurvedic (India), acupuncture (China), Arabic and Egyptian¹⁻⁶ medicines, the use of well-defined metal complexes for medicinal purposes began in the 1950s with the discovery of the antibacterial and anticancer properties of ruthenium polypyridyl complexes by Dwyer.⁷ A decade later, the landmark discovery of the anti-tumour properties of cisplatin by Barnett Rosenberg and coworkers⁸⁻¹⁰ marked the advent of modern medicinal inorganic chemistry. Since its approval in 1978, cisplatin has continued to be the most widely used chemotherapeutic anticancer agent in clinical use.^{11,12}

1.2.1 Platinum Drugs with Anticancer Properties

Platinum anticancer drugs presently play a huge role in cancer chemotherapy. Together with the archetypical cisplatin, the 2nd generation Pt-drugs (Figure 1.1a) carboplatin, designed also by Rosenberg in the 1970s,¹³ and oxaliplatin, discovered by Yoshinori Kidani in 1978,¹⁴ are administered to cancer patients globally. They are presently amongst the most effective chemotherapeutic agents in clinical use. Cisplatin is mainly used in the treatment of testicular cancers, where the survival rate is ~ 100% with early detection. Carboplatin is considered to be a safer analogue to cisplatin and is mostly used in the treatment of ovarian cancer.¹⁵ Oxaliplatin is a more recently-developed treatment option,

which is used mainly for colorectal cancer in combination with organic drugs.¹⁶ In addition, nedaplatin,¹⁷ lobaplatin^{18,19} and heptaplatin^{20,21} are clinically approved drugs in Japan, China and Korea respectively. The most favourable candidate under development is satraplatin, Figure 1.1b, the only orally active Pt^{IV} prodrug due to kinetic inertness, which is in Phase III clinical trials for hormone refractory prostate cancer.^{16,22,23}

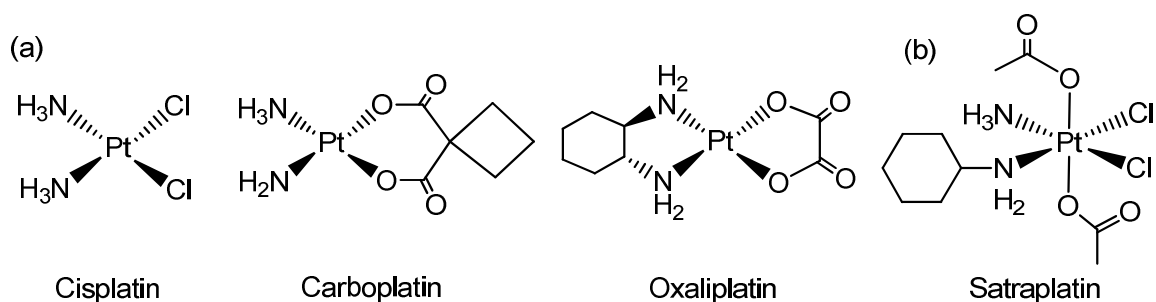


Figure 1.1: Structure of globally approved Pt^{II} anticancer drugs in clinical use (a); Pt^{IV} prodrug undergoing Phase III clinical evaluation (b)

Although cisplatin and other platinum drugs are arguably the most successful metallo anticancer drugs today, their clinical efficacy is diminished by a high general toxicity (neuro-, hepato- and nephrotoxicity). This leads to undesirable side-effects, which limit the administered dose. Additionally, it is inactive against a number of cancer cell lines including all metastatic (secondary) cancers. Most importantly, many tumors show intrinsic and acquired uni- and multicellular resistance against these drugs.²⁴ These limitations have made it necessary to search for alternative chemotherapeutic strategies that are capable of overcoming the problems associated with Pt-drugs while still maintaining an equal or greater level of activity and broadening the spectrum of the therapeutic effect.

In attempts to find new, metal-based anticancer drugs superior to cisplatin, some thousands of transition metal complexes, besides platinum, have recently been investigated

with varying degrees of success for their antitumor activity.^{23,25} Medicinal chemists are attracted by transition metal complexes as they offer a unique spectrum of reactivity and structural diversity which are not readily available in organic-based drugs. In particular, metallo-anticancer drugs based on ruthenium (Ru^{II/III}) appear to be the most promising and rapidly emerging in the last two decades.²⁶

1.2.2 Ruthenium Complexes with Anticancer Activities

Ruthenium stands out as an attractive alternative to platinum. The rich and well-established synthetic and coordination chemistry combined with several oxidation states (Ru^{II}, Ru^{III} and Ru^{IV}) available under physiological conditions make ruthenium compounds well-suited for medicinal applications.^{27,28} Ruthenium complexes have also been investigated as immunosuppressants, nitric oxide scavengers, antimicrobial agents and antimalarials.^{29,30} Interestingly, ruthenium is able to mimic iron in binding to various biomolecules, such as human serum albumin and the iron-transport protein transferrin. This stimulates a more effective delivery of ruthenium complexes to cancer cells, because such rapidly dividing cells have a greater demand for iron and exhibit an over expression of transferrin receptors.²⁷ This interaction can be part of the reason why these complexes are less toxic than their platinum counterparts.³¹ Moreover, their metal–ligand exchange kinetics ranges over many orders of magnitude and can be tuned via ligand variation. This is a key advantage for kinetic stability and drug development.

1.2.2.1 Ruthenium (III) Complexes with Anticancer Properties

The first report of anticancer activity from a ruthenium complex was published in 1976 by Durig *et al.* for the simple coordination complex *fac*-[RuCl₃(NH₃)₃] (Figure 1.2a). This complex was also found to induce filamentous growth of *Escherichia coli* at the similar concentration as required for the same effect by cisplatin.³² Subsequently, this compound and analogues (*e.g.* *cis*-[Ru(NH₃)₄Cl₂]) were evaluated for their anti-tumour properties by Clarke in 1980.³³ Unfortunately, the poor solubility of these complexes prevented further pharmacological application.³⁴ Since then, intense efforts have been made to develop ruthenium compounds as anti-cancer agents and many active agents are currently emerging as potential new drugs.²⁶ To date, two Ru^{III} complexes NAMI-A, *trans*-[Ru^{III}Cl₄(DMSO)(Im)](ImH) (where Im = imidazole), and KP1019, *trans*-[Ru^{III}Cl₄(Ind)₂](IndH) (where Ind = indole), Figure 1.2b, have entered clinical trials with promising results.^{23,26,35,36} Although both display octahedral geometry, NAMI-A and KP1019 show distinct antitumor behaviours.

NAMI-A, developed by Mestroni, Alessio and coworkers,^{37,38} was the first ruthenium drug to reach human clinical development in 1999 and currently is in Phase I/II clinical evaluation as an antitumor and more importantly as an antimetastatic agent. Clinical studies showed that it inhibits matrix metalloproteinases and prevents tumor invasion of nearby tissues (antimetastatic effect) but appears to lack direct cytotoxic effects (also see section 1.3.2).³⁹ The reduced analogue of NAMI-A was interestingly more active than NAMI-A itself against metastatic growth.⁴⁰ KP1019, developed by Keppler and coworkers,³⁵ is in Phase II trials for the treatment of colorectal cancer. Phase I clinical studies on KP1019 revealed direct

antitumor activity against a wide range of primary explants of human tumors by inducing apoptosis (also see section 1.3.2). Advantageously, it is not associated with dose-limiting toxicity.^{41,42}

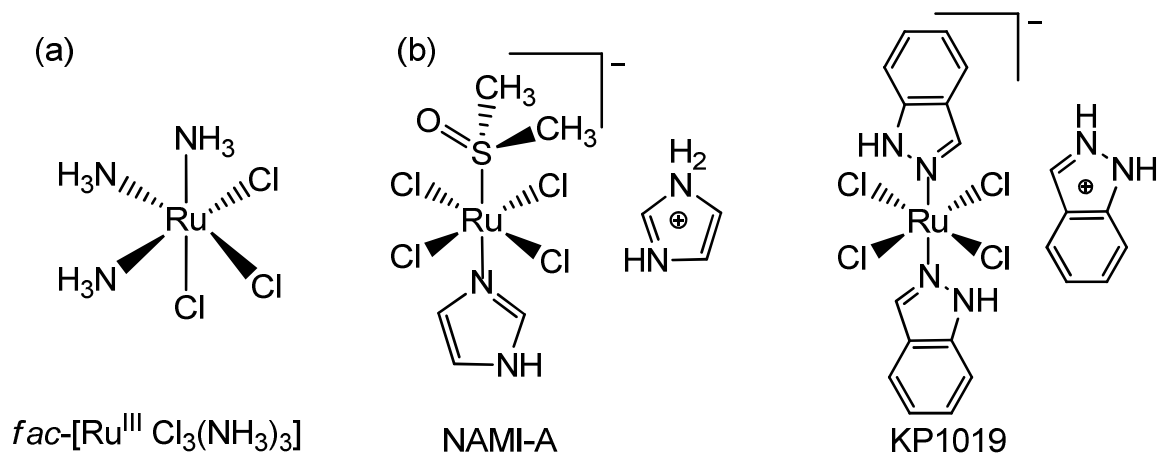


Figure 1.2: Chemical structures of first reported ruthenium complex $fac-[RuCl_3(NH_3)_3]$ with anticancer activity (a) and other Ru^{III} complexes currently in clinical evaluation NAMI-A and KP1019(b)

1.2.2.2 Ruthenium (II) Complexes with Anticancer Properties

As initially proposed by Clarke,⁴³ Ru^{III} complexes are relatively inert toward ligand substitution, acting principally as prodrugs that undergo “activation by reduction” *in vivo* to become more labile Ru^{II} counterparts which are consequently responsible for the observed cytotoxicity (also see section 1.3.2). By considering this activation mechanism, a large number of Ru^{II} complexes have been systematically developed and tested for anticancer activity in cultured tumor cells and animal models.^{44–48} Among them, the most encouraging Ru^{II} arene complexes (RM175, RAPTA-T and DW1/2 - racemic mixture of DW1 and DW2) are discussed in this section.

Ru^{II} Arene Complexes with Anticancer Activities

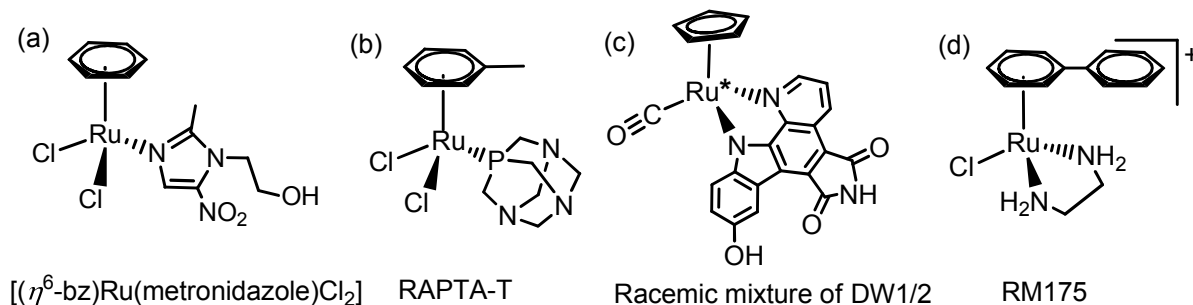


Figure 1.3: General structure of some important Ru^{II} arene complexes with anticancer property

The era of investigating the Ru^{II} arene complexes as anticancer drugs has first started with the compound $[(\eta^6\text{-C}_6\text{H}_6)\text{Ru}(\text{metronidazole})\text{Cl}_2]$ (metronidazole = 1- β -hydroxyethyl-2-methyl-5-nitroimidazole), Figure 1.3a, reported with anticancer activity by Tocher *et al.* in 1992.⁴⁹ The complex exhibits a greater and more selective cytotoxicity than the ligand metronidazole, a widely used antibiotic and antifungal agent; however, further biological studies have not been disclosed.⁵⁰

Presently, RAPTA (*Ruthenium-Arene-PTA*, Figure 1.3b), DW1/2 (Dwyer 1/2, 1.3c) and RM175 (Figure 1.3d) are the three families of organometallic half-sandwich Ru^{II}-arene complexes drawing increasing attention as antitumor and/or antimetastatic agents.^{51,52} Interestingly, these three complexes show some similarities in their structure but demonstrate distinctly different antitumor activities.

RAPTA: In RAPTA complexes, developed by Dyson and coworkers in 2004,^{46,53} the piano stool shape is occupied by an arene and by three monomer ligands, one of them being a PTA (1,3,5-triaza-7-phosphoadamantane) ligand. These complexes are weakly cytotoxic but the toxicity is better expressed on tumor cells than in healthy cells due to the biological characteristic of the PTA ligand.^{46,54,55} In addition to antitumor activity,⁵⁶ they also exhibit

antimetastatic,⁴⁶ and antiangiogenic⁵⁷ properties with negligible side effects. Interestingly, they only show a low cytotoxicity *in vitro* but a high metastatic activity *in vivo*.⁴⁶ Thus, they are inactive against primary tumors but active towards secondary metastasis tumours (also see section 1.3.3 for activation mechanism).³⁸

DW1/2: An intriguing example of Ru^{II} half-sandwich complexes which entered the field with a purported different mode of action, was developed by Meggers and coworkers in 2004. It has strong similarity to the natural product Staurosporine, isolated from *Streptomyces Staurosporeus* bacterium and possess anti-cancer properties.^{47,58,59} These complexes were studied as organometallic enzyme inhibitors^{58,60} and the relevant anticancer activity has only been reported recently.⁶¹ They specifically bind to PIM-1, proto-oncogene of the serine-threonine kinase instead of DNA.^{61,62} This is one of the first ruthenium anticancer drugs targeting a signal transduction pathway as a mechanism for anti-tumour activity.⁶³ Therefore, a promising *in vivo* application is expected for highly selective organometallic protein kinases, PIM-1 inhibitors, such as DW1/2.⁶⁴

RM175: The group of RM175 complexes, “piano stool” shaped Ru^{II} arene diamines developed by Sadler and coworkers in 2001,⁴⁵ are enormously promising. The success of these Ru^{II} complexes is that they simply circumvent the activation by reduction mechanism. The specific design of these complexes, piano stool or half-sandwich, is to intentionally retain its antitumor activity in cisplatin-resistant cancer cells by a unique mode of binding: direct monofunctional coordination to the metal center accompanied with arene intercalation.^{65,66} In contrast to RAPTA, the RM175 family of complexes shows very high cytotoxicity *in vitro* as well as *in vivo* against human ovarian cancer cells (A2780)^{67,68} with IC₅₀ values comparable to

that of carboplatin (6 μM).⁴⁵ In addition, the more hydrophobic tetrahydroanthracene (tha) derivative $[(\eta^6\text{-tha})\text{Ru}(\text{en})\text{Cl}]^+$ shows equipotent activity to cisplatin (0.6 μM).⁶⁷

The above examples show that the anticancer activity of these complexes highly depends on their structural design. Investigations of the ancillary ligand modification and mode of action of these complexes through their electronic structure are a major focus of this thesis. Therefore, these complexes are reviewed in detail below.

Rational Design of Ru^{II}-arene Anticancer Complexes

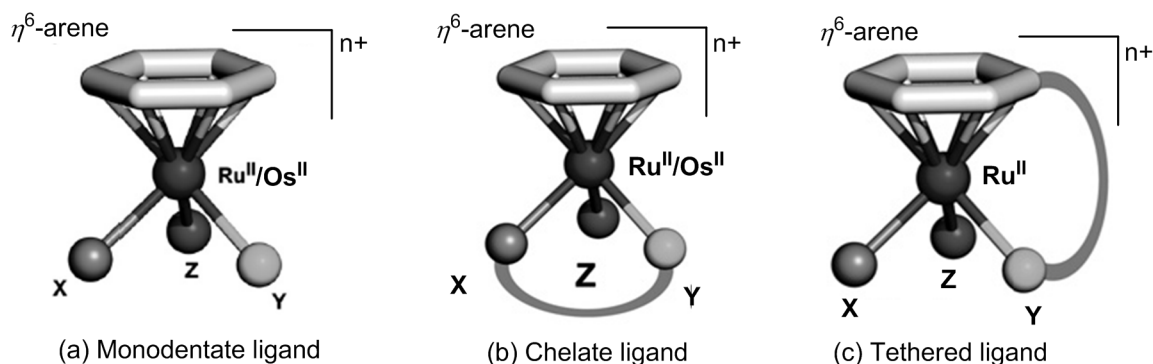


Figure 1.4: The general structure of half-sandwich Ru^{II} arene complexes with monodentate ligand (a), bidentate chelating ligand (b) and tethered ligand (c). Reprinted from Bruijninx *et. al.*, *Adv. Inorg. Chem.* 2009, 61, 1–62., Copyright (2009), with permission from Elsevier.

Three different building blocks define the ligand set of the piano stool structure and can be fine-tuned to optimize the activity of these complexes. The anti-tumour and anti-metastatic properties of Ru^{II} and Os^{II} η^6 -bound arene complexes of the type $[\text{M}^{\text{II}}(\eta^6\text{-ar})(\text{X})(\text{Y})(\text{Z})]$ have recently been explored.^{29,45,67,69} The three legs of the ‘piano stool’ are designed in three different ways. As shown in Figure 1.4, it can be three monodentate ligands (X, Y and Z) or one bidentate ligand (X-Y) with one monodentate ligand (Z) or one of the ligands can be tethered to the arene ring (*e.g.* arene-Y). Combinations of the ligand sets

lead to a wide range of relatively labile or rather inert complexes depending on the nature of X, Y, Z and the arene ligand. In addition, the three legs can possibly be occupied by one tridentate ligand (X-Y-Z). They are rarely seen as potential candidates in Sadler and/or Dyson complexes due to their inertness towards substitution reactions.⁷⁰

Arene Ligand: The “seat” of the “piano stool” is the arene ligand, binding as a η^6 -electron donor and a π -acceptor. It stabilizes the metal in its +2 oxidation state.⁷¹ These complexes possess an excellent amphiphilic character (hydrophobicity provided by the arene ligand is counterbalanced by the hydrophilic metal centre),⁵¹ which is believed to increase their interaction with biomolecules. The hydrophobic face provided by the arene plays an important role during the transportation of ruthenium through the cell membranes.²⁸ Most importantly, arene ligands can be excellent DNA intercalators, or form π - π arene-nucleobase stacks - a unique mode of DNA binding involved with Ru^{II} arene complexes.⁶⁶ In addition, the synthetic diversity of the arene ligands is an excellent scaffold for the coupling of organic segments for targeted chemotherapy.^{27,51}

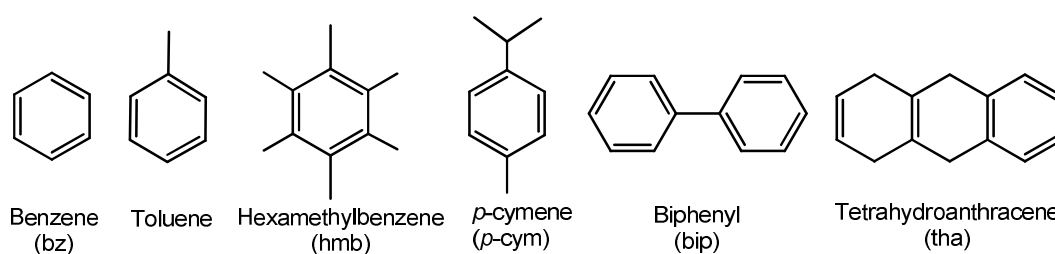


Figure 1.5: Arene ligands substituted with Ru^{II} -arene complexes developed by Sadler and Dyson.

Sadler and coworkers⁷² found a correlation between hydrophobicity (measured in log P, where P is partition coefficients in an octanol-water system), cellular uptake and cytotoxicity as follows, from less toxic to more toxic, tha (tetrahydroanthracene) > bip (biphenyl) > p-cym (p-cymene) > bz (benzene), Figure 1.5, in a series of Os^{II} -arene $[Os(\eta^6\text{-ar})(4\text{-methyl-}$

picolinate)Cl] complexes. Therefore, log P seems to be a valuable tool for predicting the cytotoxicity of these complexes.

On the other hand, the effect of different arene ligands on the cytotoxicity of RAPTA complexes follows the order of toluene > hmb (hexamethylbenzene) > benzene > *p*-cymene,⁴⁶ Figure 1.5. Interestingly, there is no correlation reported between log P and cytotoxicity. A next generation of RAPTA complexes that are functionalized via their arene ligand with a biologically active organic group (e.g. ethacrynic acid (Figure 1.6a),⁷³ human serum albumin (HSA) through hydrazone (Figure 1.6b),⁷⁴ naphthalimide,⁷⁵) display improved drug efficiency and delivery through multiple modes of activity. Thus, a new horizon has very recently been investigated for targeted chemotherapy.

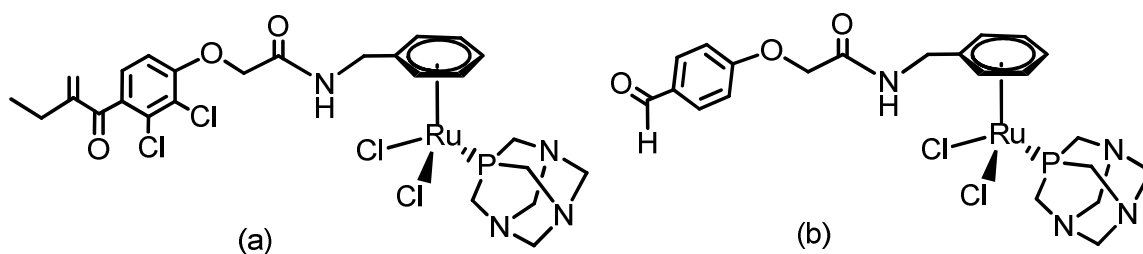


Figure 1.6: Biologically active ethacrynic acid tagged to RAPTA complexes via arene (a) and imidazole (b) ligands (next generation RAPTA complexes)

The above mentioned studies show that the arene ligand can play an important role in the properties and activity of such complexes. It suggests that arene modifications have a major impact on the electronic structure of the resulting complexes and mode of activity.⁷⁶ Therefore, investigating the arene effect on the electronic structure of these complexes is essential to understand their actual role in their activity and mechanism. The effect of arene substitution (*p*-cym vs hmb) on the geometry and electronic structure of Ru^{II}-arene thiolato

complexes is investigated through the metal-ligand covalency of Ru^{II}-arene thiolato complexes studied in Chapter 3.

Monodentate and Tethered Ligands: RAPTA-T (Figure 1.3b) and its analogues are the best example for a successful candidate belonging to the sub-family of Ru^{II}-arene complexes with three monodentate ligands, Figure 1.4a.^{27,51,77} The effect of ancillary ligand modifications of these complexes has been surveyed recently.⁴⁸ The water soluble phosphine ligand PTA, highly influences the selectivity of RAPTA complexes towards cancer cells. Any modification on the PTA ligand, however, seems to lead to a loss of selectivity.⁴⁶

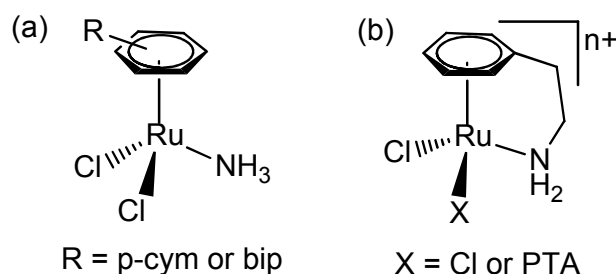


Figure 1.7: Ru^{II}-arene complexes with monodentate ligands (a) and tethered arene ligand (b) developed by Sadler

On the other hand, other complexes with three monodentate ligands, such as $[(\eta^6\text{-ar})Ru(NH_3)Cl_2]$ (where ar = *p*-cym, bip), in Figure 1.7a, are not active towards cancer cells even at high concentrations (100 μ M) and undergo rapid hydrolysis followed by loss of the arene ligand.⁷⁸ For the same reason, the piano-stool Ru^{II}-tethered complex, $[(\eta^6:\eta^1\text{-C}_6\text{H}_5(\text{CH}_2)_2\text{NH}_2)RuCl_2]$, Figure 1.7b, developed by Sadler *et al.* in 2007 is also inactive.⁷⁹ Structural modifications and activity relationship of monodentate ligands and tethered ligand complexes are beyond the scope of this thesis but have been recently reviewed by Noffke *et al.*⁷⁰

Bidentate Chelating Ligand: The most promising complexes developed by Sadler, including RM175, belong to the sub family of $[(\eta^6\text{-ar})\text{Ru}(\text{XY})\text{Z}]^+$, where XY is a bidentate chelating ligand and Z is a monodentate ligand. Chelate complexes are generally more stable towards ligand substitution; with an appropriate choice of the labile Z-ligand, the other building blocks in the structure, allow to selectively controlling aquation and substitution reactions. Thereby the cytotoxicity of this class of complexes can be fine-tuned in cancer cells.^{67,80} Structure activity relationships showed that the most active complexes contain a stable bidentate *N,N*-donor ligand, a more hydrophobic arene ligand, and a halide as exchangeable ligand. The perfect example is RM175.⁴⁵

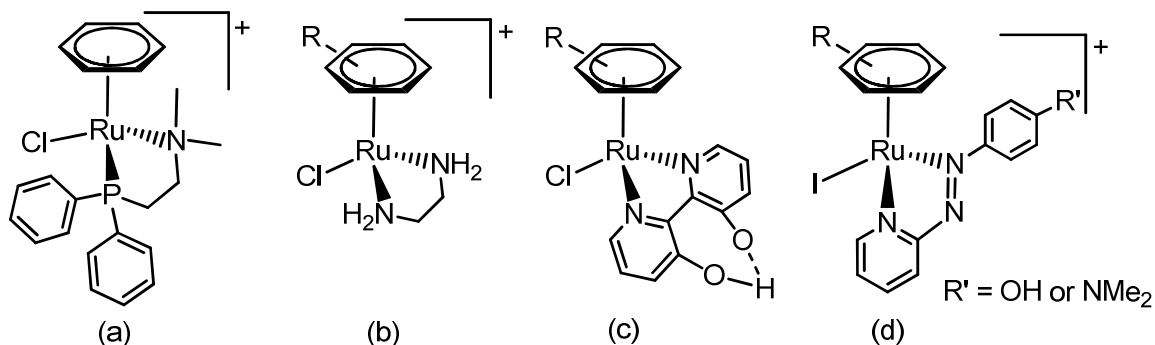


Figure 1.8: Systematic chelate variation in Ru^{II} -arene complexes developed by Sadler. R denotes to arene

The first complex of a bidentate amino-phosphine (*P,N*-bidentate) chelating ligand, $[(\eta^6\text{-bz})\text{Ru}(\text{Me}_2\text{NCH}_2\text{CH}_2\text{PPh}_2\text{-}N,P)\text{Cl}]^+$, Figure 1.8a, developed by Sadler showed cytotoxicity towards cancer cells but suffered from poor aqueous solubility.^{81,82} To increase solubility, a σ -donor *N,N*-bidentate, ethylenediamine (en), Figure 1.8b, was introduced. Later on, en became one of the most promising bidentate ligands, which leads to the discovery of a series of Ru^{II} -arene anticancer complexes with reasonable solubility and significant cytotoxicity (*e.g.* RM175).⁴⁵ Potentially, primary and secondary amine *N,N*-ligands (*e.g.* en) are excellent

hydrogen bond (H-bond) donors and therefore enhance the selectivity for G-binding by H-bond formation to the C6O of the guanine nucleobase.⁴⁰ A loss of cytotoxicity was observed in an effort to modify the en ligand.⁸⁴

However, complexes containing 2,2'-bipyridine-3,3'-diol [bipy(OH)₂] as chelating ligand showed a dramatic increase in the anticancer activity. In aqueous solution, only the neutral species $[(\eta^6\text{-ar})\text{Ru}(\text{N,N-bipyOHO})\text{Cl}]$, Figure 1.8c, is actively present (with deprotonated chelating ligand) over a pH range of 2-10 and strongly binds to 9-ethylguanine, a DNA model nucleobase.⁸⁵ Ru^{II}-arene complexes with other bidentate systems, such as *N,O*- and *O,O*- chelating ligands, have also been studied and showed moderate cytotoxicity and coordination to guanine (N7 binding). Intriguingly, Ru^{II}-arene complexes with a *para*-substituted phenylazopyridine chelating ligand, and iodo monodentate ligand $[(\eta^6\text{-ar})\text{Ru}(\text{N,N-azpyR})\text{I}]^+$ (where R = NMe₂ or OH), Figure 1.8d, do not undergo activation by hydrolysis but are highly cytotoxic toward cancer cells with an IC₅₀ of 2-6 μM. Iodine is preferred as monodentate ligand over chloride, however the reason is not known.

Recently, Keppler and coworkers have developed Ru^{II}-arene complexes with biologically active bidentate ligands (indoloquinolines as *N,N*- ligands,⁸⁶ hydroxypyridones as *O,O*- ligands,⁸⁷ thiomaltols as *S,O*- ligands,⁸⁸ Figure 1.9) a strategy to selectively enhance the cytotoxicity via a dual-action mechanism. Os^{II} derivatives of indoloquinolines and hydroxypyridones as ligands are also prepared and those analogues seem more active than their Ru analogues. The mode of action is not known for $[(\eta^6\text{-arene})\text{Ru}^{\text{II}}(\text{indoloquinoline})\text{Cl}]^+$ complexes.⁸⁶ A remarkable shift in cytotoxicity was observed with thiomaltol complexes, $[(\eta^6\text{-arene})\text{Ru}^{\text{II}}(\text{thiomaltol})\text{Cl}]$ when they were switched from maltol complexes. The shift in

cytotoxicity is correlated with the higher stability of the *S,O*-chelate ligands in aqueous solution.⁸⁸ However, the later complex $[(\eta^6\text{-arene})\text{Ru}^{\text{II}}(\text{hydroxypyrrone})\text{Cl}]^+$ undergoes hydrolysis of the Ru-Cl bond and forms aqua $[(\eta^6\text{-arene})\text{Ru}^{\text{II}}(\text{hydroxypyrrone})\text{OH}_2]^{2+}$ species. Those aqua species directly coordinate to N7 of GMP, in addition to react with amino acids upon loss of the hydroxypyrrone ligand.⁸⁷ Therefore, they show only low potency to inhibit the growth of the cancer cells but high potency to inhibit the CDK2/Cyclin A protein kinase.

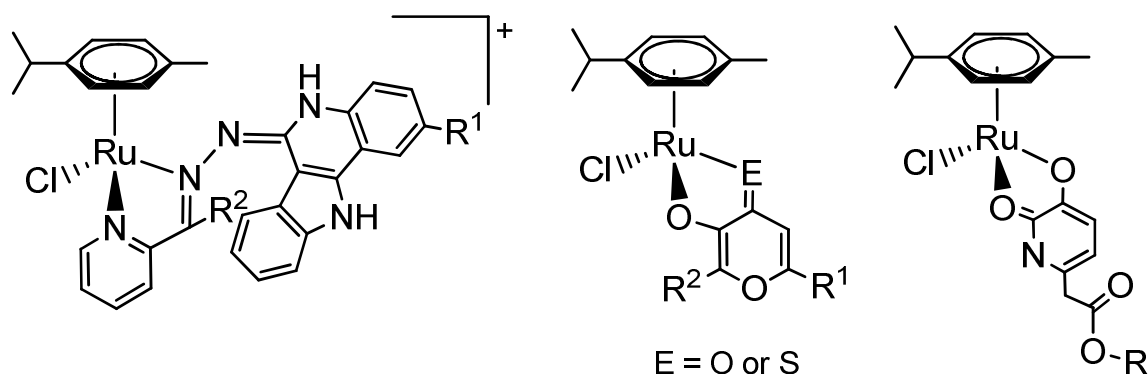


Figure 1.9: Ru^{II}-arene complexes developed by Keppler with biologically active chelating ligands

These studies suggest that bidentate chelating ligands play a critical role in recognition of the complex by biological targets⁸³ besides altering the pK_a of the aqua complex.⁸⁹ Therefore, developing metallo-arene complexes combined with bioactive (such as antibiotic, antifungal, anticancer) chelating ligands is a very recent successful approach to make more efficient anticancer drugs with different modes of activities.^{86,87,90-93} In that effort, a series of biologically potent sulfur containing bidentate ligands (*i.e.* thiosemicarbazones, Figure 1.10) hybrid with Ru^{II}-arene complexes are currently under investigation by Sadler and coworkers. These complexes do not readily crystallise which limits the structure elucidation by X-ray crystallographic methods. Therefore, the geometric and electronic structure, metal-ligand

covalency and structure activity relationship of newly developed Ru^{II}-arene thiosemicarbazone complexes are investigated using XAS and DFT in Chapters 5.

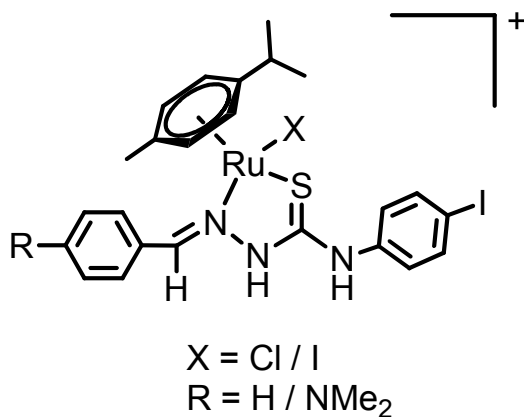


Figure 1.10: Novel Ru^{II}-arene anticancer complexes under investigation

The biological mechanism of water soluble complexes belonging to this class is activated by hydrolysis of the monodentate ligand (*i.e.* Ru-Z bond as in Figure 1.8).⁹⁴ Therefore, an appropriate choice of the monodentate ligand is vital to optimize the cytotoxicity of these complexes. The rate and extent of hydrolysis of the Ru-Z bond are highly dependent on the nature of Z ligand. A study which investigated the hydrolysis rate on a series of monodentate ligands $[(\eta^6\text{-hmb})\text{Ru}(\text{en})\text{Z}]^+$, where Z = Cl, Br, I, N₃, (Figure 1.11) shows a good correlation (experimentally Cl⁻ ≈ Br⁻ < I⁻ < N₃⁻ as well as theoretically Br⁻ < Cl⁻ < I⁻ < N₃⁻) between hydrolysis rate, hydrolysis equilibrium and cytotoxicity. However, sterically-demanding ligands can significantly affect the rate of aquation.⁸⁰ The effect of monodentate ligand (I vs Cl) on the electronic structure (covalency) of Ru^{II}-arene thiosemicarbazone complexes is investigated using XAS and DFT will be discussed in Chapter 5.

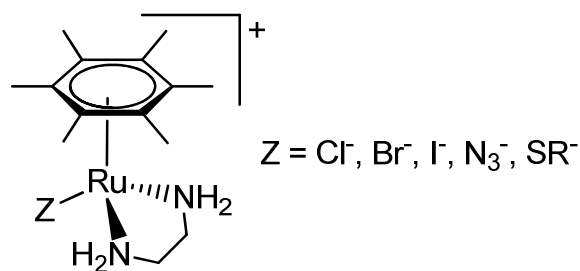
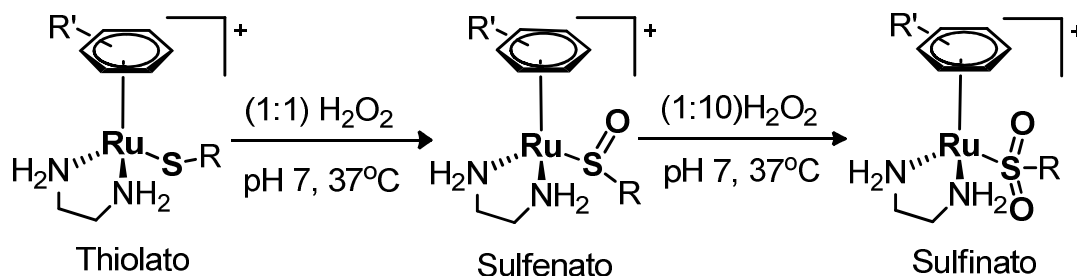


Figure 1.11: Ru^{II}-arene complex [(η^6 -hmb)Ru(en)Z]⁺ studied for monodentate ligand (Z) substitution reactions.

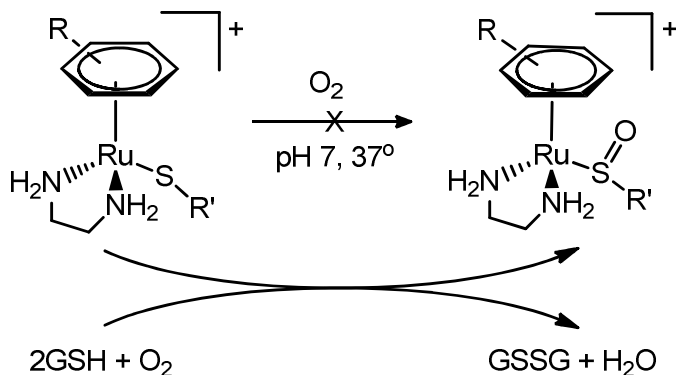
Ru^{II}-arene thiolates: Generally, but not always, complexes that spontaneously hydrolyze are cytotoxic. Intriguing exceptions to this rule are biologically relevant Ru^{II}-arene thiolato, [(η^6 -arene)Ru(en)SPh]⁺, complexes prepared by Fuyi Wang from the Sadler group in 2005.⁸⁰ They do not hydrolyze but undergo faster substitution reaction with guanosine-3',5'-cyclic monophosphate, GMP. Therefore, the cytotoxicity of these complexes is believed to be activated by oxidation of the thiolato ligand to its sulfenato or sulfinato form, a similar mode of activation also observed for Ru-glutathione adducts, [(η^6 -bip)Ru(en)(GS-S)] formed during the reaction of RM175 and glutathione, GSH.⁹⁵ This novel concept forms the counter hypothesis to the "activation by reduction" theory discussed earlier for Ru^{III} complexes and is thus very important to explore in detail.

Furthermore, the biochemical studies done by Dr. Holm Petzold show that Ru^{II}-arene thiolato (**1**) complexes, when reacted with one molar equivalent of hydrogen peroxide (H₂O₂), exclusively yield the corresponding sulfenato (**2**) complexes, whereas excess H₂O₂ leads to corresponding sulfinato (**3**) complexes, Scheme 1.1. The crystallographic data of these complexes shows that the Ru-S bond gets remarkably shorter with oxidation.^{76,96} A similar trend is observed in other Ru^{II},^{97,98} Ni^{II}⁹⁹⁻¹⁰¹ and Co^{III}¹⁰² sulfinato complexes; in contrast, elongation is also observed in Pt^{II}¹⁰³ and Ni^{II}¹⁰⁰ sulfenato complexes. Therefore, shortening

of the M-S bond upon oxidation is an apparent contradiction to the conventional wisdom that the S-donor strength decreases during the oxidation.¹⁰¹



Scheme 1.1: Direct Synthesis of sulfenato (2) and sulfinato (3) complexes from thiolato (1) complex, where R' = *p*-cym or hmb; R = *i*Pr or Ph



Scheme 1.2: Oxidation of Ru^{II}-arene thiolato complex in the presence of GSH and O₂, where R = *p*-cym or hmb; R' = *i*Pr or Ph

Interestingly, Holm also noticed that thiolato complexes undergo oxidation reactions in the presence of GSH (Scheme 1.2),¹⁰⁴ a biologically important activation reaction. This reaction of Ru^{II}-arene thiolato complexes partially elucidates that these complexes would be activated through ligand oxidation. The intra molecular hydrogen bonds within the molecule and inter molecular hydrogen bond presence in the crystallized structures of sulfenato (with solvent molecule -CH₃OH) and sulfinato (with neighbouring molecule) might also play a role in the shorter Ru-S bond.^{76,96} In addition, the key species responsible for the mechanism (*i.e.* either sulfenato or sulfinato or both), geometric and electronic structures of these complexes

and the effect of thiolato ligand oxidation on the metal center was not clear from the analysis of nuclear magnetic resonance (NMR), X-ray crystallography and mass spectrometry. Therefore, a detailed investigation of the electronic and geometric properties of Ru^{II} arene thiolato, sulfenato and sulfinato complexes will be discussed in Chapters 3 and 4.

1.2.3 Os^{II} Arene Complexes with Anticancer Properties

Following the growing success of ruthenium complexes as potential anticancer drugs, organometallic osmium(II) complexes, $[(\eta^6\text{-arene})\text{Os}(\text{XY})\text{Z}]^+$, have recently been investigated and show a wide range of *in vitro* and *in vivo* cytotoxic activity. Their activity varies all the way from inactive¹⁰⁵ to an order of magnitude more potent than either cisplatin or their Ru counterparts with negligible toxicity.^{91,92,106,107} In the last five years, most of the Ru-complexes as anticancer agents in the front line (*i.e.* in clinical and preclinical trials) have been reported with their osmium analogues (*vide infra*). Importantly the osmium analogue of NAMI-A exhibits better *in vitro* anticancer activity.¹⁰⁸ The osmium analogue of RAPTA shows similar cytotoxicity,¹⁰⁹ while, in contrast that of KP1019¹¹⁰ and RM175, AFAP51¹¹¹ reveal more and less potent activity in different cancer cell lines. It appears now that the world leading researchers (Sadler,^{105,107,112–114} Dyson^{109,115} and Keppler^{86,93,110,116,117}) in this field explore their new strategies for both Ru^{II} and Os^{II} equivalents.

However, the aqueous chemistry and pharmacological properties of osmium complexes have been explored in only a limited way. Sadler and coworkers have recently reported a series of Os^{II}-arene complexes with promising new and unusual features.^{28,72,91,92,105–107,111–114,118–120} Third row transition metals are usually considered to be more inert than those of the 1st and 2nd rows. Consequently, although Ru^{II} and its heavier

congener Os^{II} arenes are isostructural, their chemical reactivity is different which reflects in the biological activity. The rate of aquation is up to 100x slower (more inert),^{105,109} and the resulting aqua complexes are *ca.* 1.5 pK_a units more acidic for Os^{II}.¹¹⁴ Therefore, at physiological pH, the osmium complexes can exist largely in the less reactive [Os-OH]⁺ form¹¹⁴ which might explain why they are negligibly toxic to normal cells.

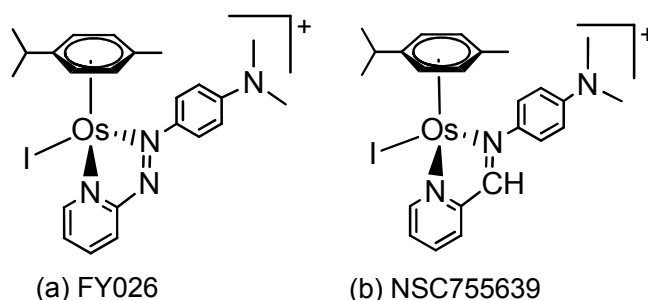


Figure 1.12: Most potent Os^{II}-arene anticancer complexes reported to date by Sadler

To date, two of the most active Os^{II}-arene anticancer complexes are isoelectronic complexes, of azopyridine, [(η^6 -p-cym)Os(Azpy-NMe₂)I]⁺, FY026,^{92,106,107} and iminopyridine, [(η^6 -p-cym)Os(Impy-NMe₂)I]⁺, NSC755639,⁹¹ Figure 1.13, which are even more active than the clinical drug cisplatin *in vitro*. Even though, these bioisosteres show similar activity, interestingly their mode of action is completely different. Os^{II}-arene azopyridine complexes are stable and inert toward aquation. Their cytotoxic activity appears to involve redox mechanisms of GSH by azopyridine ligand.¹⁰⁷ Conversely, iminopyridine complexes show a dual mode of action; direct interaction of DNA by hydrolysis and increasing the level of reactive oxygen species (ROS) via oxidizing the NADH to NAD⁺.⁹¹ Therefore, the mode of activation is different in nature and suggests that subtle changes in structure can lead to dramatic changes in chemical reactivity and biological activity.

1.2.3.1 Rational Design of Os^{II}-arene Complexes with Anticancer Properties

Most of the Os^{II}-arene complexes have a half-sandwich “piano-stool” geometry with the general formula $[(\eta^6\text{-ar})\text{Os}(\text{XY})(\text{Z})]^{n+}$, Figure 1.4b, except the Os^{II} analogue of RAPTA developed by Dyson. As with the analogous Ru(II) arene complexes, this scaffold is attractive for drug design as it allows for fine tuning of the three main building blocks, the arene, the XY bidentate chelating ligand and the monodentate leaving group Z, to optimize the cytotoxicity. The nature of the arene can influence cell uptake and DNA intercalation. The lability of the leaving group Z (Cl or I) is important in hydrolysis activation. The bidentate chelating ligand (XY) controls the stability and the ligand exchange rates of these complexes. The effect of different arene ligands and monodentate leaving group (Z) are analogous to that of its Ru counterparts as discussed in Section 1.2.2.2. However, the effect of different bidentate ligands shows some variations in the stability and kinetics of these complexes as discussed here.

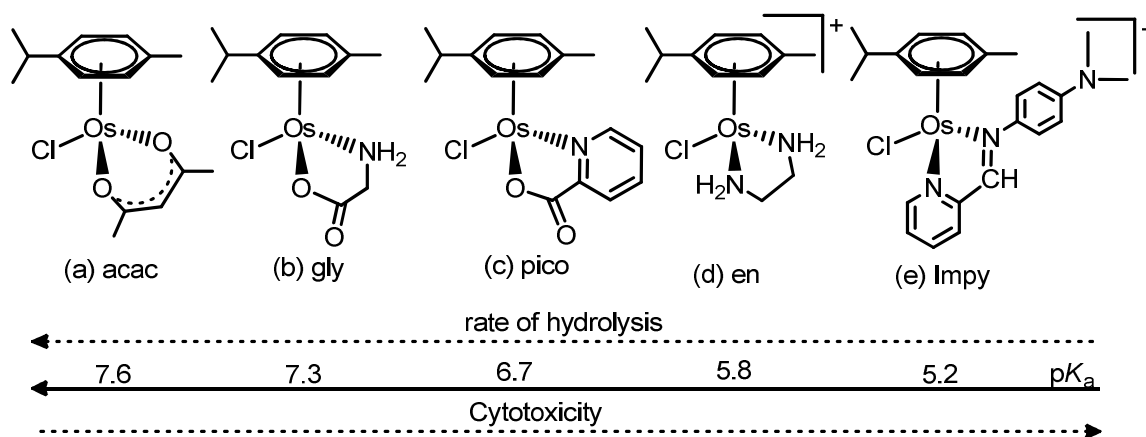


Figure 1.13: Systematic chelating ligand variation in Os^{II}-arene complexes prepared by Sadler.

The lack of information on the aqueous chemistry of Os^{II}-arene complexes under biologically-relevant conditions has been a major obstacle in current attempts to design

anti-cancer drugs. Therefore, current research has focused on the effects of the bidentate ligand XY on the overall reactivity of Os^{II}-arene complexes. Changing the bidentate ligand from *O,O*- to *N,O*- to *N,N*-, Figure 1.13, decreases the hydrolysis rate and increases the acidity.^{105,122} Therefore the resulting Os^{II}-arene aqua complexes are more acidic and hydrolyse more slowly.

The complexes with acac and gly ligands lack cytotoxicity due to their rapid hydrolysis reaction, whereas picolinate complexes, Figure 1.13c, hydrolyse much more slowly, form kinetically stable DNA adducts and exhibit equipotent cytotoxicity to cisplatin in human ovarian cancer cells.^{112,113} Recently reported *N,N*-chelated ligand iminopyridine complexes, Figure 1.13e, fascinatingly show excellent cytotoxicity even higher than cisplatin via dual mode of action, DNA binding via substitution and induce level of ROS.⁹¹

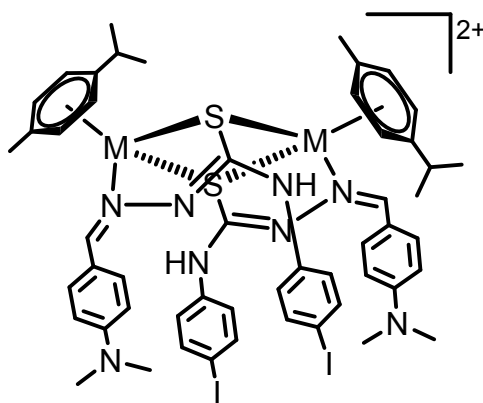


Figure 1.14: Novel Os^{II}-arene complex presently under investigation

As discussed above, the newly developed series of Os^{II}-arene organometallic complexes (Figure 1.13) are good examples of how to tune a family of organometallic complexes all the way from a lack of cytotoxic activity to even more potent than the clinical used drugs cisplatin and carboplatin. Rational design of the chelating ligands and structure of the Os^{II}-arene

complexes play an important role in controlling the reactivity (*i.e.* hydrolysis, acidity of aqua adducts) and biological behaviour (oxidation of GSH and NADH) of these anticancer drugs. To extend this series further, Os^{II} arene complexes with biologically related *S,N*- (thiosemicarbazone) ligands (Figure 1.15) are presently under development by Sadler and coworkers. Investigation of their electronic and geometric structures of these newly developed complexes is described in Chapters 5.

1.3 Cytotoxicity of Ruthenium and Osmium Arene Complexes

Sadler's Ru^{II} and Os^{II} arene complexes generally show very high cytotoxicity against human ovarian cancer cells (A2780) with IC₅₀ values comparable to cisplatin and carboplatin. The anticancer activity of these complexes is compared with that of carboplatin and cisplatin in Table 1.1.

Table 1.1: Cytotoxicity (IC₅₀) of Ru^{II} and Os^{II} complexes toward human ovarian cancer cells, A2780

Ru ^{II} complex	IC ₅₀ /μM	Os ^{II} complex	IC ₅₀ /μM
[(η ⁶ - <i>p</i> -cym)Ru(en)Cl] ⁺	10 ± 1.1 ⁶⁷	[(η ⁶ - <i>p</i> -cym)Os(pico)Cl] ⁺	4.2 ¹¹³
[(η ⁶ -bip)Ru(en)Cl] ⁺	5 ± 0.4 ⁶⁷	[(η ⁶ -bip)Os(pico)Cl] ⁺	4.5 ¹¹³
[(η ⁶ -tha)Ru(en)Cl] ⁺	0.5 ± 0.1 ^{67,80}		
[(η ⁶ -hmb)Ru(en)SPh] ⁺	22 ⁸⁰		
Carboplatin	6 ± 0.7 ^{67,80}		
Cisplatin	0.6 ± 0.06 ^{67,80}		

1.4 Activation Mechanisms of Organometallic Anticancer Complexes

Organometallic anticancer drugs are often prodrugs, *i.e.* precursors to medicinally-active molecules that must undergo either chemical or enzymatic transformation *in vivo* to generate the active drug.¹²³ Metal prodrugs are commonly activated by ligand

substitution, ligand oxidation, a change in oxidation state (redox process), a photochemical process, or combinations of these.²⁸

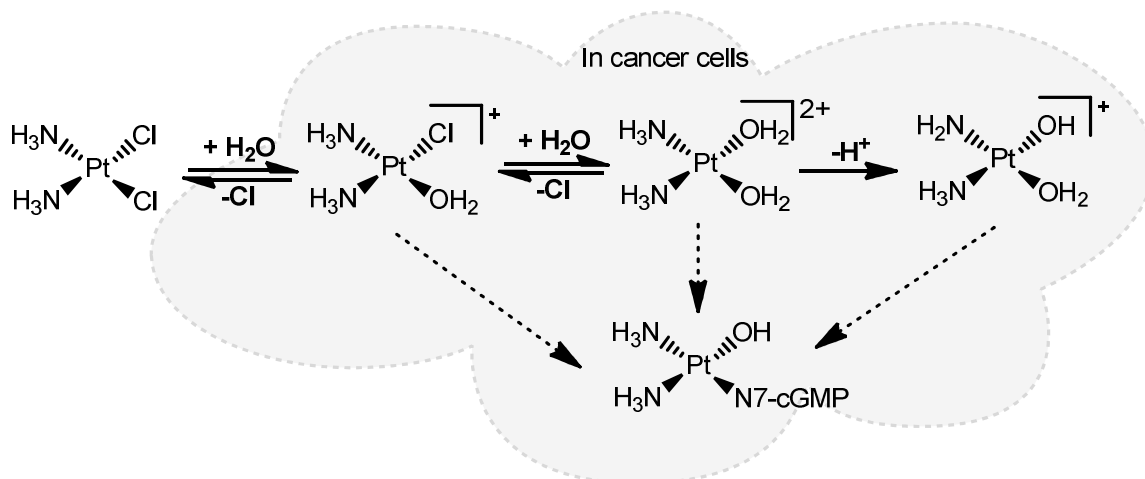
Unlike most organic-based drugs, the metal centre in organometallic chemotherapeutics allows for a wide range of possible coordination numbers, geometries, accessible redox states, and thermodynamic and kinetic properties.¹²⁴ Along with this greater landscape of chemical possibilities provided by the metal centre, the intrinsic properties of the different building blocks (cationic metal ion and ligands) offer different modes of interaction. Combinations of these features provide a wide spectrum of reactivity and mechanisms by which to interact with biological molecules and DNA.

Anticancer properties are achieved via inhibiting the cell growth either by direct interaction with DNA or indirectly by inhibition of DNA synthesis and replication, and cell death (apoptosis). The cytotoxic effects of complexes are experienced by the rapidly dividing tumor cells, but this mode of action invariably affects the normal cells. Therefore, selective cytotoxicity and (multi)drug resistance are currently the biggest challenges in cancer chemotherapy. Promisingly, new candidates have advanced to clinical trials to possibly overcome these problems.²⁶ Accepted and proposed mechanisms for metallo anticancer complexes and some challenges in investigating those mechanisms are discussed in this section.

1.4.1 Mode of Action: Platinum Anticancer Drugs

Cisplatin is a prototypical example of a prodrug that has been extensively studied. The prodrug is activated through hydrolysis of the Pt-Cl bonds. The chloride ligands remain attached to the Pt(II) centre in the blood stream, where the Cl⁻ ion concentration is relatively

high (≈ 100 mM).^{15,16} Inside cancer cells, a decreased Cl⁻ ion concentration (4–20 mM) favours drug aquation with the loss of one or both of the chloride ligands, Scheme 1.3.¹⁵



Scheme 1.3: Activation mechanism of cisplatin

The aquated active cisplatin adducts binds to DNA at the N⁷ position of guanine, and to a lesser extent adenine, through the formation of a covalent bond with the nitrogen atom.¹⁵ Ring closure through the formation of a second DNA bond forms intrastrand and interstrand crosslink bis-adducts. These adducts cause distortions in DNA, including unwinding and bending, and activate various signal-transduction pathways. However, the pathway(s) from Pt-DNA binding to apoptosis remains incompletely elucidated.

Carboplatin was designed to improve the clinical performance of cisplatin.¹³ Aquation of carboplatin yields the same active component as cisplatin and forms the same DNA adducts in a slower rate.^{125,126} Therefore, it is considered as a clinically safer analogue to cisplatin, although it has its own side effect and showed similar drug resistance.¹²⁷

Oxaliplatin is the first approved drug that was capable of overcoming cisplatin/carboplatin resistance.^{15,128} The specific ligand set of oxaliplatin, bidentate ligand

1,2-diaminocyclohexane (dach) combined with another bidentate oxalate ligand, appears to play a crucial role in the non-cross-resistant character with cisplatin. Oxaliplatin predominantly forms oxaliplatin-induced-1,2-intrastrand crosslink DNA (GpG intrastrand)^{129,130} adduct with the bulky hydrophobic dach ligand pointing into the DNA major groove, which prevents binding of DNA repair proteins.¹²⁹ The oxalate ligand also greatly reduces the severity of the side effects of the drug compared with cisplatin.¹³¹

1.4.2 Mode of Action: Ruthenium Complexes

Initially ruthenium anticancer drugs were hypothesized to exert their anticancer activity by direct interaction with DNA as observed with platinum. However, it is now evident that ruthenium shows a number of differences with platinum.¹³² Prominently, ruthenium appears to accumulate favourably in neoplastic masses rather than normal tissues perhaps because it is transported by transferrin into tumors.¹³³ Neoplastic tissues are rich in transferrin receptor therefore transferrin–ruthenium complexes can be actively transported, liberated and then internalized by the tumor.¹³⁴

Intriguingly, some ruthenium anticancer complexes demonstrate greater antimetastatic properties in addition to anticancer activity.^{46,111,135} This antimetastatic effect is likely to be mediated through interactions with extracellular matrix components.^{136,137} A study on biological strengths of Ru and Os analogues suggests that ruthenium seems to play a key role in antimetastatic activity;¹¹¹ however, further studies should be conducted to confirm this property. Due to the above mentioned properties, ruthenium is predicted to show patterns of antitumor activity and clinical toxicity that are unique in nature and distinct from those of platinum.

1.4.2.1 Ru^{III} complexes (NAMI-A and KP1019)

Octahedral Ru^{III}-complexes are relatively inert towards ligand substitution. Therefore, they are essentially prodrugs and remain in their relatively inactive Ru^{III} state until they reach the tumor cells. In a tumor, under lower oxygen content and acidic extracellular pH, the appreciable amounts of cellular reducing agents such as glutathione and ascorbic acid provide physiologically accessible Ru^{III}/Ru^{II} redox potential to selectively reduce the drugs from inactive Ru^{III} to more reactive Ru^{II} species.¹³⁸ This is called the “activation-by-reduction” mechanism.³³ These Ru^{III} complexes therefore show selective cytotoxicity towards tumor and even hypoxic tumors that are more likely to be resistant to chemotherapy and radiation.¹³⁹

The mechanism of action of NAMI-A is recognized by substitution of Cl⁻ ligand^{140,141} followed by multiple interactions with biological molecules outside and inside the cells.^{20,30} This leads to a direct coordination to nucleic acids and tumor cell DNA.¹⁴³ However, molecular level investigation of these interactions is not well documented. The mode of activation of KP1019 is initiated with its binding to transferrin by substitution of Cl⁻ ligand.¹⁴⁴ Initially, it was suggested that it would undergo a redox reaction followed by apoptosis via the mitochondrial pathway,^{138,145} but this suggestion is not well supported by recent experimental findings and it appears that the adducts of both species (Ru^{III} and Ru^{II}) are found to be active.^{144,146} However, formation of ROS species and DNA interactions are also reported.^{147,148} Unfortunately, KP1019 also has no clear molecular level mechanism of action and/or on the main molecular target responsible for the anticancer activity.²⁶

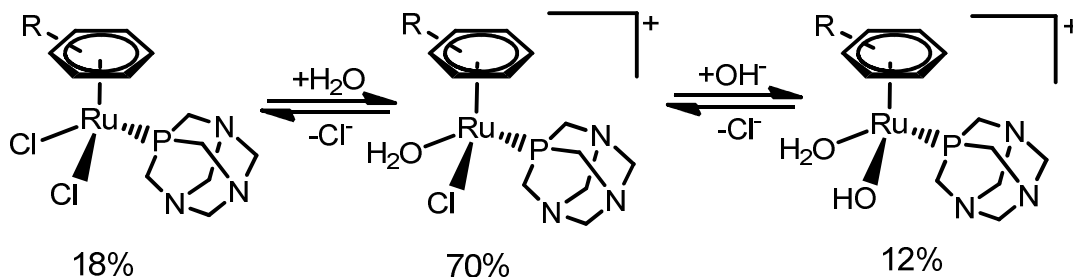
Therefore, it appears that lack of understanding of not only their structure or behaviour in biological environment but also their exact molecular mechanisms of action, is a major disadvantage in their further clinical developments.

1.4.3 Mode of Action: Ru^{II}-arene Complexes (RAPTA and RM175)

Half-sandwich, pseudo-octahedral Ru^{II}/Os^{II}-arene complexes of the three main groups do not possess similarities in their activity (as discussed in Section 1.2.2.2) or their mechanism. The mode of activity of these complexes is unique in their nature and different from that of NAMI-A or KP1019.

1.4.3.1 RAPTA Family complexes

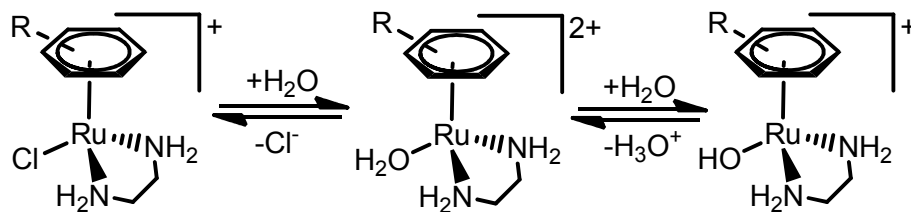
Studies on the mode of action of these RAPTA-type complexes are limited.³⁸ However, available studies suggested that the major intracellular targets of RAPTA compounds appear to be proteins, although DNA binding is also observed.⁵³ In the RAPTA-C complex, aquation seems to be the activation step for their cytotoxicity, Scheme 1.4. Hydrolysis of this complex is suppressed in the blood plasma where Cl⁻ concentration is about 100 mM, but occurs once it enters the cell cytoplasm where Cl⁻ concentration is much lower.⁵¹ Then the labile aqua species undergo substitution by biomolecules.⁵¹ However, the hydrolysis-resistant (RAPTA-oxalato and RAPTA-diketonato) complexes, which are also equally cytotoxic, undergo a different mode of mechanism called “ring slippage” of the arene to create a vacant coordination site.^{149,150}



Scheme 1.4: Hydrolysis mechanism of RAPTA-C complexes in pure water, where R is *p*-cym

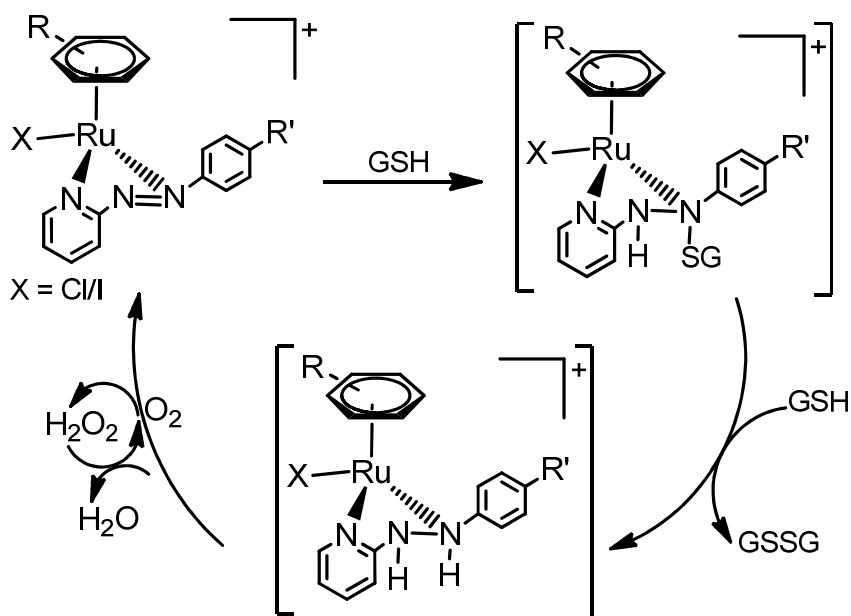
1.4.3.2 Sadler's RM175-type complexes

The biological activity of these complexes appears to be initiated by Ru-Z (Z = Cl, I or N₃) ligand hydrolysis, Scheme 1.5.^{89,94} The hydrolysis of the prodrug, $[(\eta^6\text{-ar})\text{Ru}(\text{en})\text{Cl}]^+$, is suppressed outside cells by the high concentration of chloride ions, a common suppression mechanism applied for Pt and Ru prodrugs. However, in the nucleus and cytoplasm, where the Cl⁻ concentration is lower, the hydrolysed species are predominant.⁸³ The aqua species, $[(\eta^6\text{-ar})\text{Ru}(\text{en})\text{OH}_2]^{2+}$, is more reactive and it appears that the predominant species at that particular pH might influence the cytotoxicity. The pK_a value of the corresponding aqua complexes of this series is ≈ 8 .⁹⁴ Therefore, at physiological pH 7.4, the more active aqua adducts should prevail.⁷⁰ The rate and extent of hydrolysis is highly depend on the nature of the monodentate ligand and sterically-hindered ligands can significantly affect the rate of aquation.⁸⁰



Scheme 1.5: M-Cl bond activation mechanism of Ru^{II}/Os^{II} – arene bidentate complexes, where R denotes arene

The hydrolysis reaction appears to be very similar to that of cisplatin but these complexes are active toward cisplatin-resistant cells. This suggests that the mode of interaction to DNA is different.^{151,152} In fact, the [Ru-ar-en] species strongly interact with DNA through a dual mode of binding: monofunctional coordination to N7 of guanine,⁶⁶ which is different from the bifunctional adduct of cisplatin,¹⁵¹ accompanied by arene intercalation in addition to strong stereospecific hydrogen bonding (between an en NH group and the C6 carbonyl group of the guanine system).^{65,153} The intercalation ability, hydrophobic π - π arene-nucleobase stacking interaction, increases with hydrophobicity (bz < *p*-cym < bip < tha)⁶⁶ and length (*p*-terp > *o*, *m*-terp)¹⁵⁴ of the arene ring. Further, bioanalytical studies on these interactions show that the [Ru-ar-en] species bind preferentially to guanine residues in double-helical DNA.¹⁵¹



Scheme 1.6: Proposed mechanism for Ru^{II}-arene azopyridine, $[(\eta^6\text{-ar})\text{Ru}(\text{azpy-R})(\text{X})]^+$, complexes

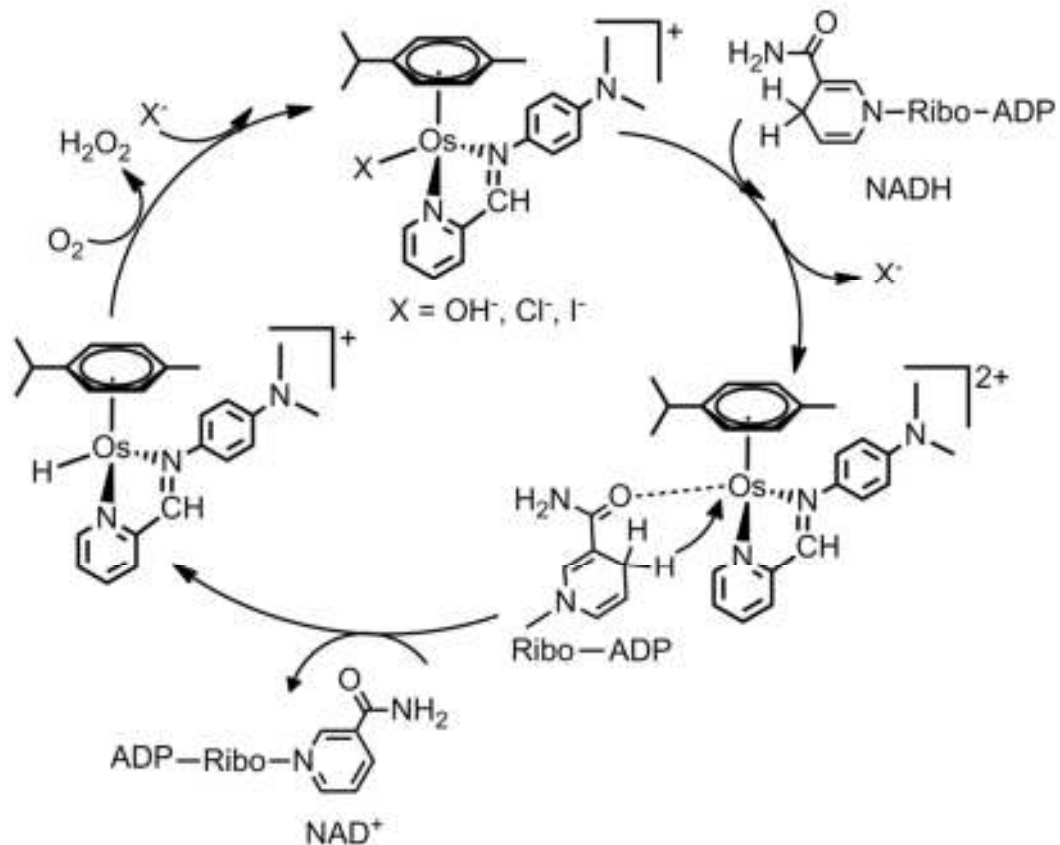
Intriguingly, an unusual mechanism was recently reported for azopyridine complexes, $[(\eta^6\text{-ar})\text{Ru}(\text{azpy-R})(\text{X})]^+$ where $\text{X} = \text{Cl}$ or I , which are substitution inert but highly cytotoxic. The

iodido complex is equipotent to cisplatin in ovarian and lung cancer cells. In contrast, the chlorido complexes are an order of magnitude less potent and less inert. They slowly lose the arene in aqueous solution. The role of the iodide ligand in their cytotoxicity is not known. However, cytotoxicity appears to involve an increase in ROS, formed during activation by reduction of the ligand by GSH, Scheme 1.6. The reduction potential for azopyridine ligands is high but it is biologically achievable when the ligand coordinates to Ru^{II}.¹⁵⁵ However, the effect of the metal center has not been investigated.

1.4.4 Mode of Action: Os^{II}-arene Complexes

The activation mechanism of osmium analogues, prepared by Dyson, Sadler and Keppler, appears to follow a very similar mechanism to that proposed and accepted (hydrolysis followed by DNA binding or protein interaction) for their ruthenium analogues.^{109,116,122,156} However the Os complex AFAP51 binds to DNA in a different mode of interaction (unwinding without bending) which induces non-repairable damage to DNA by causing a large degree of DNA unwinding (21-27°)¹⁵⁶ compared to that of Ru^{II} complexes (7-14°)¹⁵¹ or cisplatin (6° and 13° for mono- and bi-functional respectively).¹⁵⁷

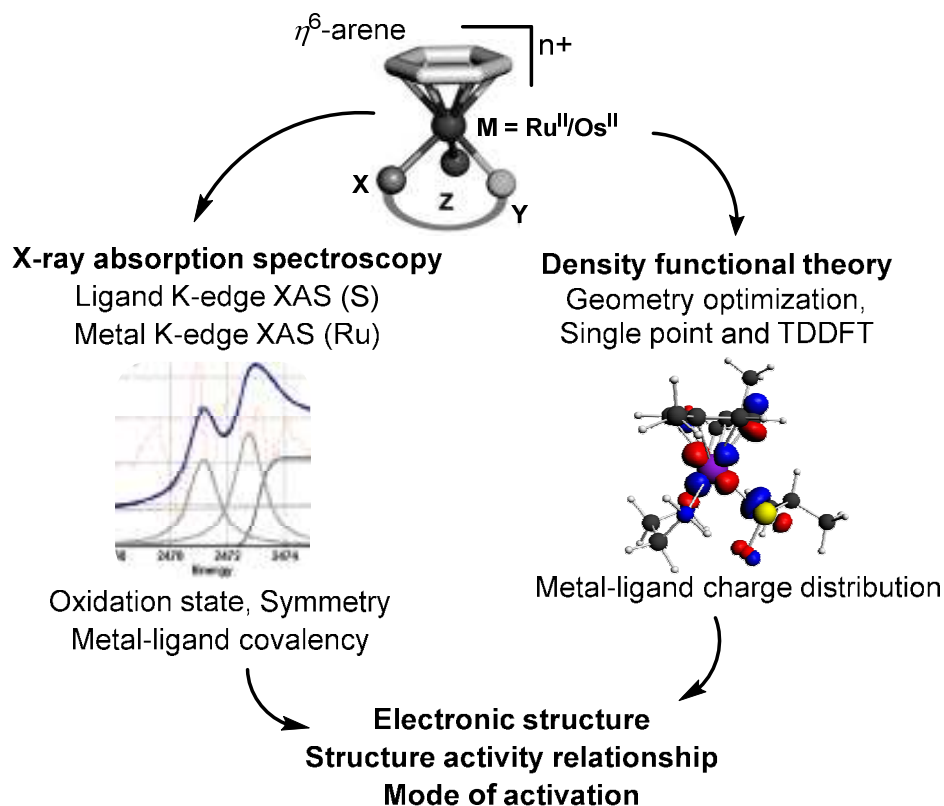
A novel mechanism has recently been proposed for Os^{II}-arene iminopyridine complexes that are more potent than cisplatin with nanomolar IC₅₀ values. They undergo ligand substitution in aqueous solution to bind DNA, in the meantime controlling the modulation of redox pathways by catalysing the oxidation of NADH → NAD⁺ in cancer cells (Scheme 1.7). Exceptionally, the driving force for both mechanisms comes from the activation of the Os-Z bond, where Z = I/Cl.⁹¹ These studies further suggest that Os^{II}-arene complexes own novel mechanisms of action that can be finely tuned through the choice of the ligands.



Scheme 1.7: Proposed mechanism for the oxidation of NADH to NAD⁺ catalysed by Os^{II}-arene iminopyridine complex

The mechanism described in this section clearly indicates that these organometallic complexes exhibit a wide spectrum of anticancer activity and mode of actions with biological molecules which are very unique in their nature. It is evident that a more fundamental understanding of the mechanism and the structure activity relationship of these metallodrugs is essential for a more rational design of alternatives. That should help in finding ways to reduce their side effects and also to speed up the clinical drug development process. With this goal in mind, this thesis uses an interdisciplinary approach, XAS in concert with DFT, to investigate the electronic structure of the Ru^{II} and Os^{II} arene complexes with anticancer properties. The approach is described in detail in section 1.4.

1.5 Applied Approach



Scheme 1.8: Systematic approach used to investigate the research problems described in this thesis

As illustrated in Scheme 1.8, the work presented in this thesis makes use of XAS as a primary experimental technique. XAS is an element-specific, powerful probe to study metal-ligand covalency. The edge jump is sensitive to Z_{eff} , the effective nuclear charge, and therefore well suited to resolve the research problems described in this thesis. The main experiments carried out are: (a) metal K-edge XAS, to examine the Z_{eff} on the metal center; (b) ligand (S) K-edge XAS, to examine the Ru-S and Os-S covalency and the oxidation state. The basic principles of these techniques, experimental set up and the data analysis are discussed in Section 2.1.

All the Ru and Os complexes investigated herein were prepared and characterized for purity by members of Peter Sadler's group in the United Kingdom.* Interpretation of XAS data was obtained through extensive multistep computational processing of the data combined with theoretical approaches to extract the accurate results. Several DFT calculations were performed to support the experimental XAS results. Details of these calculations are described in Section 2.2.

In recent years, XAS studies, combined with other bioanalytical techniques, have effectively been used to investigate and corroborate the postulated mechanism of Pt, Ru and other metallodrugs.^{158,159} An interesting study on octahedral Pt^{IV} compounds in cultured cancer cells shows that Pt^{IV} undergo activation by reduction to form active Pt^{II} species and the redox speciation in cancer cells.^{160,161} Another study characterized the Ru^{III} antimetastatic agent NAMI-A with bovin serum albumin (BSA) shows that Cl⁻ ligand is substituted upon binding the protein; however, the metal center remains its initial oxidation state (Ru^{III}).^{140,141} An investigation of the electronic structure of a series of Ru^{III} and Ru^{II} complexes related to NAMI-A and KP1019 was accomplished with the help of XAS and DFT calculations.¹⁶² A very recent study on KP1019 shows that the mode of activation of the complex appears to involve with two different active species: (i) Ru^{III} species with one Cl⁻ substituted (ii) Ru^{II} species with three Cl⁻ ligand substituted; formed upon binding to transferrin and GSH. Both species potentially target the cancer cells.¹⁴⁴ However further studies need to be conducted to identify the key species accountable for the anticancer activity of KP1019.

* All the complexes studied in this thesis were provided by members of Peter Sadler's group from University of Edinburgh and University of Warwick, United Kingdom

CHAPTER 2. METHODOLOGY

2.1 X-ray Absorption Spectroscopy (XAS)

2.1.1 Basic Principles of X-ray Absorption Spectroscopy

XAS is an element specific spectroscopy sensitive to the local chemical and structural environment of the absorbing atom(s). It is an effective tool for studying most elements of the periodic table and can be particularly useful for so-called “spectroscopically silent” species such as Zn^{II} , Fe^{II} and Cu^{II} .^{163,164} XAS is extremely useful for studying transition metal complexes in biological systems.^{165–167} The electronic and geometric structure of a site can be investigated from the perspective of component elements within an active site of interest, without interference from other elements. A major advantage of this approach is that it can be performed on virtually any type of sample (gas, crystalline, amorphous or solution even in μM concentration) with generally minimal sample preparation.^{164,168}

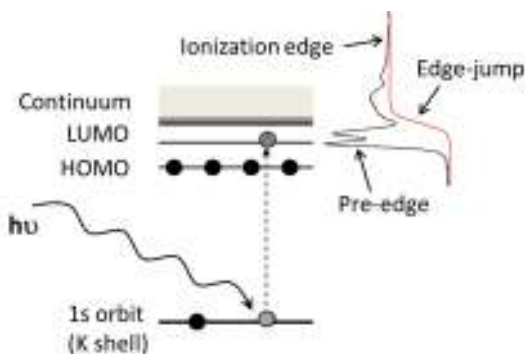


Figure 2.1: Energy transition and resulting spectrum of typical K-edge XAS experiment. Spectrum illustrating the key features (pre-edge, edge-jump and ionization edge)

An X-ray absorption spectrum is obtained when an incident monochromatic X-ray beam has sufficient energy to excite a core electron to an orbital, either partially filled or empty, or to the continuum as shown in Figure 2.1. An abrupt increase in the absorption coefficient

gives rise to the dominant feature of the K-edge XAS spectrum known as “absorption edge”, “rising edge” or “edge jump”.^{163,164} The edge jump corresponds to transitions that have adequate energy to eject a core electron from an atom to the continuum via the photoelectric effect. Given that core electrons have well-defined binding energies, the corresponding absorption edges also occur in predictable energy regions. These edges are typically labelled according to the orbital/state from which the core electron is ejected: *i. e.*, K = 1s, L₁ = 2s, L₂ = 2p_{1/2}, L₃ = 2p_{3/2}, M₁ = 3s... etc. The uppercase letter represents the principal quantum number of the orbital and the subscript number denotes a specific absorption line.¹⁶⁹

Table 2.1: Electron binding energies of the elements investigated in this thesis

Element	K-edge (eV)	L ₃ -Edge (eV)	L ₂ -Edge (eV)
Ruthenium	22117.0*	2838.0	2967.0
Sulfur	2472.0*	162.5	163.6
Chlorine	2822.4*	200.0	202.0
Osmium	73871.0	10871.0	12385.0

*experimental results presented only from K-edge of Ru, S and Cl in this thesis

The exact energy of the absorption edge also depends upon the effective nuclear charge (Z_{eff}) of the absorbing atom and has been widely used as an oxidation state marker.^{164,170,171} Table 2.1 shows the absorption edge of the elements investigated in the works herein. The absorption energy of a particular edge (*e.g.* K-edge) is well separated and unique for each element and edges even in the nearest neighbours S and Cl.¹⁶⁹ However, Ru L₃-edge (2838 eV) is always interfered by Cl K-edge (2822.4 eV) since their corresponding edge energies are very close. In that case, multiple steps of data processing is required.¹⁷²

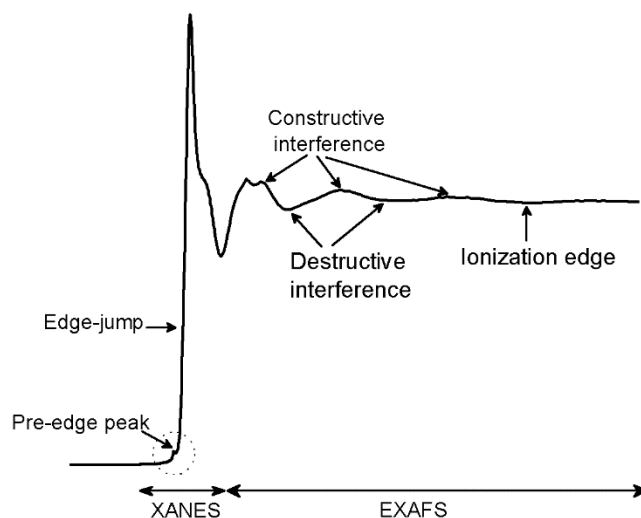


Figure 2.2: Mn K-edge XAS of $\text{rac-[Mn}^{\text{III}}(\text{EHPG})\text{]Na}$, (where EHPG - ethylenebis[*o*-hydroxyphenyl] glycine)), illustrating XANES, EXAFS regions and other spectroscopic features

XAS spectra are generally subdivided into two main regions: the X-ray absorption near edge structure (XANES) and extended X-ray absorption fine structure (EXAFS), see Figure 2.2. The XANES region is generally considered to range from a few electron-Volts (eV) below the element's absorption edge to ~ 50 eV above the edge. Key features included in this region are the aforementioned absorption edge and in some cases just below the edge, minor peaks visible are denoted as pre-edge features. In first row transition metal K-edge spectra, the pre-edge features originate from weak quadrupole allowed transition ($1s \rightarrow 3d$). The pre-edge intensity and position provide information about the electronic environment of the absorbing atom. Therefore, the XANES region of the spectrum is sensitive to the oxidation state, the immediate coordinating atom, and electronic structure of absorbing atom.^{163,164,173} In this thesis, XANES of Ru, S and Cl K-edges have been investigated to get oxidation state, covalency and geometry and electronic structures of the complexes studied.

The EXAFS region, typically defined from ~ 50 eV to up to 1000 eV above the edge, is dominated by oscillations in the intensity (Figure 2.2) as a function of incident photon energy.

These oscillations result from constructive and destructive interference of the outgoing photoelectron waves due to back-scattering from neighbouring atoms. Therefore, EXAFS provides direct information regarding the local geometric structure around the element of interest.¹⁶³ The analysis of reasonable quality EXAFS can give accurate bond lengths ($\pm 0.02 \text{ \AA}$), as well as information on coordination number (± 1) and the chemical identity of neighbouring atoms. In many respects, EXAFS analysis is a complementary technique to single-crystal X-ray diffraction (XRD) for substances in amorphous or solution state.¹⁶⁸

Like every other technique, XAS also has its limitations: it requires structural models and lacks chemical selectivity for nearest neighbouring atoms in the same row of the periodic table (e.g.: C / N / O) in the EXAFS analysis. Recent advances, such as high energy resolution fluorescence detection (HERFD)¹⁷⁴, can address some of these limitations although the required instrumentation is not generally accessible.¹⁶⁸ The EXAFS region of the XAS spectrum is not a major focus of the work described in this thesis; however details of the theory and information content of this region of the spectrum can be found in recent reviews.^{158,163,175,176}

2.1.2 Metal K-edge X-ray Absorption Near Edge Structure

Metal K-edge XANES occurs when a $1s$ core electron is excited to the valence and conduction bands ($nd \leftarrow 1s$),¹⁶⁴ Figure 2.1. Therefore, it consists of two important features of relevance to ligand effects on the metal center, *i.e.* bound state transitions in the pre-edge region and the ionization of $1s$ electrons, IE_{1s} , resulting in the absorption edge.^{177,178} The pre-edge features of the 2nd row transition metal (*e.g.* Ru) complexes are usually attributed to electric quadrupole-allowed $4d \leftarrow 1s$ transitions (analogues to $3d \leftarrow 1s$ pre-edge transitions of 1st row transition metal complexes),¹⁷⁸ as a result the intensity of the pre-edge is very

weak. However, mixing of the metal 5p orbitals into the valence 4d orbitals can occur in non-centrosymmetric complexes. The intensity of pre-edge features can be greatly enhanced by even small amounts of 5p mixing, as $5p \leftarrow 1s$ transitions are formally electric dipole allowed.¹⁶³

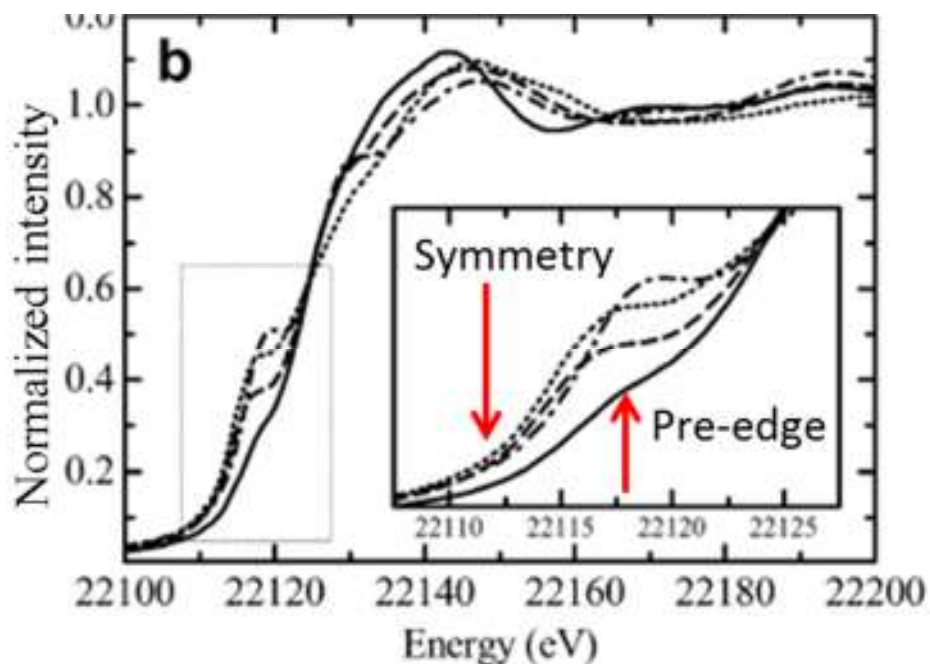


Figure 2.3: Ru K-edge XAS of Ru carbene complexes illustrating the pre-edge intensity decreases with increased centrosymmetry of the complexes. Reprinted from Getty *et al.*, *Inorg. Chim. Acta* 2008, 361, 1059–1065. Copyright 2008, with permission from Elsevier.¹⁷⁸

In cases where there can be no 5p mixing, such as in complexes with octahedral geometry, the pre-edge features gain very low-intensity and are often buried under the edge. Such issues have recently been investigated for a series of well-defined Ru^{II} carbene complexes.¹⁷⁸ This study clearly demonstrated the correlation between the intensity of the $4d \leftarrow 1s$ pre-edge features and the presence of distortions in the geometric structure that could lead to Ru 4d–5p orbital mixing (see Figure 2.3).

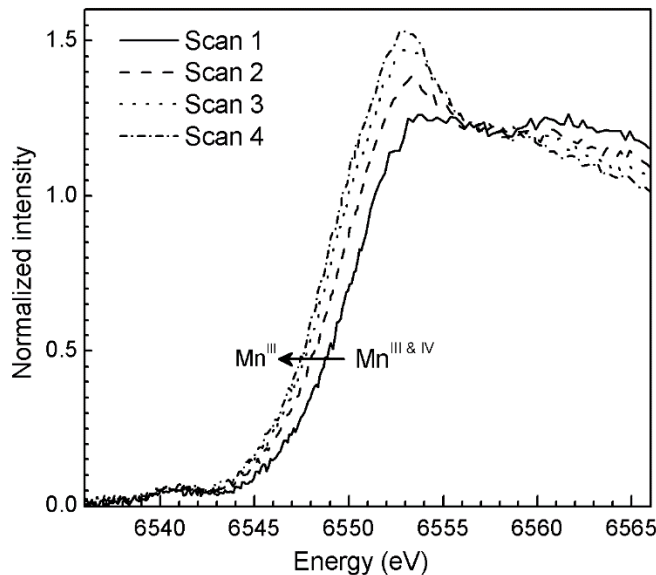


Figure 2.4: Mn K-edge XAS of Mn-transferrin complex showing the edge-jump shifts with Z_{eff} during the photoreduction of the sample with multiple scans.

The second and most dominant feature of this region is the intense absorption-edge. It corresponds to the electric dipole allowed ionization of the core $1s$ electron to continuum (e.g. $\text{Ru}_{\infty} \leftarrow 1s$). The energy at the 1st inflection point of the edge is typically used as a measure of the ionization energy of the K-shell ($1s$) electron (IE_{1s}), and it is sensitive to the effective nuclear charge of the metal center (Z_{eff}),¹⁷⁷ Figure 2.4. Generally, as the Z_{eff} of the absorbent increases, the absorption-edge shifts to higher energy. The change in Z_{eff} is felt strongly on the core $1s$ electron compared to that of weakly bound valence electrons. Consequently, the energy gap between the core and the valence level increases and thus the absorption-edge shifts to higher energy.¹⁶⁴ The energy of the absorption-edge is widely used as a marker of metal oxidation state.^{170,171,179}

It has been noted that there are some exceptions to this rule¹⁷¹ and that other factors such as ligand type, $5p \leftarrow 1s$ transition and multiple scattering features can also affect the energy position. Therefore, a shift in edge energy with the oxidation state is relative and

studies should be done with a group of complexes containing the same spin state, similar ligand systems and geometry.^{163,164,180} All the Ru complexes studied herein are mostly pseudo-octahedral complexes with similar ligand fields, therefore the Ru K-edge can be used quite reliably to probe the oxidation state of the metal, as well as the geometry of these complexes.

2.1.3 Ligand K-edge X-ray Absorption Near Edge Structure

In transition metal complexes, an important factor in bonding is the electron delocalisation between the metal and the ligand (*e.g.* mixing of Ru_{4d} with S_{3p} to form a Ru-S bonding interaction), often referred to as *covalency*.¹⁶⁷ The covalency of metal-ligand bonds is an important factor in defining chemical and physical properties.^{167,181} It can therefore be highly informative to experimentally determine the metal-ligand covalency in complexes for which the electronic structure is of interest.

Ligand K-edge XAS involves the ligand core electron ($1s$) excited to the valence (np) and conduction bands, $np \leftarrow 1s$.¹⁶⁷ It is a powerful tool to address the electronic structures of metal-ligand interactions in transition metal complexes.^{182,183} The intense pre-edge features result from dipole allowed transitions ($np \leftarrow 1s$) from ligand $1s$ core electrons into delocalized antibonding molecular orbitals, which are formed with significant contribution from metal and the ligands.¹⁸⁴ The intensity of the ligand pre-edge feature is proportional to the mixing of ligand orbitals into the metal d orbitals.¹⁸⁵ Therefore, ligand pre-edge intensity is a direct probe of the covalency of a metal-ligand bond, and the energies of ligand pre-edge transitions reflect the relative ligand field strength experienced by the metal in a ligand system.¹⁸⁴

Ligand K-edge XAS is often considered a better probe than metal K-edges to measure covalency due to the increased resolution of transitions in the soft X-ray region obtained by the combination of reduced core hole lifetime and improved monochromator resolution,^{182,184} and the increased electric dipole-allowed intensity of the ligand pre-edge features. Above all, the main advantage of XAS is it does not require a nuclear spin whereas this is necessary for analysis of covalency using EPR spectroscopy.¹⁸⁴

The quantification of sulfur K-edge to investigate the nature of metal-sulfur bonding is used extensively in this thesis and is discussed in detail in section 2.1.4.1. In addition, Cl K-edge is also used wherever possible as a secondary probe to study the ancillary ligand effect on the metal center. However it is limited to the qualitative analysis herein. Quantitative ligand K-edge XAS as a tool to measure covalency has been pioneered by Solomon, Hedman, Hodgson and coworkers.^{182,184} It has now been extensively used to determine metal-ligand covalency of S and Cl ligands in transition metal complexes.^{99,167,183,186–190} The success of this approach has created an impetus to expand the methodology to other elements – such as P,^{191–193} Br,¹⁹⁴ C,^{195,196} and O.¹⁹⁷ However, more studies should be conducted to corroborate these ligand K-edges for their wide applicability.

2.1.3.1 Sulfur K-edge X-ray Absorption Near Edge Structure

Sulfur is one of the classic examples of a spectroscopically silent element with poor NMR characteristics (small ³³S nuclear magnetic moment, low natural abundance, and large line widths)¹⁹⁸ and a few alternative spectroscopic approaches. However, sulfur K-edge XAS exhibits relatively sharp linewidths and a large chemical shift range over its range of oxidation states as shown in Figure 2.5.¹⁹⁸ Interestingly, the energy of the edge jump (consequently the

pre-edge features) increases with an increase in the formal oxidation state (Z_{eff}) of the sulfur.^{198,199} In addition, when a sulfur species is coordinated to a metal, pre-edge features corresponding to $M_{\text{nd}}-S_{\text{o}^*} \leftarrow S_{1\text{s}}$ transitions appear in the spectrum. The energy of such features depend on the Z_{eff} of the metal. Therefore, S K-edge XAS is sensitive to the chemical nature and Z_{eff} of the ligand, and the Z_{eff} of the coordinated metal.^{200,201}

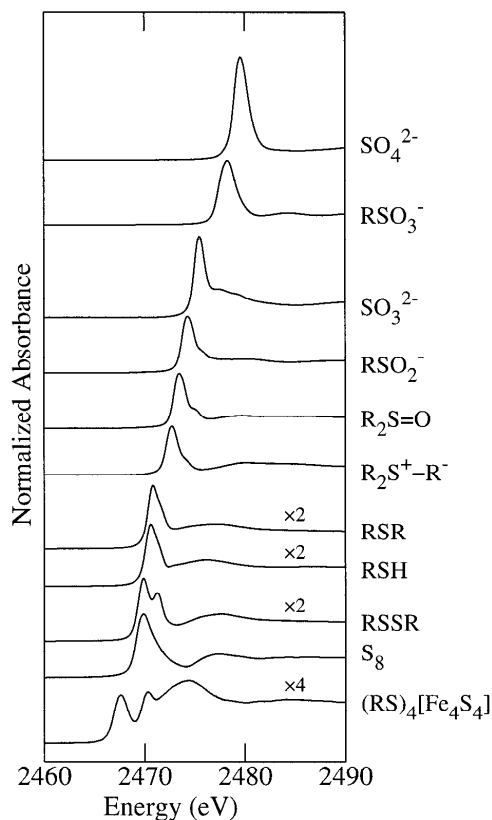


Figure 2.5: S K-edge XAS of series of sulfur redox species. Reprinted from Pickering *et al. FEBS Lett.* 1998, 441, 11–14, Copyright (1998) with permission from Elsevier

Pre-edge Intensity and Covalency: The intensity of each pre-edge feature results predominantly from redistribution of the localized electric dipole-allowed atomic $S_{3\text{p}} \leftarrow S_{1\text{s}}$ transitions to formally forbidden $M_{\text{nd}}-S_{\text{o}^*} \leftarrow S_{1\text{s}}$ transitions, through covalent $S_{3\text{p}}/M_{\text{nd}}$ mixing (see Figure 2.6). The intensity of the transition is thus directly proportional to the extent of $S_{3\text{p}}$ mixing in each antibonding orbital.¹⁸⁵ However, the studies discussed herein concentrate

on the metal-sulfur (M-S) valence orbital which is closely related to the reactivity of the complexes. In XAS, the M-S bond is studied indirectly through its M-S antibond, represented by the lowest energy feature corresponding to $M_{nd} \leftarrow S_{1s}$ transition in the spectrum, Figure 2.6. The intensity therefore reflects the amount of S_{3p} character in the $Ru_{4d\sigma^*}$ acceptor orbital (β) as shown in equation 2.1. It is assumed that the transition originates from a localized core orbital, therefore contributions from other atomic orbitals (i.e., α , χ_l in eq 2.1) do not significantly impact the total intensity of intense electric dipole transitions.^{167,200,202}

Equation 2.1: Ground state wave function of metal-sulfur ligand LUMO orbital, $Ru_{4d\sigma^*}$

$$|Ru_{4d\sigma^*}\rangle = \alpha|Ru_{4d}\rangle - \beta|S_{3p}\rangle - \sum_i \chi_i |L_i\rangle$$

Where, $|Ru_{4d\sigma^*}\rangle$ - LUMO wave function

$\alpha|Ru_{4d}\rangle$ - Ru metal atomic orbital wave function

α - Amount of Ru_{4d} character in $Ru_{4d\sigma^*}$ orbital

$\beta|S_{3p}\rangle$ - Ligand atomic orbital wave function

β - Amount of S_{3p} character in $Ru_{4d\sigma^*}$ orbital

$\sum_i \chi_i |L_i\rangle$ - Other ligands atomic orbital wave function

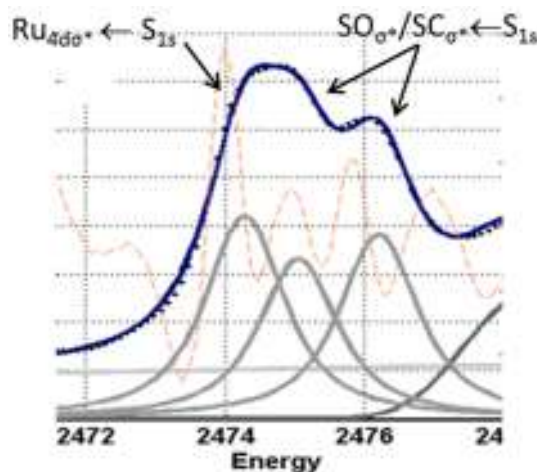


Figure 2.6: Extracting the pre-edge intensity involved in each features of S K-edge XAS obtained from $[(\eta^6\text{-hmb})Ru(en)(SOiPr)]^+$ complex (where hmb – hexamethyl benzene, *iPr* – isopropyl).

Thus, the amount of S_{3p} character (β) involved in that transition can be quantitatively determined from two parameters, as shown in equation 2.2: the total integrated area under the S K-edge peaks, ($I_{Ru_{4d\sigma^*} \leftarrow S_{1s}}$), and the dipole integral, $\langle S_{3p} | r | S_{1s} \rangle$, which gives the intensity of the parent $S_{3p} \leftarrow S_{1s}$ electric-dipole-allowed transition. The total integrated intensity can be obtained from the experimental data by systematic peak fitting. The reference dipole integral, $\langle S_{3p} | r | S_{1s} \rangle$, has been extensively studied and standardized experimentally^{184,187,203} and theoretically¹⁸⁵ by Solomon and coworkers.

Equation 2.2: Intensity of $Ru_{4d\sigma^*} \leftarrow S_{1s}$ transition

$$I_{Ru_{4d\sigma^*} \leftarrow S_{1s}} = \beta^2 \langle S_{3p} | r | S_{1s} \rangle$$

Where $\langle S_{3p} | r | S_{1s} \rangle$ – Dipole integral

β – S_{3p} character

S_{3p} Character Quantification:

The amount of S_{3p} -character involved in each antibonding orbital is reflected by the pre-edge intensity and hence, indirectly measures the S-covalency of the bonding orbitals. The dipole integral, $\langle S_{3p} | r | S_{1s} \rangle$ of each sulfur atom involved with a transition is consequently required to extract the S_{3p} character from the pre-edge intensity (equation 2.3). The dipole integral of a series of S-based ligands is calculated from the analysis of ³³S EPR superhyperfine factor¹⁸⁷ and X-ray photoelectron spectroscopy (XPS).¹⁸⁴ These studies have demonstrated that the inherent dipole integral for a $S_{3p} \leftarrow S_{1s}$ transition depends on the charge on the S ligand and the nature of the M-S overlap (σ vs π), which modulates the radial distribution function of both the S_{1s} and S_{3p} orbitals.

Equation 2.3: Relationship between dipole integral ($\langle S_{3p} | r | S_{1s} \rangle$), S_{3p} character (β) and pre-edge intensity

$$D_o = \left(\frac{A}{3n} \right) \beta^2 \langle S_{3p} | r | S_{1s} \rangle$$

Where, D_o – total area under the pre-edge transition

A – number of holes (either in metal nd or ligand np)

n – number of absorbing S atoms

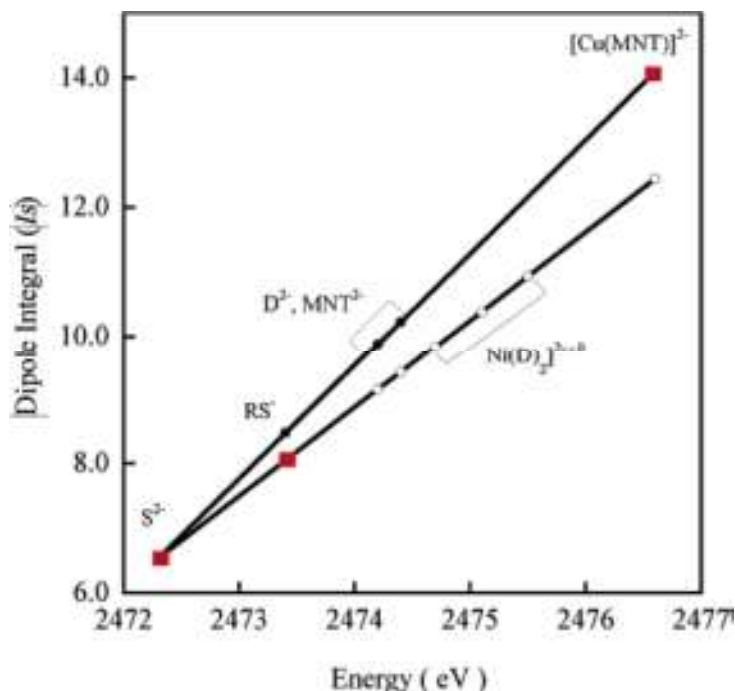


Figure 2.7: A series of S-ligands illustrating a linear relationship between dipole integral factor and $S_{3p} \leftarrow S_{1s}$ transition energy. Adapted with permission from Sarangi *et al. J. Am. Chem. Soc.* 2007, 129, 2316-2326. Copyright 2007 American Chemical Society

An accurate linear correlation is obtained between the dipole integral for the $S_{3p} \leftarrow S_{1s}$ transition and its energy as shown in Figure 2.7. This valuable experimental conclusion is supported by DFT calculations that show a nearly linear increase in the dipole integral when the charge on the absorbent S atom is increased.¹⁸⁵ This is due to the fact that an increase in charge on the S atom shifts the core 1s orbital to deeper binding energy relative to the

valence ($3p$) orbitals. Therefore, as the energy gap of S_{3p} (valence) $\leftarrow S_{1s}$ (core) transition increases, the dipole integral consequently increases.¹⁸⁷

The studies described herein involve a range of Ru^{II} and Os^{II} arene S -ligand complexes. The S -ligand on each complex shows unique Z_{eff} and mode of interaction with metal ions. Therefore, the dipole integral of each complex is directly obtained from the extrapolated graph of Figure 2.7 based on their $S_{3p}\leftarrow S_{1s}$ transition energy. The estimated values used to extract the S_{3p} character of each complex are mentioned in the relevant chapters and show reasonable agreement with literature values reported for these type of complexes.^{187,204}

2.1.4 Instrumentation and Experimental Setup

XAS requires an intense and polychromatic X-ray source. Thus it needs the use of synchrotron radiation. Synchrotron radiation is the name given to the broad spectrum of electromagnetic radiation emitted by relativistic accelerated charged particles, *i.e.* electrons or positrons, travelling in polygon accelerators. Synchrotron sources produce very intense, collimated and polarized X-rays which contain a continuous band of wavelengths spanning a wide range, from μm (infrared) to pm (hard X-ray). Such sources can be tuned to any desired wavelength using appropriate optical devices, monochromators, and filters. In addition, 3rd generation synchrotron sources produce highly intense, parallel and narrow beams of X-rays,^{205,206} optimized for photon flux and brilliance. The data presented in this thesis were collected at two 3rd generation synchrotron radiation facilities: the Stanford Synchrotron Radiation Lightsource (SSRL, Stanford, California) and the Canadian Light Source (CLS, Saskatoon, Saskatchewan).

2.1.4.1 Synchrotron Radiation Components

Figure 2.8 illustrates the main components of a synchrotron source. A hot filament in an *electron-gun* produces free electrons. Those electrons are accelerated using a linear accelerator (linac) into an evacuated *booster ring*, where they further accelerate to the energy of the electrons in the main storage ring and then are periodically injected into the *storage ring*. The storage ring is built with arced sections containing bending magnets and straight sections containing insertion devices such as wigglers and undulators. Bending magnets accelerate the electrons around the arced sections (into the next straight section). The energy lost by electrons due to emission of synchrotron radiation is replenished by the right amount of extra energy every time they pass through a radio frequency (RF) supply.^{206,207}

The beamline uses the radiation emitted from either insertion devices or the bending magnets, and therefore is positioned tangentially to the storage ring, along the axes of the insertion devices and bending magnets. A beamline is divided into three sections: the front end, the optics and the experimental hutch.²⁰⁶ The front end isolates the beamline from the storage ring, monitors the position of the photon beam, blocks the X-ray radiation when required, and filters out the low-energy tail of the synchrotron radiation spectrum. The photon beam is focused and monochromatized in the optics section before it enters the experimental hutch. Beamlines are designed specifically for a particular purpose, optimized for a particular energy range and a particular experimental setup. The work presented in this thesis was performed at three different beamlines of two different synchrotron facilities. Metal (Ru) K-edge was done at high energy beamline 7-3 of SSRL, and ligand K-edge was

performed at low and mid energy beamlines 4-3 of SSRL and soft X-ray micro-characterization beamline (SXRMB) of CLS. Details of each beamline setup are individually described in the following sections.

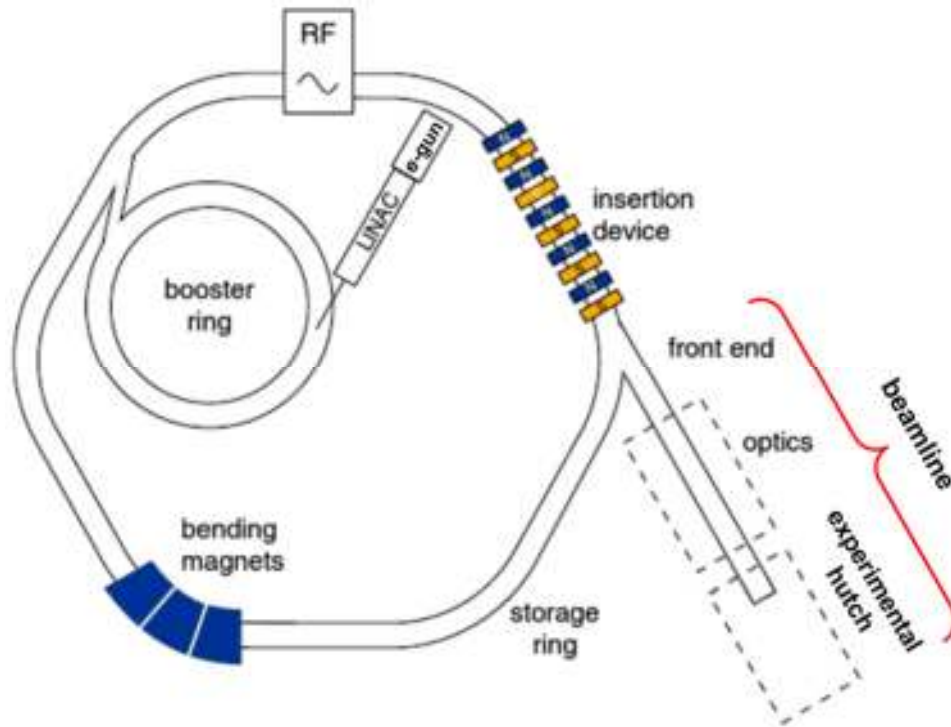


Figure 2.8: A schematic of the most important components of a 3rd generation synchrotron source. Adapted from reference 198 with permission from John Wiley and Sons, Copyright © 2011, John Wiley and Sons.²⁰⁶

2.1.4.2 Stanford Synchrotron Radiation Lightsource Beamlines 4-3 and 7-3

SSRL beamlines 4-3 and 7-3 are installed on a wiggler insertion device (Figure 2.9) therefore they produce significantly higher fluxes and brilliance than bending magnet beamlines. In both beamlines, the beam coming from the wiggler is collimated to a double crystal monochromator (DCM) by the collimating mirror (1st mirror). The monochromator (Si (111) $\phi=0^\circ$ set for BL 4-3; and Si (220) $\phi=0^\circ$ set for BL 7-3) is used to fine-tune the incident energy around the threshold energy (E_0) of the probed element and keeps the beam

propagating in a direction parallel to the initial direction following two reflections. The focusing mirror (2nd mirror) directs the beam to the sample. These mirrors also suppress higher order harmonics.

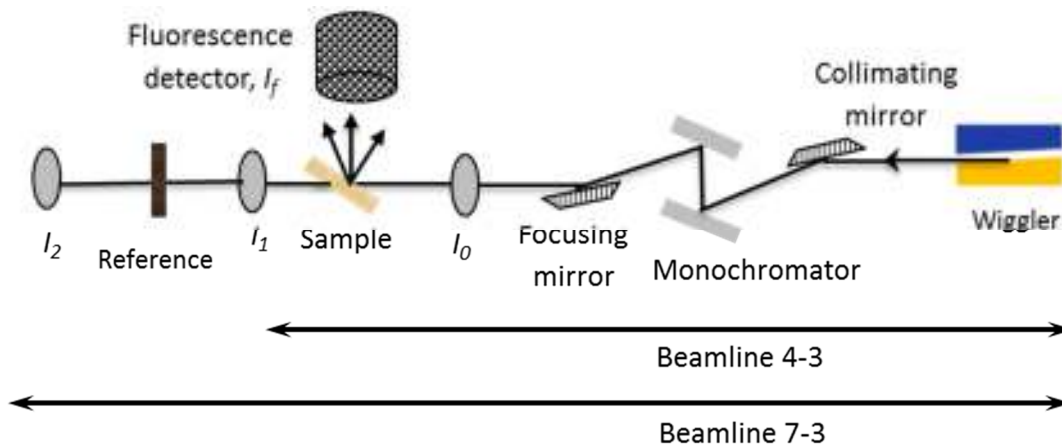


Figure 2.9: Schematic layout of beamlines configuration at SSRL

Beamline 7-3: This beamline operates at 4.6-37 keV and is dedicated to XAS of biological samples. It produces an intense and high energy beam that can be used to study dilute solid and frozen solution samples. Ru K-edge XAS data presented in Chapter 3 were collected from this beamline. In the experimental hutch, the incident beam is directed from the focusing mirror and is detected by an ionization chamber (I_0) filled with argon (Ar) gas. The sample is kept in a continuous-flow liquid He cryostat and the temperature of the cryostat is controlled at ~ 5 -10 K during the experiments to minimize the photoreduction and disorder of the samples at low temperature. The emitted fluorescence from the sample is measured using a 30- element germanium (HPGe) detector array filled with liquid N_2 .¹⁷⁷

The transmitted radiation coming from the sample, measured using the 2nd ionization chamber (I_1) filled with Ar gas, penetrates through the reference sample (e.g. Ru metal foil).

The transmittance from the reference sample is measured using the 3rd ionization chamber (I_2) filled with Ar gas. Here, the reference sample is used as an internal calibrant.¹⁷⁷

Beamline 4-3: Beamline 4-3 covers the energy range from 2.4-14 KeV, however it has special capabilities for soft-energy (2.4-6 KeV) studies in addition to hard X-rays. Hence, S K-edge XAS of solid state data presented in Chapter 3 and solution data presented in Chapter 4 were collected from this beamline. In the experimental hutch, the beam coming from the focusing mirror enters the N₂ gas-filled ionization chamber (I_0), where the intensity of the incident beam is measured. Then it penetrates through the sample placed in the sample box, filled with He gas, at a 45° angle to the incident beam to get the maximum fluorescence signals.²⁰⁸ A Lytle detector,²⁰⁹ which is operated with N₂ as an ionizing gas and installed perpendicular to the sample box, collects the fluorescence from the sample (I_f).²¹⁰

In principle, the intensity of the light transmitted through the sample can be measured using the second ionization chamber (I_1). However, this cannot be used for internal calibration since there is typically insufficient radiation to penetrate through the reference sample to provide adequate signal at these photon energies. An external calibration method is used as a common practise to calibrate the lower energy beamlines. This is done by collecting XAS data from a reference sample (*e.g.* Na₂S₂O₃ for S K-edge) in between the experimental sample.

2.1.4.3 Canadian Light Source Beamline SXRMB

SXRMB beamline at the CLS is installed on a dipole bending magnet (Figure 2.10).²¹¹ Although, SXRMB covers a wide energy range (1.7-10 KeV), it is optimized for the intermediate energy regime (2 - 5 KeV). This covers the K-edges of many important elements

(Si, P, S, Cl, and Ca), the L-edges and M-edges of 4d and 5d transition metals respectively.²¹¹

Thus, S and Cl K-edges data presented in Chapters 4 and 5 were collected from this beamline.

In SXRMB, two sets of crystals (Si-111 and InSb-111) monochromator is used to cover the desired energy range. Therefore, in addition to the expanded spectral range, it also provides capabilities to perform X-ray absorption fine structure (XAFS), microprobe, and hard X-ray photoemission with improved radiation in terms of flux, brilliance, photon and spatial resolution.²¹¹ All the XAS experiments described herein were performed using the XAFS station. The experimental setup at this beamline is presently limited to solid state samples.

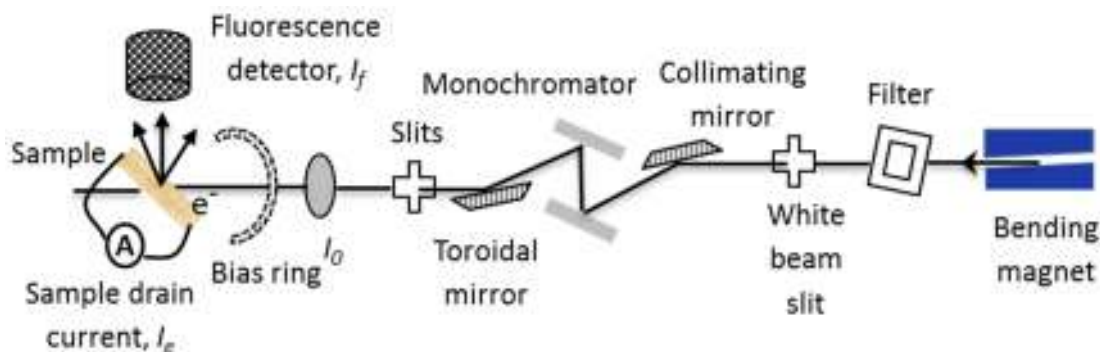


Figure 2.10: A schematic layout of the XAFS station of the SXRMB beamline at CLS²¹¹

The beam coming from the bending magnet goes through an acceptance aperture and carbon filter before it is deflected by the collimating mirror. The bendable cylindrical mirror collimates the beam to the monochromator (DCM). In addition, it reflects the higher order harmonics. The monochromator scans the energy by rotating around the first crystal while adjusting the second crystal to track the beam and to maintain a fixed exit beam.²¹¹ Then the toroidal mirror focuses the beam in both directions on to the sample. In the experimental hut, the incident beam goes through an ion chamber, kept in vacuum, for in-line I_0 monitoring.²¹¹ A major advantage provided by the SXRMB end station is that data can be

collected in two different ways. As with the previous beamlines, the intensity of the fluorescence from the sample (I_f) can be measured. However, SXRMB also allows for Total Electron Yield (TEY) detection (see below). A bias ring placed in front of the sample improves the detection efficiency.

2.1.4.4 Detection Methods

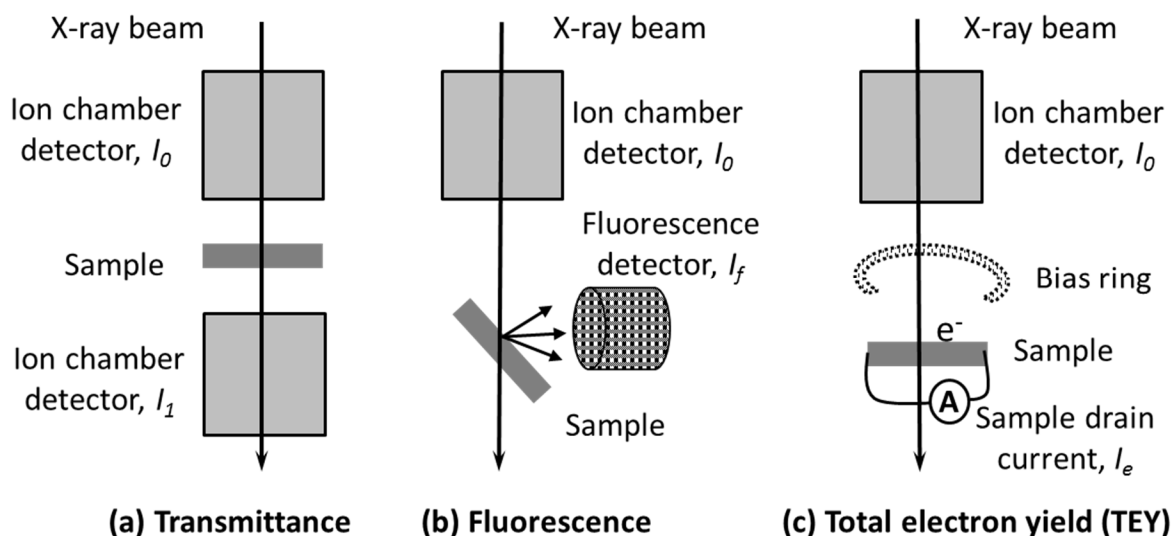


Figure 2.11: Schematic diagram for the detection methods used in this thesis work

As discussed in the above section, the XAS experiments involved with this thesis work were conducted at three different beamlines – with varying data collection and acquisition opportunities. Data were collected using three different detection methods based on the sample conditions and X-ray energies: transmittance (used for reference samples at BL 7-3), fluorescence yield (used for sample at BL 7-3 and BL 4-3) and total electron yield (used at SXRMB). General schematics of these different detection modes are shown in Figure 2.11.

Transmittance: Transmittance (Figure 2.11a) is the simplest method to measure XAS. According to the Beer-Lambert law, equation 2.4, the log of the ratio of the intensity of the

transmitted (I_1) and incident (I_0) X-ray beams yields the absorbance, A . XAS experiments detected by transmittance are thus essentially analogous to UV-vis spectroscopy. Even though transmittance is the most direct method of detection, it suffers from “transmittance thickness” or pinhole effects, spatial variations in absorption due to inhomogeneity in the thickness of the sample.²¹² For hard X-ray (> 6 KeV) experiments, these distortions are generally insignificant. However, these effects become significant for softer X-rays (< 6 KeV) where the absorption coefficient is much higher.²¹² Therefore, sample preparation is extremely important and care must be taken to make samples of uniform thickness. However, in this thesis work, transmittance was only used to measure the XAS of reference Ru foil on BL 7-3.

Equation 2.4: Beer-Lambert law

$$A = \ln(I_0/I_1)$$

Where, A – Absorbance

I_0 – Intensity of incident X-rays

I_1 – Intensity of transmitted X-rays

Fluorescence: In dilute samples, the element of interest is generally at low enough concentration that transmittance measurements are extremely challenging. However, fluorescence detection can be used to indirectly measure the absorbance. This approach yields essentially the same results as transmission with more than one order of magnitude improvement in sensitivity.²¹³ The fluorescence results from secondary processes, i.e. when an electron from a higher-energy orbital fills the hole in the core shell with concomitant emission of a photon.^{163,175} The energy of the emitted photon is characteristic for a given

element and edge, thus allowing for selective detection of fluorescence resulting from a specific excitation process. The fluorescence data is collected using an energy resolving solid state multi-channel X-ray detector positioned at 90° with respect to the incoming beam (see Figure 2.11b). For diluted samples, the detected X-ray fluorescence (I_f) is proportional to the incident X-ray absorption (I_0) and used to obtain the absorbance, $A \propto I_f/I_0$. Therefore, it is analogue to an optical fluorescence excitation spectrum.²¹²

Unfortunately, fluorescence detection carries several experimental challenges, most notably self-absorption that may distort the experimental spectrum. Self-absorption occurs in thick and/or more concentrated samples when emitted photons are reabsorbed by the sample. This effect distorts the shape of the emission spectra by diminishing intense features and shifts the maximum.¹⁹⁹ Therefore, the samples investigated herein were diluted with BN and homogeneously mixed and spread in a thin uniform layer to minimize the self-absorption effect. The fluorescence method was used at SSRL beamline 4-3 using a N_2 ionizing chamber known as a Lytle detector. By contrast, at beamline 7-3, fluorescence was measured using a 30 element Ge array detector.

Total Electron Yield (TEY): Another common detection method, particularly in the soft X-ray region, is TEY.^{212,214} Electron ejection – either via direct photoelectrons (ejected from core orbitals and have a kinetic energy that is the difference between the X-ray energy and their binding energy) and Auger electrons (emitted as part of the relaxation process as a higher-orbital electron fills the hole left behind by the photoelectron) – is a direct result of core excitation processes. Therefore, measuring the total number of electrons ejected provides a measure of the degree of photon absorption.²¹²

At beamline SXRMB at the CLS, the sample drain current (I_e) is measured as a means of detecting TEY. The drain current can be used to determine the absorbance, $A \propto I_e/I_0$. A limitation associated with this detection mode is that the sample must be conductive enough to allow for proper charge flow.^{212,214} The complexes studied in this thesis were found to be conductive enough to yield good quality data.

2.2 Density Functional Theory (DFT)

The use of density functional theory (DFT) in chemistry has dramatically been increased since Walter Kohn and John Pople received the Nobel Prize in chemistry in 1998 for their pioneering efforts in the development of the density functional theory and computational methods in quantum chemistry respectively.^{215,216} DFT is now considered to be the predominant method for evaluating the electronic structure of molecular systems containing almost all the elements in the periodic table.²¹⁶ This has been achieved by combination of computational speed and accuracy of the method in describing molecular systems.²¹⁷

DFT has gained enormous popularity as a means to gain insight in the areas of physics, chemistry, biochemistry, nanochemistry, and material science.²¹⁶ DFT has become an invaluable complementary and supporting tool to assist in the assignment and interpretation of spectroscopic data.^{165,166} Within the context of this thesis, DFT methods were used as an important complementary tool to assist in the interpretation of XAS data for Ru^{II} and Os^{II}-arene complexes. Two different software packages were used to perform the DFT calculations discussed in this thesis. The Amsterdam Density Functional (ADF, version 2007.01)^{218,219} was used to perform the calculations described in Chapter 3 and the ORCA (version 2.9) program^{220,221} was used for all other calculations.

2.2.1 Fundamentals of DFT

2.2.1.1 Functionals

The theoretical foundation for DFT is provided by the Hohenberg-Kohn (HK) theorems. It proves that the exact ground-state energy of a molecular system is uniquely determined by its total electron density $\rho(r)$.²²² This simple relationship provides a powerful alternative to solutions of the Schrödinger equation, equation 2.5, which technically requires knowledge of all electrons in the system.²¹⁷ The first HK theorem describes the basic relationship and defines a functional, $E[\rho]$, which determines the exact energy from the exact electron density of the system. It further states that the functional can be written by the terms in equation 2.6.²²² Notably, the theorem does not state the form or the exact nature of the functional that satisfies the theorem. However, the HK theorems indicate that the problem is variational such that the predicted electron correlation functional to the ground state, $(E[\tilde{\rho}])$, is greater or equal to the exact ground state electron density functional, $(E[\rho])$, *i.e.* $(E[\tilde{\rho}] \geq E[\rho])$.²²³

Equation 2.5: Schrödinger equation

$$E\Psi = \hat{H}\Psi$$

Where, Ψ – Wavefunction,

\hat{H} – Hamiltonian operator

E – Energy of the state Ψ

In principle, finding the exact electron density of a system requires that appropriate terms to the generalized functional in Equation 2.6 be determined. Of greatest concern, is the kinetic energy functional ($T[\rho]$). A formalism to address this has been achieved by the Kohn-Sham (KS) construction,²²⁴ which treats $\rho_{KS}(r) = \rho(r)$; the density of the fictitious system

is equal to that of the real or exact system. Therefore, the non-interacting kinetic energy can be calculated from the Kohn-Sham orbitals.²²³ This construction allows the second Hohenberg–Kohn theorem to be applied and yield through variation of the density the single-particle (Kohn–Sham) equations.

Equation 2.6: Electron correlation functional, $E(\rho)$, describing the electron density of a system

$$E[\rho] = V_{NN} + V_{eN}[\rho] + J[\rho] + T[\rho] + E'_{XC}[\rho]$$

Where, V_{NN} – nuclear-nuclear repulsion term

$V_{eN}[\rho]$ - nuclear-electron attraction term

$J[\rho]$ – electron-electron repulsion term

$T[\rho]$ – kinetic energy functional (universal unknown)

$E'_{XC}[\rho]$ – exchange correlation functional (universal unknown)

The second so-called “universal unknown” is the exchange correlation functional. One of the simplest functionals used is the local density approximation (LDA),²²⁵ which assumes that the electron density is uniform throughout the system. This method is very straight-forward, but leads to an overestimation of the correlation energy and generally overestimates bonding interactions.²²³ Generalized gradient approximations (GGA), first developed by Becke²²⁶ and Perdew²²⁷ provide a significantly better model for the exchange-correlation functional. The Becke-Perdew^{226,227} gradient-corrected functional, BP86, has been widely utilized in the literature and is used in all the DFT calculations described in this thesis. The functional is built by combining the Vosko-Wilk-Nusair local density approximation²²⁸ in conjunction with the gradient-corrected functional model for exchange by Becke²²⁶ and the gradient-corrected model for correlation by Perdew.²²⁷

2.2.1.2 Basis Sets

Within the Kohn-Sham formalism, a suitable basis set – which allows for the construction of appropriately flexible electron density distributions – is required.²²³ There are two types of basis sets commonly used in electronic structure calculations: Slater type orbitals (STO)²²⁹ and Gaussian type orbitals (GTO).²³⁰ STOs are implemented in ADF²¹⁹ whereas GTOs are used in ORCA,²²¹ and most other computational chemistry programs.²²³ STOs more properly represent the component atomic orbitals (AOs) near the nucleus with their cusp (discontinuous derivative) behaviour and long range decay. By contrast, GTOs has a zero slope at the nucleus and falls off too rapidly therefore three times as many GTOs as STOs are required to achieve the same level of accuracy.²³⁰ On the other hand, the integrals that involve GTOs may be solved analytically,²³¹ for which computational techniques are well developed. Therefore, double hybrid functionals can be efficiently calculated with GTOs.²²³ For aforementioned reasons both type of basis sets are widely used and well recognized by the chemistry community.

In addition to the simple form of the basis functions, the size of the basis set is absolutely critical.²³⁰ The smallest basis sets are known as single-zeta (ζ) basis sets, constructed from a single STO. Greater flexibility is afforded by describing each component orbital with a larger number of basis functions; the accuracy of the calculation increases with increasing basis set size with a concomitant increase in computational time and effort. The triple-zeta polarization (TZP) basis set is the present standard basis set used in computational chemistry to get reasonable results.²²³ TZP basis set is constructed with 4 STOs, the first three STOs to optimize the size of the orbital and the 4th STO optimize the shape of the orbital by

adding a *polarization* function (P).²³⁰ In addition, the recently reported Ahlrichs basis sets^{232,233} introduce *diffusion* (V) and polarization (P) functions to GTOs, *e.g.* def2-TZVP (where TZVP - triple zeta valence polarization) to get more accurate results. The def2 basis sets are designed to provide consistent accuracy across the whole periodic table. In this thesis, the calculations performed using ADF utilized the TZP basis set and the calculations performed using ORCA utilized def2-TZVPP (double polarization function) for Ru and Os atoms and TZVP for rest of the molecule.

2.2.2 Utilized DFT Calculations

The DFT calculations performed in this thesis are intentionally designed to support and interpret the experimental spectroscopic data by elucidating the electronic structure of the complexes of interest. Therefore, geometry optimizations, single point calculation and time-dependant density functional calculation were performed. The detail of each calculation is discussed below.

2.2.2.1 Geometry Optimization

Geometry optimization is a procedure that attempts to find the molecular geometry of minimum energy using an iterative procedure. During this process, the derivative (1st) of the energy is analytically calculated with respect to nuclear displacements of a particular geometry at the end of the self-consistent field (SCF) procedure.²¹⁹ Geometry optimization is normally the initial procedure for any DFT analysis and often initiated from the available crystal structure of the molecule, considered as a reference point. In all cases presented in this thesis, the optimized geometry was in good agreement with the crystal structure (where

available). In cases where crystal structures are not available, it was assumed that DFT-optimized structures would provide a reasonable estimate of the overall molecular structure of the complexes. It has been shown by other researchers that the accuracy of the DFT optimized structures of transition metal complexes is appreciably better than that of medium resolution crystal structures.^{217,234}

To achieve more accurate and faster convergence, special corrections and approximations which account for physical effects that are not directly included in the functional and basis sets were incorporated in the geometry optimization calculations. Such corrections include frozen core approximation, scalar relativistic effect and solvent effects using conductor-like screening model (COSMO).

Frozen Core Approximation: It was applied for the calculations involved with heavy transition metal (Ru) complexes in Chapter 3 using ADF.²¹⁸ The frozen core orbitals are taken from very accurate and large STO basis sets and treated together with nucleus of the atom (Ru) of interest. Therefore, the core electrons are not included in the perturbation treatment, because deep-core atomic orbitals change very little upon bond formation and insignificantly effect relative energies or geometry parameters. Thus, the core functions do not add variational freedom to the (valence) basis set, and hence, reduce the size of the variational basis set and consequently cut down the computational time without sacrificing the quality. Therefore, a frozen core calculation provides the total charge density and potential in the valence and core region, by excluding the deep-core orbitals.²¹⁹ Frozen virtual orbitals are not allowed in the geometry optimization calculation done by ORCA.²²⁰

Relativistic Effects: Physical phenomena observed when the speeds of particles, v , are comparable with the speed of light, c , are referred to as relativistic effects.²³⁵ Relativistic effects can strongly influence the chemical and physical properties of heavy elements and their complexes (*e.g.* Ru and Os).²³⁵ Therefore, scalar relativistic effect was employed for all the Ru and Os complexes studied in this thesis using the zero-order regular approximation (ZORA) method. At the zeroth order this expansion contains relativistic corrections to the non-relativistic energy. This relatively simple correction has been shown to provide an excellent description of valence and sub-valence electrons in heavy elements.^{219,236}

Solvent Effects: The effect of solvation for complexes in solution was achieved using the conductor-like screening model (COSMO) developed by Klamt.²³⁷ This method is an efficient way to calculate the energies, structures and properties of molecules in solution.²²⁰ Here the environment effects are treated in an approximate fashion. The solvent is represented as a dielectric medium that induces charge polarization on a suitably defined surface around the molecule, the cavity, immersed in the solution is called dielectric polarizable continuum. COSMO (aqueous) model calculations are performed to obtain the geometry optimization of particular Ru complexes studied in Chapters 4 and 5.

2.2.2.2 Single Point Calculation

Single point calculation often follows the geometry optimization because it utilizes the optimized geometry of the complex of interest. Single point calculation provides important information (*e.g.* energy, electron occupancy, % contribution from each atomic orbital) about molecular orbitals.^{218,220} These results are used to construct the valence MO diagram, MO pictures and electronic structure of the molecule. Single point analysis using ADF calculates

the atomic charges for each atom based on Mulliken population,²³⁸ Voronoi and Hirshfeld²³⁹ analyses; additionally Löewdin charges²⁴⁰ can be calculated in ORCA.

2.2.2.3 Time Dependent Density Functional Theory (TDDFT)

DFT is a ground-state based methodology (since its foundations are based on HK theorems), which approaches the calculation of excited states and their properties indirectly. In this respect, DFT has greatly profited from the analogous developments in the ab initio area where time-dependent linear response theory has been worked out in great detail.²³⁴ The most straightforward treatment in which the basis functions do not depend on the perturbation and the exchange correlation potential is assumed to be time-independent (adiabatic approximation).²²³ TDDFT calculations are used to simulate and rationalize the XAS and UV-vis (excited-state techniques) spectra of Ru and Os complexes, discussed in Chapters 4 and 5.

2.2.2.4 Natural Bond Orbital (NBO) Analysis

In contrast to DFT, natural bond orbital analysis describes the hybridization and bonding of a system using polyatomic wavefunctions (Ψ), based on one particle density matrix.²⁴¹ A set of bonding and antibonding orbitals are constructed from self-consistent field (SCF) quantum mechanical calculations and referred as NBOs. The calculated orbitals are best possible and/or most rapidly convergent orbitals with maximum electron density.²⁴² NBO is also referred as “chemist’s basis set” as it illustrates the molecular structures with the picture of localized bonds and lone pairs as basic units.

The NBO analysis, presented in this thesis, is done using natural bond orbital program (NBO 5.0)²⁴² combined with an as yet unreleased version of ORCA (version 2.9*). The NBO 5.0 program not only satisfies the Pauli exclusion principle (maximum-occupancy 2.000) but also includes coefficients for factors such as polarization, symmetry adaption, delocalization and atomic hybridization to achieve the highest possible percentage of the electron density. Therefore, it provides the most accurate possible *natural Lewis structure* of Ψ .²⁴² NBO analysis is herein used to obtain the natural Lewis structure of metal-ligand (i.e. Ru-S, Ru-X) bonds to show the extent of metal-ligand interaction in a series of Ru-arene complexes in addition to DFT analysis.

CHAPTER 3. EFFECT OF OXYGENATION ON THE REACTIVITY OF RUTHENIUM (II) ARENE THIOLATO COMPLEXES

3.1 Introduction[†]

In recent years, there has been rapid growth in the design of organometallic anticancer complexes and studies focusing on biological mechanisms to selectively increase their reactivity in cancer cells.^{12,29,46,243–246} Ru^{II} arene complexes have attracted significant interest because they have shown to bind strongly to DNA¹⁵¹ and induce conformational changes, including denaturation. This damage can lead to further downstream effects, such as apoptosis.^{3,152} However, the biological specificity of these complexes has, to date, not been adequately defined.

Clearly, ligand substitution at these coordinatively saturated octahedral complexes is required in order for DNA binding. However, some of the complexes with the greatest therapeutic potential – the Ru^{II} arene thiolate prodrugs (see Figure 3.1) are highly inert towards substitution in their initial form. It has been shown that these complexes are quite susceptible to ligand oxidation at the sulfur atom. Interestingly, recent work has shown that reversible post-translational oxygenation of cysteine thiolate (SR⁻) to sulfenato (SOR⁻) and sulfinato (SO₂R⁻) functions as a redox-based signal transduction mechanism, which plays an important role in cellular regulatory processes.^{247–249} In addition, these thiolate redox processes in biological systems are sometimes controlled by metal coordination (Zn^{II}, Fe^{III} or

[†] This chapter is based on collaborative work with Prof. Peter J. Sadler and co-workers Drs. Holm Petzold, Pieter C. A. Bruijninx and Abraha Habtemariam from University of Edinburgh and University of Warwick, UK. Most of the work presented herein is already published and reprinted with permission from *J. Am. Chem. Soc.* **2009**, 131, 13355-13361. Copyright 2009 American Chemical Society.

Co^{III}) to the S atom.^{250,251} One might thus postulate that sulfur oxygenation might play a role in the biological fate of Ru(II) arene thiolato complexes.

As discussed in section 1.2.2.2, the cytotoxic half-sandwich $[(\eta^6\text{-ar})\text{Ru}(\text{en})(\text{SR})]^+$ complexes (where ar = arene (*p*-cym or hmb); en = ethylenediamine) seem to be activated via thiolate oxygenation towards DNA binding. Furthermore, the primary class of Ru^{II} arene complexes (X = Cl) form a thiolate adduct when they react with glutathione (GSH),^{95,252} an abundant thiol in cells, and human albumin,²⁵³ and also readily undergo thiolate oxygenation. Therefore, redox activation may play a general role in the mechanism of action of a wide variety of these Ru^{II} arene complexes.

The work presented in this chapter focuses on defining the properties of Ru-S bonds as a function of (i) the extent of thiolate oxygenation, (ii) the nature of the thiolate substituent (alkyl or aryl) and (iii) the arene (*p*-cym or hmb). In order to understand the relevance of ligand-centered oxidation on its mechanism of action, it is necessary to study the influence of electronic effects on the bonding of the sulfenato and sulfinato complexes. The synthesis of metal-sulfenato complexes has been a great challenge. However, our collaborators have recently succeeded in synthesizing the Ru^{II} complexes containing a monodentate sulfenato ligand by direct oxidation of thiolato ligand using H₂O₂ (Scheme 1.1).⁷⁶ This result allowed for comparison of a series of complexes containing monodentate thiolato, sulfenato, and sulfinato ligands (Figure 3.1).

Previous studies have explored the effect of thiolate oxygenation in transition metal complexes.^{201,251,254–268} In general, such studies have involved complexes with multiple thiolato-based ligands, specifically in relation to the study of nitrile hydratase (NHase)-like

model systems with Fe^{III},^{201,257,259,260,264,266,267} Co^{III},^{254–256,262,265,266,268} Ni^{II},^{251,261,265} Zn^{II}²⁶¹ and Ru^{II}²⁶³ centres. By contrast, this study allows for a direct comparison of the electronic effects of a single sulfur-containing ligand and its impact on the nature of the resultant sulfenate and sulfinate metal ligands.

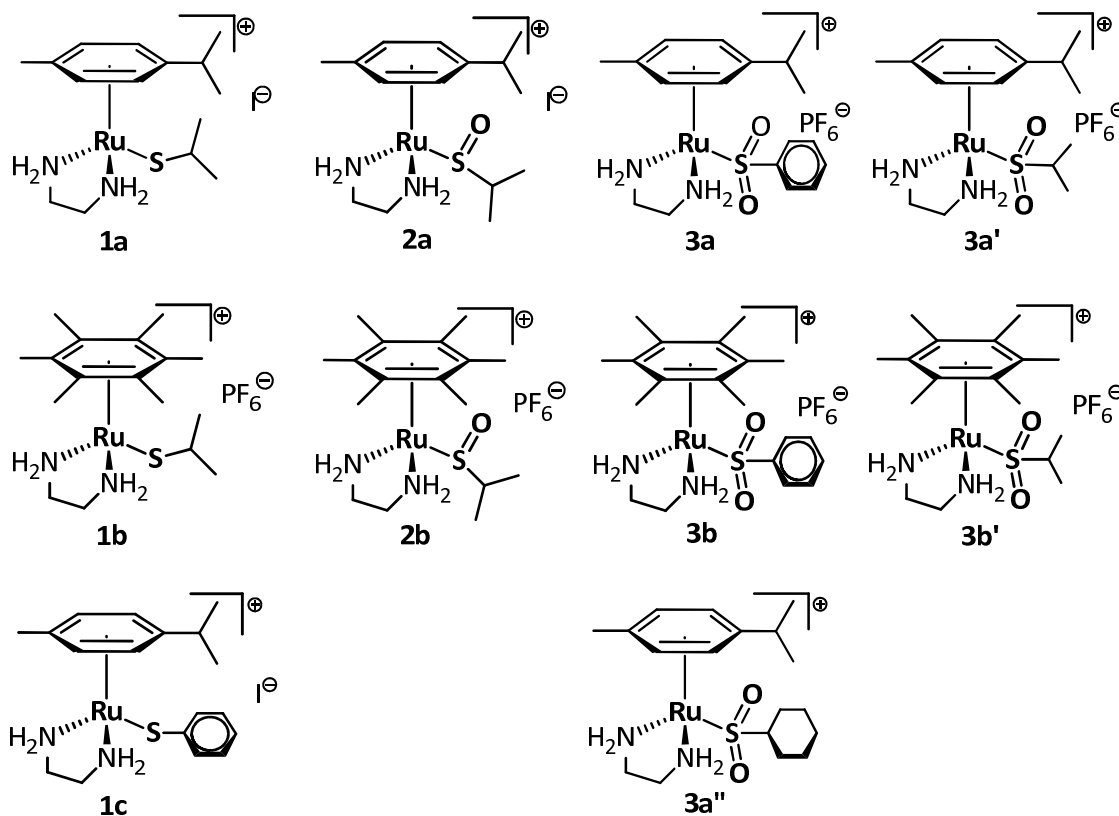


Figure 3.1: Molecular structures of $[(\eta^6\text{-ar})\text{Ru}(\text{en})(\text{SO}_n\text{R})]^+$ complexes investigated using XAS and DFT. Complexes **1**, **2** and **3** are thiolates, sulfenates and sulfinate respectively. In series **a** ar = *p*-cymene and in series **b** ar = hmb. In **3a**, **3b** and **1c** R = Ph; in **3a''** R = cyclohexyl; Complexes **3a'** and **3b'** are *in silico* models only.

In Ru^{II} arene complexes, oxidation of the thiolato ligand in complex **1** to sulfenato (**2**) and/or sulfinate (**3**) ligands plays an important role in controlling its stability and reactivity.⁷⁶ Studies of these complexes with biologically relevant molecules such as GSH,^{95,104,252} cGMP (guanosine-3',5'-cyclic monophosphate)⁹⁵ and human serum albumin²⁵³ have implied that

sulfur-centered oxidation labilizes the Ru-S bond. However, available crystallographic data indicate that a shortening of the Ru-S bond occurs upon the oxidation of the ligand (*e.g.*, **1**→**2**).^{76,268} A similar observation was also made in Ru^{II} arene sulfinato complexes by White and coworkers.⁹⁷ It was postulated that the lability of the Ru-S bond should be quite sensitive to H-bonding and ancillary ligand effects, however this has not been verified.^{80,104,252}

X-ray absorption spectroscopy (XAS)^{167,198,200} in concert with density functional theory (DFT) calculations was used to probe the above mentioned issues of the Ru-S bond in a series of $[(\eta^6\text{-ar})\text{Ru}(\text{en})(\text{SO}_n\text{R})]^+$ complexes ($n=0-2$) in greater detail. Herein we have shown that ligand oxidation seems to be necessary but not sufficient for biological activation. Therefore, it is postulated that protonation of the sulfenate complex, $[(\eta^6\text{-ar})\text{Ru}(\text{en})(\text{SOR})]^+$, would allow for ligand dissociation and DNA binding. The specific electronic factors that contribute to observed variations in reactivity of these complexes are also discussed.

3.2 Experimental and Computational Aspects

This section describes sample preparation and data collection for S K-edge and Ru K-edge XAS followed by data processing and fitting with specifically designed software programs. The chosen computational model utilized for DFT calculations of these systems is also discussed.

3.2.1 Sample Preparation

All complexes studied in this chapter were prepared by Drs. Holm Petzold, Pieter C. A. Bruijninx and Abraha Habtemariam using reported procedures⁷⁶ except complexes **3a** and **3b**. Complexes **3a,b** were synthesized by oxidation of the corresponding thiolate (20 mg,

0.035 mmol), with an excess amount of hydrogen peroxide (10 mol) in methanol (10 ml). Then, the reaction mixture was stirred for 16 hours. The solvent was removed to dryness under vacuum, and the residue was washed with diethyl ether. The pure products were obtained by crystallization from methanol. All the complexes were fully characterized by ^1H NMR spectroscopy, ESI-MS spectrometry and elemental analysis.⁹⁶ S K-edge XAS samples were mounted as a finely ground 1:1 mixture of the complex to boron nitride (BN) dusted on sulfur-free Kapton tape across the window of an Al plate. All the samples with a 1:4 ratio of the complex to BN for Ru K-edge XAS were finely ground and then compactly pressed in between a 0.5 mm thick Al spacer, tightly sealed on both sides with Kapton tape.

3.2.2 XAS Data Collection

XAS measurements for S K-edge were gathered at SSRL beamline 4-3 using a modified “low Z” setup allowing for low temperature data acquisition under ring conditions of 3.0 GeV and 100 mA current. The specific beamline setup for these experiments were described in section 2.1.5.2 and further detail about data acquisition is described in the literature.^{210,269} Energies were calibrated using sodium thiosulfate ($\text{Na}_2\text{S}_2\text{O}_3$) as a reference standard, with the 1st derivative of the first pre-edge feature being calibrated at 2472.02 eV.¹⁸⁴ Reference samples remained throughout the run and scanned before and after each data set to ensure stability of the monochromator and beam. Signal was detected with a Lytle fluorescence detector filled with N_2 gas at ambient temperature (298 K) and pressure (~1 atm). XAS Collect software²⁷⁰ was used to collect the data in the energy range from 2430-2550 eV. At least three scans were taken for each sample and the experiment was repeated at least twice to confirm reproducibility.

Ru K-edge XAS data were collected at SSRL on beamline 7-3 under ring conditions of 80-100 mA at 3.0 GeV. This beamline has a 20-pole, 2 T wigglers, 0.8 mrad beam, and a Si (220) double-crystal monochromator that was detuned by 50% intensity to attain harmonic rejection. Detail of the experimental configuration of the beamline was described in section 2.1.5.2. Energy calibration was done using the 1st derivative of the first lowest energy inflection point of Ru metal foil assigned at 22117 eV. The incident X-ray intensity (I_0), sample absorption (I_1), and Ru reference absorption (I_2) were measured as transmittance using argon-filled ionization chambers. Six to eight sweeps were taken for each sample, and all data were measured to $k = 15 \text{ \AA}^{-1}$ at $13 \pm 3 \text{ K}$ within an Oxford Instruments CFI208 continuous-flow liquid helium cryostat. Each measurement was repeated twice to ensure the reproducibility of the results.

3.2.3 Data Processing and Analysis

XAS data reduction, i.e. averaging, calibration and background removal of S K-edge was done using SIXPack.²⁷¹ Prior to normalization, all acceptable scans were averaged and a linear background was subtracted from the entire energy range. Normalization of the data was accomplished by fitting cumulative pseudo-Voigt functions to the post edge region and normalizing the edge jump to 1.0 at 2490 eV.

A Matlab based toolbox for the fitting and analysis of XAS spectra, *Blueprint XAS* version 0.5,^{272,273} was used to fit experimental pre-edge features by using pseudo-Voigt functions (sum of Lorentzian and Gaussian functions, Equation 3.1). A Monte Carlo based method is used to simultaneously fit the background and the spectroscopic features. Experimental line shapes are expected to be a convolution of a Lorentzian transition envelope and the beamline

spectrometer optics (monochromator resolution) imposed the Gaussian line shape.^{274,275}

Therefore, a fixed 1:1 ration of Lorentzian : Gaussian (pseudo-Voigt) contribution successfully reproduced the pre-edge features. The ionization edge jump was fit with cumulative pseudo-Voigt line shapes.

Equation 3.1: Approximate Voigt lineshape

$$I_v = H \left[\eta \left(\frac{\left(\frac{\Gamma}{2}\right)^2}{(E-P)^2 + \left(\frac{\Gamma}{2}\right)^2} \right) + (1 - \eta) e^{-1/2 \left(\frac{E-P}{c}\right)^2} \right]$$

Where, η – Lorentzian fraction

Γ – Full Width at Half Maximum (FWHM) of the Voigt profile

H – Maximum value of the function

P – Position of the peak

E – Energy

C – Constant [$c = 2\sqrt{\ln 4} = 2.355$]

Ru K-edge XAS data were analyzed using SIXPack.²⁷¹ Scans were averaged and energy calibration was reconfirmed using the 1st derivative of the first lowest energy inflection point of reference Ru foil assigned as 22117 eV. Background subtraction and normalization were performed simultaneously using a linear pre-edge function and a quadratic post edge function.

3.2.4 DFT Calculations

Starting geometries used for the DFT calculations were obtained directly from the crystallographic information file (CIF) of these complexes. All the DFT calculations discussed

in this chapter were performed using the Amsterdam Density Functional (ADF) modeling suite 2007.01.^{218,219} The model used for calculations is a Becke-Perdew, BP86,^{226,227} gradient-corrected functional with a triple-zeta polarization (TZP) basis set. The relativistic correction for Ru metal was applied using scalar ZORA,^{235,276} unless otherwise stated. The small frozen core basis set approximation was applied with no molecular symmetry and a high numerical integration (6.0) was used to maintain numerical accuracy in the optimizations. The initial geometry optimization was followed by single-point calculations and fragment analysis. Fragment analysis calculations were carried out on the $[(\eta^6\text{-ar})\text{Ru}(\text{en})(\text{SO}_n\text{R})]^+$ complexes with labelled fragments of Ru, ar (cym and hmb), en, S, O_n (where n=0-2) and R (*i*Pr, Ph) to explain the ligands to metal contributions and transition assignments. ADF input files can be obtained from the supporting information of the related publication.⁹⁶ Natural bond order (NBO) analysis is done on geometry optimized structures using NBO 5.0 program²⁴² combined with ORCA (version 2.9*)[‡]. Single point calculations using ADF and ORCA yield similar results with only minor differences attributable to minor methodological differences between the two software programs. The above model with the smaller split valence polarization, SVP, basis set is used to illustrate the extent of Ru-S bond interaction in thiolato, sulfenato and sulfinato complexes.

3.3 Results and Analysis

The effects of sulfur ligand oxygenation on the Ru metal center and S ligand are investigated through Ru K-edge XAS and S K-edge XAS respectively. In addition, modifications

[‡] ORCA (version 2.9*) is a modified version of ORCA 2.9, which allows for NBP analysis. This version is as yet unavailable for general users.

to the ancillary ligand are also investigated using S K-edge XAS. Since XAS is an element specific technique, this methodology seems to be appropriate for investigating the crucial mechanism of Ru^{II} arene complexes discussed herein.

3.3.1 Effect of Oxygenation on Ru Metal Center

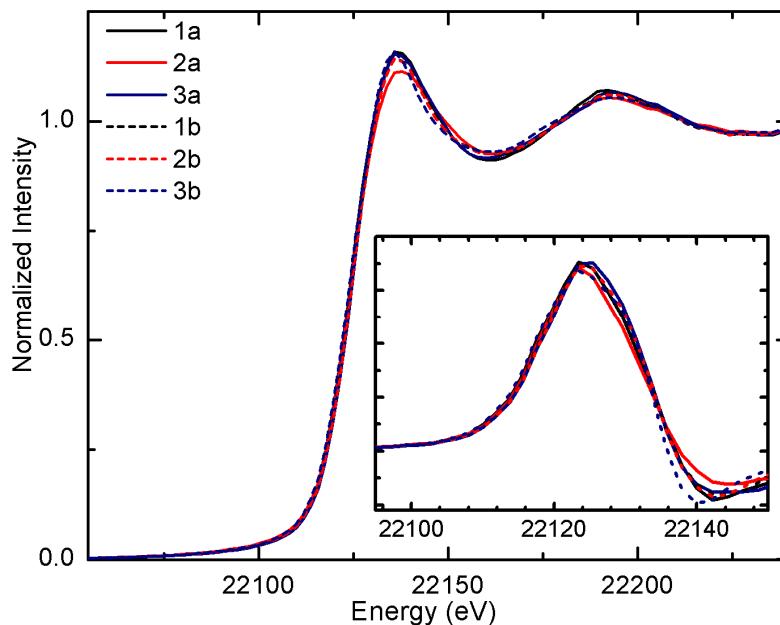


Figure 3.2: Normalized Ru K-edge XANES spectra of complexes of **1a,b - 3a,b**. Inset shows the 1st derivative spectra indicating the edge jump position.

Ru K-edge XAS spectra for solid state thiolato (**1a,b**), sulfenato (**2a,b**), and sulfinato (**3a,b**) complexes are shown in Figure 3.2. The XANES region of the spectrum clearly indicates that the edge region is nearly superimposable, which is confirmed by comparison of first derivatives of the spectra. The striking similarities between these spectra imply that there is no change in metal oxidation state upon ligand oxidation. Each complex is best described as a Ru^{II} with a low spin 4d⁶ configuration; oxygenation of the ligand does not *directly* affect the metal center and its electronic structure. The absence of pre-edge features in the Ru K-edge data shows that there is little or no mixing of Ru_{5p} character into the empty Ru_{4dσ*} orbitals.

Therefore, the ligand environment around the metal centre is well described as pseudo-octahedral in all complexes,^{178,277} and the acceptor orbitals are a set of two *gerade*, e_g ($4d_{x^2-y^2}$ and $4d_{z^2}$) orbitals. This further strengthens the conclusion that ligand oxidation causes only minor perturbations at the metal center.

3.3.2 Effect of Oxygenation on S-Ligand

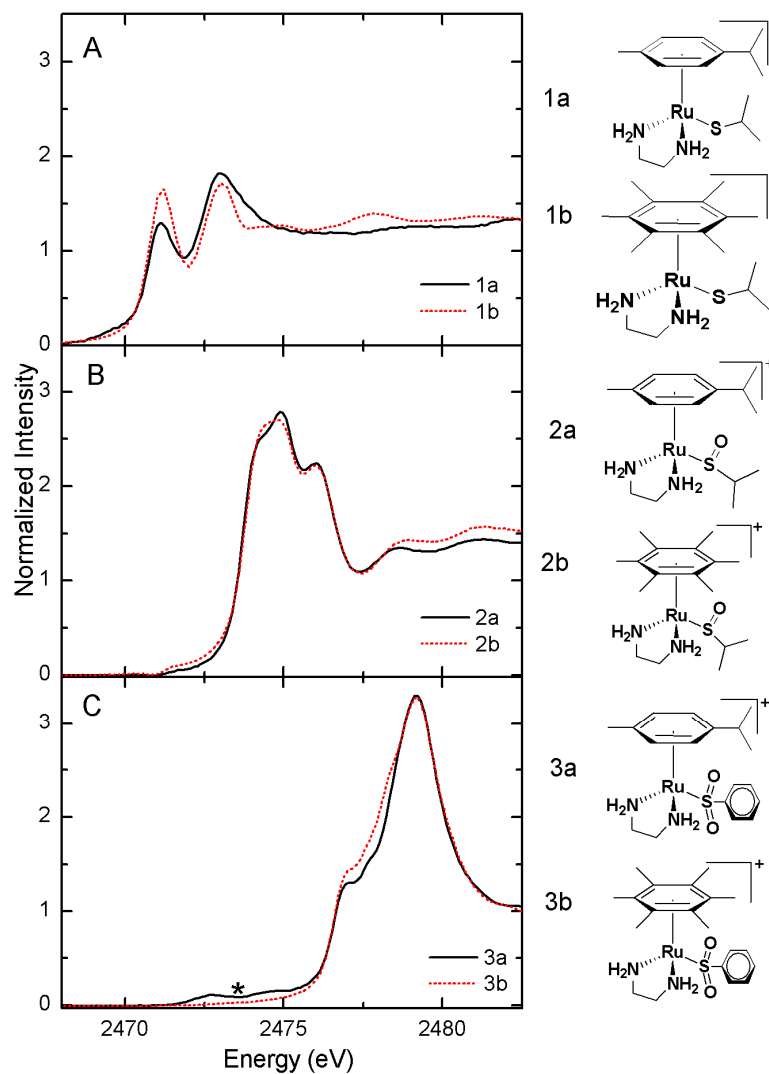


Figure 3.3: S K-edge spectra of Ru^{II} arene A - thiolato **1a** and **1b**, B - sulfenato **2a** and **2b**, and C - sulfinato **3a** and **3b** complexes. An asterisk (*) denotes features due to thiolato-based impurities in the sulfenato/sulfinato complexes (>5%).

As shown in Figure 3.3, the S K-edge spectra of these complexes differ markedly as the nature of the sulfur-containing ligand and its degree of oxidation change. Sulfur ligand oxygenation shifts the absorption edge to higher energy by ~ 3 eV from **1**→**2** as well as from **2**→**3**, due to a decrease of the S_{1s} orbital energy with increasing Z_{eff} . DFT calculations predict that the lowest energy feature in each of the complexes corresponds to a $Ru_{4d\sigma^*} \leftarrow S_{1s}$ transition. The intensity of the transition derives from the electric dipole-allowed character of the atomic $S_{3p} \leftarrow S_{1s}$ transition. Therefore the intensity can be correlated with the amount of S_{3p} character in the $Ru_{4d\sigma^*}$ acceptor orbital as shown in Equation 2.2. The quantification methodology is explained in section 2.1.4.

Table 3.1: Experimental peak energies and transition assignments and experimentally determined S_{3p} character in the acceptor orbital as estimated from normalized fit intensities*

Complex	S K-edge XAS Transition		% S_{3p} in Acceptor	
	Energy (eV)	Acceptor \leftarrow Donor	XAS	DFT
1a	2471.2	$Ru_{4d\sigma^*} \leftarrow S_{1s}$	$22.5 \pm 1.5\%$	20
	2472.8	$SC_{\sigma^*} \leftarrow S_{1s}$	$29.0 \pm 2.0\%$	33
1b	2471.2	$Ru_{4d\sigma^*} \leftarrow S_{1s}$	$24.0 \pm 1.6\%$	19
	2473.0	$SC_{\sigma^*} \leftarrow S_{1s}$	$17.1 \pm 1.1\%$	29
1c	2471.4	$Ru_{4d\sigma^*} \leftarrow S_{1s}$	$17.1 \pm 1.4\%$	16
	2472.7	$\varphi_{\pi^*} \leftarrow S_{1s}$	$11.7 \pm 0.8\%$	8
	2473.5	$SC_{\sigma^*} \leftarrow S_{1s}$	$27.1 \pm 1.8\%$	^a
2a	2474.2	$Ru_{4d\sigma^*} \leftarrow S_{1s}$	$22.2 \pm 1.2\%$	17
	2475.0	$SO_{\sigma^*}/SC_{\sigma^*} \leftarrow S_{1s}$	$24.8 \pm 1.2\%$	^a
	2476.2	$SO_{\sigma^*}/SC_{\sigma^*} \leftarrow S_{1s}$	$21.4 \pm 1.1\%$	^a
2b	2474.3	$Ru_{4d\sigma^*} \leftarrow S_{1s}$	$22.8 \pm 0.9\%$	18
	2475.1	$SO_{\sigma^*}/SC_{\sigma^*} \leftarrow S_{1s}$	$17.8 \pm 0.7\%$	^a
	2476.2	$SO_{\sigma^*}/SC_{\sigma^*} \leftarrow S_{1s}$	$20.6 \pm 0.8\%$	^a
3a	2477.1	$Ru_{4d\sigma^*} \leftarrow S_{1s}$	$11.2 \pm 1.3\%$	6 (6) ^b
	2478.1	$\varphi_{\pi^*} \leftarrow S_{1s}$	$5.8 \pm 1.0\%$	^a
	2479.2	$SO_{\sigma^*}/SC_{\sigma^*} \leftarrow S_{1s}$	$27.7 \pm 2.9\%$	^a
3b	2477.2	$Ru_{4d\sigma^*} \leftarrow S_{1s}$	$13.2 \pm 0.4\%$	7 (4) ^b
	2478.4	$\varphi_{\pi^*} \leftarrow S_{1s}$	$8.8 \pm 0.3\%$	^a
	2479.4	$SO_{\sigma^*}/SC_{\sigma^*} \leftarrow S_{1s}$	$33.2 \pm 1.0\%$	^a

*DFT-calculated S_{3p} contributions to the acceptor orbitals as determined from a Mulliken charge decomposition of the Kohn-Sham orbitals are also included for comparison and included in Appendix B. ^aExact values in these cases cannot be extracted since S_{3p} character is dispersed over a wide energy range and multiple acceptor orbitals. ^cValues in parentheses are for **3a'** and **3b'** where R = *iPr*.

Systematic peak fitting^{272,273} and assignment of the observed spectroscopic features were performed for each complex and is presented in Appendix A. The dipole integral, $\langle S_{3p}|r|S_{1s}\rangle$ as described in Equation 2.2, of thiolato and sulfinato complexes used to estimate the contributions of the experimental S_{3p} character to the $Ru_{4d\sigma^*}$ have been obtained from the literature; the values of $\langle SR_{3p}^-|r|S_{1s}\rangle \simeq 8$ ^{184,187} and $\langle SO_2R_{3p}^-|r|S_{1s}\rangle \simeq 18$ ^{185,187} were used, respectively. The value of the dipole integral for the sulfenato complexes was interpolated from that of the thiolato and sulfinato complexes since it has been previously shown that the relationship between the dipole integral and Z_{eff} is effectively linear^{184,185,187} and i.e. $\langle SOR_{3p}^-|r|S_{1s}\rangle \simeq 13$.

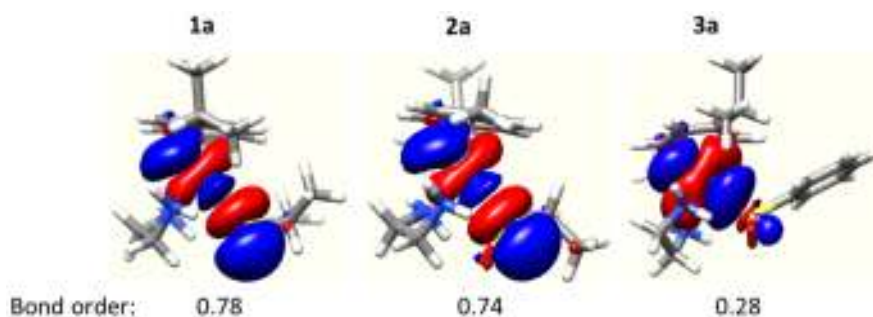


Figure 3.4: Natural bond orbital (NBO) picture of $Ru-S_{\sigma^*}$ in complexes **1a**, **2a** and **3a**.

Table 3.1 summarizes the results with estimates of uncertainties obtained from the fitting procedure. Notably, there is little change in the S_{3p} contributions to the $Ru_{4d\sigma^*}$ upon oxidation from **1**→**2** (e.g., **1a** vs **2a**), however, there is a substantial drop in S_{3p} character in the fully oxygenated species (**3a,b**). A natural bond orbital (NBO)²⁴² analysis of the DFT results provides a useful way of visualizing localized bonding in these complex systems. The localized NBO $Ru-S_{\sigma^*}$ antibond for each of the complexes is shown in Figure 3.4), illustrating S_{3p}

contributions to the $Ru_{4d\sigma^*}$. The NBO derived bond order[§] of the $Ru-S_{\sigma^*}$ bond is found to be 0.78, 0.74 and 0.28 in **1a**, **2a** and **3a** respectively. These results are in agreement with the experimental S K-edge XAS results. Slight variations of the arene ligand (*i.e.*, **a**, where ar = *p*-cym vs **b**, where ar = hmb) generate only minor differences in the spectroscopic data that cannot be distinguished within experimental error.

3.3.3 DFT Analysis

To explore the influence of oxygenation from the oxygen atom(s) end, we have investigated our DFT results in greater detail. Earlier studies on Fe-sulfinato complexes suggested that contributions from the oxygen atoms in defining the overall charge donation from oxidized ligands cannot be neglected.^{201,251} The ADF input files and the obtained molecular orbital descriptions derived from the output are included in Appendix B.

3.3.3.1 Relativistic Effect and Hydrogen Bonding on Geometry Optimization

To study the factors influencing the geometric structure of these species, systematic changes to the computational model were performed. Most notably, the effect of relativistic effects (Figure 3.5) and the potential influence of explicit H-bonding to the sulfur-containing ligand (Figure 3.6) were explored. Important bond distances from the resulting molecular structures are tabulated in Tables 3.2 and 3.3. Geometries calculated without including relativistic effects or inter molecular hydrogen bonding tended to yield M-L bond distances that were significantly longer relative to experiment. However, geometries obtained with

[§] NBO derived bond order is calculated using the formula: $\frac{(Bonding\ occup - Antibonding\ occup)}{2}$; It is anticipated that the Ru-S bond is single.

scalar ZORA relativistic corrections and H-bonding (wherever appropriate based on crystallographic coordinates) are in better agreement with available crystallographic data.⁷⁶

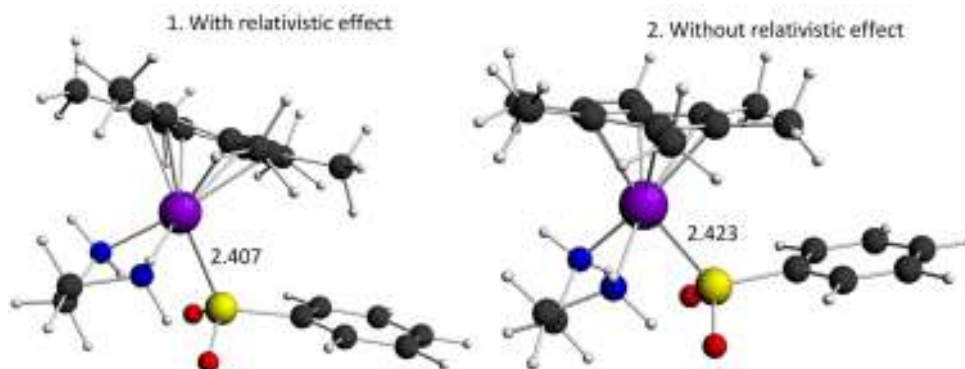


Figure 3.5: Geometry optimized structure of **3b** with (structure 1) and without (structure 2) scalar ZORA relativistic effects included during optimization

Table 3.2: Selected bond lengths from DFT optimized structures of **3b** with (structure 1) and without (structure 2) scalar ZORA relativistic effect are compared with parameters derived from the X-ray structure

Bond (Å)	Structure 1	Structure 2	X-ray
S-Ru	2.407	2.423	2.3144(7)
S-O	1.511/1.504	1.508/1.504	1.472(3)/1.470(3)
S-C	1.819	1.818	1.806(3)

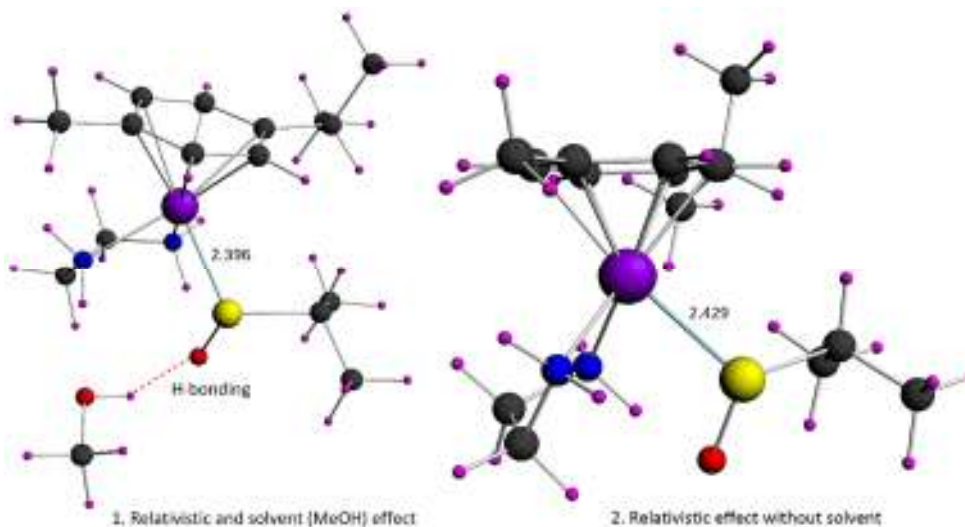


Figure 3.6: Geometry optimized structure of **2a** with relativistic effect and solvent MeOH (structure 1) and without solvent (structure 2)

Table 3.3: Selected bond lengths of DFT optimized structure of **2a** with scalar relativistic effect and solvent (structure 1) and without solvent (structure 2)

Bond (Å)	Structure 1	Structure 2	X-ray
S-Ru	2.396	2.429	2.3790(8)
S-O	1.581	1.566	1.552(2)
S-C	1.885	1.891	1.823(4)

3.3.3.2 Effect of Ligand Oxidation

As seen in the x-ray crystallographic structures, Ru-S bond distances decrease with ligand oxygenation from **1**→**2**→**3**. The resultant valence MO descriptions are also in reasonable agreement with the overall qualitative trends derived from the S K-edge XAS spectra (see Table 3.1 and Appendix B). Calculations suggested that although $S_{3p} \Rightarrow Ru_{4d}$ charge donation decreases upon oxidation, the overall ligand donor contributions remain essentially unchanged (20-23%, Figure 3.7). This is partly due to a compensatory effect of the oxygen atoms of the oxidized ligands. These consequences are consistent with those obtained on model systems of iron-and cobalt-containing nitrile hydratases active site.^{201,251,267,278} Figure 3.7 summarizes the effects of ligand oxidation on charge donation to the metal center and large effects are observed as a function of oxidation. The observed trends are consistent for both hmb and *p*-cym series of complexes. To probe ligand oxidation exclusively, *in silico* model complexes **3a'** and **3b'** (where R = *i*Pr) are included in the comparison study, due to fully oxidized alkylsulfonato complexes akin to **3a,b** have not as yet been isolated.

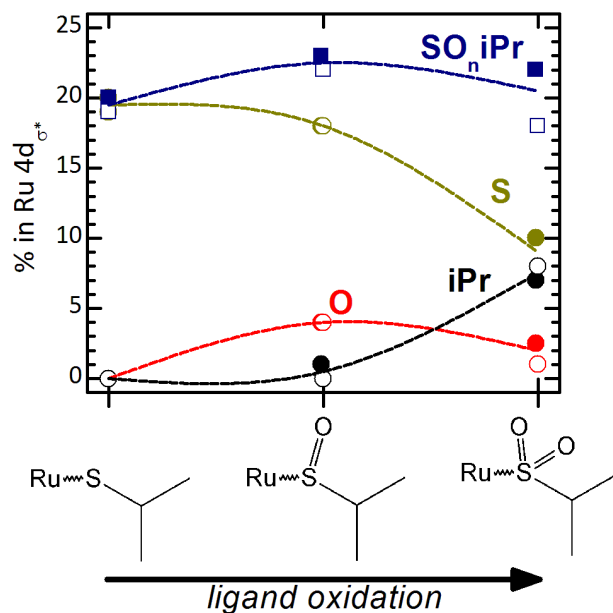


Figure 3.7: Breakdown of SO_nR ligand donor contributions to Ru_{4d σ^*} orbital (in %) for **1a**→**2a**→**3a'** and for **1b**→**2b**→**3b'** (open symbols) including the total ligand charge donation (blue squares) as well as specific contributions from sulfur (green circles), oxygen (per atom, red circles), and isopropyl (black circles). Lines are used to indicate general trends only.

Although the *overall* charge donation from the sulfur-containing ligand remains similar in all three oxidation states, the origin of the charge donation changes rather remarkably upon oxidation. For example, in the thiolato complexes, the Ru-S coordination bond is dominated by direct S_{3p}⇒Ru_{4d} charge donation. Sulfur donation changes little in the sulfenato complexes, but a new and relatively large contribution from the sulfenato oxygen emerges, which increases overall charge donation from the ligand. By contrast, sulfur donation in the sulfinato complexes is dramatically decreased, with some compensatory effects by the appearance of contributions from the alkyl R group. Importantly, the addition of a second terminal oxo group causes a net decrease in charge donation by each of these terminal oxygen atoms. This effect is attributed to a loss of S-O π character in the S-O bonds on going from the sulfenato to the sulfinato species, switching off an efficient mechanism for charge delocalization in the ligand. A significant conclusion drawn from these data is that

charge donation from the terminal oxo groups is largest in **2**, implying that the sulfenato species should be most susceptible to chemical perturbations by having a direct interaction with Ru_{4d} orbital(s).

3.3.4 Ancillary Ligand Effects

3.3.4.1 Arene Ligand Effects

In principle, ancillary ligands may also have an impact on the Ru-S bond. However, in these complexes, changes in the arene ligand (i.e., when changing from *p*-cym to hmb) do not result in spectroscopically significant changes in the Ru_{4d}*←S_{1s} transition. DFT calculations also similarly predict only a very little change (~1%) in the S_{3p} contribution to the antibonding, which is within the experimental error of the measurements (see Table 3.1). However, the SC_σ*←S_{1s} transition, is predicted to be more sensitive to the nature of the arene ligand, and we do observe a marked change in the relative intensities of the Ru_{4d}*←S_{1s} and SC_σ*←S_{1s} transitions for **1b** (ar=hmb) as compared to **1a** (ar=*p*-cym) as well as a drop in the S_{3p} contribution for **1b** (see Table 3.1); this is consistent with greater electron donation from hmb²⁷⁹ to the Ru center as compared to *p*-cym. A similar effect is also observed in the S K-edge data for the sulfenato complex (see **2a** vs **2b** in Table 3.1). It has formerly been suggested that observed differences in the pK_a between protonated **2a** (3.37) and **2b** (3.61) result from increased charge donation from hmb in **2b** vs *p*-cym in **2a**. Both XAS data and DFT calculations support this interpretation.

3.3.4.2 Sulfur Ligand Substitution Effect

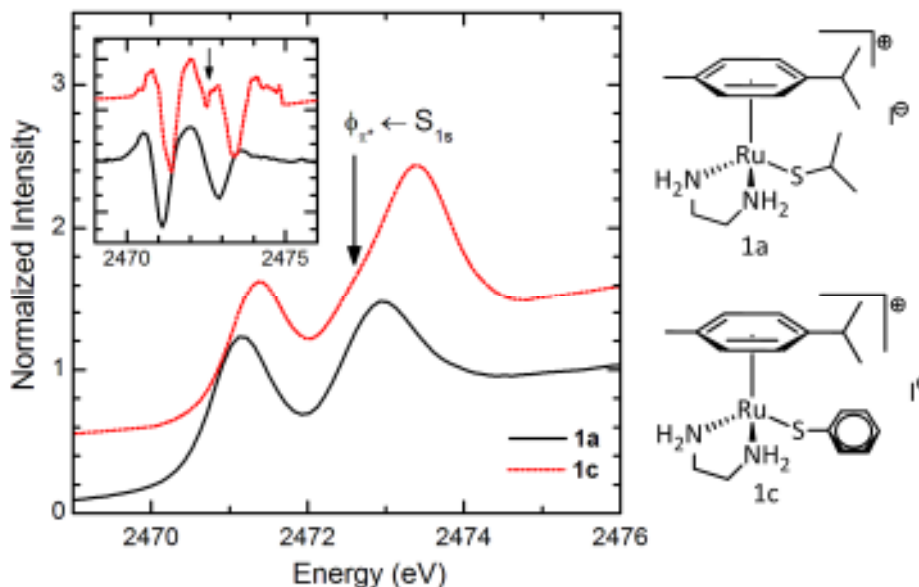


Figure 3.8: Normalized S K-edge XAS spectra of **1a** (black) and **1c** (red). Inset shows second derivative spectra indicating presence of a shoulder at 2472.7 eV in **1c** due to a low-lying ϕ_{π^*} orbital from the aryl moiety.

It has previously been noted that arylthiolato complexes of the type discussed herein are less susceptible to oxidation¹⁰⁴ and generally more inert than their alkylthiolato counterparts. The S K-edge XAS spectrum of the arylthiolato complex **1c** (R = Ph in Figure 3.8) differs from **1a** in that a new feature appears as a low-energy shoulder on the intense $SC_{\sigma^*} \leftarrow S_{1s}$ feature as clearly shown in the inset of Figure 3.6. Similar features has been observed in organic sulfones due to S_{3p} character mixing into aryl π^* orbitals (ϕ_{π^*}) through excited state hyperconjugation.²⁸⁰ Therefore the intensity of this feature results from redistribution of intensity from the main $Ru_{4d^*} \leftarrow S_{1s}$ transition as pictured in Figure 3.9, which must be considered when interpreting the transition intensities.

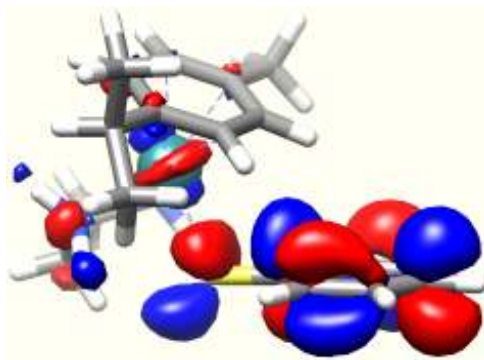


Figure 3.9: Illustration of hyperconjugation in complex **1c** due to S_{3p} character mixing into aryl π^* orbitals (ϕ_{π^*})

From **1a** to **1c**, the intensity of the lowest energy transition, $Ru_{4d^*} \leftarrow S_{1s}$, would predict a moderate decrease in charge donation to the metal center (from 22% to 17%, as in Table 3.1); however the intensity redistributed through hyper-conjugation (see $\phi_{\pi^*} \leftarrow S_{1s}$ in Table 3.1) must be included for the total donation from the S ligand. This indicates that the overall $S_{3p} \Rightarrow Ru_{4d}$ charge donation is, in fact, greater in **1c** (~29%) than **1a** (~22%). The slightly increased energy of the $Ru_{4d^*} \leftarrow S_{1s}$ transition is also consistent with greater Ru-S covalency in **1c**. Both the increased charge donation from the ligand and available delocalization over the aryl substituent should contribute to a modest strengthening of the Ru-S bond, which is consistent with decreased susceptibility to oxidation in the aryl complex. This higher covalency of the Ru-S bond appears to be carried through even in oxidized species. A shoulder at ~2477.5 eV in the S K-edge spectrum of complex **3a** (see Figure 3.10) results from excited state hyperconjugation ($\phi_{\pi^*} \leftarrow S_{1s}$ as shown in Table 3.1), i.e., S_{3p} mixing into aryl π^* orbitals (ϕ_{π^*}), which concomitantly redistributes the antibonding character of the Ru-S bond. This is also supported by the slightly increased energy of the $Ru_{4d^*} \leftarrow S_{1s}$ transition.

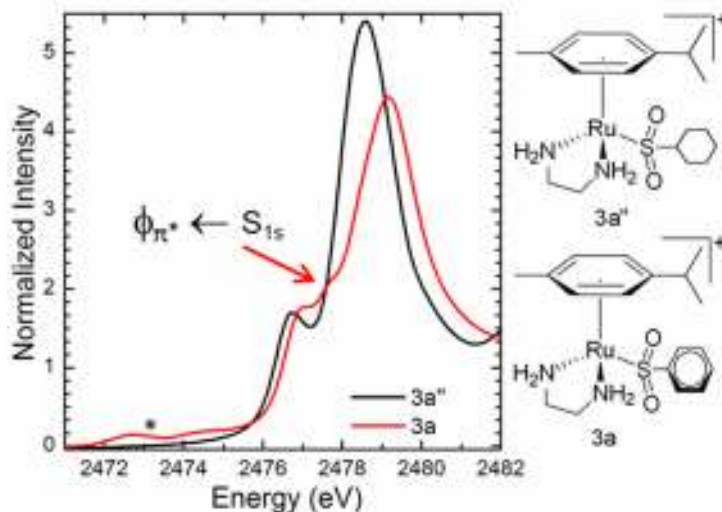


Figure 3.10: S K-edge XAS spectra of **3a''** (R = cyclo hexyl, black) and **3a** (R = Ph, red). Presence of a shoulder at ~2477.5 eV in **3a** indicating a low-lying ϕ_{π^*} orbital from the aryl moiety.

3.4 Discussion

Results obtained from XAS and DFT indicate that the Ru-S bond in these species is quite sensitive to ligand oxygenation and subtle modifications in ancillary ligands. Ru K-edge XAS is consistent with the fact that only minor perturbations occurred to the overall pseudo-octahedral geometry of these complexes, and the oxidation state of metal center remains as Ru^{2+} , low spin $4d^6$, regardless of the thiolate ligand oxidation state. This is also in agreement with the observed total charge donation from the S-containing ligand which changes only slightly upon oxygenation due to the compensation between S atom, terminal oxygen(s) and the R group. This implies that S-oxygenation should have very little impact on the inherent strength and/or lability of the Ru-S bond in sulfenate. It should be noted here that the second oxygenation drastically decreases the Ru-S covalency in sulfinato but the formation of such species under the biological condition is very difficult. Therefore, these studies suggest that involvement of the terminal oxo group is particularly important in the sulfenato derivative, particularly through a $\text{S-O}\pi$ bonding interaction. In addition,

observed in the previous study, protonation would also weaken the H-bond (specified in Figure 3.11) between the sulfenato ligand and the NH₂ of the adjacent en-ligand under acidic conditions.⁷⁶

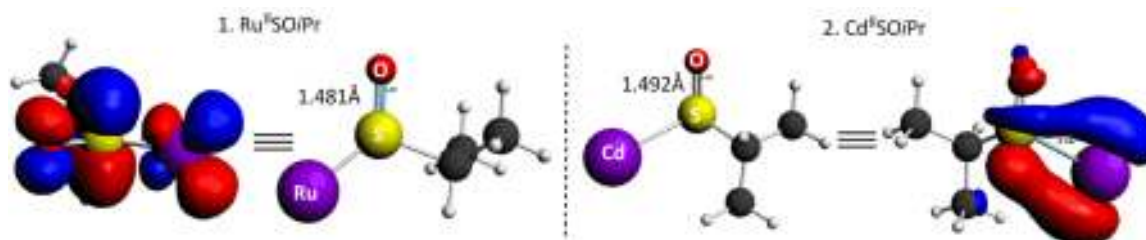
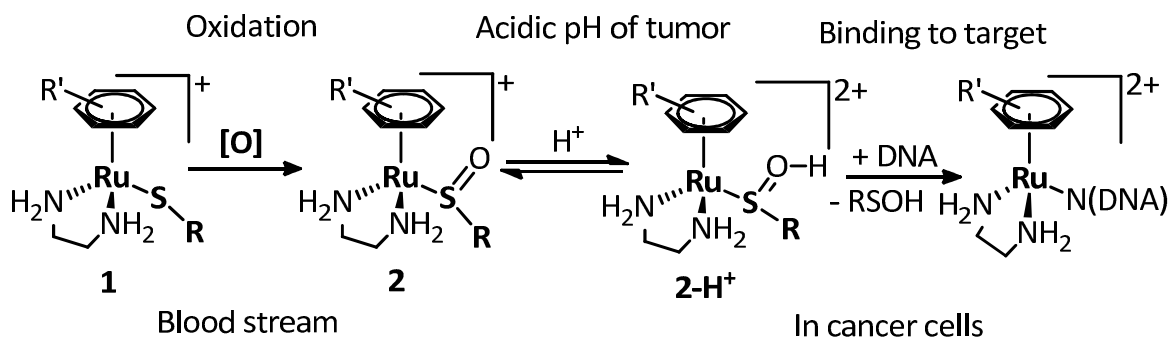


Figure 3.12: Comparison of S-O bond distance and orbital mixing in Ru^{II} vs Cd^{II}.

Based on our studies, a mechanism of activity is postulated for the parent Ru^{II} arene thiolato complexes as depicted in Scheme 3.1. The oxidation step may involve reactive oxygen species such as peroxides formed by the oxidation of GSH or NADH (β -nicotinamide adenine dinucleotide) by oxygen.^{104,283} First, ligand oxygenation would make the prodrug susceptible to protonation at the terminal oxo group, which is followed by hydrolysis and DNA binding under acidic conditions. In cancer cells, the pH of intracellular and extracellular fluids can be acidic (pH 6-7); however lysosomal compartments in cells can attain more acidic condition, such as pH 4-5.^{284,285} Fundamentally, to activate these complexes, even relatively low conversion to the protonated form (**2**→**2-H**⁺) should be sufficient for ligand substitution and subsequent DNA binding. The Ru-S bond could also be weakened by Lewis acid activation as has been noticed by Kovacs and coworkers in nitrile hydratase (NHase) model complexes, where Zn^{II} binding to the terminal oxo position has a significant impact on the Fe-S bond and the observed effect is very similar to that of proton addition in a smaller extent.²⁶⁷ In cancer cells, protonation would be the primary source for activating the sulfenato ligand, however

recent studies shows a higher accumulation of mobile Zn^{II} ion in breast cancer cells.^{286,287}

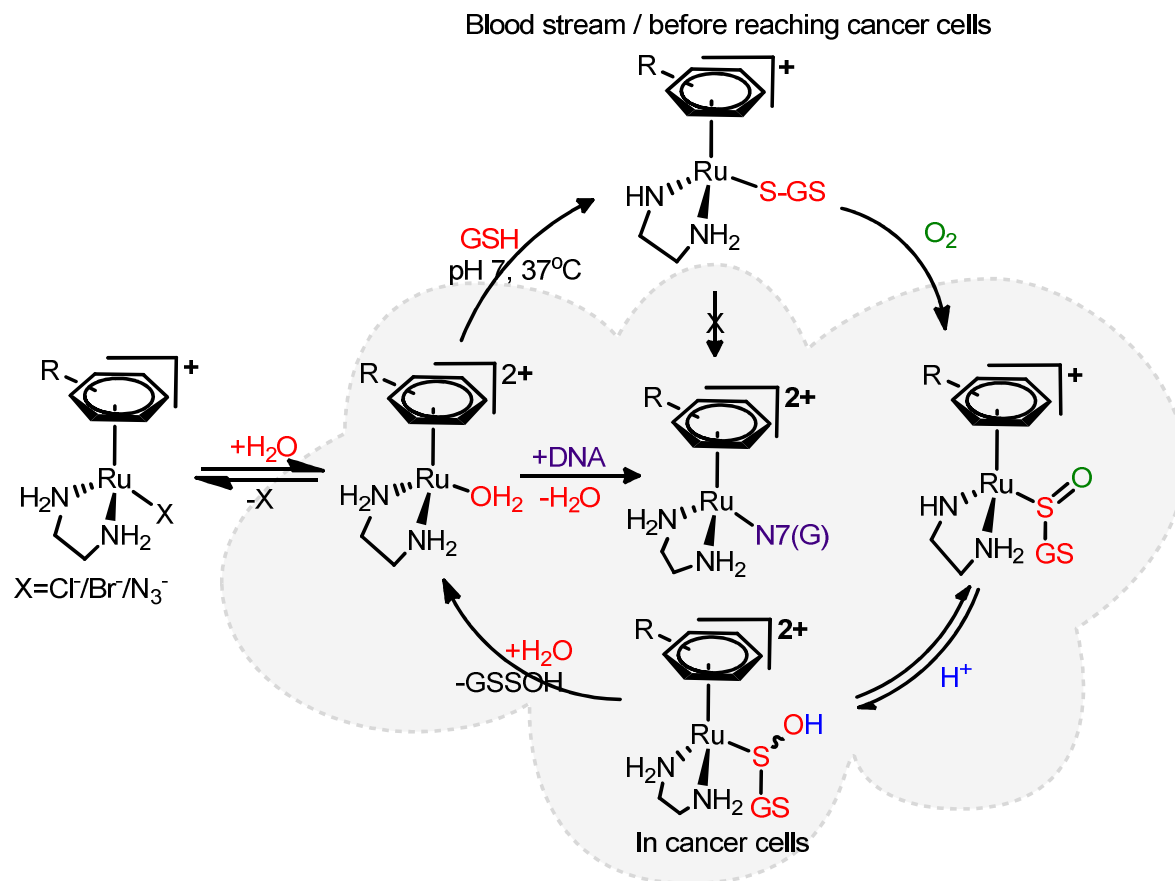
Therefore, Lewis acid activation of sulfenato species cannot be neglected. Nevertheless in either case, activation toward ligand substitution should occur through the mono-oxygenated sulfenato species of the complex.



Scheme 3.1: Proposed pathway for DNA binding by Ru^{II} arene Thiolate, **1**, [(η^6 -ar)Ru(en)(SR)]⁺ complexes

It should be pointed out here that the reactivity of sulfenato and sulfinato adducts are clearly important for understanding the factors which affect the metabolism and distribution of the primary class of Ru^{II} arene [(η^6 -ar)Ru(en)(X)]⁺ complexes, where X = Cl, Br or N₃, generally a labile ligand. Interestingly, the chloride complexes of this family have been shown to form adducts with natural thiols such as cysteine,²⁸⁸ glutathione⁹⁵ and albumin²⁵³ outside and inside cells. Ru-S coordination appears to induce the oxidation of thiolates to sulfenates or sulfinates^{95,252,253} and subsequently stabilize the sulfenato ligands,^{76,95} often unstable free ligands and highly reactive.^{281,282} Taken together these biochemical studies in combination with our results, allowed us to develop a global model (Scheme 3.2) that explains the biochemical mechanism of action for the primary class of Ru^{II} arene complexes (in addition to hydrolysis reaction). The Ru-S bond strength is remarkably similar in complexes **1**, **2** and **3**,

which explains why protein sulfenic and sulfinic acids^{289,290} can compete with thiols as the preferred metal binding site in such complexes.



Scheme 3.2: Postulated global model for biological mechanism of primary Ru^{II} arene, $[(\eta^6\text{-ar})\text{Ru}(\text{en})(\text{X})]^+$ complexes

3.5 Conclusions

The effect of thiolato oxygenation on the nature of the Ru-S bonds, and the influence of arene and thiolato ligand modification on this reaction have been effectively investigated using X-ray absorption spectroscopic and density functional theory computational analysis, in a series of Ru arene anticancer complexes. Metal complexes used for therapeutics are often prodrugs. They frequently undergo ligand exchange or redox reactions before they reach the cancer cells. Detailed knowledge about such activation processes is vital to the drug

design process as well as the construction of meaningful structure-activity relationships for metallodrugs. In this study, we propose a modified mechanism of activation that is ligand-centered, and it is therefore important to understand how oxidation of ar-Ru-SR (thiolate) bonds to ar-Ru-S(O)R (sulfenato) and ar-Ru S(O₂)R (sulfinato) affects the reactivity of these complexes.

Herein we have recognized that the total charge donation from the sulfur ligand to the metal center is not altered by the thiolato ligand oxygenation. Therefore, the ligand oxygenation should have little impact on the lability of the ligand directly. Our work therefore suggests a need for an additional activation step for biological activity. Insight analysis of the Ru-S bonding in the sulfenato species indicates that this bond should strongly be affected by protonation (H⁺ addition) and/or Lewis acid activation of the terminal oxo group (Figure 3.11). Sulfur ligand oxidation also provides an additional pro-drug activation pathway to the primary Ru^{II} arene complexes. This is further supported by the competitive reaction of GSH/cGMP with parent [(η⁶-ar)Ru(en)Cl]⁺ complex, where the complex is directly coordinated to GSH followed by oxidation of thiolato ligand in the coordinated GSH. The oxygenation appears to provide a facile route for displacement of S-bound glutathione by G N7, leading to formation of the cGMP adduct [(η⁶-ar)Ru(en)(cGMP-N7)]⁺ as the major product even in the presence of a 250-fold molar excess of GSH.⁹⁵

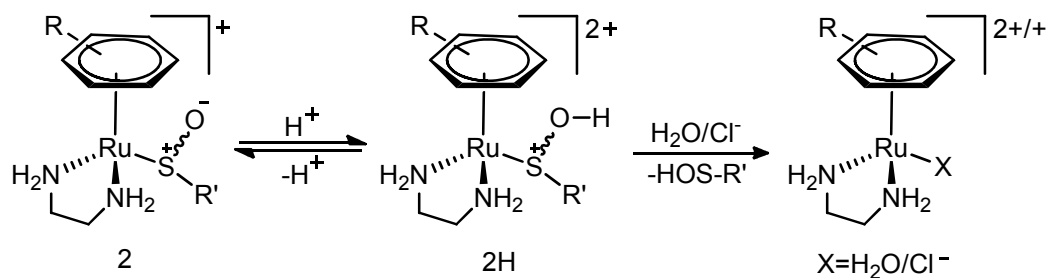
We further noticed that the slight variation of arene (*p*-cym vs hmb) and thiolato ligand (*i*Pr vs Ph) on the thiolato complexes seem to be *amplified* in the oxidized complexes as evidenced by larger changes in charge donation of individual atoms besides the energies of the empty valence orbitals. Thus, small modifications in the parent complexes can lead to

major effects in the oxidized species, a finding which is significant in optimizing the design of this family of antitumor complexes in the future.

CHAPTER 4. ACTIVATION OF OXIDIZED SULFUR LIGANDS AND ITS IMPACT ON THE REACTIVITY OF RUTHENIUM (II) ARENE COMPLEXES

4.1 Introduction

Ruthenium (II) arene complexes are attractive targets for non-Pt metallodrugs. They offer a versatile platform for anticancer drug design and exhibit a distinct mode of biological activity. In earlier work (Chapter 3), we have shown that sulfur oxidation is an essential but insufficient step for the activation of Ru^{II} arene thiolate, $[(\eta^6\text{-ar})\text{Ru}(\text{en})(\text{SR})]^+$, prodrugs.⁹⁶ This proposal was developed based on the electronic structure of these complexes upon sulfur oxygenation and supported by the observed hydrolysis chemistry of the sulfenate complexes under acidic conditions (Scheme 4.1).⁷⁶ It is therefore highly feasible that combined oxidation and protonation are required for efficient substitution of thiolato ligands by guanine N7⁷⁶ and DNA binding.⁹⁵



Scheme 4.1: Protonation of complex **2** followed by hydrolysis under acidic condition (HCl).⁷⁶

Generally sulfenates are too reactive to be isolated²⁹¹ and readily disproportionate to sulfinates and thiolates²⁸² unless coordinated to a transition metal. Interestingly, the only Ru complex reported with protonated sulfenate on the oxygen atom (sulfenic acid) is stabilized by strong hydrogen bonds on the OH group.²⁹² Petzold *et. al.* showed that protonation of **2b**, $[(\eta^6\text{-hmb})\text{Ru}(\text{en})(\text{SOiPr})]^+$, is possible in aqueous HCl solution at pH 2.11 (pK_a of the

protonated sulfenic acid is 3.61). The reaction is completed in 16 hours with partial hydrolysis of **2b**. The reaction yields the reactive aqua adduct, $[(\eta^6\text{-hmb})\text{Ru}(\text{en})(\text{H}_2\text{O})]^{2+}$ and chloride complex, $[(\eta^6\text{-hmb})\text{Ru}(\text{en})(\text{Cl})]^+$ (Scheme 4.1).⁷⁶

As shown in Figure 3.11, the DFT model calculations of complex **2a** indicates that protonation of the oxygen should lead to a decrease in the Ru-S covalency, which presumably weakens the Ru-S bond. We wished to test this hypothesis as a means of confirming the proposed activation mode of oxidized sulfur in Ru^{II}-arene complexes. Unfortunately, the protonated species have not been isolable due to instability of the resulting complexes.⁷⁶ Therefore, isolating the protonated sulfenato species for further spectroscopic studies is highly impractical. However, the influence of Lewis acids on the metal-sulfur bonding has been used as an indirect method of evaluating the effect of perturbations at the sulfur-oxygen bond in such complexes.

There has been a growing interest in studying redox-inactive metal ions (such as Zn^{II}) serving as Lewis acids to evaluate their potential impact on the reactivity of biologically-relevant metal complexes.²⁹³ Kovacs, Solomon and co-workers^{201,267} investigated the effect of direct interaction of Zn^{II} on an iron-sulfenato complex, $[\text{Fe}^{\text{III}}(\text{ADIT})(\text{ADIT-O})]^+$, where ADIT is 6-amino-2,3-dimethyl-4-azahex-3-ene-2-thiolate. Crystallographic data of $[\text{Fe}^{\text{III}}(\text{ADIT})(\text{ADIT-O-ZnCl}_3)]$ confirmed that sulfenato oxygen is bound to the Zn^{II} centre and due to this interaction the S-O bond is slightly elongated. Furthermore, the electronic absorption spectrum of the $[\text{Fe}^{\text{III}}(\text{ADIT})(\text{ADIT-O})]^+$ complex is perturbed in the presence of Zn^{II}. Specifically, the lowest energy ligand to metal charge transfer (LMCT) band experiences a bathochromic/red shift – a similar result is also observed upon protonation of that

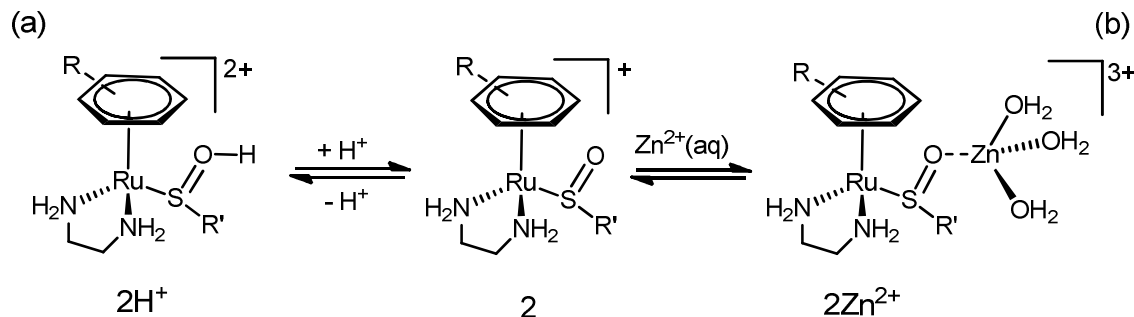
complex.²⁶⁷ The effect of other Lewis acidic metal ions such as Na⁺,^{268,294} Li⁺,²⁹⁵ and Pt²⁺,²⁹⁶ with the metal-sulfenato oxygen has also been explored.

As discussed in Section 3.4, we have developed a model for the biological mode of action of Ru^{II} arene complexes, which suggests that the mono-oxygenated sulfenato species is most susceptible to ligand exchange under acidic conditions.⁹⁶ We thus seek to explore the effect of exogenous metal ions on the bonding in Ru^{II} arene complexes as a means of indirectly probing the effect of protonation on these species. Particular attention is paid to sulfenato species due to their importance in the proposed mode of action, although the effect on sulfinato species is also explored for comparative purposes. In addition, sulfinato species is also reported as a co-product with sulfenato species during the biological reaction of parent Ru^{II}-arene chlorido complex, $[(\eta^6\text{-ar})\text{Ru}(\text{en})(\text{Cl})]^+$, with glutathione (GSH)²⁵² and human albumin.²⁵³

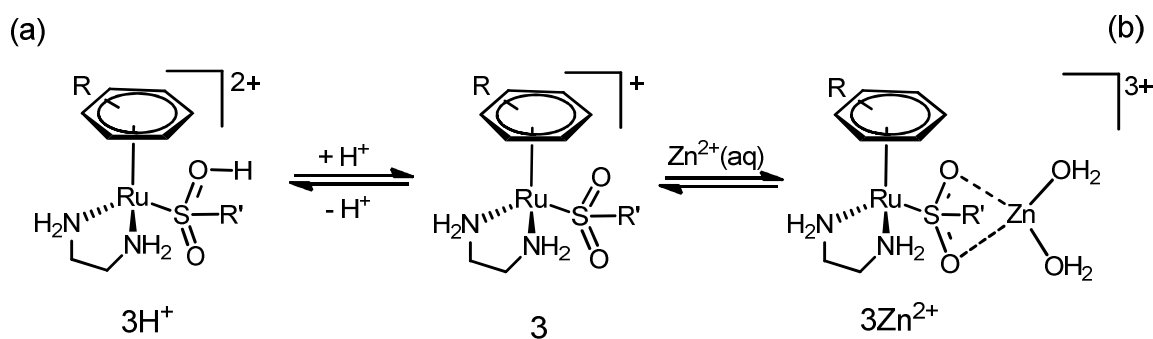
This chapter explores the effect of protonation and Lewis acid complexation on complexes **2a** ($[(\eta^6\text{-}p\text{-cym})\text{Ru}(\text{en})(\text{SO}i\text{Pr})]^+$) and **3a** ($[(\eta^6\text{-}p\text{-cym})\text{Ru}(\text{en})(\text{SO}_2\text{Ph})]^+$) as shown in Scheme 4.2 and Scheme 4.3 respectively. Synthesis of the sulfenato-Lewis acid adducts has been more challenging, and as a result, the Lewis acid effect of sulfenates has been investigated using *in silico* models. However, an analogous series of Lewis acid (Zn^{II}, Co^{II} and Cr^{III}) adducts of sulfinato complexes have been successfully synthesized,** which made it possible for both experimental and computational studies on these systems to be conducted.

**This chapter is based on the work collaborated with Prof. Sadler and co-workers Drs. Petzold and Habtemariam from Department of Chemistry, University of Warwick, Coventry, UK.

Importantly, data available for the sulfinato complexes provide a useful means to evaluate the computational models used to probe the more reactive sulfenato species.



Scheme 4.2: Brønsted acid protonation (a)⁷⁶ and Lewis acid interaction (b) of Ru^{II} arene sulfenato (**2**) complex, where R = *p*-cym, R' = *i*Pr



Scheme 4.3: Brønsted acid protonation (a) and Lewis acid interaction (b) of Ru^{II} arene sulfinato (**3**) complex, where R = *p*-cym, R' = Ph

4.2 Experimental and Computational Aspects

Herein, the preparation of solid and solution samples and data collection at the CLS beamline SXRMB as well as BL 4-3, SSRL are described. Data processing and analysis are accomplished using the following software packages: SIXpack²⁷¹ and Blueprint XAS.^{272,273} All DFT and TDDFT calculations in this Chapter are performed using the ORCA²²⁰ program. MOAnalyzer²⁹⁷ is used to analyze the results from the DFT and TDDFT calculations. Furthermore, it is also used to compare the XAS and simulated TDDFT spectra.

4.2.1 Sample Preparation

Complexes $[(p\text{-cym)Ru(en)(SOiPr)]^+$ - **2a**, $[(hmb)Ru(en)(SOiPr)]^+$ - **2b** and $[(p\text{-cym)Ru(en)(SO}_2\text{Ph)]}^+$ - **3a** was initially prepared by Dr. Holm Petzold using a previously published procedure.⁷⁶ Lewis adducts of **3a**, *i.e.* **3aZn²⁺**, **3aCo²⁺**, and **3aCr³⁺** were prepared by Dr. Abraha Habtemariam as follows. A solution of 1 mM concentration of **3a** was prepared in doubly deionized water. Then, 1 mL of aliquots was added to 0.6 mM (3 mole equivalent) of the 5 ml of Zn(NO₃)₂, CoBr₂ and CrCl₃ solutions to prepare **3aZn²⁺**, **3aCo²⁺**, and **3aCr³⁺** respectively. They were mixed well by shaking for couple of minutes to get a clear solution and freeze dried immediately. XAS data at the S K- edge were collected on these freeze-dried samples. XAS spectra were not collected at the Zn K-, Co K-, or Cr K-edges due to their presence in large excess. Samples were mounted as finely ground powders homogeneously diluted with 25% BN and spread evenly on sulfur-free double sided carbon tape attached to a long copper sample holder. Reference samples were placed on the top and bottom of the holder to check the monochromator readings.

A solution sample of **2b** prepared in 1mM concentration, was buffered (with PBS - phosphate-buffered saline) at pHs 7.4 and 2.5. 1 M HCl solution was used to adjust the pH of the buffer. The solution was mixed with ~40% glycerol, a glassing agent, to reduce diffraction produced by ice crystals in XAS. Freshly prepared samples were pre-equilibrated in a water-saturated He atmosphere for an hour to minimize bubble formation in the sample cell. Then, the solution was injected into XAS cells sealed with a polypropylene window on the front, and rapidly frozen in liquid nitrogen.

4.2.2 XAS Data Collection

XAS measurements of S K-edge were performed at soft X-ray micro characterization beamline (SXRMB) of the Canadian Light Source (CLS), using a Si(111) double-crystal monochromator with the higher-order harmonics rejected with Pt-coated mirrors under standard operating conditions of 2.9 GeV and 250 mA beam current. Detailed descriptions of beamline configuration and data acquisition are described in section 2.1.5.3 and are also found in literature.²¹¹ Energy calibration of S K-edge was performed using sodium thiosulfate ($\text{Na}_2\text{S}_2\text{O}_3$) with the first pre-edge feature being calibrated at 2472.02 eV.

Reference samples were scanned at the beginning and end of each sample to ensure stable monochromator readings. Signal was recorded under vacuum with the surface sensitive total electron yield (TEY) which was complemented by the bulk sensitive total fluorescence yield (FLY) detected with a channel plate detector. Three scans were taken for each sample and the experiment was repeated twice to confirm reproducibility. Solution sample data of **2b** was collected at BL 4-3 at SSRL according to the procedure described in Section 3.2.2.

4.2.3 Data Processing and Analysis

Sulfur K-edge XAS data were analysed using SIXpack.²⁷¹ Energy calibration was reconfirmed via the inflection point of the first derivative of the lowest energy pre-edge peak of $\text{Na}_2\text{S}_2\text{O}_3$ (=2472.02 eV). All acceptable scans were averaged and fit to a linear background and subtracted from the entire spectrum and normalized to an edge jump of 1.0. *BluePrint XAS* version 1.1,^{272,273} was used to simultaneously fit the background, edge jump, and spectroscopic features. Peaks in the spectrum were modelled using pseudo-Voigt functions,

whereas edges are modelled using cumulative pseudo-Voigt functions. Restrictions are set for each fit parameter but actual fit parameters are assigned using a Monte Carlo algorithm to reduce the user bias in analysis. For each spectrum, 100 sets of initial fit parameters were generated, yielding 100 unique fits. Fit results can be investigated for robustness (relative to initial fit parameters) and the best and most representative fits can be filtered.

4.2.4 DFT Calculations

Initial structures for geometry optimization of all complexes were obtained by modifying the solid-state molecular structures of **2a**⁷⁶ and **3a**⁹⁶ using MOLDEN²⁹⁸, a general pre- and post-processing program for computational chemistry. DFT calculations were performed using ORCA²²⁰ version 2.9, a combined *ab Initio*, DFT and semiempirical electronic structure package. Geometry optimizations were obtained using the BP86^{226,227} exchange correlation functional and a TZVP + def2-TZVP/J basis set was used for all light atoms; the RI-J approximation was employed for faster convergence. The TZVPP+TZVPP/J basis set was used for ruthenium metal. Scalar relativistic effects were evaluated using the built-in ZORA module within ORCA 2.9.^{235,276} Relativistic effects were applied to the auxiliary (/J) basis sets. A dense integration grid (grid4) was employed for good numerical accuracy and tight geometry convergence criteria (*TightSCF*) were enforced. Due to the overall size of the computational model, convergence was accomplished with damped convergence (using the *SlowConv* keyword). Solvation was included (where applicable) with COSMO, as implemented within ORCA.²³⁷

The molecular structures obtained from geometry optimization were utilized for “single point” (*i.e.*, with fixed atomic positions) TDDFT simulations of sulfur K-edge XAS spectra. MO

Analyzer version v1.1beta²⁹⁷ (a Matlab-based numerical and graphical analysis toolbox for ORCA output file) was used to visualize simulated TDDFT spectra and to compare these with experimental data. A systematic energy shift of ~ 60.4 eV was applied to the spectra to align with experimental XAS. This shift is consistent with the calibration value (60.01 ± 0.11 eV) reported by Debeer *et. al.* for TDDFT of the S K-edge calculation done with BP86 functional + ZORA scalar relativistic effect.²⁹⁹

Natural bond orbitals (NBO) analysis was performed using the NBO version 5.0 program.²⁴² Due to limitations within the NBO program, full BP86 calculations using a smaller SVP basis set was used. Although quantitative differences exist between SVP and TZVP results, the qualitative bonding description and trends are the same. *TightSCF* was applied for single point convergence and *VeryslowConv* applied for SCF convergence. Examples of input files for each type of computation performed in this Chapter are given in Appendix B.2.

4.3 Results and Analysis

Given the experimental challenge of directly probing the protonated forms of **2** (**2H⁺**) and **3** (**3H⁺**), computational studies have been used to evaluate the effect of terminal oxo-group protonation in these species. Attempts were made to experimentally evaluate the effect of an acidic environment on **2b** (*vide infra*). As the preparation of Lewis acid adducts of complex **2** has been unsuccessful to date, both the effect of protonation and that of Lewis acids on Ru^{II} arene sulfenato complexes has been explored using computational studies. By contrast, Lewis acid adducts of Ru^{II} arene *sulfinato* (**3**) complexes have been investigated both experimentally and computationally. In addition, solvation effects of water are investigated

in silico for sulfenato, **2a** → **2a_{aq}**, and sulfinato, **3a** → **3a_{aq}**, complexes. Results obtained for the sulfinato complexes are described first, followed by that for the sulfenato species.

4.3.1 Lewis acid Interaction and Brønsted Acid Protonation on Sulfinato

The effect of solvation and protonation on the sulfinato complexes is investigated using *in silico* models of **3a_{aq}** and the Ru^{II} arene sulfinic acid derivative, **3aH⁺** using DFT/COSMO calculations respectively. In addition, the effect of Lewis acids on sulfinato complexes is evaluated using a combination of spectroscopic and computational data.

Table 4.1: Selected bond length (Å) of **3a**, **3aZn²⁺** and **3aH⁺** from the DFT analysis

Complex	Ru-S Bond length	S-O Bond length
3a	2.408	1.531, 1.535
3a_{aq}	2.383	1.539, 1.542
3aZn²⁺	2.297	1.594
3aH⁺	2.321	1.516, 1.689

The computational results for solvated (**3a_{aq}**), protonated (**3aH⁺**) and Zn^{II}-perturbed (**3aZn²⁺**) complex **3a** show that solvation and perturbation result in slight structural changes to those complexes. Elongation of the S-O bond and concomitant shortening of the Ru-S bond occur as shown in Table 4.1. Importantly, either one or both of the S-O bonds can undergo perturbation. In the case of protonation, only the first protonation is explored, which elongates the S-O bond directly attached to proton. This concomitantly shortens the other S-O bond which also mitigates the effect on the Ru-S bond. On the other hand, Zn^{II} can, in principle, bind to either one or both oxygens. Overall, it is found that a single Zn(II) binding to both terminal oxo groups (**3aZn²⁺**) yield results that are most consistent with the

experimental XAS data.^{††} In this model, both S-O bonds are elongated whereas the Ru-S bond is shortened.

It has been postulated that perturbation of these oxidized species would directly affect the Ru-S_{σ*} bond. Therefore, the charge contribution of Kohn-Sham acceptor orbital, Ru_{4dσ*}, is investigated in detail to study the solvation and protonation effect of sulfinato complexes as shown in Table 4.2.

Table 4.2: Experimentally determined S_{3p} character* and calculated charge distribution of acceptor (Ru_{4dσ*} ← S_{3p}) orbital in sulfinato complexes

Complex	% S _{3p} in acceptor		SO ₂ R(%)	H/M(H ₂ O) ₂ (%)	Ru(%)	ar(%)	en(%)
	XAS	DFT					
3a	6.3 ± 1.3%	6.2	23.1	-	45.7	21.5	6.0
3a_{aq}	-	5.5	16.9	-	45.9	23.4	9.7
3aZn²⁺	5.8 ± 1.5%	5.2	12.7	1.3	45.6	25.1	11.4
3aH⁺	-	5.8	11.3	0.0	43.7	25.7	15.6

* DFT-calculated S_{3p} contribution to the acceptor orbital, Ru_{4dσ*} ← S_{3p}, is determined from a Mulliken charge decomposition of the Kohn-Sham orbital. Zn²⁺ accompanied with two H₂O molecules and bound to both oxygen of the sulfinato to complete the tetrahedral coordination sphere.

Löwdin analysis of the Kohn-Sham orbitals shows that solvation and perturbation of the sulfinato oxygen via either protonation or a Lewis acid directly affects the S-O bonding. The observed electronic changes also reflect changes in bonding due to solvation and perturbations of the S-O bond. Surprisingly, there is only a small decrease in the S_{3p} contribution to the Ru_{4dσ*} orbital, the overall contribution from the sulfinato ligand to Ru_{4dσ*} orbital substantially decreases due to both solvation and perturbation, as in Table 4.2. These

^{††} TDDFT simulated XAS spectra of **3aZn²⁺.2H₂O** (where Zn^{II} binds to both sulfinato oxygens) and **3aZn²⁺.3H₂O** (where Zn^{II} binds to one of the sulfinato oxygens) were compared with experimental XAS of **3aZn²⁺**. This indicates that the binding mode for Zn^{II} with **3a** appears to be **3aZn²⁺.2H₂O**

changes are mostly compensated by increased charge donation from the ethylenediamine (en) and arene ligand but not necessarily affected the charge of the metal (Ru) centre. In contrast, the slight decreases in the S_{3p} contribution do not agree with the shortened Ru-S bonds in **3a_{aq}**, **3aZn²⁺** and **3aH⁺** during solvation, perturbation and protonation respectively. This would lead to suggest that the nature of the Ru-S bond in **3a** is dominated by electrostatic interaction between the Ru^{II} and sulfinato (RSO_2^-) group rather than the covalent bonding interaction of S_{3p} charge donation, $Ru_{4d\sigma^*} \leftarrow S_{3p}$.

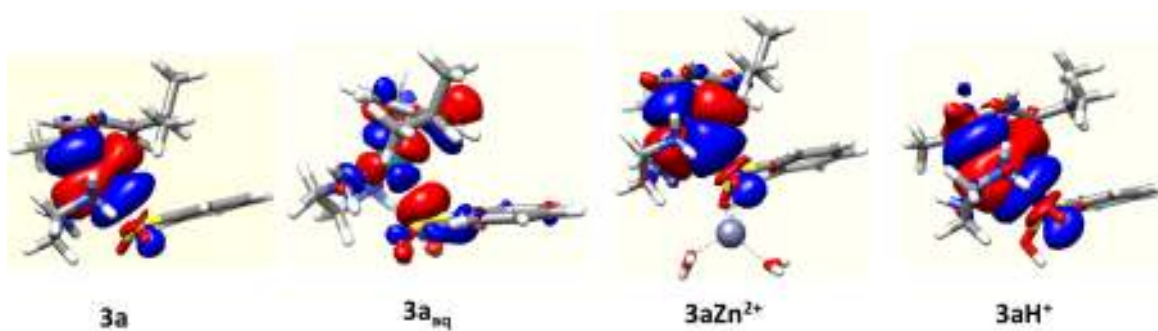


Figure 4.1: Natural bond orbital (NBO) picture of $Ru-S_{\sigma^*}$ in complexes **3a**, **3a_{aq}**, **3aZn²⁺** and **3aH⁺**

In addition, the NBO derived bond order of the Ru-S bond is found to be 0.28 in **3a**; this indicates that the covalent Ru-S interaction in **3a** is weaker than the Ru-S bond in **2a** (where NBO bond order is 0.74). By contrast, the NBO analysis of Ru-S bonding in **3a_{aq}**, **3aZn²⁺** and **3aH⁺** predicts that there is no actual bonding between Ru and S and therefore the pictured $Ru-S_{\sigma^*}$ orbital in Figure 4.1 is listed as lone-pair with occupancy of 1.19, 1.35 and 1.32 respectively. This is also seen in Ru sulfinato complexes by Shearer *et al.*²⁰⁴ The slight increase in occupancy suggests increasing electrostatic contributions to a Ru-S bond that is already dominated by electrostatics.

As shown in Figure 4.2, an additional approach – comparing the relative energies of the relevant molecular orbitals – is applied to study the effect of solvation and perturbations of the sulfinato oxygen(s). The greatest perturbation is observed in the relative MO energies when comparing **3a**, **3a_{aq}**, **3aZn²⁺** and **3aH⁺** (Figure 4.2). Solvation and protonation leads to a dramatic decrease in the energy of the SO_{σ*}, reflecting a weakening of the S-O bond. However, the relative energy of Ru-S_{σ*} remains essentially unchanged due to perturbation of acids, presumably because there is no significant SO_{π*} interaction found in the Ru_{4dσ*} of sulfinato complexes (also see Figure 3.7). Overall, the effect of perturbation is greater than just aqueous solvation.

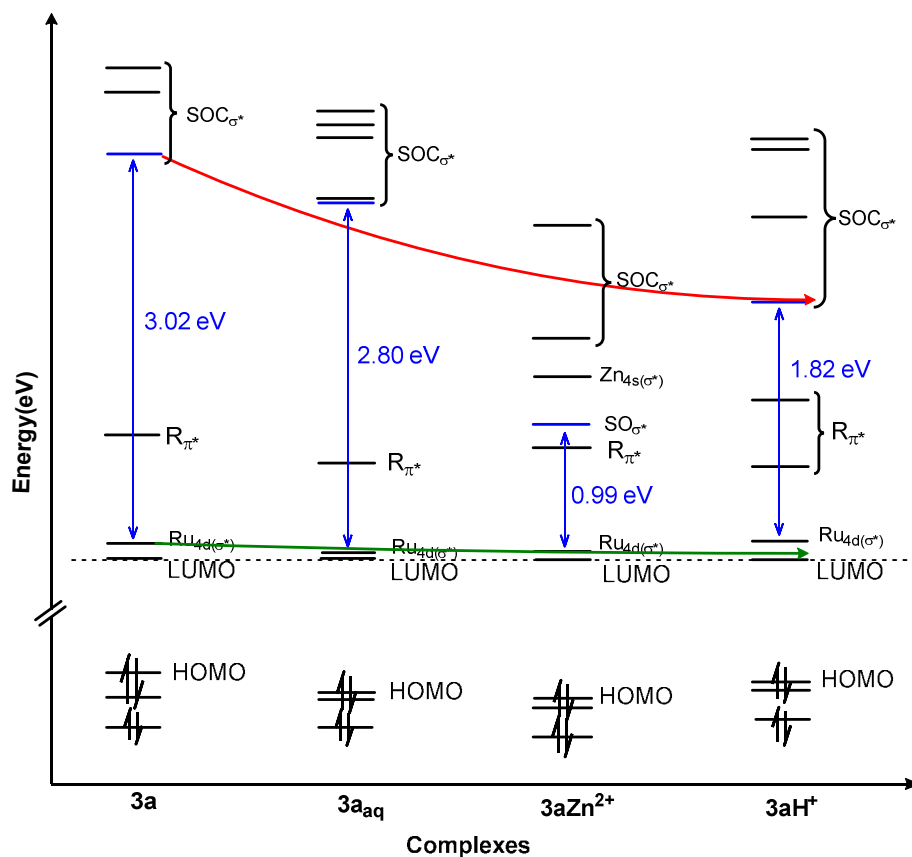


Figure 4.2: Frontier MO diagram of complexes **3a**, **3a_{aq}**, **3aZn²⁺** and **3aH⁺**. Only α orbitals are shown but α and β orbitals are identical. Red and green arrows indicate the energy change in the SO_{σ*} and Ru-S_{σ*} with protonation respectively. Orbitals are normalized to LUMO in each molecule.

The effect of Lewis acids on the sulfinato complexes was evaluated both experimentally and computationally. The sulfinato-Lewis acid adducts $3aZn^{2+}$, $3aCo^{2+}$ and $3aCr^{3+}$ were investigated using Sulfur K-edge XAS as a means of determining the effect of these metal ions on the sulfur atom and its interactions. The S K-edge XAS data, Figure 4.3a, indicate that the Ru^{II} arene sulfinato complex **3a** is dramatically influenced by the Lewis acid interaction. The perturbation effect on these complexes is distinct by the nature of Lewis acidity and coordination chemistry of Zn^{2+} , Co^{2+} and Cr^{3+} .^{300,301}

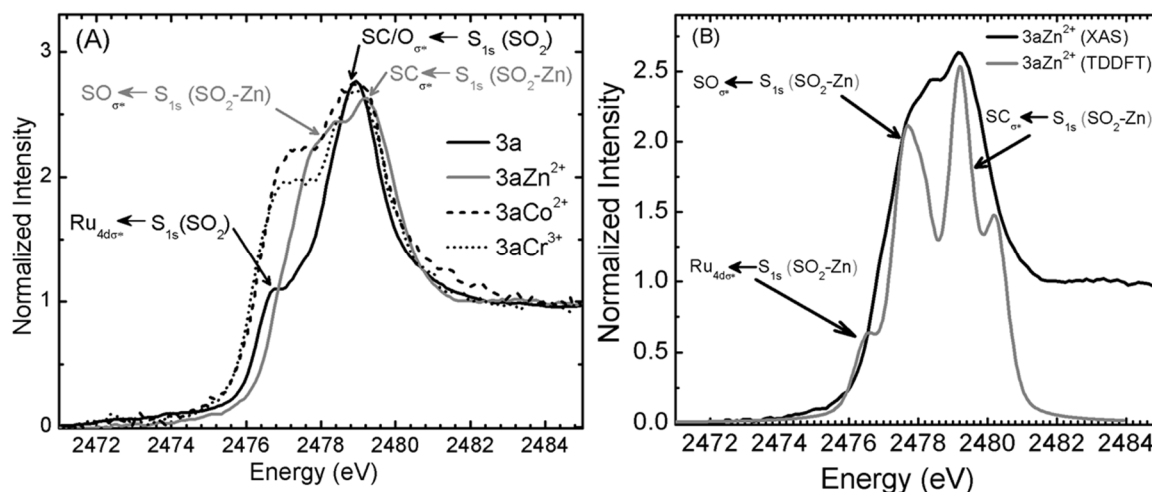


Figure 4.3: (A) Normalized S K-edge XAS of complexes **3a**, $3aZn^{2+}$, $3aCo^{2+}$ and $3aCr^{3+}$, (B) XAS and simulated TDDFT of complex $3aZn^{2+}$.

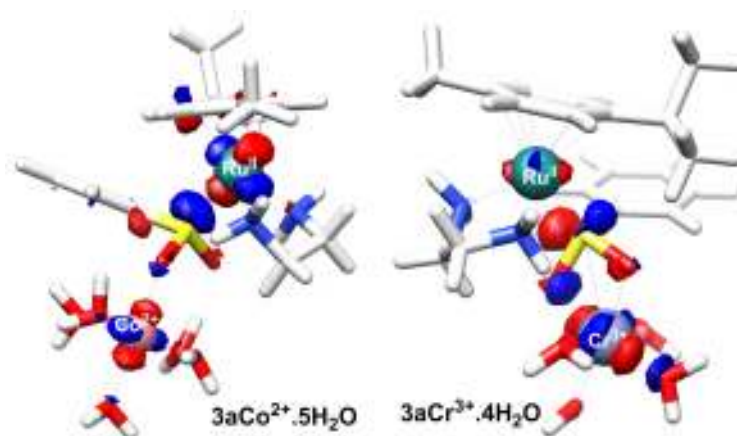


Figure 4.4: The Ru-S σ^* orbital of $3aCo^{2+}$ and $3aCr^{3+}$ showing the interaction of metal 3d with S 3p and Ru 4d orbitals

The relatively featureless high energy feature of **3a**, assigned to the combined SC/SO←S_{1s} transitions (2478.0 - 2479.0 eV), split into two well-resolved features upon addition of Zn²⁺. This effect is similar to that which is observed in DFT calculations, which suggest that Zn²⁺ binding lowers the energy of the SO_{σ*}. A similar effect is observed with Co(II) and Cr(III), although the analysis is much more complex due to the presence of empty 3d orbitals, allowing for greater S 3p delocalization, shown in Figure 4.4.

As discussed in Section 2.1.4, the intensity of the Ru_{4dσ*}←S_{1s} transition is proportional to the amount of S_{3p} character (β) in the Ru_{4dσ*} acceptor orbital, as given in equation 2.2. A systematic peak fitting and assignment (shown in Appendix A.2) were performed on the S K-edge XAS of **3aZn²⁺** to extract the S_{3p} character using the dipole integral value of $\langle SO_2R^-_{3p}|r|S_{1s}\rangle \approx 18$.^{185,187} As shown in Table 4.2, the analysis indicates that there is little change in the S_{3p} contribution and therefore, consistent with that of DFT analysis. Furthermore, the TDDFT simulation of the **3aZn²⁺** XAS is in good correlation with the experimental S K-edge XAS, Figure 4.3b.

4.3.2 Lewis Acid Interaction and Brønsted Acid Protonation on Sulfenato

The model system **2a** was used for all computational studies on the sulfenato species, with a primary focus on the *in silico* solvated (**2a_{aq}**), protonated (**2aH⁺**) complexes and the perturbed Zn^{II} adduct (**2aZn²⁺**). The Zn^{II} adduct was modelled as a tetrahedral Zn^{II} ion with three explicit water ligands and the 4th coordination position being taken by the sulfenato oxygen from complex **2a** (a tetrahedral coordination of Zn^{II} with oxygen(s) is indicated by XAS and TDDFT results of **3aZn²⁺**). The aqueous solvation and acidic perturbatory effect on the overall geometric structure of **2a** is generally quite small and localized to 1-2 bonds from the

terminal oxygen atom. The interactions trigger elongation of the S-O bond and that results concomitantly in a slight contraction of the Ru-S bond (Table 4.3). A similar trend is also observed in the Lewis acid adduct of Fe^{III}-sulfenato complex, [Fe^{III}(ADIT)(ADIT-O-ZnCl₃)].^{201,267}

Table 4.3: Selected bond length (Å) of **2a**, **2a_{aq}**, **2a-Zn²⁺** and **2aH⁺** from the DFT analysis

Complex	Bond length Ru-S	Bond length S-O
2a	2.442	1.589
2a_{aq}	2.396	1.618
2aZn²⁺	2.384	1.677
2aH⁺	2.359	1.724

Table 4.4: DFT-calculated S_{3p} contribution* (Ru_{4dσ*} ← S_{3p}) and the total charge distribution of Kohn-Sham acceptor orbital, Ru_{4dσ*} of **2a**, **2aZn²⁺** and **2aH⁺** complexes

Complex	% S _{3p} in acceptor	SOR (%)	H/M(H ₂ O) ₃ (%)	Ru (%)	Ar (%)	En (%)
2a	12.7	20.9	-	41.1	20.0	6.1
2a_{aq}	11.2	18.9	-	42.6	20.5	6.1
2aZn²⁺	10.6	17.0	6.2	46.4	20.5	6.4
2aH⁺	9.2	14.9	0.4	48.3	19.5	6.1

DFT-calculated S_{3p} contribution to the acceptor orbital, Ru_{4dσ} ← S_{3p}, is determined from a Mulliken charge decomposition of the Kohn-Sham orbital. Cation Zn²⁺ is accompanied with three H₂O molecules to complete the tetrahedral coordination sphere.

As with sulfinato complexes, the Löwdin analysis of the Kohn-Sham orbitals shows that aqueous solvation of the complex and perturbation of the sulfenato oxygen via either protonation or a Lewis acid directly affect bonding. Solvation and both perturbations moderately decrease S_{3p} contributions in the Ru-S_{σ*}, reflecting a decrease in donation into the metal centre. The effect is greater in **2aH⁺** as compared to **2aZn²⁺**, which reflects the greater influence of protonation. The overall charge donation from the S-ligand (SOR) to that

acceptor orbital is also decreased, again with a larger effect being observed for **2aH⁺** than for **2aZn²⁺**. These differences are consistent with protonation of the oxygen atom having a greater influence than Zn^{II} coordination. Contrasting to sulfinato, the observed reduction in overall charge contribution from the sulfenato ligand does not result in compensatory charge donation from the other ligands (*i.e.* arene and en).

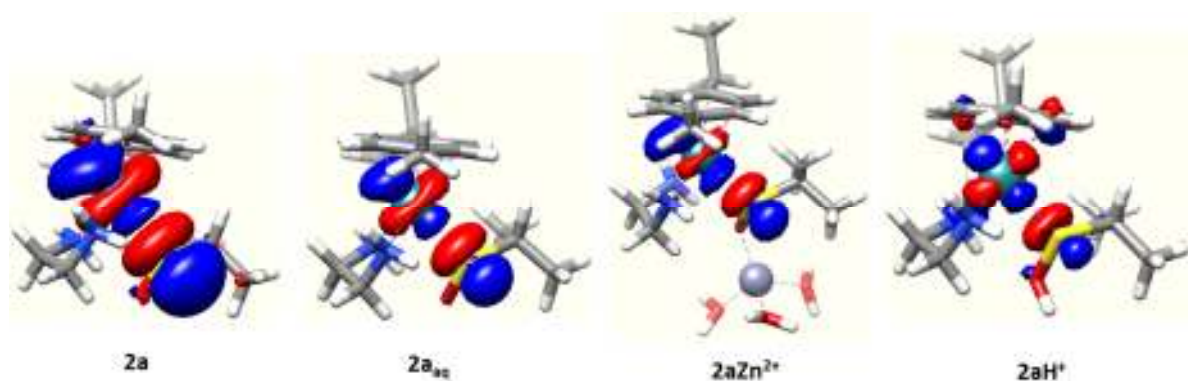


Figure 4.5: Natural bond orbital (NBO) picture of Ru-S σ^* in complexes **2a**, **2a_{aq}**, **2aZn²⁺** and **2aH⁺**

A natural bond orbital (NBO) analysis for **2a**, **2aZn²⁺** and **2aH⁺** was used to estimate bond orders and visualize the localized Ru-S bonding (the NBO of Ru-S σ^* antibond is shown in Figure 4.5). For complexes **2aZn²⁺** and **2aH⁺**, the NBO bond order analysis suggests no formal covalent bonding between the Ru and S atoms, as compared to 0.74 and 0.72 of a bond in the parent **2a** (see Section 3.3.2) and **2a_{aq}** complexes respectively. This qualitatively suggests that solvation followed by protonation or the presence of a Lewis acid is sufficient to weaken the Ru-S interaction as predicted.

Another approach to defining the effect of perturbations of the sulfenato oxygen is to compare the relative energies of the relevant molecular orbitals. Frontier molecular orbital diagrams for **2a**, **2a_{aq}**, **2aZn²⁺** and **2aH⁺** are shown in Figure 4.6. Most notably, perturbation

of the sulfenato oxygen lowers the energy of both the Ru-S σ^* and SO σ^* empty orbitals. As anticipated, the effect is significantly greater for the SO σ^* than for the Ru-S σ^* .

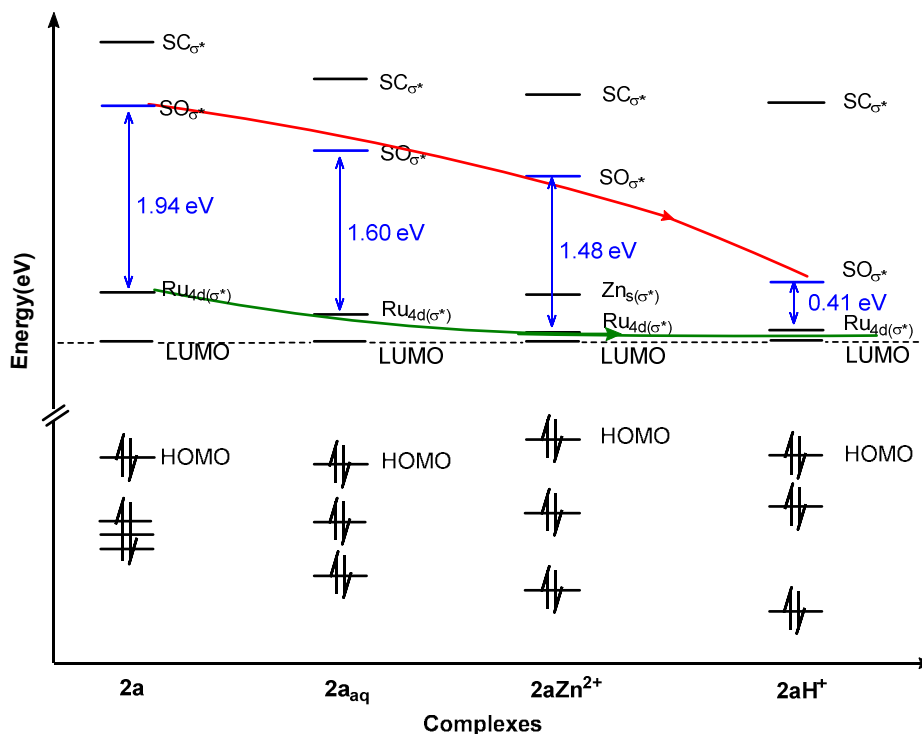


Figure 4.6: Frontier MO diagrams for complexes **2a**, **2a_{aq}**, **2aZn²⁺** and **2aH⁺**. Only α orbitals are shown but α and β orbitals are identical. Red and green arrows indicate the energy change in the SO σ^* and Ru-S σ^* with protonation respectively. Orbitals are normalized to LUMO in each molecule.

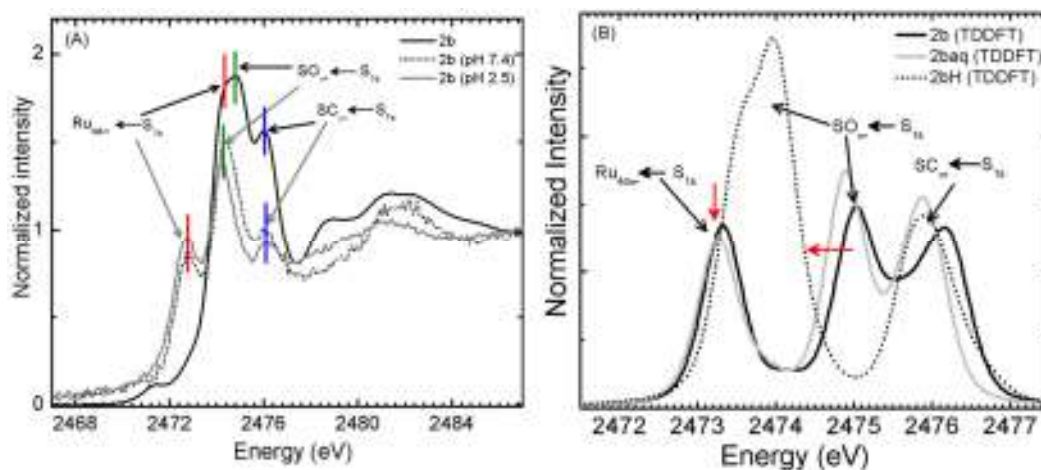


Figure 4.7: (A) S K-edge XAS of **2b** and the first scan of **2b** solutions at pH 2.5 and pH 7.4; (B) simulated TDDFT of **2b**, **2b_{aq}** and **2bH⁺**. An energy shift of 60.0 eV applied to simulated spectra to calibrate them with experimental data.

Attempts to probe the effect of protonation through experiment were more challenging. Sulfur K-edge XAS data of complex **2b** were obtained at pH 7.4 and 2.5. The data are shown in Figure 4.7a in comparison to that which is obtained for **2b** in the solid state. Photoreduction of the solution samples was a major problem, thus data obtained from single rapid scans are shown.

Data are significantly poorer at the lower pH, but there is no indication of any major changes in the S K-edge XAS spectrum. However, protonation of the sulfenato oxygen should have a major effect on the spectrum, as seen from simulated spectra in Figure 4.7b. By contrast, however, a rather large difference between the solution and solid state spectra were observed. The lowest energy feature of the spectrum (the $Ru4d\sigma^* \leftarrow S_{1s}$ transition) drops by ~ 1.5 eV upon solvation. Such large effects are not observed *in silico* using the COSMO solvation model, suggesting that the solvation model does not adequately reflect changes in the localized bonding upon solvation. However, there is a slight decrease in the S_{3p} character contribution, Table 4.4 and the energy of the $Ru-S_{\sigma^*}$ orbital (Figure 4.6) due to the solvation.

The Frontier MO diagrams of these complexes, Figure 4.6, show that the energy of $S-O_{\sigma^*}$ and $Ru-S_{\sigma^*}$ orbitals decreases upon solvation/protonation. In the simulated TDDFT spectra, only the $S-O_{\sigma^*}$ shifted to lower energy. However, the energy of $S-C_{\sigma^*}$ orbital is not necessarily changed due to the same effects; thus in the S K-edge spectra the higher energy peak at 2476.2 eV, assigned to $SC_{\sigma^*} \leftarrow S_{1s}$ transition, does not affected by solvation. Simulated TDDFT spectrum of **2b_{aq}** is in closer agreement with the solvated spectra **2b** (pHs 7.4 and 2.5) as seen in Figure 4.7. Therefore complex **2b** is solvated in pHs 7.4 and 2.5 but the protonated species is not identified in the lower pH.

4.4 Discussion

DFT and XAS studies performed on the solvated, protonated and perturbed Ru^{II} arene sulfenato and sulfinato complexes show that both solvation and perturbation of the terminal oxo groups redistribute S_{3p} character of the sulfur-containing ligands. Unsurprisingly, solvation and perturbation of the sulfenato oxygen affect both the Ru-S and S-O bonds without a strong effect on the S-C bond. The Ru-S bond in the sulfenato complexes is thus quite sensitive to relatively small perturbations. Moreover, protonation of the sulfenato ligand results in significant changes in bonding. By contrast, the effect of solvation and other perturbations on sulfinato complexes is more limited and only affects the S-O bond with little or no effect on the Ru-S bond covalency. It should be noted here that the effect of Lewis acid on **3a** appears to be slightly higher than the effect observed in **2a**; however in **3a** the Zn^{II} ion interacts with both oxygen of the sulfinato ligand, thus the total effect seems to be higher but the average effect caused by a single oxygen would be slightly lower to that caused by **2a**. These results are in agreement with the idea that protonation of the *sulfenato* should have a strong impact on the strength and lability of the Ru-S bond whereas protonation of the *sulfinato* has little or no impact on the strength and lability of the Ru-S bond.

Interestingly, aqueous solvation partially activates the Ru^{II} arene sulfenato and sulfinato complexes by lowering the energy of the Ru-S σ^* . Complex **2** and **3** have intra (SO--H₂N) and inter H-bonds between neighbouring en ligand and solvent MeOH (or in the complex **3** the neighbouring dimer molecule) respectively. These two H-bonds are removed or weakened due to solvation effects. Therefore, in the H-bond free-complex **2**, the Ru-S bond is elongated which concomitantly decreases the covalency and makes the molecule more

labile. However, this effect is minimized in complex 3 due the nature of the Ru-S bond (*vide infra*).

As discussed in Chapter 3, formation of the sulfenato species via ligand oxygenation is a necessary but insufficient step for biological activation of these complexes. However, the Ru-S interaction in the sulfenato complex is quite different due to the more pronounced pi contributions in the S-O bond, Figure 3.11. Due to this unique property, protonation of the sulfenato oxygen directly weakens the covalency of Ru-S bond and also the H-bond between the sulfenato group and the NH₂ of the en ligand, as observed in the hydrolysis of sulfenato complexes.⁷⁶ These results agreed with the postulated mechanism in Scheme 3.1. In contrast, the Ru-S bond in the sulfinato does not involve pi contributions to a terminal oxo. Therefore, protonation of the sulfinato species has only a minor effect on the covalency of Ru-S bond.

Protonation of the sulfenato is therefore observed to be an effective method of labilizing the Ru-S bond, specifically by weakening the S-O π -bond in the ligand. In addition, a recent study on breast cancer tissues reveals a positive association between the amount of mobile Zn^{II} and cancer.^{286,287} Therefore, Zn^{II} can act as a Lewis acid for the protonation of the sulfenato complexes in cancer cells.

4.5 Conclusions

The effect of solvation, protonation and perturbation of sulfenato and sulfinato complexes is investigated using X-ray absorption spectroscopy and density functional theory. Examining, understanding and controlling the biological mechanism of the metal prodrugs are important for their faster pre-clinical and clinical development. Our earlier study (described in Chapter 3) shows that sulfur ligand oxygenation does not necessarily change

the charge distribution to the metal center and therefore does not directly have impact on the lability of the ligand. The present study shows that the second and most important step, solvation followed by protonation of the sulfenato complexes, decreases the charge donation from the sulfur ligand to the metal center. Therefore, it does play a vital role on the lability of the ligand. Therefore, activation mechanism of Ru arene thiolato complexes is unique and leads through the ligand-centered oxidation followed by solvation and protonation.

CHAPTER 5. SPECTROSCOPIC INVESTIGATION OF RUTHENIUM (II) AND OSMIUM (II) ARENE THIOSEMICARBAZONE COMPLEXES

5.1 Introduction

Thiosemicarbazones (TSCs) are one of the Schiff base motifs that have been extensively studied for a broad spectrum of chemotherapeutic properties over the past decade.^{302,303} In medicinal chemistry, TSCs have emerged as an important class of ligands due to their variable donor properties, structural diversity, and biological applications.³⁰³ Interestingly, it has been postulated that inside the cells, thiosemicarbazone (TSC) ligands coordinate to metal ions to form complexes and the redox properties of those complexes would be responsible for their biological properties.³⁰² In addition, studies have shown that the biological properties of TSCs can be modified and in fact enhanced, by metal ion binding.³⁰² Substituted and metal coordinated heterocyclic TSC complexes have shown a wide range of medicinal properties including cytotoxic and antitumor,³⁰⁴ antibacterial,^{305,306} antiviral,³⁰⁷ anti-trypanosomal³⁰⁸ and anti-alzheimer³⁰⁹ properties.

One of the first concepts applied in developing organometallic Ru^{II} anticancer drugs is to combine metal-arene moieties with bioactive ligands. In fact, the first organometallic ruthenium complex, [Ru(η^6 -bz)Cl₂(metronidazole)], tested for anticancer activity involved such a combination.⁴⁹ Since then, the use of non-cytotoxic ligands, *i.e.* ethylenediamine and PTA, with metal-arene systems has led to complexes with significant anticancer activity such as the RM175-type and RAPTA-family complexes. In recent years, however, researchers have revisited the original strategy and generated highly efficient anticancer drugs with different modes of activity such as paullones,¹¹⁶ ethacrynic acid,⁷³ and staurosporine.³¹⁰ A series of

biologically potent TSC ligands hybrid with Ru^{II} and Os^{II} arene complexes have been recently developed by Sadler and coworkers (see Figure 5.1). The anticancer activity, cellular accumulation and mode of activity of these complexes are currently under investigation.³¹¹

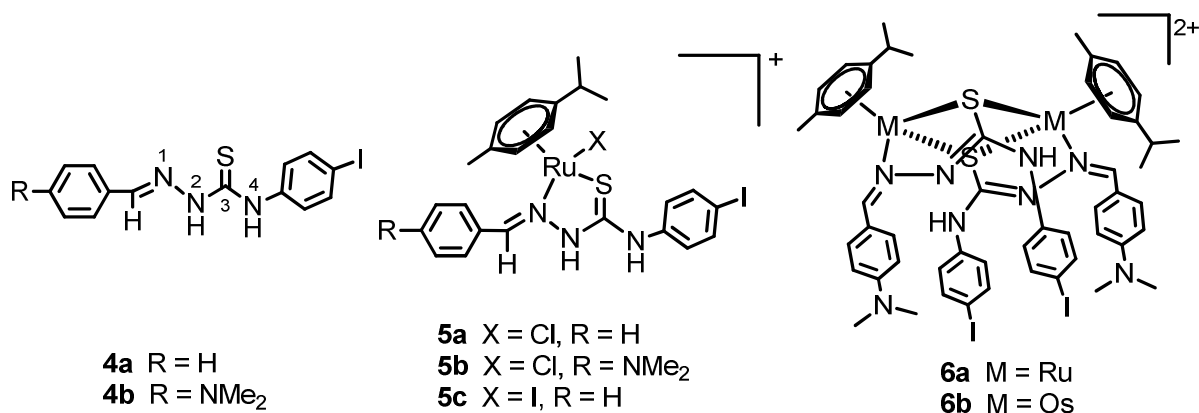


Figure 5.1: Ru^{II}/Os^{II}-arene thiosemicarbazone complexes investigated in this Chapter

A number of bonding modes have been observed for TSCs in their neutral or anionic forms with metals.³⁰³ Recently, Beckford and coworkers reported Ru^{II}-arene complexes coordinated with neutral TSC as a bidentate ligand, which possess both anticancer and antimicrobial properties.^{312–316} Fluorescence studies of these complexes with human serum albumin (HSA) suggest their interactions with biological molecules;³¹³ however, there is little discussion of structure activity relationships or plausible mechanisms of action. Other studies show that TSCs can also coordinate to the metal in a monodentate fashion through the sulfur atom.^{317,318} Newly developed half sandwich mononuclear and sandwich dinuclear Ru^{II}, Os^{II}-*p*-cym-TSC complexes, Figure 5.1, studied herein lack good quality crystal structures. As a result, they are characterized using NMR, mass spectrometry, infrared, and UV-vis spectroscopy.³¹¹ It is therefore necessary to investigate their electronic structure to confirm

the geometry and the coordination fashion of the TSC ligand. This investigation will further be useful to investigate the biological mechanism of these complexes in detail.

Ru(II) and Os(II) arene complexes with bidentate chelating ligands, developed by Sadler and co-worker, show promising anticancer activity in a range of cancer cell-lines.^{3,28,52,69} The mode of action of these complexes has been comprehensively investigated and a consensus mechanism has been postulated.^{28,96,121} However, cellular speciation and distribution of such complexes is challenging. Ru metal accumulation in cells and their compartments can be determined by ICP-MS, but there is no confirmation on the ligand set of the complex as it was first administered. Therefore, the complexes studied herein have been synthesized with iodine-substituted thiosemicarbazone ligands, Figure 5.1. Here, the iodine (-I) label can be used for ligand cellular uptake studies. Thus, both the metal and the ligand can be traced and quantified inside cells. The ratio of metal to ligand can be used as an indicator about the state of the complex.

The investigation of structure-activity relationships for Ru and Os arene complexes have shown that changing the metal centre, making a small modification on the chelate ligand⁹¹ or exchanging the monodentate ligand, *e.g.* from chloride to iodide, can have a major effect on biological activity.^{90,319} Therefore, in this study the effects of monodentate ligand (Cl vs I), metal centre (Ru vs Os) and the modification of the TSC ligand are investigated through their electronic structure. X-ray absorption spectroscopy combined with DFT and TDDFT calculations is used to investigate the TSC ligands as well as their Ru/Os-*p*-cym-TSC complexes.

5.2 Experimental and Computational Aspects

5.2.1 Experimental Aspects

All the complexes studied here were prepared and characterized by Anna Louisa Noffke from the Sadler group^{††} according to the procedure to be published in our collaborative manuscript.³¹¹ These complexes were characterized using NMR, electron spray ionization mass spectrometry, infrared spectroscopy and elemental analysis. XAS experiments on S K-edge were performed at the soft X-ray micro characterization beamline (SXRMB) of the Canadian Light Source (CLS).²¹¹ Samples for the experiments were prepared according to the procedure mentioned in Section 4.2.1. S K-edge XAS data was collected and analysed using the methods described in Section 4.2.2 and 4.2.3, respectively.

5.2.2 DFT Calculations

The initial coordinates for the geometry optimization of TSCs **4a** and **4b** were obtained from ChemBio3D structures and that of complexes **5a-c**, $[(p\text{-cym})\text{Ru}^{\text{II}}(\text{TSC})\text{X}]^+$ ($\text{X} = \text{I}/\text{Cl}$) were obtained by modifying the X-ray crystal structure of simplified alkyl substituted $[(p\text{-cym})\text{Ru}^{\text{II}}(\text{TSC})\text{Cl}]$ complex using MOLDEN.²⁹⁸ The coordinates for complexes **6a** and **6b** were obtained from the crystal structures. DFT calculations were performed using the ORCA²²⁰ quantum chemistry program, version 2.9. Geometry optimization was obtained using BP86 (Becke-Perdew 86) gradient-corrected functional,^{226,227} in combination with the TZVP basis set and def2-TZVP/J auxiliary basis sets.²³³ Combined TZVPP and TZVPP/J auxiliary basis sets were applied on the metal center Ru and Os. Scalar relativistic effects were

^{††} This chapter is based on collaborative work with Prof. Sadler and co-worker Anna Louisa Noffke from Department of Chemistry, University of Warwick, Coventry, UK

introduced using ZORA.^{320,321} A dense integration grid (grid4) and tight convergence criteria were enforced unless otherwise stated. The geometry optimized structures were utilized to perform single point TDDFT calculations of the XAS spectra. An energy shift of ~ 60.5 eV was applied to the spectra when it was constructed with experimental XAS for comparison using MO Analyzer (version 1.1 beta).²⁹⁷ Simulation of UV-vis spectra of **5b** and **6a** were done using BP86 and B3LYP +VDW10 (Van der Waals corrections) functionals.

5.3 Results and Analysis

S K-edge XAS in concert with DFT and TDDFT calculations are extensively used to probe the electronic structure of complexes **4** - **6**. Additionally, effects of substitution of the NMe₂ group on the TSC pro-ligand, changing the metal centre from Ru to Os and the monodentate ligand from Cl to I are also investigated. In addition, an attempt was made to simulate the UV-vis spectra of **5b** and **6a**.

5.3.1 Effect of TSC Ligand Modification

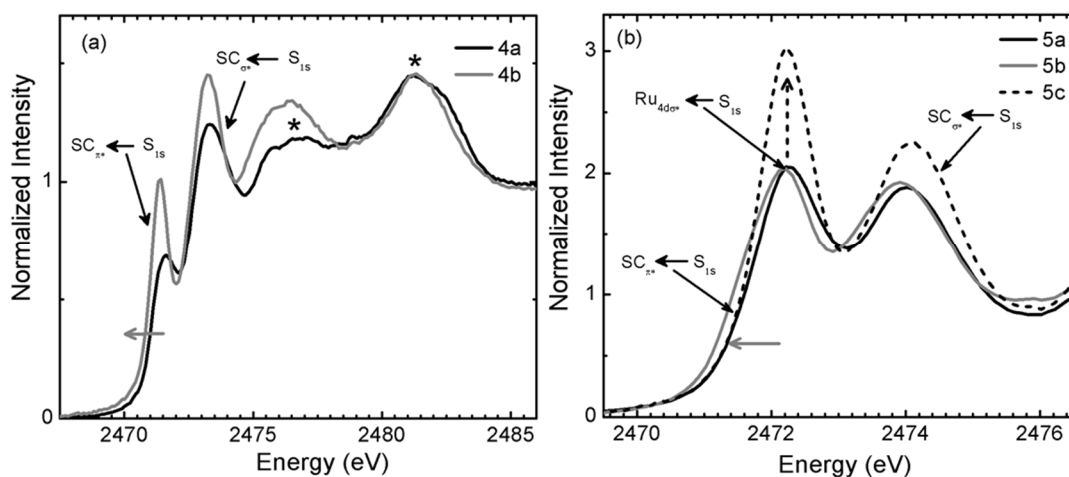


Figure 5.2: Normalized S K-edge XAS of unmodified (**4a**) and modified (**4b**) TSC ligands (a) and complexes **5a-c** (b). * denotes the thiolate based impurities. TDDFT spectra of these complexes are provided in Appendix A.3.1.

The effect of thiosemicarbazone ligand modification is investigated in proligands (**4a** and **4b**) and in metal-ligated complexes (**5a** and **5b**) using S K-edge XAS. As shown in Figure 5.2a, the S K-edge XAS spectra of unmodified (**4a**) and modified (**4b**) proligands exhibit two dominant features in the near edge between 2470 - 2475 eV. Based on the literature²⁸⁰ and results from DFT calculations, these two features are attributed to $SC_{\pi^*} \leftarrow S_{1s}$ (at 2471.5 eV) and $SC_{\sigma^*} \leftarrow S_{1s}$ (at 2472.3 eV) transitions. Furthermore, DFT also predicts there are three empty π^* orbitals with sulfur character in the TSC proligand (also see the π^* orbitals of the model complex in Figure 5.3). Transitions to all three of these π^* orbitals contribute to the first features as shown in the TDDFT spectra of **4a** and **4b** (see Appendix A.1.3). S K-edge XAS data indicate that NMe₂ substitution on the TSC proligand results in larger contributions from the S 3p into the π -system. In addition, S 3p contributions to the SC_{π^*} and SC_{σ^*} final states also increase, in agreement with DFT calculations.

The S K-edge XAS of unmodified (**5a**) and modified (**5b**) Ru^{II} metal complexes also exhibit two clearly resolved features in that region. The lowest energy feature in these spectra are much more intense than for the corresponding proligand due to the presence of the $Ru_{4d\sigma^*} \leftarrow S_{1s}$ transition. A closer look at the spectrum for **5b** indicates the presence of low energy shoulder at 2471.5eV, which likely corresponds with one component of the $SC_{\pi^*} \leftarrow S_{1s}$ features. This assignment is in good agreement with DFT calculations (see the Frontier MO diagram in Figure 5.4)

Interestingly, our experimental and computational data suggest that the TSC possess an extended π -system, running through the backbone of the ligand. As anticipated, the π -system is preserved in the metal complexes as well. A simplified model complex,

$[\text{CH}_2=\text{NH}-\text{CS}-\text{NH}-\text{N}=\text{CH}_2]^+$, of TSC is used to illustrate those π -orbitals as shown in Figure 5.3.

The three π^* orbitals listed in the MO diagram are the ones which contribute to the $\text{SC}\pi^* \leftarrow \text{S}_{15}$ transitions in the S K-edge XAS. The simulated XAS spectra of TSCs show that these three transitions are added together in the first lower energy peak.

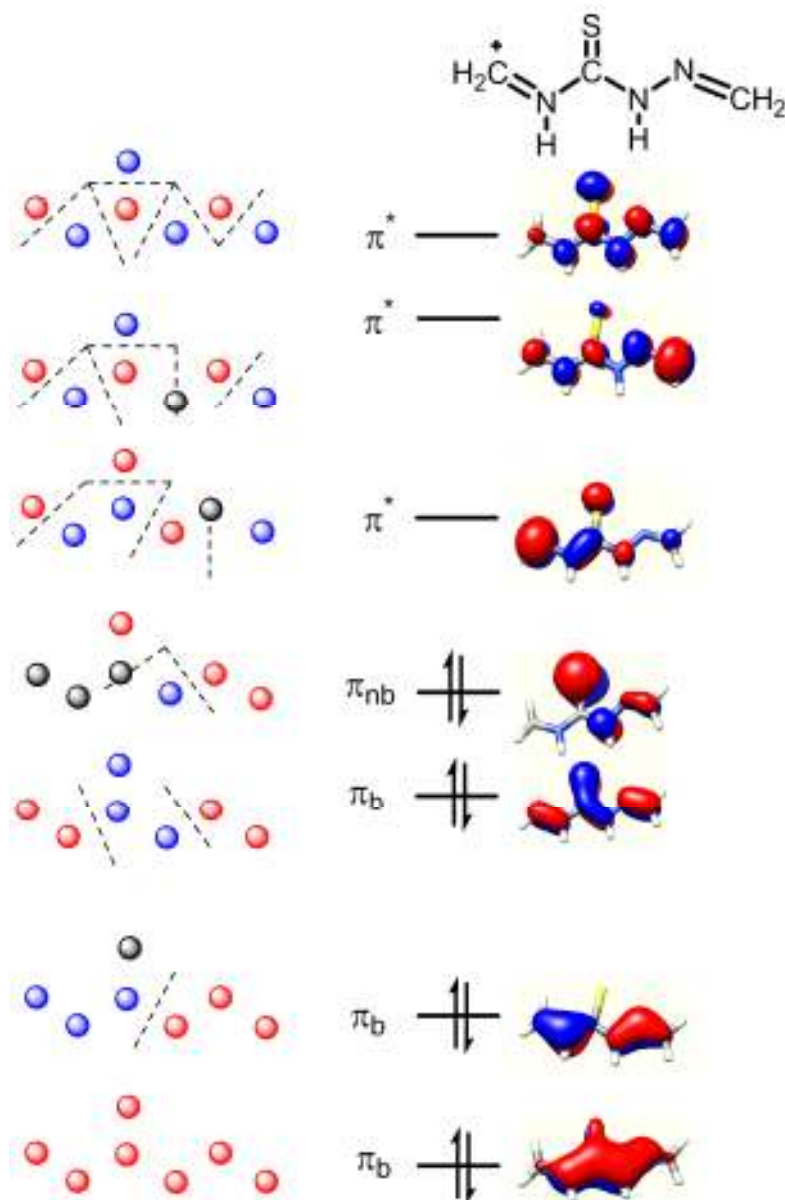


Figure 5.3: MO diagram of the π -systems of Thiosemicarbazone molecule described using model complex $[\text{CH}_2=\text{NH}-\text{CS}-\text{NH}-\text{N}=\text{CH}_2]^+$

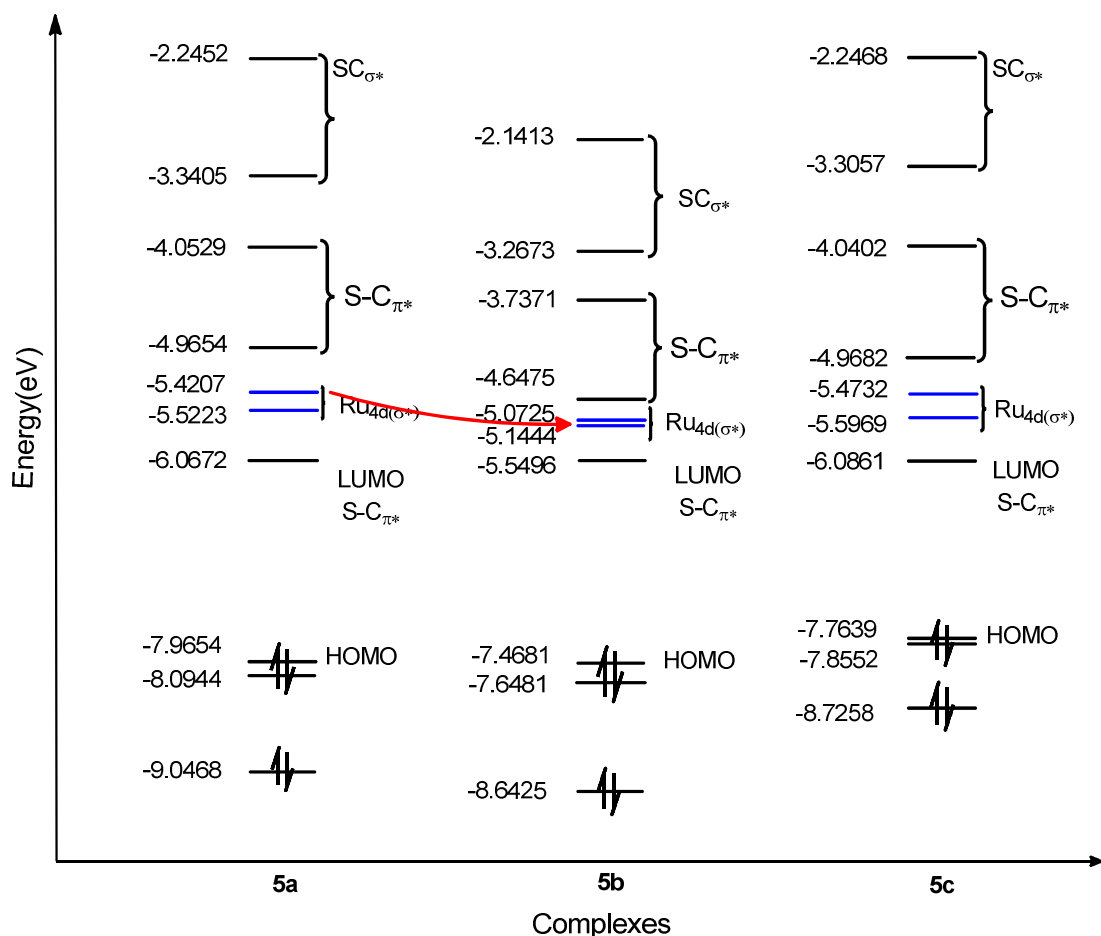


Figure 5.4: Frontier MO diagram of complexes **5a-c**. Only α orbitals are shown (α and β are identical). Red arrow indicates the energy shift from **5a** \rightarrow **5b**. Orbitals are normalized to LUMO in each complex.

As mentioned in earlier Chapters, the intensity of each of the experimental features in the S K-edge XAS spectra results predominantly from redistribution of the localized electric dipole-allowed $S_{3p} \leftarrow S_{1s}$ transition to each of the final states, as defined by equation 2.2. Thus, the intensity of a particular spectroscopic feature depends on the amount of S_{3p} character in that final state.

Systematic fits to the data in each case allow for the extraction of experimentally derived S_{3p} contributions to each of the features in the spectrum. The dipole integral (as in equation 2.2 $\langle S_{3p} | r | S_{1s} \rangle$) used to estimate the S_{3p} character from complex **5a, b, c** is

$\langle SR_{3p}^- | r | S_{1s} \rangle \approx 13$ and that of complexes **6a**, **b** is ≈ 14 . The results from these fits are given in Table 5.1. For comparison, results from density functional calculations are also included in the table. The S_{3p} character, extracted from the XAS spectra for $Ru_{4d\sigma^*} \leftarrow S_{1s}$ and $SC_{\sigma^*} \leftarrow S_{1s}$ transitions, agrees well with that obtained from DFT; however, the S_{3p} character, extracted from XAS for the $SC_{\pi^*} \leftarrow S_{1s}$ transition is lower than that obtained from DFT. That might imply that the $SC_{\pi^*} \leftarrow S_{1s}$ transition is weaker in these complexes.

Table 5.1: S K-edge XAS peak energies and transition assignments with experimentally estimated S_{3p} character in the acceptor orbitals from normalized fit intensities compared with calculated DFT value

Comp	S K-edge XAS Transition		% S_{3p} in Acceptor orbital		
	Energy (eV)	Assignment	XAS	DFT	
				SC_{π^*}	$Ru_{4d\sigma^*}$
5a	2472.3	$SC_{\pi^*} + Ru_{4d\sigma^*}$	$16.0 \pm 1.4\%$	3.1	12.9
	2473.3	SC_{π^*}	$4.0 \pm 0.3\%$		12.9
	2474.1	SC_{σ^*}	$22.5 \pm 2.8\%$		16.6
5b	2472.3	$SC_{\pi^*} + Ru_{4d\sigma^*}$	$18.1 \pm 0.8\%$	2.9	13.2
	2473.3	SC_{π^*}	$8.9 \pm 0.8\%$		12.4
	2474.1	SC_{σ^*}	$11.8 \pm 1.0\%$		12.1
5c	2472.3	$SC_{\pi^*} + Ru_{4d\sigma^*}$	$18.5 \pm 1.2\%$	3.3	12.7
	2473.2	SC_{π^*}	$6.8 \pm 1.6\%$		12.9
	2474.1	SC_{σ^*}	$16.5 \pm 1.7\%$		16
6a	2472.4	$Ru_{4d\sigma^*}$	$15.4 \pm$		19.3
	2473.2	$SC_{\pi^*} / SC_{\sigma^*}$	$21.8 \pm$		a
6b	2473.2	$OS_{5d\sigma^*}$	$10.7 \pm$		12.2
	2474.2	$SC_{\pi^*} / SC_{\sigma^*}$	$29.8 \pm$		a

Detail fit result for each complex is provided in Appendix A.3.1. ^a S_{3p} character is dispersed over a wide energy range and multiple acceptor orbitals

The NMe_2 group substitution on the TSC ligand appears to have a mild influence on bonding in the metal complex as seen from the slightly increased intensity of the $Ru_{4d\sigma^*} \leftarrow S_{1s}$

transition in complex **5b** compared to that of **5a**. In addition, the whole spectrum is down shifted in energy by ~ 0.6 eV (shown by arrow in Figure 5.2) in **5b**. A similar shift is also observed in **4b**. This can be attributed to the more electron rich environment of the TSC due to the electron donating property of alkylamino (NMe_2) group. It is also consistent with a slightly higher charge donation from S_{1s} to $\text{Ru}_{4d\sigma^*}$ which leads to a higher covalency of the Ru-S bond in complex **5b**. The increased charge donation from S concomitantly decreases the charge donation from the Cl ligand (13.5% in **5a** and 12% in **5b**) as noticed from the DFT results. In addition, it also reduces the energy gap between the $\text{Ru}_{4d\sigma^*}$ orbitals. Therefore, NMe_2 group substitution in **5b** might lead to a more covalent Ru-S bond and more labile Ru-Cl bond compared to a less covalent Ru-S bond in **5a**. Interestingly, the bond strength and lability of these complexes appear to correlate well with their solution chemistry. *i.e.* the complex **5a** forms fragments in solution with no distinct species. In contrast, the complex **5b** forms dimeric species (**6a**) through an intermediate (may be aqua) species³¹¹ (this is further investigated in Section 5.3.4).

5.3.2 Effect of the Monodentate Ligand

The effect of the monodentate halide ligand is investigated using S K-edge XAS by exchanging the chloride ligand in **5a** to iodide ligand in **5c**. As shown in **Error! Reference source not found..2b**, when the ligand is exchanged from chloride to iodide (from **5a** to **5c**), there is a noticeable increase (16% \rightarrow 18.5%) in the intensity of the first feature, which correlates to the $\text{Ru}_{4d\sigma^*} \leftarrow \text{S}_{1s}$ transition. It suggests that the covalency of the Ru-S bond is slightly greater in **5c** compare to that of **5a**. Our DFT results are consistent with this

interpretation as the calculated covalency of the Ru-I bond (I_{5p} character is 16.9%) in **5c** is also more covalent than the Ru-Cl bond (Cl_{3p} character is 13.5%) in complex **5a**.

These complexes are only poorly soluble in water, but they exhibit cytotoxicity in μM concentration.³¹¹ The biological activity of complexes **5a** and **5c** at the same concentration is under investigation. However, preliminary studies suggest that less soluble complexes might be more active. Based on these studies and prior studies, one might predict that the substitution of monodentate ligand may not be the only activation mechanism for these complexes.

5.3.3 Effect of Metal (Ru vs Os) in Dimeric Complexes

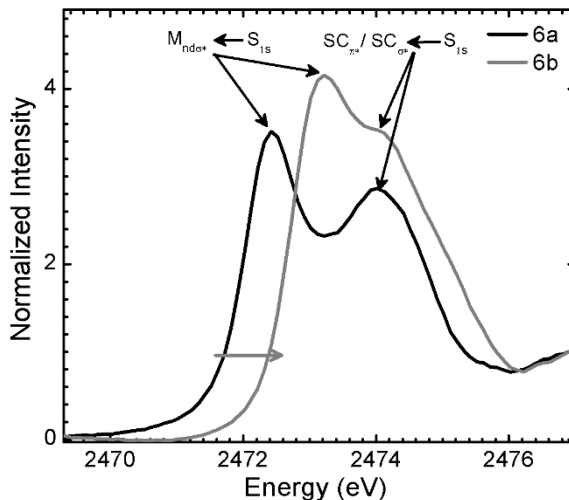


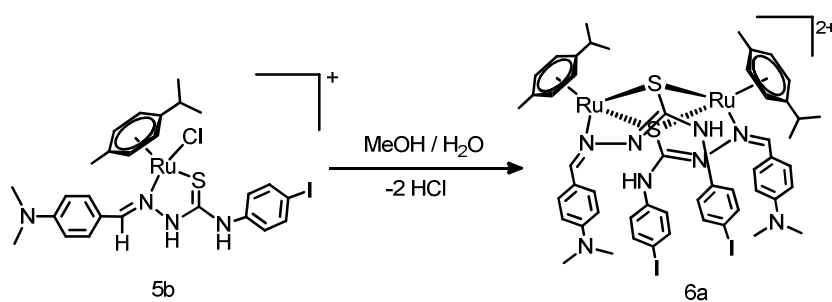
Figure 5.5: S K-edge XAS of complexes **6a** and **6b**. Os M_{3-} edge background is not subtracted from the spectrum **6b**.

S K-edge XAS spectra of the sandwich dinuclear Ru^{II} and Os^{II} -*p*-cym-TSC complexes are shown in Figure 5.5. The near edge region of the spectra is dominated by two intense features. The lower energy feature is assigned to the $M_{nd\sigma^*} \leftarrow S_{1s}$ transition. The higher energy feature is assigned to the $SC_{\pi^*} / SC_{\sigma^*} \leftarrow S_{1s}$ transition. Importantly, the π -system of the TSC ligand is strongly affected by deprotonation of ^2N on the TSC ligand (Figure 5.1). Metal

exchange from ruthenium (**6a**) to osmium (**6b**) results in a large shift in the energy of the $M_{nd\sigma^*} \leftarrow S_{1s}$ transition to higher energy. This change reflects the higher energy of the Os_{5d} orbitals compared to the Ru_{4d} orbitals. The $M_{nd\sigma^*} \leftarrow S_{1s}$ transition in **6a** is thus shifted to higher energy (2472.4 \rightarrow 2473.2 eV) in **6b**.

General estimates for the M-S covalency have also been extracted from the data for complexes **6a** and **6b**. Results are tabulated in Table 5.1 with available DFT analysis. Both XAS and DFT suggest that the Ru-S covalency in **6a** is higher than Os-S covalency in **6b**.

5.3.4 Monomer to Dimer formation using UV-Vis Spectroscopy and DFT



Scheme 5.1: Conversion of **6a** from **5b** in methanol or water

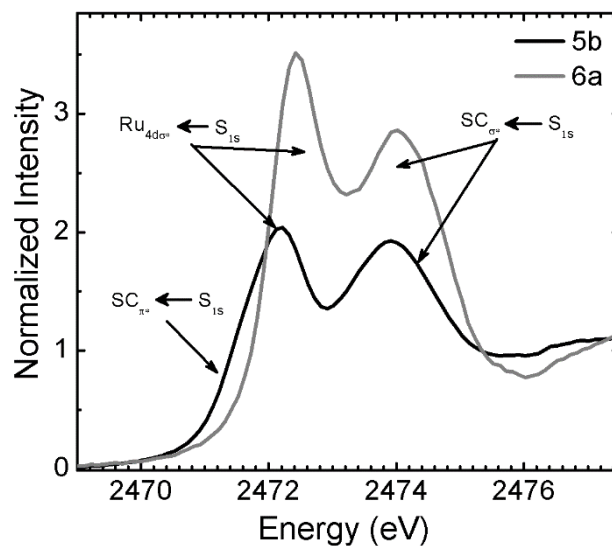


Figure 5.6: S K-edge XAS of **5b** and **6a**

Interestingly, it is noticed that **5b** converts into **6a** in methanol or water in 14 hours, as shown in Scheme 5.1. During conversion, deprotonation occurs on ^2N (hydrazinic nitrogen) of the TSC ligand. The reaction has been followed by NMR and UV-vis spectroscopy and the results from the analysis suggest that the electronic environment of the TSC ligand in dimer **6a** is different from that of monomer **5b**. S K-edge XAS results further suggest a rather significant change in the electronic environment of the sulfur atoms, as shown in Figure 5.6.

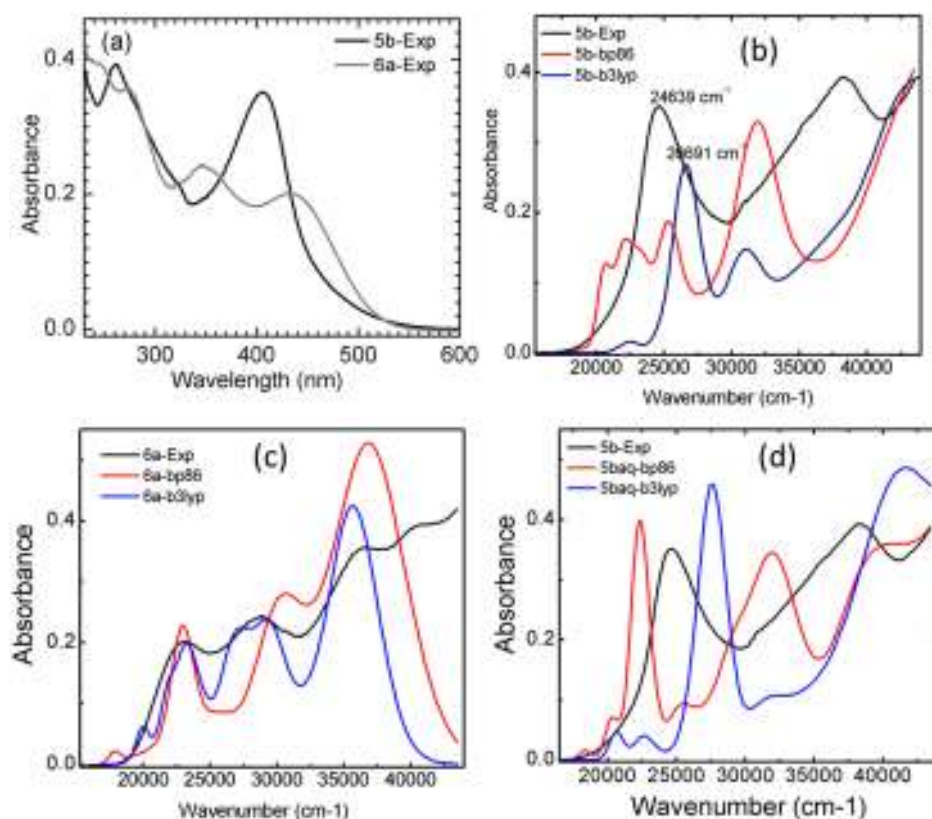


Figure 5.7: (a) UV-vis spectra of complexes **5b** and **6a**. (b) simulated spectra of **5b** with functionals BP86 and B3LYP. (c) simulated spectra of **6a** with functionals BP86 and B3LYP. (d) simulated UV-vis spectra of **5baq** compared with **5a** spectrum

NMR studies suggest that dimerization may proceed through initial solvolysis of the monoemeric species to form a dicationic aqua monomer. However, such species have not been isolated or identified by any analysis. DFT calculations have been performed on *in silico*

models of **5b**, **6a** and the putative aqua species (**5baq**) to generate simulated electronic absorption spectra of these complexes using valence TDDFT calculations. The calculations were performed using both the BP86 and B3LYP functionals and the resulting spectra are compared with experimental spectra in Figure 5.7.

The simulated UV-vis spectra of **6a** are in reasonable agreement with experiment, reproducing the main features of the experimental spectrum as seen in Figure 5.7c. The two functionals yield differences in the specific energies of the main features, with a somewhat better agreement using the B3LYP functional. By contrast, simulated spectra for **5b** are in much poorer agreement with the experimental spectrum (Figure 5.7b). The simulated spectra are far more sensitive to the nature of the functional, but in both cases, additional features are observed that are not observed in the experimental data. The simulated spectra of **5baq** (Figure 5.7d) are somewhat simpler (due to the loss of intense Ru ← Cl LMCT transitions) and yield a somewhat better overall agreement with the experimental spectra. However, these results are sufficiently ambiguous to require further study.

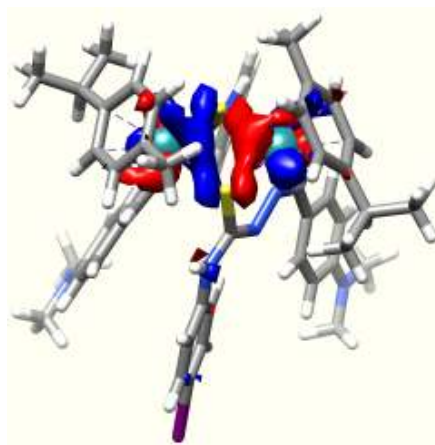


Figure 5.8: MO orbital 324 showing the S-S interaction in **6a**.

Interestingly, a systematic change is observed in the UV-vis spectroscopic features in the region between 300 – 500 nm (Figure 5.7a) during the dimer formation, *i.e.* when **5b** converts into **6a**. The feature at 406 nm in **5b** is divided into two new features (at 345 and 435 nm) in **6a**. TDDFT calculations predict that these features arise from Ru ← L charge transfer (LMCT). The nature of the splitting of the feature indicates that the electronic environment around the Ru-S bond is divided in the dimer molecule. As anticipated, the MO picture of Ru-S bond in **6a** shows that the electronic environment of the Ru-S bonds in dimer **6a** is divided by S_{3p} - S_{3p} interaction through Ru 4d as shown in figure 5.8.

5.4 Discussion

A series of half sandwich $[(p\text{-cym})\text{Ru}^{\text{II}}(\text{TSC})\text{X}]^+$ complexes and sandwich Ru^{II} and $\text{Os}^{\text{II}}\text{-}p\text{-cym-TSC}$ complexes are investigated using S K-edge XAS with the help of DFT calculations. The effects of the ancillary ligand modification and metal are investigated in those complexes. Most importantly, the experimental and computational data are in strong agreement when comparing the different complexes in the series. DFT optimized geometries reasonably reproduce the available crystallographic data of **5b** and **6a**. The valence molecular orbital descriptions are in good agreement with the trend observed in the XAS spectra, Figure 5.4. Overall, the experimental and computational results are in reasonable agreement.

NMe_2 substitution of TSC directly influences its π -system as seen when comparing the spectra of proligands **4a** and **4b**. These differences are also observed in complexes **5a/5b**, where the electron donating NMe_2 appears to strengthen the Ru-S bond and concomitantly weaken the Ru-Cl bond in complex **5b**. It is tempting to speculate that such a modification could strongly influence the chemical and biochemical behaviour of these complexes; the

potency of these complexes as anticancer agents is currently under investigation. However, there is a universal agreement in the literature that dialkylation of the ^4N of the TSC ligand increases *in vitro* cytotoxicity of both the free ligands and metal complexes.^{302,322}

At this point, it is not clear that exchanging the monodentate ligand from Cl to I should have a major influence on the biological activity of these complexes; however, the chloro complex **5a** rapidly dissociates in solution and leads to decomposition. Decreasing the lability of the M-X bond would thus likely be very beneficial. This is achieved in the iodo complex (**5c**) whose solution chemistry is still as yet unexplored. Interestingly, it has recently been noticed that the substitutionally inert iodo osmium azopyridine complex, $[\text{Os}(\eta^6\text{-bip})(\text{azpy-NMe}_2)\text{I}]^+$ and the related iodo iminopyridine complex, $[\text{Ru}(\eta^6\text{-p-cym})(\text{p-Impy-NMe}_2)\text{I}]^+$ are more potent than their chloride analogues.^{90,106,107}

A drastic increase in biological activity is also observed in the Os complex **6b** compared to its Ru analogue, **6a**. Generally, osmium complexes are more potent than their ruthenium equivalents,⁷⁰ which indicates that the metal center plays a major role in the biological activity of these types of complexes.

5.5 Conclusions

Structural modification of metal-arene-thiosemicarbazone complexes is investigated through their electronic structure using XAS and DFT calculation. An electron donating group (NMe_2), substituted on the TSC ligand, directly interacts with the π -system of the TSC ligand and increase the Ru-S covalency. This effect also appears to stabilize the complexes in solution and possibly moderates their mechanism of action. It was long believed that the metal coordination can increase the cellular uptake of these complexes, however the studies

herein show that metal coordination to TSC ligand can play a huge role in their mode of activity. Above all, the studies indicate that deeper investigation of the electronic structure of these complexes is a crucial factor in the rational design and development of improved metal arene complexes for medicinal applications.

CHAPTER 6. CONCLUSIONS AND FUTURE DIRECTIONS

A combination of X-ray absorption spectroscopic methods have been exploited to investigate the electronic structure of ruthenium(II) and osmium(II) arene complexes that have shown promise as metalloanticancer drugs; many of these complexes are currently under preclinical evaluation. The studies described herein have contributed to testing and evaluating postulated biological modes of action. In addition, these studies have provided a systematic approach to evaluating the effect of ancillary ligand modifications and their impact on both their chemical and biochemical properties. In these studies, computational methods have also been utilized to support the experimental results and provide further insights – especially in cases where appropriate experimental data are unavailable. Results from this thesis clearly demonstrate the importance of both the metal centre and ancillary ligands in determining the biological activity of metalloanticancer drugs. Furthermore, the work provides an example where defining the mode of activation necessitates an understanding of the fundamental chemical properties of the prodrug and biological intermediates. Such fundamental aspects must be considered when designing and optimizing new metallopharmaceutical agents in the future.

The electronic structure of Ru^{II}-arene thiolato complexes has been successfully investigated through the thiolato, **1**, sulfenato, **2**, and sulfinato, **3**, complexes using Ru K-edge and S K-edge XAS in concert with computational methods. Analysis indicates that the sulfur ligand oxygenation have little impact on the lability of the oxidized ligand directly. However, this process creates a sulfenato species in which the Ru-S bond is highly correlated with the

nature of the adjoining S-O bond. The nature of the Ru-S=O bonding in these species provides for a specific pathway for prodrug activation in Ru^{II} arene thiolato complexes.

These ideas are tested by exploring the effect of protonation and/or Lewis acid activation on the sulfenato species as well as the sulfinato species (where the S-O π -bonding is observed to be less important). Results suggest that perturbation at the terminal oxo of the sulfenato has a larger impact on the degree of charge donation from the sulfur ligand to metal centre; directly affecting the lability of the ligand. The impact is significantly smaller in the sulfinato species, which supports the importance of the SO π -bonding in the observed effects. Altogether, these results suggest that the activation mechanism of Ru^{II}-arene thiolato complexes proceeds through the ligand-centered oxygenation followed by solvation and protonation.

This thesis further explores the effect of relatively small modifications to ancillary ligands – noting that they can lead to rather large effects in the oxidized species, a finding which is particularly important to the design and structure optimization of this family of complexes. It is notable, however, that current studies have been limited to *in vitro* experiments. It would be of great interest to extend these studies to determine the fate of Ru^{II}-arene thiolato complexes *in vivo* using the actual cancer cells model. Data from this thesis provide a firm foundation for the application of XAS-based imaging methods (e.g. STXM-scanning transmission X-ray microscopy, and/or microprobe XAS imaging) to treated tumour cells. Such studies would allow for direct speciation in tumour cells, both from the perspective of the metal centre as well as the sulfur-containing ligand in the appropriate biological environment.

Recent studies from Sadler group show that the thiolato ligand formed during the reaction between $[(\eta^6\text{-ar})\text{Ru}(\text{en})\text{Cl}]^+$ complex and glutathione (GSH) yield an interesting $[\text{Ru}\text{-ar}\text{-en}\text{-SG}]$ adduct which can be subsequently oxidized by dioxygen to afford an unique sulfenate intermediate. The competitive reaction between GSH and cGMP with $[(\eta^6\text{-ar})\text{Ru}(\text{en})\text{Cl}]^+$ complex showed that the oxidation of coordinated GSH in the thiolato complex appears to provide a facile route for displacement of S-bound glutathione by G N7, leading to formation of the cGMP adduct $[(\eta^6\text{-ar})\text{Ru}(\text{en})(\text{cGMP}\text{-N7})]^+$ as the major product even in the presence of a 250-fold molar excess of GSH. Surprisingly, protonation is not observed during this reaction. Therefore, it appears to be an interesting aspect to investigate the electronic structure of Ru-arene-glutathione adduct, $[\text{Ru}\text{-ar}\text{-en}\text{-SG}]^+$ and its mono-oxygenated product ($[\text{Ru}\text{-ar}\text{-en}\text{-SOG}]^+$) to study the insight changes in Ru-S bond in those species. This investigation would further provide an understanding of the correlation between structure-activity relationships of ligand design around the metal centre.

Beyond the parent metal arene complexes that form the foundation of this thesis, several divergent ligand design motifs continue to be explored to improve efficacy. The initial work lends itself to broader studies of the electronic structure of $\text{Ru}^{\text{II}}/\text{Os}^{\text{II}}$ -arene complexes using a wide range of ancillary ligands. For example, thiosemicarbazone complexes **4-6** have been studied using a similar approach applied for Ru^{II} -arene thiolato complexes. In these cases, our studies on the free TSC proligand indicate that the conjugated π -system is quite sensitive to slight modifications, which translates into changes in the properties of the metal complexes themselves. Additional insights from detailed spectroscopic studies have lead to directed modifications of the ligand structure that are currently being explored. In such

complexes, it has further been observed that monomer/dimer equilibria may play an important role in defining the biologically-relevant species. Initial studies have been performed, but a better understanding of the factors that control this equilibrium is an area of current intense exploration.

In addition, preliminary studies on Ru^{II}/Os^{II}-arene-TSC complexes show prominent differences between the cytotoxicity of Ru^{II} and Os^{II} complexes. It appears to suggest that metal centre might also play a role in anticancer activity, therefore further investigation should have been focused with more Ru^{II} and Os^{II}-arene counterparts to investigate the actual role of the metal.

Overall, the work presented herein provides a particular approach to exploring the nature of metal complexes of interest as therapeutics. The application of element-specific spectroscopies provides a unique perspective that can lead to important insights into chemical and biochemical properties of such complexes. The initial methodology is being applied to a number of related species – providing useful information in developing our understanding of such biologically-active metal-based drugs. This general approach should be able to significantly contribute to our understanding of other metallopharmaceuticals - as a correlation between their electronic structure and their biological mode of action is explored.

REFERENCES

- (1) Orvig, C.; Abrams, M. J. *Chem. Rev.* **1999**, *99*, 2201–4.
- (2) Thompson, K. H.; Orvig, C. *Dalton Trans.* **2006**, 761–764.
- (3) Ronconi, L.; Sadler, P. J. *Coord. Chem. Rev.* **2007**, *251*, 1633–1648.
- (4) Gaynor, D.; Griffith, D. M. *Dalton Trans.* **2012**, *41*, 13239–13257.
- (5) Sarkar, P. K.; Das, S.; Prajapati, P. K. *Ancient Sci. Life* **2010**, *29*, 1–6.
- (6) Koch, I.; Moriarty, M.; House, K.; Sui, J.; Cullen, W. R.; Saper, R. B.; Reimer, K. J. *Sci. Total Environ.* **2011**, *409*, 4545–4552.
- (7) Dwyer, F. P.; Gyarfas, E. C.; Rogers, W. P.; Koch, J. H. *Nature* **1952**, *170*, 190–191.
- (8) Rosenberg, B.; VanCamp, L.; KRIGAS, T.; Van Loretta, C. *Nature* **1965**, *205*, 698–699.
- (9) Rosenberg, B.; VanCamp, L.; Trosko, J. E.; Mansour, V. H. *Nature* **1969**, *222*, 385–386.
- (10) Rosenberg, B.; VanCamp, L. *Cancer Res.* **1970**, *30*, 1799–1802.
- (11) Lippert, B.; Editor. *Cisplatin: Chemistry and Biochemistry of a Leading Anticancer Drug.*; Verlag Helvetica Chimica Acta, 1999; p. 563 pp.
- (12) Bruijninx, P. C. A.; Sadler, P. J. *Curr. Opin. Chem. Biol.* **2008**, *12*, 197–206.
- (13) Di Pasqua, A. J.; Goodisman, J.; Dabrowiak, J. C. *Inorg. Chim. Acta* **2012**, *389*, 29–35.
- (14) Kidani, Y.; Inagaki, K.; Iigo, M.; Hoshi, A.; Kuretani, K. *J. Med. Chem.* **1978**, *21*, 1315–1318.
- (15) Kelland, L. *Nat. Rev. Cancer* **2007**, *7*, 573–584.
- (16) Wheate, N. J.; Walker, S.; Craig, G. E.; Oun, R. *Dalton Trans.* **2010**, *39*, 8113–8127.
- (17) Alberto, M. E.; Lucas, M. F. A.; Pavelka, M.; Russo, N. *J. Phys. Chem. B* **2009**, *113*, 14473–14479.
- (18) *Drugs in R&D* **2003**, *4*, 369–372.
- (19) Gietema, J. A.; Guchelaar, H. J.; de, V. E. G.; Aulenbacher, P.; Sleijfer, D. T.; Mulder, N. H. *Anti-cancer drugs* **1993**, *4*, 51–55.
- (20) Kim, D.-K.; Kim, G.; Gam, J.; Cho, Y.-B.; Kim, H.-T.; Tai, J.-H.; Kim, K. H.; Hong, W.-S.; Park, J.-G. *J. Med. Chem.* **1994**, *37*, 1471–1485.
- (21) Kim, N. K.; Im, S.-A.; Kim, D.-W.; Lee, M. H.; Jung, C. W.; Cho, E. K.; Lee, J. T.; Ahn, J. S.; Heo, D. S.; Bang, Y.-J. *Cancer* **1999**, *86*, 1109–1115.
- (22) Simpson, D.; Dunn, C.; Curran, M.; Goa, K. L. *Drugs* **2003**, *63*, 2127–2156.
- (23) Farrer, N. J.; Sadler, P. J. *Medicinal Inorganic Chemistry : State of the Art, New Trends, and a Vision of the Future*; Alessio, E., Ed.; WILEY-VCH Verlag GmbH & Co. KGaA, Weinheim, 2011; pp. 1–47.
- (24) Wang, D.; Lippard, S. J. *Nat. Rev. Drug Discov.* **2005**, *4*, 307–320.
- (25) Ott, I.; Gust, R. *Arch. Pharm.* **2007**, *340*, 117–126.
- (26) Bergamo, A.; Gaiddon, C.; Schellens, J. H. M.; Beijnen, J. H.; Sava, G. *J. Inorg. Biochem.* **2012**, *106*, 90–99.
- (27) Ang, W. H.; Dyson, P. J. *Eur. J. Inorg. Chem.* **2006**, *2006*, 4003–4018.
- (28) Bruijninx, P. C. a; Sadler, P. J. *Adv. Inorg. Chem.* **2009**, *61*, 1–62.
- (29) Yan, Y. K.; Melchart, M.; Habtemariam, A.; Sadler, P. J. *Chem. Commun.* **2005**, 4764–4776.
- (30) Clarke, M. J. *Coord. Chem. Rev.* **2002**, *232*, 69–93.

- (31) Jakupec, M. A.; Galanski, M.; Arion, V. B.; Hartinger, C. G.; Keppler, B. K. *Dalton Trans.* **2008**, 183–194.
- (32) Durig, J. R.; Danneman, J.; Behnke, W. D.; Mercer, E. E. *Chem. Biol. Interact.* **1976**, *13*, 287–94.
- (33) Clarke, M. J. *Met. Ions Biol. Syst.* **1980**, *11*, 231–283.
- (34) Clarke, M. J.; Zhu, F.; Frasca, D. R. *Chem. Rev.* **1999**, *99*, 2511–2533.
- (35) Lentz, F.; Drescher, A.; Lindauer, A.; Henke, M.; Hilger, R. a; Hartinger, C. G.; Scheulen, M. E.; Dittrich, C.; Keppler, B. K.; Jaehde, U. *Anti-cancer drug* **2009**, *20*, 97–103.
- (36) Antonarakis, E. S.; Emadi, A. *Cancer chemother. Pharmacol.* **2010**, *66*, 1–9.
- (37) Alessio, E.; Mestroni, G.; Bergamo, A.; Sava, G. *Curr. Top. Med. Chem.* **2004**, *4*, 1525–1535.
- (38) Dyson, P. J.; Sava, G. *Dalton Trans.* **2006**, 1929–33.
- (39) Bergamo, A.; Gagliardi, R.; Scarcia, V.; Furlani, A.; Alessio, E.; Mestroni, G.; Sava, G. *J. Pharmacol. Exp. Ther.* **1999**, *289*, 559–564.
- (40) Sava, G.; Bergamo, A.; Zorzet, S.; Gava, B.; Casarsa, C.; Cocchietto, M.; Furlani, A.; Scarcia, V.; Serli, B.; Iengo, E.; Alessio, E.; Mestroni, G. *Eur. J. Cancer* **2002**, *38*, 427–435.
- (41) Hartinger, C. G.; Jakupec, M. A.; Zorbas-Seifried, S.; Groessler, M.; Egger, A.; Berger, W.; Zorbas, H.; Dyson, P. J.; Keppler, B. K. *Chem. Biodivers.* **2008**, *5*, 2140–2155.
- (42) Jakupec, M. A.; Arion, V. B.; Kapitza, S.; Reisner, E.; Eichinger, A.; Pongratz, M.; Marian, B.; Graf N., von K.; Keppler, B. K. *Int. J. Clin. Pharmacol. Ther.* **2005**, *43*, 595–596.
- (43) Clarke, M. J. M. J.; Bitler, S.; Rennert, D.; Buchbinder, M.; Kelman, A. D. *J. Inorg. Biochem.* **1980**, *12*, 79–87.
- (44) Gaiddon, C.; Jeannequin, P.; Bischoff, P.; Pfeffer, M.; Sirlin, C.; Loeffler, J. P. *J. Pharmacol. Exp. Ther.* **2005**, *315*, 1403–1411.
- (45) Morris, R. E.; Aird, R. E.; Murdoch, P. D. S.; Chen, H. M.; Cummings, J.; Hughes, N. D.; Parsons, S.; Parkin, a; Boyd, G.; Jodrell, D. I.; Sadler, P. J. *J. Med. Chem.* **2001**, *44*, 3616–21.
- (46) Scolaro, C.; Bergamo, A.; Brescacin, L.; Delfino, R.; Cocchietto, M.; Laurenczy, G.; Geldbach, T. J.; Sava, G.; Dyson, P. J. *J. Med. Chem.* **2005**, *48*, 4161–4171.
- (47) Kilah, N. L.; Meggers, E. *Aust. J. Chem.* **2012**, *65*, 1325–1332.
- (48) Süß-Fink, G. *Dalton Trans.* **2010**, *39*, 1673–1688.
- (49) Dale, L. D.; Tocher, J. H.; Dyson, T. M.; Edwards, D. I.; Tocher, D. A. *Anti-Cancer Drug Des.* **1992**, *7*, 3–14.
- (50) Hartinger, C. G.; Metzler-Nolte, N.; Dyson, P. J. *Organometallics* **2012**, *31*, 5677–5685.
- (51) Dyson, P. J. *Chimia* **2007**, *61*, 698–703.
- (52) Dougan, S. J.; Sadler, P. J. *Chimia* **2007**, *61*, 704–715.
- (53) Allardyce, C. S.; Dyson, P. J.; Ellis, D. J.; Heath, S. L. *Chem. Commun.* **2001**, 1396–1397.
- (54) Scolaro, C.; Geldbach, T. J.; Rochat, S.; Dorcier, A.; Gossens, C.; Bergamo, A.; Cocchietto, M.; Tavernelli, I.; Sava, G.; Rothlisberger, U.; Dyson, P. J. *Organometallics* **2006**, *25*, 756–765.

- (55) Scolaro, C.; Chaplin, A. B.; Hartinger, C. G.; Bergamo, A.; Cocchietto, M.; Keppler, B. K.; Sava, G.; Dyson, P. J. *Dalton Trans.* **2007**, 5065–5072.
- (56) Chatterjee, S.; Kundu, S.; Bhattacharyya, A.; Hartinger, C. G.; Dyson, P. J. *J. Biol. Inorg. Chem.* **2008**, *13*, 1149–1155.
- (57) Nowak-Sliwinska, P.; Van Judy R., B.; Casini, A.; Nazarov, A. A.; Wagnieres, G.; Van Hubert, den B.; Dyson, P. J.; Griffioen, A. W. *J. Med. Chem.* **2011**, *54*, 3895–3902.
- (58) Bregman, H.; Williams, D. S.; Atilla, G. E.; Carroll, P. J.; Meggers, E. *J. Am. Chem. Soc.* **2004**, *126*, 13594–13595.
- (59) Zhang, L.; Carroll, P.; Meggers, E. *Org. Lett.* **2004**, *6*, 521–523.
- (60) Meggers, E.; Atilla-Gokcumen, G. E.; Bregman, H.; Maksimoska, J.; Mulcahy, S. P.; Pagano, N.; Williams, D. S. *Synlett* **2007**, 1177–1189.
- (61) Smalley, K. S. M.; Contractor, R.; Haass, N. K.; Kulp, A. N.; Atilla-Gokcumen, G. E.; Williams, D. S.; Bregman, H.; Flaherty, K. T.; Soengas, M. S.; Meggers, E.; Herlyn, M. *Cancer Res.* **2007**, *67*, 209–217.
- (62) Bullock, A. N.; Russo, S.; Amos, A.; Pagano, N.; Bregman, H.; Debreczeni, J. E.; Lee, W. H.; Von Frank, D.; Meggers, E.; Knapp, S. *PLoS One* **2009**, *4*, No pp. given.
- (63) Xie, P.; Streu, C.; Qin, J.; Bregman, H.; Pagano, N.; Meggers, E.; Marmorstein, R. *Biochemistry* **2009**, *48*, 5187–5198.
- (64) Merkel, A. L.; Meggers, E.; Ocker, M. *Expert Opin. Investig. Drugs* **2012**, *21*, 425–436.
- (65) Chen, H. M.; Parkinson, J. A.; Parsons, S.; Coxall, R. a; Gould, R. O.; Sadler, P. J. *J. Am. Chem. Soc.* **2002**, *124*, 3064–3082.
- (66) Chen, H. M.; Parkinson, J. A.; Morris, R. E.; Sadler, P. J. *J. Am. Chem. Soc.* **2003**, *125*, 173–186.
- (67) Aird, R. E.; Cummings, J.; Ritchie, A. A.; Muir, M.; Morris, R. E.; Chen, H. M.; Sadler, P. J.; Jodrell, D. I. *Br. J. Cancer* **2002**, *86*, 1652–1657.
- (68) Guichard, S. M.; Else, R.; Reid, E.; Zeitlin, B.; Aird, R. E.; Muir, M.; Dodds, M.; Fiebig, H.; Sadler, P. J.; Jodrell, D. I. *Biochem. Pharmacol.* **2006**, *71*, 408–415.
- (69) Melchart, M.; Sadler, P. J. In *Bioorganometallics*; Wiley-VCH Verlag GmbH & Co. KGaA, 2006; pp. 39–64.
- (70) Noffke, A. L.; Habtemariam, A.; Pizarro, A. M.; Sadler, P. J. *Chem. Commun.* **2012**, *48*, 5219–46.
- (71) Pizarro, A. M.; Melchart, M.; Habtemariam, A.; Salassa, L.; Fabbiani, F. P. A.; Parsons, S.; Sadler, P. J. *Inorg. Chem.* **2010**, *49*, 3310–3319.
- (72) Van Sabine H., R.; Mukherjee, A.; Pizarro, A. M.; Sadler, P. J.; Van Rijjt, S. H. *J. Med. Chem.* **2010**, *53*, 840–9.
- (73) Ang, W. H.; Parker, L. J.; De Anastasia, L.; Juillerat-Jeanneret, L.; Morton, C. J.; Lo Mario, B.; Parker, M. W.; Dyson, P. J. *Angew. Chem. Int. Ed.* **2009**, *48*, 3854–3857.
- (74) Ang, W. H.; Daldini, E.; Juillerat-Jeanneret, L.; Dyson, P. J. *Inorg. Chem.* **2007**, *46*, 9048–9050.
- (75) Kilpin, K. J.; Clavel, C. M.; Edefe, F.; Dyson, P. J. *Organometallics* **2012**, *31*, 7031–7039.
- (76) Petzold, H.; Xu, J. J.; Sadler, P. J. *Angew. Chem. Int. Ed.* **2008**, *47*, 3008–3011.
- (77) Ang, W. H.; Casini, A.; Sava, G.; Dyson, P. J. *J. Organomet. Chem.* **2011**, *696*, 989–998.
- (78) Betanzos-Lara, S.; Habtemariam, A.; Clarkson, G. J.; Sadler, P. J. *Eur. J. Inorg. Chem.* **2011**, *2011*, 3257–3264.

- (79) Melchart, M.; Habtemariam, A.; Novakova, O.; Moggach, S. A.; Fabbiani, F. P. A.; Parsons, S.; Brabec, V.; Sadler, P. J. *Inorg. Chem.* **2007**, *46*, 8950–8962.
- (80) Wang, F. Y.; Habtemariam, A.; Van der Geer, E. P. L.; Fernandez, R.; Melchart, M.; Deeth, R. J.; Aird, R. E.; Guichard, S.; Fabbiani, F. P. A.; Lozano-Casal, P.; Oswald, I. D. H.; Jodrell, D. I.; Parsons, S.; Sadler, P. J.; Fernández, R. *Proc. Natl. Acad. Sci. U.S.A.* **2005**, *102*, 18269–18274.
- (81) Guo, Z.; Habtemariam, A.; Sadler, P. J.; James, B. R. *Inorg. Chim. Acta* **1998**, *273*, 1–7.
- (82) Morris, R. E.; Habtemariam, A.; Guo, Z.; Parsons, S.; Sadler, P. J. *Inorg. Chim. Acta* **2002**, *339*, 551–559.
- (83) Melchart, M.; Habtemariam, A.; Parsons, S.; Moggach, S. a.; Sadler, P. J. *Inorg. Chim. Acta* **2006**, *359*, 3020–3028.
- (84) Habtemariam, A.; Melchart, M.; Fernandez, R.; Parsons, S.; Oswald, I. D. H.; Parkin, A.; Fabbiani, F. P. A.; Davidson, J. E.; Dawson, A.; Aird, R. E.; Jodrell, D. I.; Sadler, P. J. *J. Med. Chem.* **2006**, *49*, 6858–6868.
- (85) Bugarcic, T.; Habtemariam, A.; Stepankova, J.; Heringova, P.; Kasparkova, J.; Deeth, R. J.; Johnstone, R. D. L.; Prescimone, A.; Parkin, A.; Parsons, S.; Brabec, V.; Sadler, P. J. *Inorg. Chem.* **2008**, *47*, 11470–86.
- (86) Filak, L. K.; Muehlgassner, G.; Bacher, F.; Roller, A.; Galanski, M.; Jakupec, M. A.; Keppler, B. K.; Arion, V. B. *Organometallics* **2011**, *30*, 273–283.
- (87) Hanif, M.; Henke, H.; Meier, S. M.; Martic, S.; Labib, M.; Kandioller, W.; Jakupec, M. A.; Arion, V. B.; Kraatz, H.-B.; Keppler, B. K.; Hartinger, C. G. *Inorg. Chem.* **2010**, *49*, 7953–7963.
- (88) Kandioller, W.; Hartinger, C. G.; Nazarov, A. A.; Bartel, C.; Skocic, M.; Jakupec, M. A.; Arion, V. B.; Keppler, B. K. *Chem.-Eur. J.* **2009**, *15*, 12283–12291, S12283/1–S12283/32.
- (89) Fernandez, R.; Melchart, M.; Habtemariam, A.; Parsons, S.; Sadler, P. J. *Chem.-Eur. J.* **2004**, *10*, 5173–5179.
- (90) Romero-Canelon, I.; Pizarro, A. M.; Habtemariam, A.; Sadler, P. J. *Metallomics* **2012**, *4*, 1271–1279.
- (91) Fu, Y.; Romero, M. J. M. J.; Habtemariam, A.; Snowden, M. E.; Song, L.; Clarkson, G. J.; Qamar, B.; Pizarro, A. M.; Unwin, P. R.; Sadler, P. J. *Chem. Sci.* **2012**, *3*, 2485–2494.
- (92) Shnyder, S. D.; Fu, Y.; Habtemariam, A.; Van Rijt, S. H.; Cooper, P. a.; Loadman, P. M.; Sadler, P. J. *Med. Chem. Commun.* **2011**, *2*, 666.
- (93) Muehlgassner, G.; Bartel, C.; Schmid, W. F.; Jakupec, M. A.; Arion, V. B.; Keppler, B. K. *J. Inorg. Biochem.* **2012**, *116*, 180–187.
- (94) Wang, F. Y.; Chen, H. M.; Parsons, S.; Oswald, I. D. H.; Davidson, J. E.; Sadler, P. J. *Chem. Eur. J.* **2003**, *9*, 5810–20.
- (95) Wang, F. Y.; Xu, J. J.; Habtemariam, A.; Bella, J.; Sadler, P. J. *J. Am. Chem. Soc.* **2005**, *127*, 17734–17743.
- (96) Srisankandakumar, T.; Petzold, H.; Bruijnincx, P. C. A.; Habtemariam, A.; Sadler, P. J.; Kennepohl, P. *J. Am. Chem. Soc.* **2009**, *131*, 13355–61.
- (97) Lindsay, C.; Cesarotti, E.; Adams, H.; Bailey, N. A.; White, C. *Organometallics* **1990**, *9*, 2594–2602.
- (98) Grapperhaus, C. a; Poturovic, S.; Mashuta, M. S. *Inorg. Chem.* **2005**, *44*, 8185–8187.

- (99) Dey, A.; Green, K. N.; Jenkins, R. M.; Jeffrey, S. P.; Darensbourg, M.; Hodgson, K. O.; Hedman, B.; Solomon, E. I. *Inorg. Chem.* **2007**, *46*, 9655–60.
- (100) Buonomo, R. M.; Font, I.; Maguire, M. J.; Reibenspies, J. H.; Tuntulani, T.; Darensbourg, M. Y. *J. Am. Chem. Soc.* **1995**, *117*, 963–973.
- (101) Farmer, P. J.; Reibenspies, J. H.; Lindahl, P. A.; Darensbourg, M. Y. *J. Am. Chem. Soc.* **1993**, *115*, 4665–4674.
- (102) Tyler, L. A.; Noveron, J. C.; Olmstead, M. M.; Mascharak, P. K. *Inorg. Chem.* **2000**, *39*, 357–362.
- (103) Petzold, H.; Braeutigam, S.; Goerls, H.; Weigand, W.; Romanski, J.; Mloston, G. *Eur. J. Inorg. Chem.* **2007**, 5627–5632.
- (104) Petzold, H.; Sadler, P. J. *Chem. Commun.* **2008**, *37*, 4413–4415.
- (105) Peacock, A. F. A.; Habtemariam, A.; Fernández, R.; Walland, V.; Fabbiani, F. P. a; Parsons, S.; Aird, R. E.; Jodrell, D. I.; Sadler, P. J. *J. Am. Chem. Soc.* **2006**, *128*, 1739–48.
- (106) Fu, Y.; Habtemariam, A.; Pizarro, A. M.; Van Rijt, S. H.; Healey, D. J.; Cooper, P. a; Shnyder, S. D.; Clarkson, G. J.; Sadler, P. J. *J. Med. Chem.* **2010**, *53*, 8192–6.
- (107) Fu, Y.; Habtemariam, A.; Basri, A. M. B. H.; Braddick, D.; Clarkson, G. J.; Sadler, P. J.; Editor, G.; Orvig, C.; Board, E.; Edwards, P. G.; Hahn, F. E.; Champness, N. R.; Dempsey, J. L.; Winkler, J. R.; Gray, H. B.; Stephenson, A.; Ward, M. D. *Dalton Trans.* **2011**, *40*, 10553–62.
- (108) Cebrian-Losantos, B.; Krokhin, A. A.; Stepanenko, I. N.; Eichinger, R.; Jakupec, M. A.; Arion, V. B.; Keppler, B. K. *Inorg. Chem.* **2007**, *46*, 5023–5033.
- (109) Dorcier, A.; Ang, W. H.; Bolano, S.; Gonsalvi, L.; Juillerat-Jeannerat, L.; Laurency, G.; Peruzzini, M.; Phillips, A. D.; Zanobini, F.; Dyson, P. J. *Organometallics* **2006**, *25*, 4090–4096.
- (110) Buchel, G. E.; Stepanenko, I. N.; Hejl, M.; Jakupec, M. A.; Keppler, B. K.; Arion, V. B. *Inorg. Chem.* **2011**, *50*, 7690–7697.
- (111) Bergamo, A.; Masi, A.; Peacock, A. F. A.; Habtemariam, A.; Sadler, P. J.; Sava, G. J. *Inorg. Biochem.* **2010**, *104*, 79–86.
- (112) Van Rijt, S. H.; Peacock, A. F. A.; Johnstone, R. D. L.; Parsons, S.; Sadler, P. J. *Inorg. Chem.* **2009**, *48*, 1753–62.
- (113) Peacock, A. F. A.; Parsons, S.; Sadler, P. J. *J. Am. Chem. Soc.* **2007**, *129*, 3348–57.
- (114) Peacock, A. F. a; Habtemariam, A.; Moggach, S. a; Prescimone, A.; Parsons, S.; Sadler, P. J. *Inorg. Chem.* **2007**, *46*, 4049–59.
- (115) Dorcier, A.; Dyson, P. J.; Gossens, C.; Rothlisberger, U.; Scopelliti, R.; Tavernelli, I. *Organometallics* **2005**, *24*, 2114–2123.
- (116) Schmid, W. F.; John, R. O.; Arion, V. B.; Jakupec, M. A.; Keppler, B. K. *Organometallics* **2007**, *26*, 6643–6652.
- (117) Hanif, M.; Nazarov, A. A.; Hartinger, C. G.; Kandioller, W.; Jakupec, M. A.; Arion, V. B.; Dyson, P. J.; Keppler, B. K. *Dalton Trans.* **2010**, *39*, 7345–7352.
- (118) Rijt, S. H. van; Kostrhunova, H.; Brabec, V.; Sadler, P. J. *Bioconjugate Chem.* **2011**, *22*, 218–26.
- (119) Peacock, A. F. a; Melchart, M.; Deeth, R. J.; Habtemariam, A.; Parsons, S.; Sadler, P. J. *Chem. Eur. J.* **2007**, *13*, 2601–13.

- (120) Van Rijt, S. H.; Hebden, A. J.; Amaresekera, T.; Deeth, R. J.; Clarkson, G. J.; Parsons, S.; McGowan, P. C.; Sadler, P. J. *J. Med. Chem.* **2009**, *52*, 7753–64.
- (121) Pizarro, A. M.; Habtemariam, A.; Sadler, P. J. *Top. Organomet. Chem.* **2010**, *32*, 21–56.
- (122) Rijt, S. H. van; Peacock, A. F. A.; Sadler, P. J.; Bonetti, A.; Leone, R.; Muggia, F. M.; Howell, S. B. In *Platinum and Other Heavy Metal Compounds in Cancer Chemotherapy*; Bonetti, A.; Leone, R.; Muggia, F. M.; Howell, S. B., Eds.; Humana Press: Totowa, NJ, 2009; pp. 73–79.
- (123) Rautio, J.; Kumpulainen, H.; Heimbach, T.; Oliyai, R.; Oh, D.; Jaervinen, T.; Savolainen, J. *Nat. Rev. Drug Discov.* **2008**, *7*, 255–270.
- (124) Guo, Z.; Sadler, P. J. *Angew. Chem. Int. Ed.* **1999**, *38*, 1512–1531.
- (125) Neidle, S.; Ismail, I. M.; Sadler, P. J. *J. Inorg. Biochem.* **1980**, *13*, 205–212.
- (126) Frey, U.; Ranford, J. D.; Sadler, P. J. *Inorg. Chem.* **1993**, *32*, 1333–1340.
- (127) Laurie, S. A.; Siu, L. L.; Winqvist, E.; Maksymiuk, A.; Harnett, E. L.; Walsh, W.; Tu, D.; Parulekar, W. R. *Cancer* **2010**, *116*, 362–368.
- (128) Simpson, D.; Dunn, C.; Curran, M.; Goa, K. L.; Beale, P.; Oncology, M.; Centre, C.; Wales, N. S.; Chatelut, E.; Regaud, I. C. *Drugs* **2003**, *63*, 2127–2156.
- (129) Kasparkova, J.; Vojtiskova, M.; Natile, G.; Brabec, V. *Chem. -Eur. J.* **2008**, *14*, 1330–1341.
- (130) Spingler, B.; Whittington, D. A.; Lippard, S. J. *Inorg. Chem.* **2001**, *40*, 5596–5602.
- (131) Boulikas, T.; Vougiouka, M. *Oncol. Rep.* **2003**, *10*, 1663–1682.
- (132) Heffeter, P.; Jungwirth, U.; Jakupec, M.; Hartinger, C. G.; Galanski, M.; Elbling, L.; Micksche, M.; Keppler, B. K.; Berger, W. *Drug Resist. Updat.* **2008**, *11*, 1–16.
- (133) Sava, G.; Zorzet, S.; Giraldo, T.; Mestroni, G.; Zassinovich, G. *Eur. J. Cancer Clin. Oncol.* **1984**, *20*, 841–847.
- (134) Sava, G.; Bergamo, A. *Int. J. Oncol.* **2000**, *17*, 353–365.
- (135) Gagliardi, R.; Sava, G.; Pacor, S.; Mestroni, G.; Alessio, E. *Clin. Exp. Metastasis* **1994**, *12*, 93–100.
- (136) Bergamo, A.; Masi, A.; Dyson, P. J.; Sava, G. *Int. J. Oncol.* **2008**, *33*, 1281–1289.
- (137) Levina, A.; Mitra, A.; Lay, P. A. *Metallomics* **2009**, *1*, 458–470.
- (138) Schluga, P.; Hartinger, C. G.; Egger, A.; Reisner, E.; Galanski, M.; Jakupec, M. A.; Keppler, B. K. *Dalton Trans.* **2006**, 1796–1802.
- (139) Rockwell, S.; Dobrucki, I. T.; Kim, E. Y.; Marrison, S. T.; Vu, V. T. *Curr. Mol. Med.* **2009**, *9*, 442–458.
- (140) Ascone, I.; Messori, L.; Casini, A.; Gabbiani, C.; Balerna, A.; Dell’Unto, F.; Castellano, A. C. *Inorg. Chem.* **2008**, *47*, 8629–8634.
- (141) Liu, M.; Lim, Z. J.; Gwee, Y. Y.; Levina, A.; Lay, P. A. *Angew. Chem. Int. Ed.* **2010**, *49*, 1661–1664, S1661/1–S1661/9.
- (142) Bergamo, A.; Sava, G. *Dalton Trans.* **2007**, 1267–1272.
- (143) Plum, D.; Van Robert C. A. M., W.; Beijnen, J. H.; Schellens, J. H. M. *Cancer chemother. Pharmacol.* **2004**, *54*, 71–78.
- (144) Hummer, A. a; Heffeter, P.; Berger, W.; Filipits, M.; Batchelor, D.; Büchel, G. E.; Jakupec, M. A.; Keppler, B. K.; Rompel, A. *J. Med. Chem.* **2013**.

- (145) Reisner, E.; Arion, V. B.; Keppler, B. K.; Pombeiro, A. J. L. *Inorg. Chim. Acta* **2008**, *361*, 1569–1583.
- (146) Bergamo, A.; Masi, A.; Jakupec, M. A.; Keppler, B. K.; Sava, G. *Metal-based drugs* **2009**, *2009*, 681270.
- (147) Hartinger, C. G.; Zorbas-Seifried, S.; Jakupec, M. A.; Kynast, B.; Zorbas, H.; Keppler, B. K. *J. Inorg. Biochem.* **2006**, *100*, 891–904.
- (148) Kapitza, S.; Jakupec, M. A.; Uhl, M.; Keppler, B. K.; Marian, B. *Cancer Lett.* **2005**, *226*, 115–121.
- (149) Ang, W. H.; Daldini, E.; Scolaro, C.; Scopelliti, R.; Juillerat-Jeannerat, L.; Dyson, P. J. *Inorg. Chem.* **2006**, *45*, 9006–9013.
- (150) Vock, C. A.; Renfrew, A. K.; Scopelliti, R.; Juillerat-Jeanneret, L.; Dyson, P. J. *Eur. J. Inorg. Chem.* **2008**, 1661–1671.
- (151) Novakova, O.; Chen, H. M.; Vrana, O.; Rodger, A.; Sadler, P. J.; Brabec, V. *Biochemistry* **2003**, *42*, 11544–11554.
- (152) Novakova, O.; Kasparkova, J.; Bursova, V.; Hofr, C.; Vojtiskova, M.; Chen, H. M.; Sadler, P. J.; Brabec, V. *Chem. Biol.* **2005**, *12*, 121–129.
- (153) Liu, H.-K.; Sadler, P. J. *Acc. Chem. Res.* **2011**, *44*, 349–59.
- (154) Bugarcic, T.; Novakova, O.; Halamikova, A.; Zerkankova, L.; Vrana, O.; Kasparkova, J.; Habtemariam, A.; Parsons, S.; Sadler, P. J.; Brabec, V.; Halámiková, A.; Zerkánková, L.; Vrána, O.; Kaspárková, J. *J. Med. Chem.* **2008**, *51*, 5310–5319.
- (155) Dougan, S. J.; Habtemariam, A.; McHale, S. E.; Parsons, S.; Sadler, P. J. *Proc. Natl. Acad. Sci. U.S.A.* **2008**, *105*, 11628–11633.
- (156) Kostrhunova, H.; Florian, J.; Novakova, O.; Peacock, A. F. A.; Sadler, P. J.; Brabec, V. *J. Med. Chem.* **2008**, *51*, 3635–3643.
- (157) Keck, M. V.; Lippard, S. J. *J. Am. Chem. Soc.* **1992**, *114*, 3386–3390.
- (158) Aitken, J. B.; Levina, A.; Lay, P. A. *Curr. Top. Med. Chem.* **2011**, *11*, 553–71.
- (159) P, G. M. J. D.; Groessl, M.; Dyson, P. J. *Curr. Top. Med. Chem.* **2011**, *11*, 2632–2646.
- (160) Hall, M. D.; Foran, G. J.; Zhang, M.; Beale, P. J.; Hambley, T. W. *J. Am. Chem. Soc.* **2003**, *125*, 7524–7525.
- (161) Hall, M. D.; Dillon, C. T.; Zhang, M.; Beale, P.; Cai, Z.; Lai, B.; Stampfl, A. P. J.; Hambley, T. W. *J. Biol. Inorg. Chem.* **2003**, *8*, 726–732.
- (162) Harris, T. V.; Szilagy, R. K.; McFarlane Holman, K. L. *J. Biol. Inorg. Chem.* **2009**, ASAP.
- (163) Penner-Hahn, J. E. *Coord. Chem. Rev.* **2005**, *249*, 161–177.
- (164) Sarangi, R. *Coord. Chem. Rev.* **2013**, *257*, 459–472.
- (165) Solomon, E. I.; Brunold, T. C.; Davis, M. I.; Kemsley, J. N.; Lee, S.-K.; Lehnert, N.; Neese, F.; Skulan, A. J.; Yang, Y.-S.; Zhou, J. *Chem. Rev.* **2000**, *100*, 235–349.
- (166) Solomon, E. I.; Lowery, M. D. *Science* **1993**, *259*, 1575–1581.
- (167) Solomon, E. I.; Hedman, B.; Hodgson, K. O.; Dey, A.; Szilagy, R. K. *Coord. Chem. Rev.* **2005**, *249*, 97–129.
- (168) Ortega, R.; Carmona, A.; Llorens, I.; Solari, P. L. *J. Anal. At. Spectrom.* **2012**, *27*, 2054.
- (169) Thompson, A.; Attwood, D.; Gullikson, E.; Howells, M.; Kim, K.-J.; Kirz, J.; Kortright, J.; Lindau, I.; Liu, Y.; Pianetta, P.; Robinson, A.; Scofield, J.; Underwood, J.; Williams, G.; Winick, H. *X-ray Data Booklet*; Thompson, A. C., Ed.; 3rd editio.; Lawrence Berkeley National Laboratory, University of California, Berkeley: California, 2009.

- (170) Ressler, T.; Brock, S. L.; Wong, J.; Suib, S. L. *J. Synch. Rad.* **1999**, *6*, 728–30.
- (171) Colpas, G. J.; Maroney, M. J.; Bagyinka, C.; Kumar, M.; Willis, W. S.; Suib, S. L.; Mascharak, P. K.; Baidya, N. *Inorg. Chem.* **1991**, *30*, 920–928.
- (172) Delgado-Jaime, M. U.; Conrad, J. C.; Fogg, D. E.; Kennepohl, P. *Inorg. Chim. Acta* **2006**, *359*, 3042–3047.
- (173) Dillon, C. T. *Aust. J. Chem.* **2012**, *65*, 204–217.
- (174) Glatzel, P.; Jacquamet, L.; Bergmann, U.; De Frank M. F., G.; Cramer, S. P. *Inorg. Chem.* **2002**, *41*, 3121–3127.
- (175) Levina, A.; Armstrong, R. S.; Lay, P. A. *Coord. Chem. Rev.* **2005**, *249*, 141–160.
- (176) Rehr, J. J.; Albers, R. C. *Rev. Mod. Phys.* **2000**, *72*, 621–654.
- (177) Getty, K. J.; Delgado-Jaime, M. U.; Kennepohl, P. *J. Am. Chem. Soc.* **2007**, *129*, 15774–15776.
- (178) Getty, K. J.; Delgado-Jaime, M. U.; Kennepohl, P. *Inorg. Chim. Acta* **2008**, *361*, 1059–1065.
- (179) Yano, J.; Kern, J.; Irrgang, K.-D.; Latimer, M. J.; Bergmann, U.; Glatzel, P.; Pushkar, Y.; Biesiadka, J.; Loll, B.; Sauer, K.; Messinger, J.; Zouni, A.; Yachandra, V. K. *Proc. Natl. Acad. Sci. U.S.A.* **2005**, *102*, 12047–12052.
- (180) De Frank, G.; De Groot, F. *Chem. Rev.* **2001**, *101*, 1779–1808.
- (181) Holm, R. H.; Kennepohl, P.; Solomon, E. I. *Chem. Rev.* **1996**, *96*, 2239–2314.
- (182) Hedman, B.; Hodgson, K. O.; Solomon, E. I. *J. Am. Chem. Soc.* **1990**, *112*, 1643–1645.
- (183) Glaser, T.; Hedman, B.; Hodgson, K. O.; Solomon, E. I. *Acc. Chem. Res.* **2000**, *33*, 859–868.
- (184) Shadle, S. E.; Penner-Hahn, J. E.; Schugar, H. J.; Hedman, B.; Hodgson, K. O.; Solomon, E. I. *J. Am. Chem. Soc.* **1993**, *115*, 767–776.
- (185) Neese, F.; Hedman, B.; Hodgson, K. O.; Solomon, E. I. *Inorg. Chem.* **1999**, *38*, 4854–4860.
- (186) Shadle, S. E.; Hedman, B.; Hodgson, K. O.; Solomon, E. I. *Inorg. Chem.* **1994**, *33*, 4235–4244.
- (187) Sarangi, R.; George, S. D.; Rudd, D. J.; Szilagyi, R. K.; Ribas, X.; Almeida, M.; Hodgson, K. O.; Hedman, B.; Solomon, E. I.; Synchrotron, S.; Linear, S.; Rovira, C. *J. Am. Chem. Soc.* **2007**, *129*, 2316–2326.
- (188) George, S. D.; Brant, P.; Solomon, E. I. *J. Am. Chem. Soc.* **2005**, *127*, 667–74.
- (189) Lugo-Mas, P.; Dey, A.; Xu, L.; Davin, S. D.; Benedict, J.; Kaminsky, W.; Hodgson, K. O.; Hedman, B.; Solomon, E. I.; Kovacs, J. A. *J. Am. Chem. Soc.* **2006**, *128*, 11211–11221.
- (190) Dey, A.; Jenney, F. E.; Adams, M. W. W.; Johnson, M. K.; Hodgson, K. O.; Hedman, B.; Solomon, E. I. *J. Am. Chem. Soc.* **2007**, *129*, 12418–31.
- (191) Yoon, W.-S.; Chung, K. Y.; Nam, K.-W.; McBreen, J.; Wang, D.; Huang, X.; Li, H.; Chen, L.; Yang, X.-Q. *J. Power Sources* **2008**, *183*, 427–430.
- (192) Yoon, W.-S.; Chung, K. Y.; McBreen, J.; Zaghbi, K.; Yang, X.-Q. *Electrochem. Solid St.* **2006**, *9*, A415–A417.
- (193) Shirakawa, J.; Nakayama, M.; Wakihara, M.; Uchimoto, Y. *J. Phys. Chem. B* **2006**, *110*, 17743–17750.
- (194) Rehder, D.; Schulzke, C.; Dau, H.; Meinke, C.; Hanss, J.; Epple, M. *J. Inorg. Biochem.* **2000**, *80*, 115–121.

- (195) Jeong, H. K.; Park, B.-G.; Kim, J.-Y.; Noh, H.-J. *EPL* **2011**, *95*, 47005/1–47005/4.
- (196) Shimada, H.; Imamura, M.; Matsubayashi, N.; Sato, T.; Hayakawa, T.; Takehira, K.; Kure, S.; Kinoshita, A.; Nishijima, A. *J. Phys. IV* **1997**, *7*, 919–920.
- (197) Bradley, J. A.; Yang, P.; Batista, E. R.; Boland, K. S.; Burns, C. J.; Clark, D. L.; Conradson, S. D.; Kozimor, S. A.; Martin, R. L.; Seidler, G. T.; Scott, B. L.; Shuh, D. K.; Tylliszczak, T.; Wilkerson, M. P.; Wolfsberg, L. E. *J. Am. Chem. Soc.* **2010**, *132*, 13914–13921.
- (198) Pickering, I. J.; Prince, R. C.; Divers, T.; George, G. N. *FEBS Lett.* **1998**, *441*, 11–14.
- (199) Pickering, I. J.; George, G. N.; Yu, E. Y.; Brune, D. C.; Tuschak, C.; Overmann, J.; Beatty, J. T.; Prince, R. C. *Biochemistry* **2001**, *40*, 8138–45.
- (200) Williams, K. R.; Hedman, B.; Hodgson, K. O.; Solomon, E. I.; Rose Williams, K. *Inorg. Chim. Acta* **1997**, *263*, 315–321.
- (201) Dey, A.; Chow, M.; Taniguchi, K.; Lugo-Mas, P.; Davin, S.; Maeda, M.; Kovacs, J. A.; Odaka, M.; Hodgson, K. O.; Hedman, B.; Solomon, E. I. *J. Am. Chem. Soc.* **2006**, *128*, 533–541.
- (202) Solomon, E. I.; Gorelsky, S. I.; Dey, A. *J. Comput. Chem.* **2006**, *27*, 1415–1428.
- (203) Rose, K.; Shadle, S. E.; Glaser, T.; De Simon, V.; Cherepanov, A.; Canters, G. W.; Hedman, B.; Hodgson, K. O.; Solomon, E. I. *J. Am. Chem. Soc.* **1999**, *121*, 2353–2363.
- (204) Shearer, J.; Callan, P. E.; Masitas, C. a; Grapperhaus, C. a *Inorg. Chem.* **2012**, *51*, 6032–45.
- (205) Clarke, R. *Incoherent sources: Synchrotron*, in *Encyclopedia of Modern Optics*; Elsevier, 2005; pp. 217–224.
- (206) Willmott, P. *Introduction to Synchrotron Radiation : Techniques and Applications*; Wiley: Hoboken, NJ, USA, 2011.
- (207) Duke, P. J. *Synchrotron Radiation: Production and Properties*; Oxford University Press: Oxford, 2000.
- (208) Cramer, S. P.; Peng, G.; Christiansen, J.; Chen, J.; Van J., E.; George, S. J.; Young, A. T. *J. Electron. Spectrosc. Relat. Phenom.* **1996**, *78*, 225–229.
- (209) Lytle, F. W.; Greegor, R. B.; Sandstrom, D. R.; Marques, E. C.; Wong, J.; Spiro, C. L.; Huffman, G. P.; Huggins, F. E. *Nucl. Instr. & Meth. in Phys. Res. A* **1984**, *226*, 542–548.
- (210) Kennepohl, P.; Wasinger, E. C.; George, S. D. *J. Synch. Rad.* **2009**, *16*, 484–488.
- (211) Hu, Y. F.; Coulthard, I.; Chevrier, D.; Wright, G.; Igarashi, R.; Sitnikov, A.; Yates, B. W.; Hallin, E. L.; Sham, T. K.; Reininger, R. In *THE 10TH INTERNATIONAL CONFERENCE ON SYNCHROTRON RADIATION INSTRUMENTATION*; Garrett, R; Gentle, I; Nugent, K; Wilkins, S., Ed.; 2010; Vol. 1234, pp. 343–346.
- (212) George, G. N.; Gnida, M.; Bazylnski, D. A.; Prince, R. C.; Pickering, I. J. *J. Bacteriol.* **2008**, *190*, 6376–6383.
- (213) Jaklevic, J.; Kirby, J. A.; Klein, M. P.; Robertson, A. S.; Brown, G. S.; Eisenberger, P. *Solid State Commun.* **1977**, *23*, 679–682.
- (214) Vlachos, D.; Craven, A. J.; McComb, D. W. *J. Synchrotron Rad.* **2005**, *12*, 224–233.
- (215) Kohn, W. Electronic structure of matter - wave functions and density functionals **1999**, 213–237.
- (216) Kepp, K. P. *Coord. Chem. Rev.* **2013**, *257*, 196–209.
- (217) Ryde, U. *Dalton Trans.* **2007**, 607–625.

- (218) Baerends, E. J. ADF 2007.01ed.; SCM, Theoretical Chemistry, Vrije Universiteit: Amsterdam, The Netherlands **2007**.
- (219) Velde, G. T.; Bickelhaupt, F. M.; Baerends, E. J.; Fonseca C., G.; Van S. J. A., G.; Snijders, J. G.; Ziegler, T.; Fonseca Guerra, C.; Van Gisbergen, S. J. a. *J. Comput. Chem.* **2001**, *22*, 931–967.
- (220) Neese, F. ORCA, an Ab Initio, Density Functional and Semiempirical Electronic Structure Program Package, version 2.9, Universitat Bonn, Germany **2012**.
- (221) Neese, F. *WIREs Comput. Mol. Sci* **2012**, *2*, 73–78.
- (222) Hohenberg, P.; Kohn, W. *Phys. Rev. B* **1964**, *136*, B864–B871.
- (223) Neese, F. *Coord. Chem. Rev* **2009**, *253*, 526–563.
- (224) Kohn, W.; Sham, L. J. *Phys. Rev.* **1965**, *140*, 1133–&.
- (225) Eriksson, L. A.; Pettersson, L. G. M.; Siegbahn, P. E. M.; Wahlgren, U. *J. Chem. Phys.* **1995**, *102*, 872–878.
- (226) Becke, A. D. *Phys. Rev. A: At. Mol. Opt. Phys.* **1988**, *38*, 3098–3100.
- (227) Perdew, J. P. *Phys. Rev. B: Condens. Matter* **1986**, *33*, 8822–8824.
- (228) Vosko, S. H.; Wilk, L.; Nusair, M. *Can. J. Phys.* **1980**, *58*, 1200–1211.
- (229) Slater, J. C. *Phys. Rev.* **1930**, *36*, 57–64.
- (230) Jensen, F. *Introduction to computational chemistry*; Second Edi.; John Wiley & Sons, Ltd., 2007; pp. 193–231.
- (231) Delgado-Jaime, M. U. Electronic structure studies of ruthenium-based catalysts for olefin metathesis: an x-ray absorption spectroscopy perspective, 2009.
- (232) Weigend, F.; Furche, F.; Ahlrichs, R. *J. Chem. Phys.* **2003**, *119*, 12753–12762.
- (233) Weigend, F.; Ahlrichs, R. *Phys. Chem. Chem. Phys.* **2005**, *7*, 3297–3305.
- (234) Neese, F. *J. Biol. Inorg. Chem.* **2006**, *11*, 702–711.
- (235) Van E., L.; Baerends, E. J.; Snijders, J. G. *J. Chem. Phys.* **1993**, *99*, 4597–4610.
- (236) Filatov, M.; Cremer, D. *Mol. Phys.* **2003**, *101*, 2295–2302.
- (237) Klamt, A.; Schueuermann, G. *J. Chem. Soc., Perkin Trans. 2* **1993**, 799–805.
- (238) Mulliken, R. S. *J. Chem. Phys.* **1962**, *36*, 3428–3440.
- (239) Hirshfeld, F. L. *Theor. Chim. Acta* **1977**, *44*, 129–138.
- (240) Lowdin, P. O. *Adv. Quantum Chem.* **1970**, *5*, 185–199.
- (241) Reed, A. E.; Curtiss, L. a.; Weinhold, F. *Chem. Rev.* **1988**, *88*, 899–926.
- (242) Weinhold, F.; Landis, C. R. *Chem. Edu. Res. Pract. Eur.* **2001**, *2*, 91–104.
- (243) Bregman, H.; Carroll, P. J.; Meggers, E. *J. Am. Chem. Soc.* **2006**, *128*, 877–884.
- (244) Gras, M.; Therrien, B.; Suss-Fink, G.; Stepnicka, P.; Renfrew, A. K.; Dyson, P. J. *J. Organomet. Chem.* **2008**, *693*, 3419–3424.
- (245) Nguyen, A.; Top, S.; Pigeon, P.; Vessières, A.; Hillard, E. A.; Plamont, M. A.; Huché, M.; Rigamonti, C.; Jaouen, G. *Chem.-Eur. J.* **2009**, *15*, 684–696.
- (246) Novakova, O.; Nazarov, A. A.; Hartinger, C. G.; Keppler, B. K.; Brabec, V. *Biochem. Pharmacol.* **2009**, *77*, 364–374.
- (247) Roos, G.; Messens, J. *Free Radic. Biol. Med.* **2011**, *51*, 314–326.
- (248) Charles, R. L.; Schroder, E.; May, G.; Free, P.; Gaffney, P. R. J.; Wait, R.; Begum, S.; Heads, R. J.; Eaton, P. *Mol. Cell. Proteomics* **2007**, *6*, 1473–1484.
- (249) Jacob, C.; Knight, I.; Winyard, P. G. *Biol. Chem.* **2006**, *387*, 1385–1397.
- (250) Maret, W. *Antioxid. Redox Signaling* **2006**, *8*, 1419–1441.

- (251) Dey, A.; Jeffrey, S. P.; Darensbourg, M.; Hodgson, K. O.; Hedman, B.; Solomon, E. I. *Inorg. Chem.* **2007**, *46*, 4989–4996.
- (252) Wang, F. Y.; Weidt, S.; Xu, J. J.; Mackay, C. L.; Langridge-Smith, P. R. R.; Sadler, P. J. J. *Am. Soc. Mass. Spectrom.* **2008**, *19*, 544–549.
- (253) Hu, W.; Luo, Q.; Ma, X.; Wu, K.; Liu, J.; Chen, Y.; Xiong, S.; Wang, J.; Sadler, P. J.; Wang, F. Y. *Chem. Eur. J.* **2009**, *15*, 6586–94.
- (254) Yano, T.; Aii, H.; Yamaguchi, S.; Funahashi, Y.; Jitsukawa, K.; Wawa, T.; Masuda, H. *Eur.J. Inorg. Chem.* **2006**, 3753–3761.
- (255) Yano, T.; Wasada-Tsutsui, Y.; Aii, H.; Yamaguchi, S.; Funahashi, Y.; Ozawa, T.; Masuda, H. *Inorg. Chem.* **2007**, *46*, 10345–53.
- (256) Rat, M.; De Sousa, R. A.; Tomas, A.; Frapart, Y.; Tuchagues, J. P.; Artaud, I. *Eur.J. Inorg. Chem.* **2003**, 759–765.
- (257) O'Toole, M. G.; Kreso, M.; Kozlowski, P. M.; Mashuta, M. S.; Grapperhaus, C. a J. *Biol. Inorg. Chem.* **2008**, *13*, 1219–1230.
- (258) Mascharak, P. K. *Coord. Chem. Rev.* **2002**, *225*, 201–214.
- (259) Lee, C. M.; Hsieh, C. H.; Dutta, A.; Lee, G. H.; Liaw, W. F. *J. Am. Chem. Soc.* **2003**, *125*, 11492–11493.
- (260) Kung, I.; Schweitzer, D.; Shearer, J.; Taylor, W. D.; Jackson, H. L.; Lovell, S.; Kovacs, J. A. *J. Am. Chem. Soc.* **2000**, *122*, 8299–8300.
- (261) Grapperhaus, C. a; Mullins, C. S.; Kozlowski, P. M.; Mashuta, M. S. *Inorg. Chem.* **2004**, *43*, 2859–2866.
- (262) Bourles, E.; De Sousa, R. A.; Galardon, E.; Giorgi, M.; Artaud, I. *Angew. Chem. Int. Ed.* **2005**, *44*, 6162–6165.
- (263) Begum, F. A.; Farah, A. A.; Hunter, H. N.; Lever, A. B. P. *Inorg. Chem.* **2009**, *48*, 2018–2027.
- (264) Rose, M. J.; Betterley, N. M.; Mascharak, P. K. *J. Am. Chem. Soc.* **2009**, *131*, 8340–8341.
- (265) De Sousa, R. A.; Artaud, I. *Tetrahedron* **2008**, *64*, 2198–2206.
- (266) Hopmann, K. H.; Himo, F. *Eur.J. Inorg. Chem.* **2008**, 1406–1412.
- (267) Lugo-Mas, P.; Dey, A.; Xu, L.; Davin, S. D.; Benedict, J.; Kaminsky, W.; Hodgson, K. O.; Hedman, B.; Solomon, E. I.; Kovacs, J. A. *J. Am. Chem. Soc.* **2006**, *128*, 11211–21.
- (268) Heinrich, L.; Mary-Verla, A.; Li, Y.; Vaissermann, J.; Chottard, J.-C. *Eur.J. Inorg. Chem.* **2001**, *2001*, 2203–2206.
- (269) Hedman, B.; Frank, P.; Gheller, S. F.; Roe, A. L.; Newton, W. E.; Hodgson, K. O. *J. Am. Chem. Soc.* **1988**, *110*, 3798–3805.
- (270) George, M. J. *J. Synchrotron Rad.* **2000**, *7*, 283–286.
- (271) Webb, S. M. *Phys. Scripta* **2005**, *T115*, 1011–1014.
- (272) Delgado-Jaime, M. U.; Kennepohl, P. *J. Synchrotron Rad.* **2010**, *17*, 119–128.
- (273) Delgado-Jaime, M. U.; Mewis, C. P.; Kennepohl, P. *J. Synchrotron Rad.* **2010**, *17*, 132–137.
- (274) Stohr, J. *Springer Series in Surface Sciences; 25 NEXAFS Spectroscopy*; Ertl, Gerhard; Gomer, Robert; Mills, Douglas, L. ., Ed.; 1st Ed.; Springer-Verlag: Berlin, Heidelberg, 1992; p. 213 pp.

- (275) Tyson, T. A.; Roe, A. L.; Frank, P.; Hodgson, K. O.; Hedman, B. *Phys. Rev. B* **1989**, *39*, 6305–6315.
- (276) Van Christoph., W. *J. Chem. Phys.* **1998**, *109*, 392–399.
- (277) Westre, T. E.; Kennepohl, P.; DeWitt, J. G.; Hedman, B.; Hodgson, K. O.; Solomon, E. I. *J. Am. Chem. Soc.* **1997**, *119*, 6297–6314.
- (278) Kennepohl, P.; Neese, F.; Schweitzer, D.; Jackson, H. L.; Kovacs, J. A.; Solomon, E. I. *Inorg. Chem.* **2005**, *44*, 1826–1836.
- (279) Govindaswamy, P.; Mozharivskiy, Y. A.; Kollipara, M. R. *Polyhedron* **2004**, *23*, 3115–3123.
- (280) Martin-Diaconescu, V.; Kennepohl, P. *Inorg. Chem.* **2008**, *338*, 1038–1044.
- (281) Ishii, A.; Komiya, K.; Nakayama, J. *J. Am. Chem. Soc.* **1996**, *118*, 12836–12837.
- (282) Goto, K.; Holler, M.; Okazaki, R. *J. Am. Chem. Soc.* **1997**, *119*, 1460–1461.
- (283) Votyakova, T. V.; Reynolds, I. J. *Arch. Biochem. Biophys.* **2004**, *431*, 138–144.
- (284) Vaupel, P.; Kallinowski, F.; Okunieff, P. *Cancer Res.* **1989**, *49*, 6449–6465.
- (285) Tannock, I. F.; Rotin, D. *Cancer Res.* **1989**, *49*, 4373–4384.
- (286) Grattan, B. J.; Freake, H. C. *Nutrients* **2012**, *4*, 648–675.
- (287) Cui, Y.; Vogt, S.; Olson, N.; Glass, A. G.; Rohan, T. E. *Cancer Epidemiol. Biomarkers Prev.* **2007**, *16*, 1682–1685.
- (288) Wang, F. Y.; Chen, H. M.; Parkinson, J. A.; Murdoch, P. D. S.; Sadler, P. J. *Inorg. Chem.* **2002**, *41*, 4509–4523.
- (289) Claiborne, A.; Miller, H.; Parsonage, D.; Ross, R. P. *FASEB J.* **1993**, *7*, 1483–1490.
- (290) Regulation, R.; Claiborne, A.; Yeh, J. I.; Mallett, T. C.; Luba, J.; Crane, E. J.; Parsonage, D.; Crane III, E. J.; Charrier, V. *Biochemistry* **1999**, *38*, 15407–15416.
- (291) Allison, W. S. *Acc. Chem. Res.* **1976**, *9*, 293–299.
- (292) Dilworth, J. R.; Zheng, Y.; Lu, S.; Wu, Q. *Transition Met. Chem.* **1992**, *17*, 364–368.
- (293) Leeladee, P.; Baglia, R. a; Prokop, K. a; Latifi, R.; De Visser, S. P.; Goldberg, D. P. *J. Am. Chem. Soc.* **2012**, *134*, 10397–400.
- (294) Furukawa, N.; Konno, Y.; Tsuruoka, M.; Ogawa, S. *Heteroat. Chem.* **1992**, *3*, 495–503.
- (295) O'Donnell, J. S.; Schwan, A. L. *Tetrahedron Lett.* **2003**, *44*, 6293–6296.
- (296) Aucott, S. M.; Kilian, P.; Robertson, S. D.; Slawin, A. M. Z.; Woollins, J. D. *Chem. Eur. J.* **2006**, *12*, 895–902.
- (297) Delgado-Jaime, M. U.; DeBeer, S. *J. Comput. Chem.* **2012**, *33*, 2180–2185.
- (298) Schaftenaar, G.; Noordik, J. H. *J. Comput.-Aided Mol. Des.* **2000**, *14*, 123–134.
- (299) Debeer, S.; Neese, F. *Inorg. Chem.* **2010**, *49*, 1849–53.
- (300) Brown, I. D.; Skowron, a. *J. Am. Chem. Soc.* **1990**, *112*, 3401–3403.
- (301) Brown, I. D. *Acta Crystallogr., Sect. B: Struct. Sci* **1988**, *44*, 545–553.
- (302) Dilworth, J. R.; Hueting, R. *Inorg. Chim. Acta* **2012**, *389*, 3–15.
- (303) Lobana, T. S.; Sharma, R.; Bawa, G.; Khanna, S. *Coord. Chem. Rev.* **2009**, *253*, 977–1055.
- (304) Quiroga, A. G.; Perez, J. M.; Lopez-Solera, I.; Masaguer, J. R.; Luque, A.; Roman, P.; Edwards, A.; Alonso, C.; Navarro-Ranninger, C. *J. Med. Chem.* **1998**, *41*, 1399–1408.
- (305) Offiong, O. E.; Martelli, S. *Farmaco* **1994**, *49*, 513–518.
- (306) Zhang, G.; Li, Y.; Feng, X.; Zhang, R.; Zhao, J. *Asian J. Chem.* **2013**, *25*, 2003–2006.
- (307) Hadjipavlou-Litina, D. *Pharmazie* **1996**, *51*, 468–470.

- (308) Demoro, B.; Sarniguet, C.; Sánchez-Delgado, R.; Rossi, M.; Liebowitz, D.; Caruso, F.; Olea-Azar, C.; Moreno, V.; Medeiros, A.; Comini, M. a; Otero, L.; Gambino, D. *Dalton Trans.* **2012**, *41*, 1534–43.
- (309) Crouch, P. J.; Barnham, K. J. *Acc. Chem. Res.* **2012**, *45*, 1604–1611.
- (310) Debreczeni, J. E.; Bullock, A. N.; Atilla, G. E.; Williams, D. S.; Bregman, H.; Knapp, S.; Meggers, E. *Angew. Chem. Int. Ed.* **2006**, *45*, 1580–1585.
- (311) Noffke, Anna Louisa; Srischandakumar, T.; Clarkson, G. J.; Kennepohl, P.; Sadler, P. J. *In Preparation* **2013**.
- (312) Beckford, F. A.; Leblanc, G.; Thessing, J.; Shaloski Jr, M.; Frost, B. J.; Li, L.; Seeram, N. P. *Inorg. Chem. Commun.* **2009**, *12*, 1094–1098.
- (313) Beckford, F. A. *Int. J. Inorg. Chem.* **2010**, *2010*, 1–7.
- (314) Beckford, F. A.; Dourth, D.; Shaloski, M.; Didion, J.; Thessing, J.; Woods, J.; Crowell, V.; Gerasimchuk, N.; Gonzalez-Sarrías, A.; Seeram, N. P. *J. Inorg. Biochem.* **2011**, *105*, 1019–29.
- (315) Beckford, F. A.; Thessing, J.; Shaloski Jr, M.; Mbarushimana, P. C.; Brock, A.; Didion, J.; Woods, J.; Gonzalez-Sarrías, A.; Seeram, N. P. *J. Mol. Struct.* **2011**, *992*, 39–47.
- (316) Beckford, F. A.; Shaloski, J. M.; Leblanc, G.; Thessing, J.; Lewis-Alleyne, L. C.; Holder, A. A.; Li, L.; Seeram, N. P. *Dalton Trans.* **2009**, 10757–10764.
- (317) Grguric-Sipka, S.; Alshewi, M. A. A. M.; Jeremic, D.; Kaluderovic, G. N.; Gomez-Ruiz, S.; Zizak, Z.; Juranic, Z.; Sabo, T. J. *J. Serb. Chem. Soc.* **2008**, *73*, 619–630.
- (318) Garcia, G.; Solano, I.; Sanchez, G.; Santana, M. D.; Lopez, G.; Casabo, J.; Molins, E.; Miravittles, C. *J. Organomet. Chem.* **1994**, *467*, 119–126.
- (319) Romero-Canelon, I.; Salassa, L.; Sadler, P. J. *J. Med. Chem.* **2013**, *56*, 1291–1300.
- (320) Van Lenthe, E.; Baerends, E. J. and Snijders, J. G. *J. Chem. Phys.* **1993**, *99*, 4597.
- (321) Van Wullen, C. J. *J. Chem. Phys.* **1998**, *109*, 392.
- (322) Kowol, C. R.; Trondl, R.; Heffeter, P.; Arion, V. B.; Jakupec, M. A.; Roller, A.; Galanski, M.; Berger, W.; Keppler, B. K. *J. Med. Chem.* **2009**, *52*, 5032–5043.

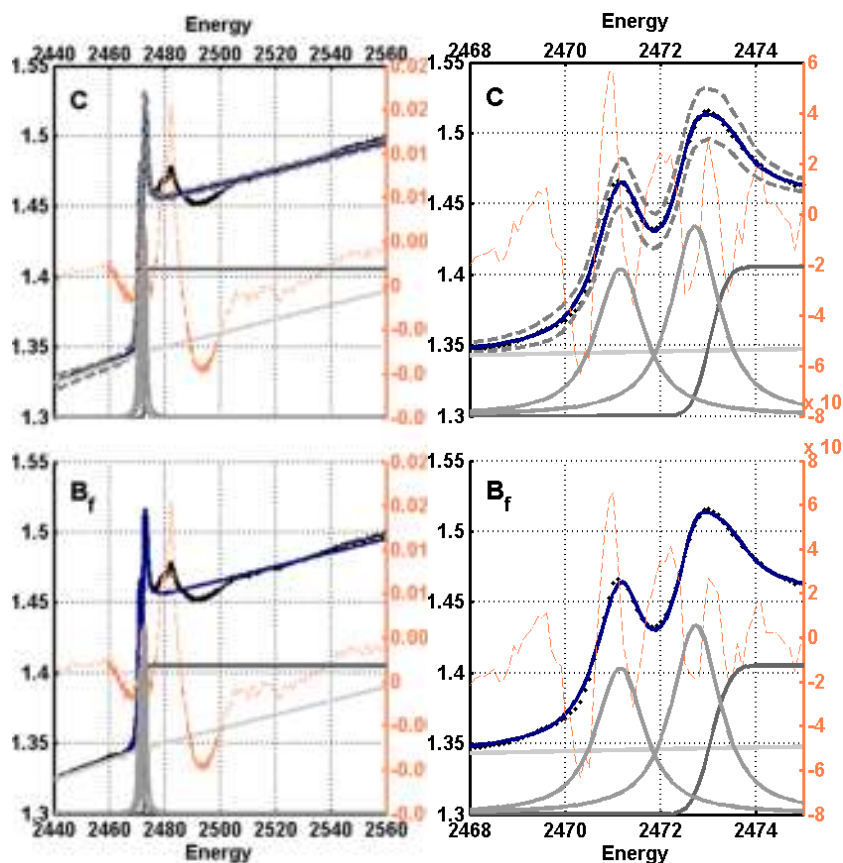
APPENDIX A: BLUEPRINT XAS FITTINGS AND TDDFT ANALYSIS

A.1. Peak fitting of S K-edge XAS for chapter 3

Complete assignment and peak fitting of S K-edge XAS of **1a,b** – **3a,b** and **1c**

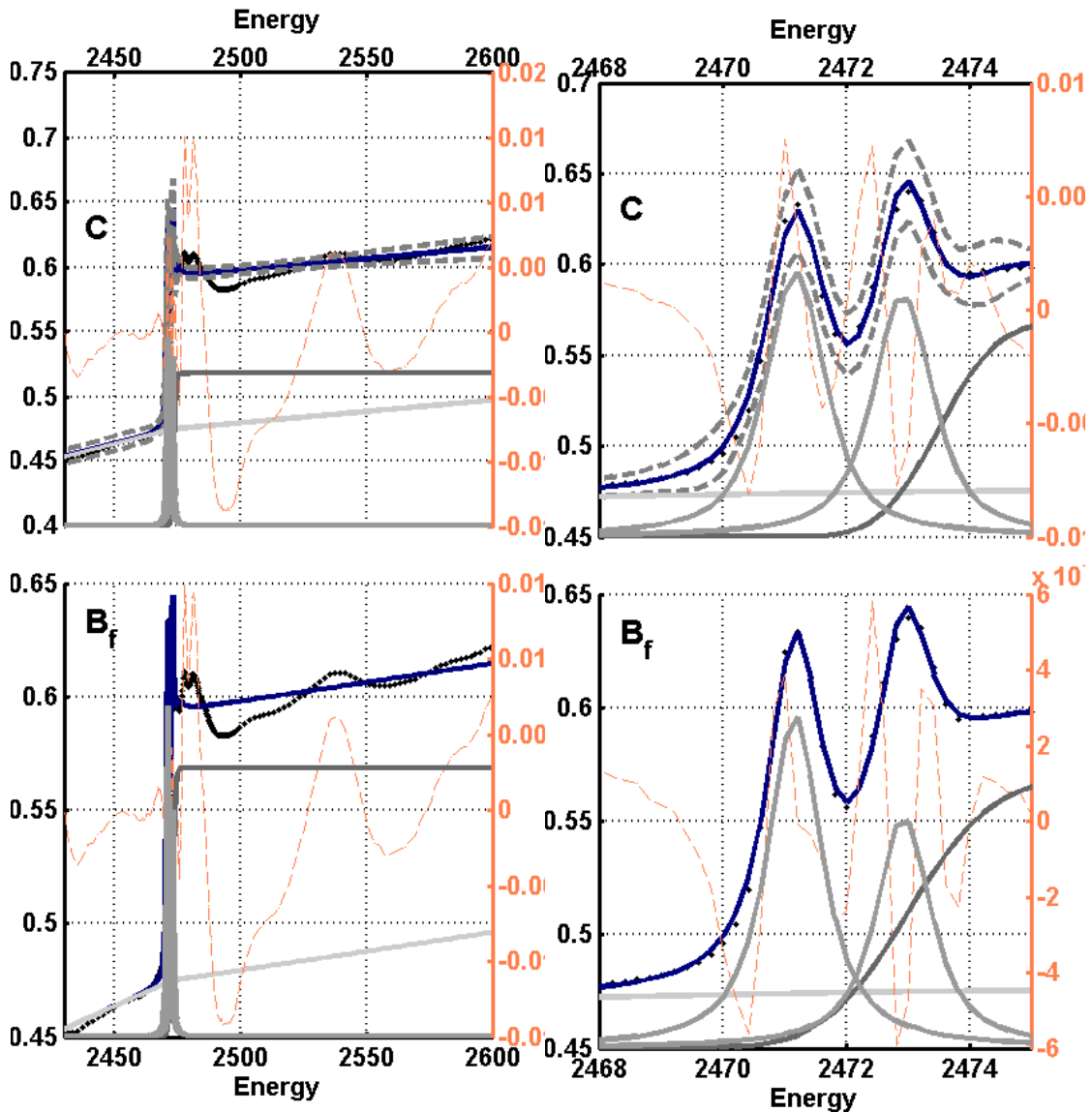
1a. Peak fitted results for complex **1a**.

Parameter	Lower	Upper	Ave. (Prefits)	Std. (Prefits)	Ave. (Fits)	Std. (Fits)	Value (SingleFit)	95% cint
I1	0.02	0.255	0.094347	0.036577	0.105296	0.001381	0.10558	0.002341
G1	0	1	0.51876	0.302984	0.999558	0.003455	1	NaN
O1	2473	2474	2473.5	0.293554	2473.07	0.128322	2473.04	0.232907
W1	0	3.88	1.71634	1.13891	0.36752	0.178785	0.336127	0.130431
I2	0	3.56	1.71355	0.960464	1.79394	0.05905	1.80089	0.131502
G2	0	1	0.483722	0.294029	0.073894	0.116267	0.049247	0.242252
W2	0	1.19	0.808472	0.272398	0.600723	0.034358	0.593142	0.063677
O2	2470.8	2471.5	2471.16	0.199457	2471.16	0.010313	2471.16	0.041139
I3	0	4.34	2.03075	1.0892	2.3207	0.087642	2.32114	0.277292
O3	1.5	2.4	1.89714	0.282309	1.589	0.093275	1.56925	0.108282



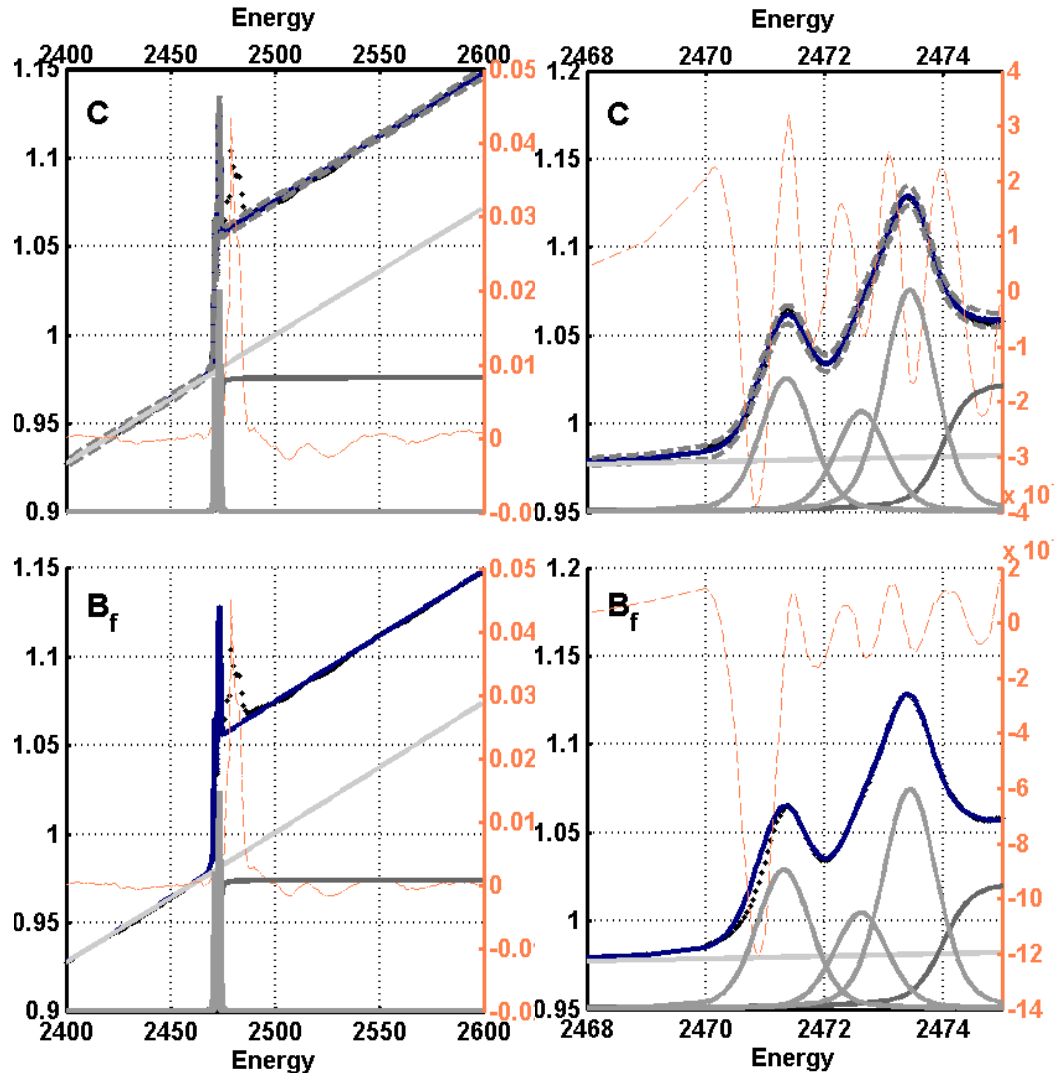
1b. Peak fitted results for complex 1b.

Parameter	Lower	Upper	Ave. (Prefits)	Std. (Prefits)	Ave. (Fits)	Std. (Fits)	Value (SingleFit)	95% cint
I1	0.05	1.25	0.150495	0.0660733	0.118601	0.00014804	0.118005	0.00275812
G1	0	1	0.436011	0.273751	0.999984	0.00011912	1	NaN
O1	2473	2475	2473.96	0.55839	2473	0.0197406	2473.5	NaN
W1	0	2.5	1.36882	0.695706	1.26668	0.0149275	0.871153	0.279167
I2	0	4.36	2.38379	1.12097	1.96383	0.00454944	2.04508	0.186581
G2	0	1	0.5284	0.290112	0.0868087	0.00949577	0.191797	0.283205
W2	0	1	0.559092	0.260856	0.525365	0.00065762	0.574753	0.0500038
O2	2470.8	2471.4	2471.09	0.163915	2471.17	0.00221263	2471.19	0.0400388
I3	0	4.64	1.98229	1.25039	1.36858	0.0196129	1.87864	0.151654
O3	1.6	2.3	1.95152	0.208485	1.76459	0.00485936	1.7337	0.063654



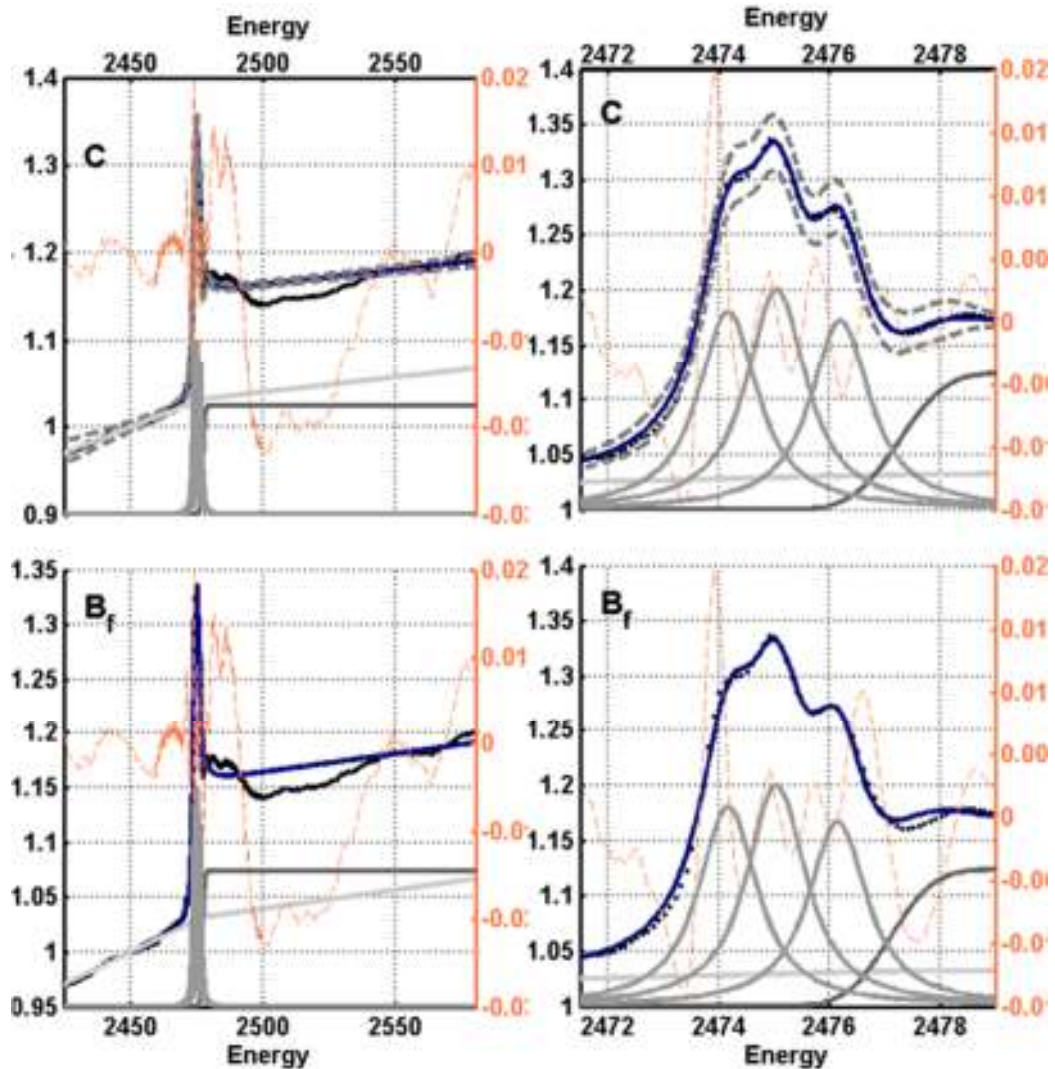
1c. Peak fitted results for complex 1c.

Parameter	Lower	Upper	Ave. (Prefits)	Std. (Prefits)	Ave. (Fits)	Std. (Fits)	Value (SingleFit)	95% cint
I1	0.0688	0.0867	0.077145	0.00506018	0.0742052	0.00089529	0.0760551	0.00155182
G1	0	1	0.459855	0.296387	0.536967	0.104378	0.519819	0.245544
O1	2474	2475.5	2474.76	0.458292	2474	1.58E-08	2474	NaN
W1	0.393	1.62	0.991814	0.378082	0.421225	0.111455	0.393	NaN
I2	0.9	3	1.8191	0.551085	1.36351	0.0855311	1.23285	0.0478363
G2	0	1	0.414276	0.292035	0.648636	0.0752171	0.631519	0.126845
W2	0.1	0.752	0.597998	0.120106	0.533627	0.0126238	0.512746	0.0139934
O2	2471.1	2471.8	2471.46	0.182577	2471.32	0.043603	2471.36	0.0171232
I3	0.236	2.94	1.52416	0.708566	0.940767	0.0561907	0.92841	0.0636473
O3	1.159	1.585	1.38348	0.121728	1.30109	0.0209332	1.26814	0.0383745
I4	0.904	3.99	2.29293	0.841133	2.15045	0.0685482	2.05248	0.0985099
O4	0.68599	0.88603	0.799364	0.05288	0.822903	0.0291481	0.815665	0.0354149



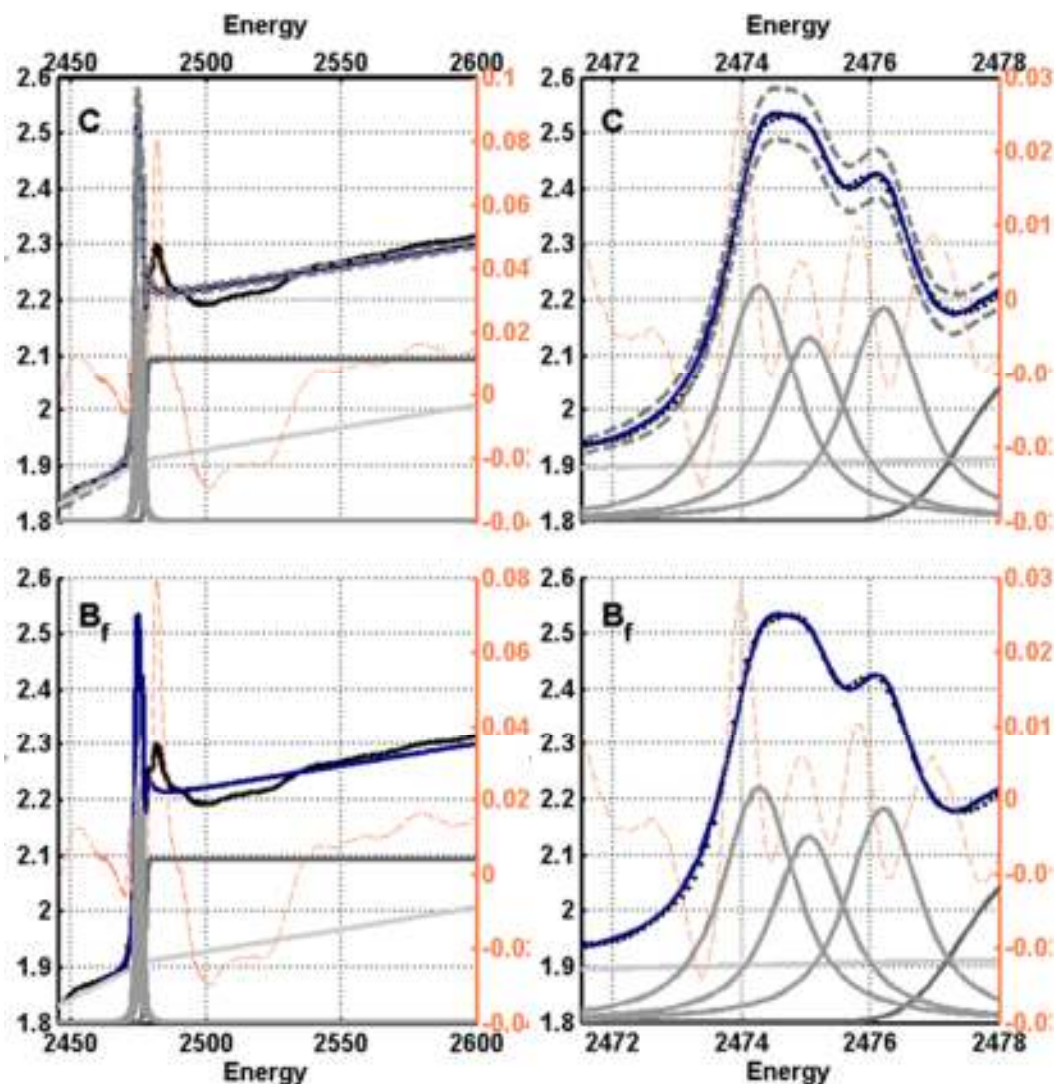
2a. Peak fitted results for complex 2a.

Parameter	Lower	Upper	Ave. (Prefits)	Std. (Prefits)	Ave. (Fits)	Std. (Fits)	Value (SingleFit)	95% cint
I1	0.12	0.255	0.155141	0.0260575	0.124316	0.00326066	0.124286	0.00333189
G1	0	1	0.503641	0.256758	0.986857	0.0893549	1	NaN
O1	2476	2478.6	2477.19	0.740609	2477.1	0.426467	2477.26	0.184795
W1	0	2.5	1.23302	0.633378	0.729058	0.216568	0.783444	0.245793
I2	0	3.56	1.71752	1.00499	2.86037	0.124814	2.89668	0.292063
G2	0	1	0.45288	0.285177	0.0271982	0.0481386	0.0129662	0.133925
W2	0	1.19	0.822904	0.238977	0.632716	0.0520398	0.637212	0.049569
O2	2473.8	2474.5	2474.19	0.193632	2474.17	0.0411194	2474.17	0.0592574
I3	0	4.34	2.2939	1.18926	3.17379	0.175754	3.22337	0.260321
O3	0.5	1.2	0.855323	0.206164	0.873168	0.0447447	0.878647	0.0550629
I4	0	3.11	1.62685	0.854773	2.64729	0.381874	2.77457	0.273186
O4	0.5	1.5	0.966931	0.27956	1.10675	0.126442	1.15095	0.0712536



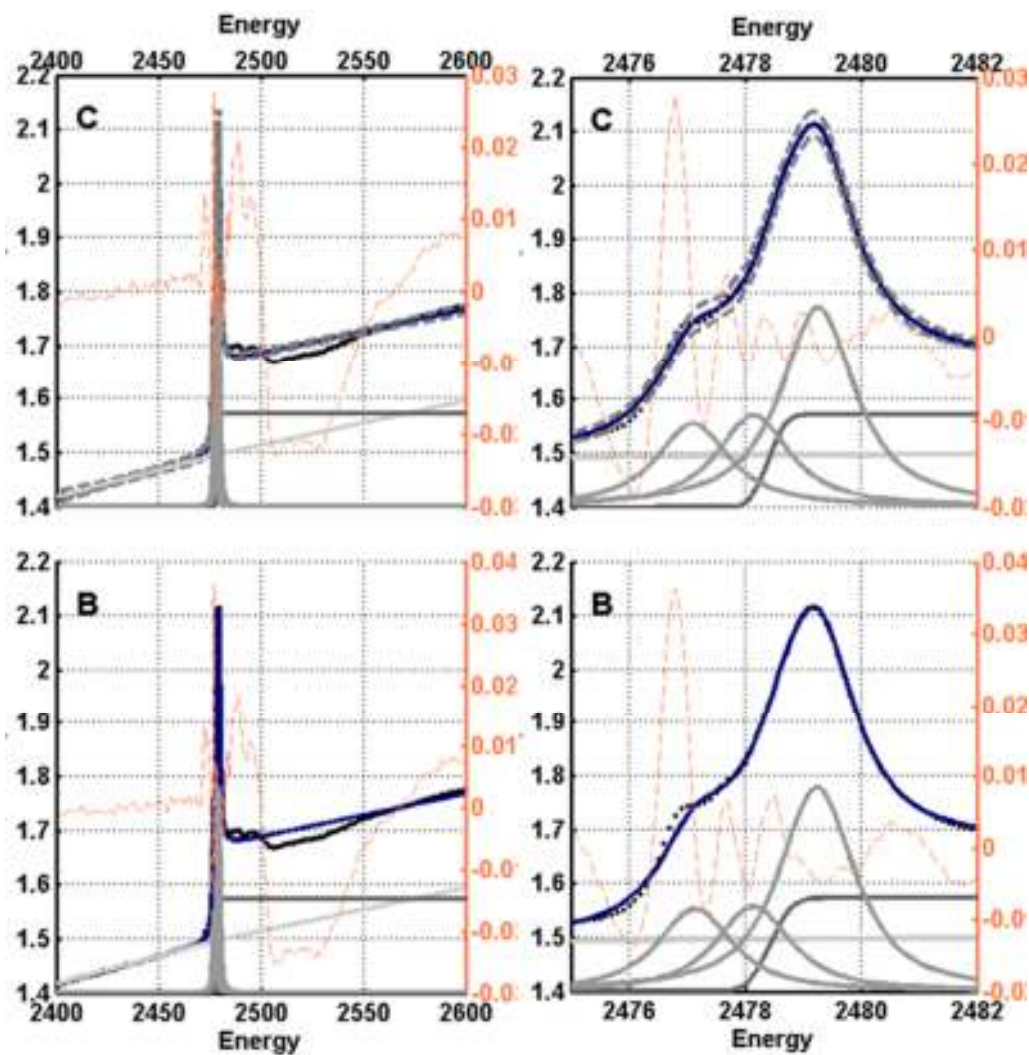
2b. Peak fitted results for complex 2b.

Parameter	Lower	Upper	Ave. (Prefits)	Std. (Prefits)	Ave. (Fits)	Std. (Fits)	Value (SingleFit)	95% cint
I1	0.12	0.855	0.306338	0.0754835	0.29327	0.00507634	0.292413	0.00604917
G1	0	1	0.504747	0.282795	1	3.80E-09	1	NaN
O1	2476	2478.6	2477.23	0.713192	2477.4	0.150895	2477.43	0.122369
W1	0	2.5	1.12051	0.699113	0.774849	0.156413	0.753549	0.173375
I2	0	3.56	1.90681	0.962012	2.92175	0.252446	2.96359	0.3829
G2	0	1	0.475225	0.274922	0.0956256	0.0641679	0.0859078	0.125486
W2	0	1.19	0.803103	0.267369	0.67574	0.013736	0.673722	0.0560822
O2	2473.8	2474.5	2474.22	0.195111	2474.27	0.0337253	2474.27	0.0637375
I3	0	4.34	2.27487	1.1978	2.30391	0.119486	2.30591	0.322586
O3	0.5	1	0.752735	0.139809	0.771694	0.0270685	0.775241	0.0735744
I4	0	3.11	1.55131	0.825494	2.65594	0.162205	2.6801	0.204692
O4	0.75	1.3	1.01587	0.153147	1.15465	0.0133195	1.15283	0.0860011



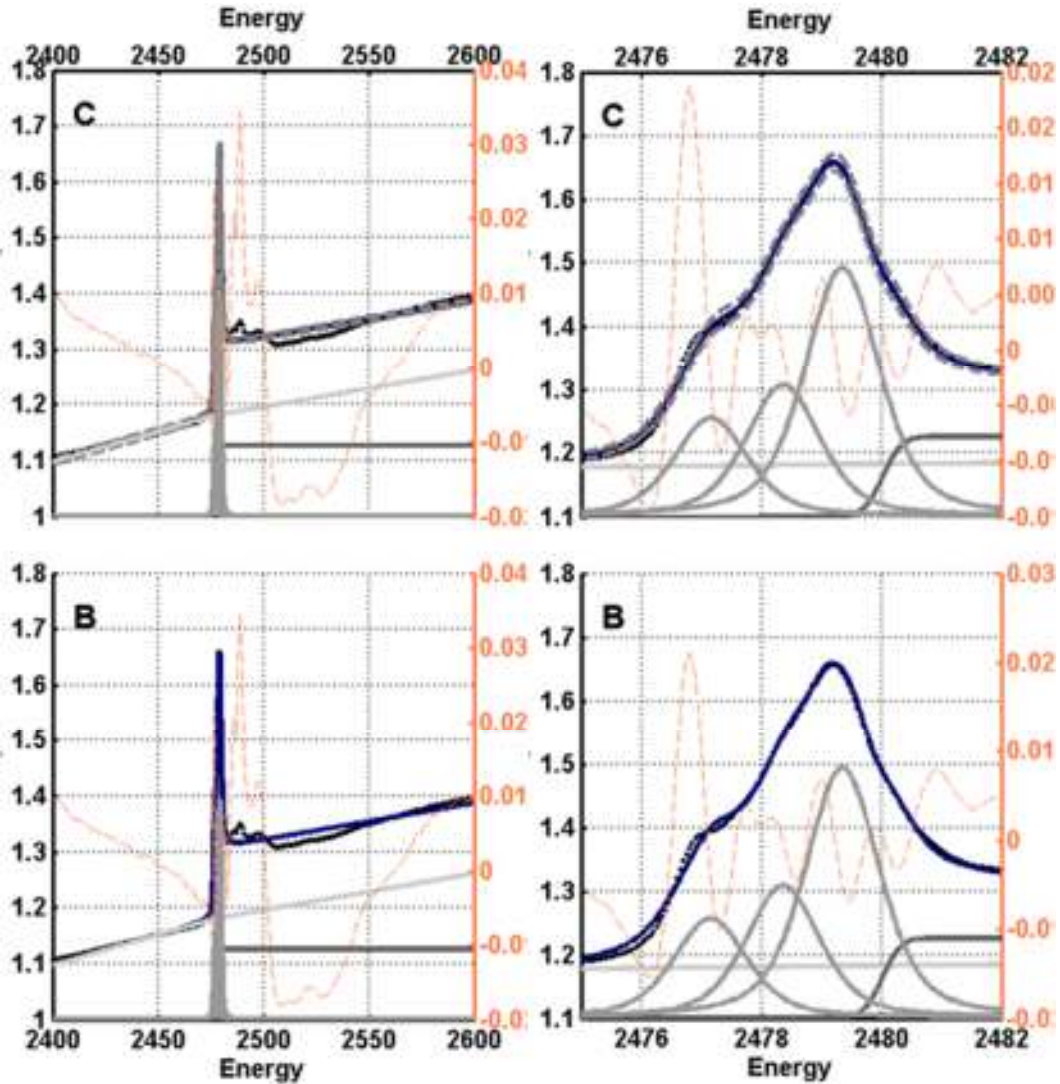
3a. Peak fitted results for complex 3a.

Parameter	Lower	Upper	Ave. (Prefits)	Std. (Prefits)	Ave. (Fits)	Std. (Fits)	Value (SingleFit)	95% cint
I1	0.068	0.191	0.162978	0.019141	0.174105	0.00329274	0.172434	0.0047692
G1	0	1	0.475496	0.278803	0.986457	0.0669339	1	NaN
O1	2478.4	2479.3	2478.78	0.245627	2478.43	0.0839717	2478.4	NaN
W1	0.00936	0.67	0.346422	0.195757	0.350154	0.118384	0.281058	0.104501
I2	0	3.13	1.5971	0.809429	2.01943	0.175363	2.08035	0.249136
G2	0	1	0.414492	0.265539	0.114988	0.0911067	0.0495228	0.097076
W2	0.125	0.823	0.665392	0.099387	0.770355	0.0223647	0.753933	0.0527629
O2	2476.5	2477.3	2476.93	0.214902	2477.14	0.0746859	2477.1	0.0758509
I3	0	4	2.58531	0.922087	2.07838	0.313944	2.28822	0.368455
O3	0.75	1.5	1.12664	0.20457	1.00366	0.091065	1.04403	0.0750988
I4	0	6	4.28231	1.32769	5.0038	0.392066	5.03086	0.3456
O4	1	1.7001	1.2955	0.176457	1.09822	0.0640549	1.11675	0.0906606



3b. Peak fitted results for complex 1a.

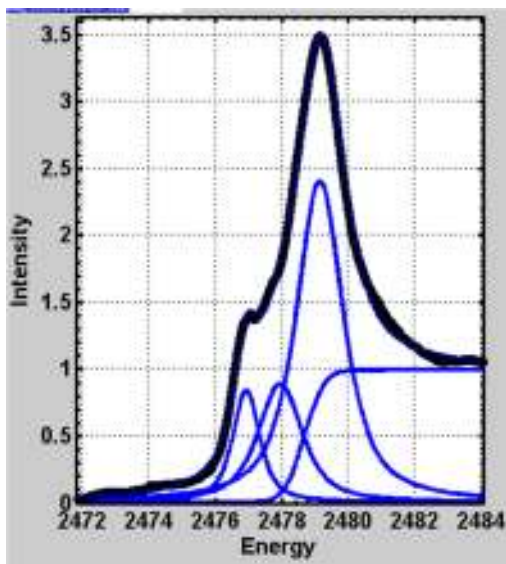
Parameter	Lower	Upper	Ave. (Prefits)	Std. (Prefits)	Ave. (Fits)	Std. (Fits)	Value (SingleFit)	95% cint
I1	0.024	0.134	0.113781	0.0111915	0.125719	6.52E-05	0.125746	0.00220012
G1	0	1	0.423544	0.30079	0.999994	4.12E-05	1	NaN
O1	2479.5	2482	2480.1	0.506445	2480.01	0.00463287	2480.02	0.0869251
W1	0.00264	0.558	0.308928	0.153539	0.296912	0.0013961	0.301583	0.0632076
I2	0.09	3.71	2.05749	0.786637	2.37437	0.0049125	2.35782	0.131116
G2	0	1	0.488711	0.256238	0.413007	0.0027241	0.419465	0.076412
W2	0.065	0.817	0.692303	0.0994842	0.72529	0.00192617	0.730295	0.0308457
O2	2476.5	2477.2	2477.05	0.131518	2477.15	0.00262287	2477.16	0.0418552
I3	0.35	4.87	3.66294	0.954029	3.16857	0.00633512	3.15302	0.196136
O3	1	1.4262	1.26027	0.114531	1.2127	0.00144236	1.20367	0.0351816
I4	0	5.97	5.30023	0.500945	5.96801	0.00683777	5.97	NaN
O4	0.7	1.2	1.00285	0.14082	0.987345	0.00137411	0.983731	0.0435188



A.2. Peak fitting of S K-edge XAS for chapter 4

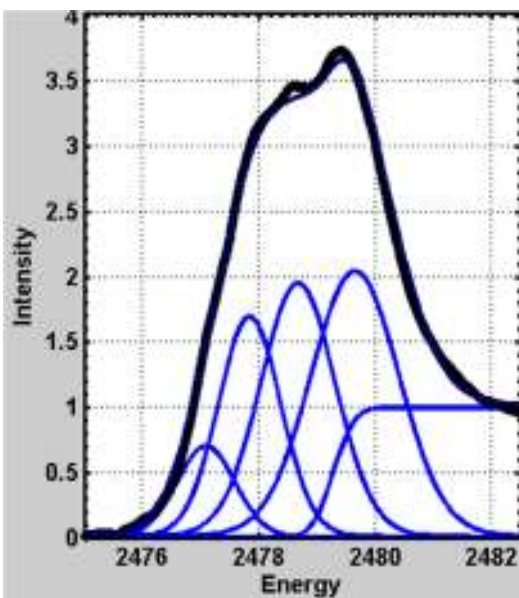
3a. Peak fitted results for complex 3a.

Coeff	Low	Up	Avg	Err
I1	0.0008	0.005	0.003438	7.82E-05
G1	0	1	0.934698	0.140492
O1	2478.5	2484	2478.68	0.338813
W1	0.25	1.5	0.555725	0.182142
m1	1.00E-08	5.00E-06	1.06E-06	1.12E-06
Y1	0.009	0.0806	0.017201	0.002747
m2	5.00E-07	0.0002	6.21E-06	2.04E-06
I2	0.9	3	1.1439	0.216804
G2	0	1	0.203669	0.102547
W2	0.1	0.7	0.474938	0.062813
O2	2476	2477.3	2476.93	0.074953
I3	1	4	2.00845	0.258904
W3	0.4	0.8	0.786062	0.042139
O3	0.7	1.2	1.01865	0.098823
I4	1	6	5.79798	0.326125
W4	0.5	1	0.841612	0.042523
O4	0.8	1.5	1.19057	0.123122



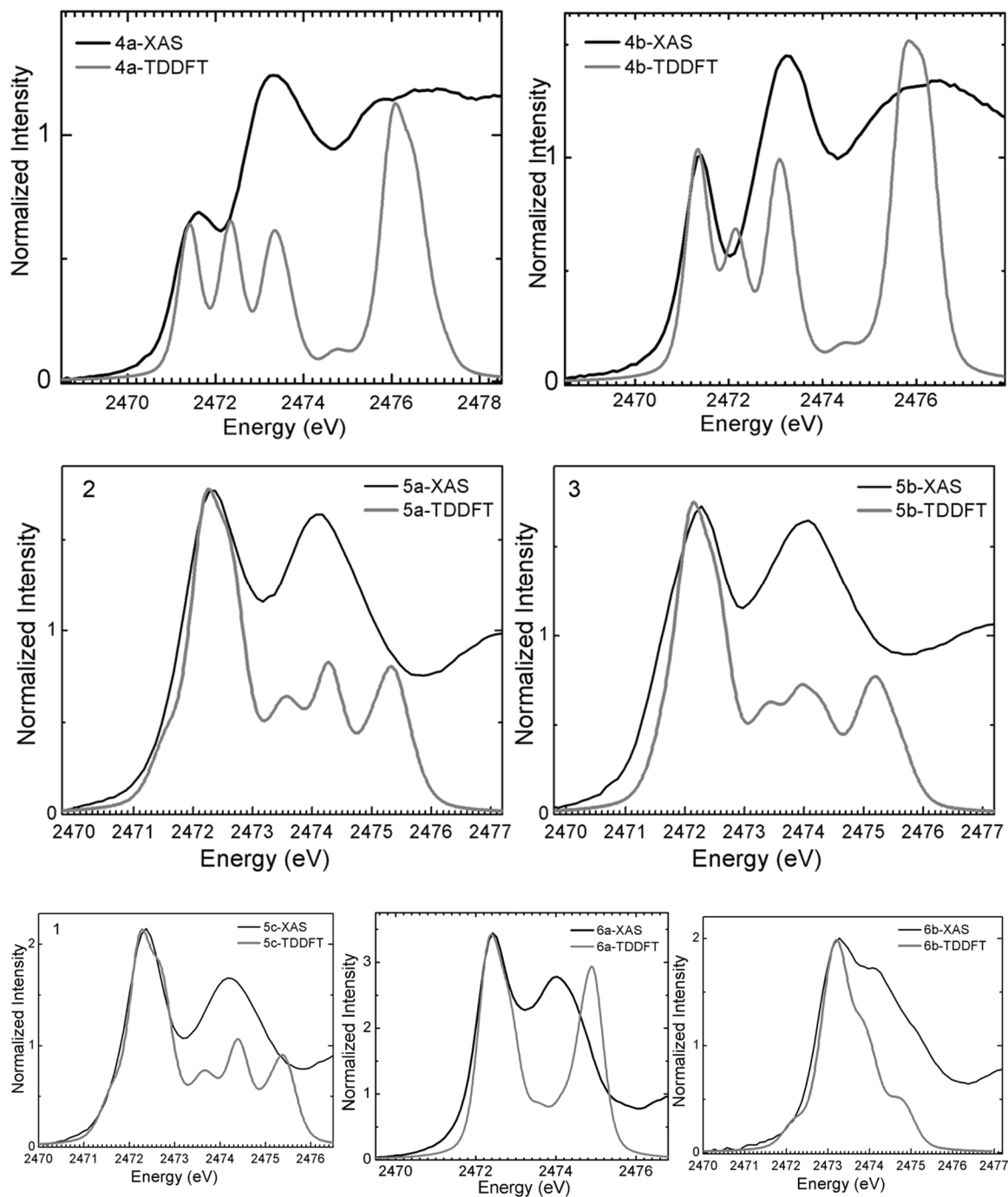
3aZn²⁺. Peak fitted results for complex 3aZn²⁺

Coeff	Low	Up	Avg	Err
I1	0.0005	0.005	0.001038	7.11E-06
G1	0	1	0.994777	0.018938
O1	2478	2484	2479.28	0.561714
W1	0.25	1.5	0.34201	0.11951
m1	1.00E-10	1.50E-05	8.92E-09	8.35E-08
Y1	0.009	0.0806	0.01529	0.000206
m2	5.00E-10	0.0002	5.34E-08	1.30E-07
I2	0.1	2	0.910188	0.550435
G2	0	1	0.890658	0.066586
W2	0.1	0.8	0.586554	0.083585
O2	2476	2477.3	2477.09	0.225226
I3	1	3	2.35504	0.384046
W3	0.4	1	0.629359	0.063246
O3	0.7	1	0.749108	0.064717
I4	2	4	3.25321	0.488368
W4	0.3	0.8	0.755317	0.046278
O4	0.5	0.9	0.832329	0.086293
I5	3	5	4.01951	0.680711
W5	0.5	0.9	0.890345	0.018289
O5	0.5	2	0.979501	0.148579



A.3.1. TDDFT spectra of complexes 4-6 and Peak fitting of S K-edge XAS for chapter 5

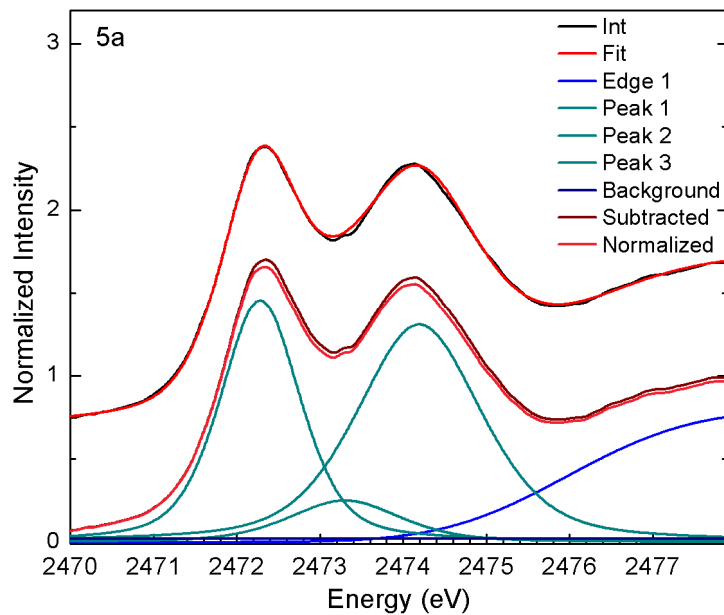
A.3.1a. TDDFT spectra of complexes 4-6



A.3.1b. Peak fitting of S K-edge XAS of complexes 4-6

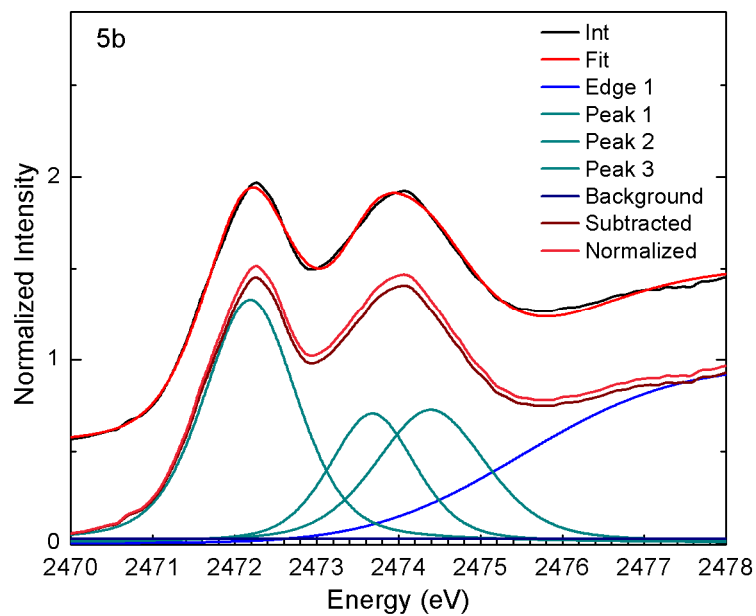
5a. Peak fitted results for complex 5a.

Coeff	Low	Up	Avg	Err
1	0.0008	0.005	0.001816	9.68E-05
	0	1	0.839146	0.15472
O1	2475.5	2480	2475.81	0.03009
W1	0.25	1.5	1.42531	0.107836
m1	2.00E-06	5.00E-06	3.53E-06	9.30E-07
Y1	0.009	0.0806	0.013711	0.002281
m2	5.00E-06	0.0002	8.54E-06	1.62E-06
I2	1.5	4	2.07707	0.159636
G2	0	1	0.460884	0.031948
W2	0.1	0.7	0.568023	0.008403
O2	2472	2472.5	2472.28	0.008984
I3	0.5	2.5	0.505111	0.038484
W3	0.4	0.8	0.799151	0.006201
O3	0.7	1.2	1.01603	0.178059
I4	1	4	2.9199	0.337419
W4	0.5	1	0.889426	0.020134
O4	0.8	1.5	0.894663	0.17079



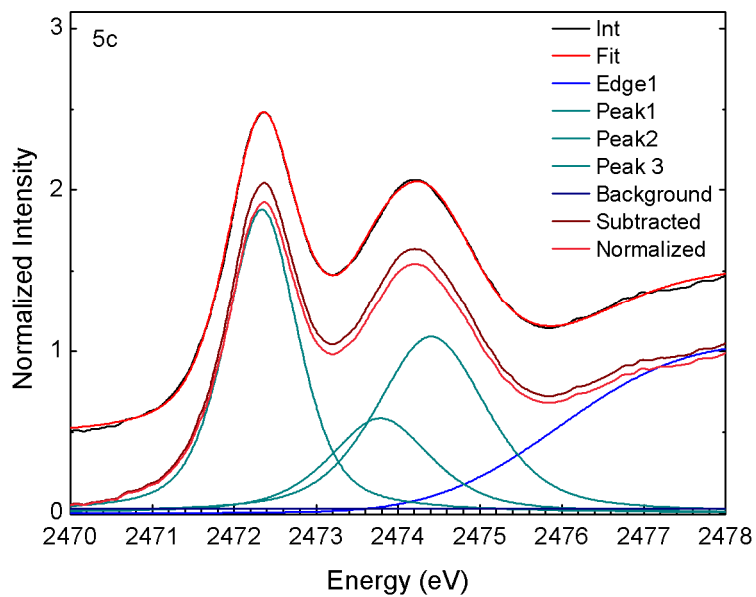
5b. Peak fitted results for complex 5b.

Coeff	Low	Up	Avg	Err
I1	0.0008	0.005	0.001918	4.51E-05
G1	0	1	0.999283	0.004088
O1	2475.5	2480	2475.5	0.001837
W1	0.25	2	1.71451	0.167347
m1	1.00E-06	4.72E-06	1.01E-06	4.72E-08
Y1	0.009	0.0806	0.018943	0.000117
m2	5.00E-06	0.0002	8.80E-06	6.71E-07
I2	1.5	5	2.35279	0.062741
G2	0	1	0.517588	0.019571
W2	0.4	0.7	0.672867	0.004059
O2	2472	2472.5	2472.19	0.001419
I3	0.5	2.5	1.1569	0.103983
W3	0.4	0.7	0.623371	0.012081
O3	0.8	1.785	1.49197	0.010745
I4	1.5	4	1.52631	0.108763
W4	0.5	0.8	0.799848	0.000977
O4	0.5	1.5	0.711385	0.009402



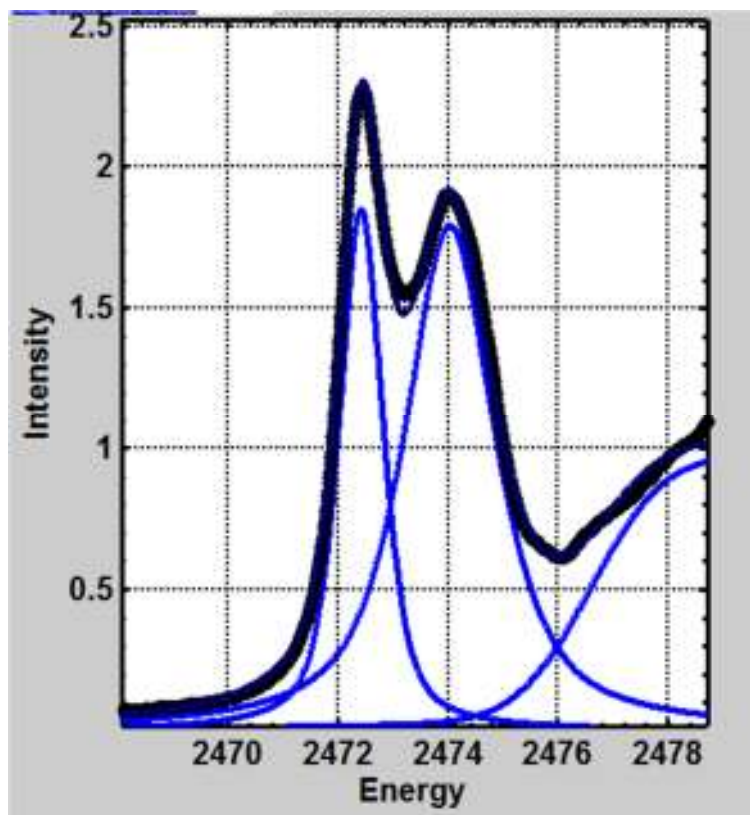
5c. Peak fitted results for complex 5c.

Coeff	Low	Up	Avg	Err
I1	0.0005	0.005	0.001592	7.68E-05
G1	0	1	0.982911	0.041207
O1	2474.5	2480	2475.96	0.036509
W1	0.25	1.5	1.39624	0.191471
m1	-4.72E-05	-4.72E-07	-8.18E-06	4.16E-06
YI	0.0206	0.0806	0.049062	0.010273
m2	6.00E-07	0.000196	5.42E-06	1.71E-06
I2	1	3	2.40103	0.115025
G2	0	1	0.414938	0.063225
W2	0.1	1	0.517129	0.00678
O2	2472.3	2472.4	2472.34	0.001552
I3	0.3	3	0.87869	0.196823
O3	0.8	1.5	1.44619	0.059105
W3	0.5	0.8	0.731353	0.042253
I4	0.5	3	2.15073	0.20933
W4	0.5	0.8	0.799492	0.003556
O4	0.5	1	0.62189	0.045914



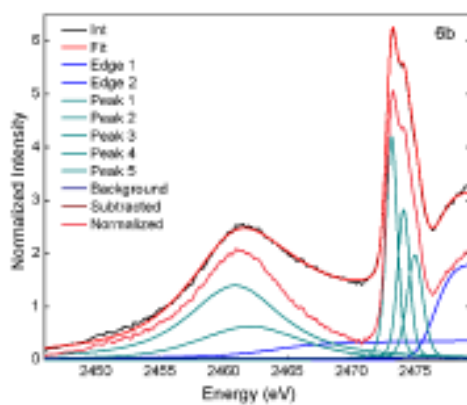
6a. Peak fitted results for complex 6a.

Coeff	Low	Up	Avg	Err
I1	0.0005	0.005	0.001767	0.000106
G1	0	1	0.9998	0.001527
O1	2474	2480	2476.67	0.08184
W1	0.25	1.5	1.45791	0.148073
m1	-0.00047	-4.72E-07	-1.67E-05	7.24E-06
Y1	0.0206	0.0806	0.054584	0.017858
m2	1.00E-08	0.000196	7.40E-07	1.77E-06
I2	1	6	2.15721	0.127548
G2	0	1	0.47571	0.054058
W2	0.1	1	0.482716	0.005518
O2	2472.2	2472.6	2472.41	0.001146
I3	1	6	3.05459	0.230126
O3	1	2	1.61176	0.006751
W3	0.5	1.5	0.995231	0.028027



6b. Peak fitted results for complex 6b.

Coeff	Low	Up	Avg	Err
I1	0.0001	0.09	0.000945	9.12E-05
G8	0	1	0.01978	0.073391
O1	2463	2467	2463.88	0.918916
W8	0.5	3.5	3.42322	0.214313
I2	0.0001	0.02	0.001697	0.000156
G9	0	1	0.995145	0.022986
O2	2476	2478	2476.53	0.056616
W9	0.5	3	1.29594	0.323296
m1	1.00E-08	0.001	3.43E-06	9.82E-07
YI	0.001	0.01	0.005445	0.002413
m2	1.00E-06	0.001	4.20E-06	2.61E-06
I3	10	18	17.7456	0.805753
G1	0	1	0.170415	0.215371
W1	2	5	4.37967	0.195036
O4	2460	2462	2460.9	0.161563
I4	2	8	7.8119	0.550408
G2	0	1	0.431663	0.234338
W2	0	2	0.39147	0.488092
O5	2462	2467	2462.08	0.150085
I6	1	3	1.49628	0.142153
G3	0	1	0.592478	0.036032
W3	0.1	1	0.522858	0.010343
O7	2473	2474.5	2473.17	0.015311
I7	1	3	2.18713	0.391832
W4	0	0.8	0.567699	0.047166
O8	0.5	1.1	0.93861	0.02155
I8	1	3	1.99216	0.473306
W5	0.5	1.5	0.742309	0.078488
O9	0.5	1.5	0.881694	0.057641



APPENDIX B: MOLECULAR ORBITAL DESCRIPTION AND INPUT FILES

B.1. Molecular Orbital (MO) Description of complexes 1a,b-3a,b

(1a) MO description of complex 1a.

Desc	orbital	energy (eV)	occ	Ru			SR			ar	en	Expt energy (eV)	Assignment		
				4d	5s	5p	3p	3s	R						
$en_{\sigma^*} - SC_{\sigma^*}$	75a	-1.667	0		5	3	4		16	23	42	2473.0	$SC_{\sigma^*} \leftarrow S_{1s}$		
$ar_{\pi^*} - SC_{\sigma^*}$	74a	-1.733					2		35	43	13				
$ar_{\pi^*} - SC_{\sigma^*}$	70a	-2.194	0				4		7	48	36				
$CH_{\sigma^*} - SC_{\sigma^*}$	69a	-2.505	0	-1	-1	-2	16	2	16	34	27				
$en_{\sigma^*} - SC_{\sigma^*}$	66a	-3.214	0		1	-3	7	1	5	17	63				
ar_{π^*}	64a	-4.263	0	20						73	3				
ar_{π^*}	63a	-4.423	0	20			1			75					
$Ru\ 4d_{\sigma^*}$	62a	-5.126	0	47			20			21	5	2471.1	$Ru_{4d(\sigma^*)} \leftarrow S_{1s}$		
$Ru\ 4d_{\sigma^*}$	61a	-5.508	0	53						28	15				
$S\ 3p_{\pi}$	60a	-7.260	2	20		1	67		4	2					
$Ru4d_{\pi} + S3p_{\pi}$	59a	-8.240	2	50			18	1	3	15	2				
$Ru\ 4d_{\pi}$	58a	-8.495	2	61	2		9		1	16	1				
$Ru4d_{\pi} + S3p_{\pi}$	57a	-8.897	2	69			16		1	3					
$S3p_{\pi} + RuS_{\sigma}$	56a	-9.234	2	41			33	2	5	7	1				
SC_{σ}	55a	-10.208	2	3			22		40	24	1				

(1b) MO description of complex 1b.

Desc	orbital	energy (eV)	occ	Ru			SR			ar	en	Expt energy (eV)	Assignment		
				4d	5s	5p	3p	3s	R						
$ar_{\pi^*} - SC_{\sigma^*}$	82a	-1.509	0				4		9	52	24	2473.0	$SC_{\sigma^*} \leftarrow S_{1s}$		
$ar_{\pi^*} - SC_{\sigma^*}$	81a	-1.624	0		7	2	5		21	47	12				
$SC_{\sigma^*} - en_{\sigma^*}$	75a	-2.327	0				13		12	24	36				
$en_{\sigma^*} - SC_{\sigma^*}$	72a	-3.179	0	-1			7		6	18	60				
$Ru - ar_{\pi^*}$	70a	-3.942	0	18						76	2				

Desc	orbital	energy (eV)	occ	Ru			SR			ar	en	Expt energy (eV)	Assignment
				4d	5s	5p	3p	3s	R				
Ru-ar _π *	69a	-4.114	0	15			1			78			
Ru-S _σ *	68a	-4.902	0	46			19			20	5	2471.2	Ru4d(σ*)←S _{1s}
Ru _{4dσ} *	67a	-5.112	0	54						24	15		
S 3p _π	66a	-7.068	2	23		1	64		2	3			
Ru4d _π +S3p _π	65a	-7.961	2	51		1	18			18			
Ru 4d _π	64a	-8.162	2	69	1		1		3	14	3		
Ru4d _π +S3p _π	63a	-8.690	2	63			19			5			
S3p _π + RuS _σ	62a	-8.969	2	32	1		41	2	5	8			
SC _σ	61a	-9.904	2	6	1		15	1	20	43	4		

(1c) MO description of complex 1c.

Desc	orbital	energy (eV)	occ	Ru			SR			ar	en	Expt energy (eV)	Assignment
				4d	5s	5p	3p	3s	R				
R _π * - SC _σ *	95a	-0.093	0		2		3		30	49	9		
en _σ * - SC _σ *	89a	-0.715	0		14	1	5		1	43	30		
CH _σ * - SC _σ *	88a	-0.816	0		6	2	1		24	57	6		
R _π * - SC _σ *	86a	-1.102	0				5	-1	41	34	14		
CH _σ * - SC _σ *	85a	-1.185	0				1		12	39	35		
CH _σ * - SC _σ *	83a	-1.371	0		26	2	2		5	42	18		
CH _σ * - SC _σ *	82a	-1.565	0		-1	2	3		9	52	27		
CH _σ * - SC _σ *	80a	-1.798	0				1		2	65	25	2473.3	SC _σ * ← S _{1s}
CH _σ * - SC _σ *	79a	-1.939	0		7		11		8	42	29		
CH _σ * - SC _σ *	78a	-2.004	0	-1			1		8	42	41		
ar _π * - SC _σ *	77a	-2.113	0		1	1	2		9	54	23		
en _σ * - SC _σ *	76a	-2.299	0		5		1		4	32	49		
CH _σ * - SC _σ *	75a	-2.601	0		1	-4	9	1	12	44	34		
en _σ * - SC _σ *	74a	-2.739	0		4		3		6	17	59		
R _π * - Ru-S _{4dσ} *	72a	-3.543	0	4			8		67	4	10	2472.5	R _π * ← S _{1s}

Desc	orbital	Energy (eV)	occ	Ru			SR			ar	en	Expt energy (eV)	Assignment
				4d	5s	5p	3p	3s	R				
Ru-ar _π *	69a	-4.250	0	22					1	72	2		
Ru-ar _π *	68a	-4.316	0	16					3	75	1		
Ru4d_σ*	67a	-5.169	0	44			16			18	5	2471.3	Ru 4d _σ * ← S _{1s}
Ru4d _σ *	66a	-5.455	0	53			1			28	14		
S 3p _π	65a	-7.602	2	21			58		1	9	4		
Ru 4d _π +S3p _π	64a	-8.162	2	20			21		42	9			
Ru 4d _π + R _π	63a	-8.659	2	69					20	2			
Ru 4d _{π(NB)}	61a	-8.785	2	70					10	10			
S3p_π + RuS_σ	60a	-9.142	2	49			26			11	1		
S3p_π + R_π	59a	-10.031	2	10			38	1	36	2	1		

(2a) MO description of complex 2a.

Desc	orbital	energy (eV)	occ	Ru			SOR				ar	en	M eO H	Expt energy (eV)	Assignment
				4d	5s	5p	3p	3s	O	R					
CH _σ *-en _σ *-SC _σ *	89a	-1.118	0		6		2			7	45	30	4		
en _σ *-SC _σ *-SO _σ *	83a	-1.976	0		5		8	1	1	15	36	18	7		
ar _π *-SC _σ *	81a	-2.139	0		1		2			1	77	6	1	2476.0	SC _σ * ← S _{1s}
CH _σ *-SC _σ *	80a	-2.305	0		-1	-1	5			3	55	32			
SC _σ *-SO _σ *	79a	-2.399	0	1	2	1	22	2	2	19	18	25			
CH _σ *-SC _σ *	77a	-2.981	0				4			7	38	41			
SO _σ *-en _σ *	76a	-3.185	0		13		30	2	5	3	21	15		2474.8	SO _σ * ← S _{1s}
en _σ *-SO _σ *	75a	-3.513	0		-6		22		2	5	15	49	2		
Ru-ar _π *	74a	-4.431	0	22							74	2			
Ru-ar _π *	73a	-4.564	0	22			2				74				
Ru4d_σ*-SO_π*	72a	-5.127	0	46			17	1	4	1	23	6		2474.2	Ru4d _σ * ← S _{1s}
Ru4d _σ *	71a	-5.579	0	53							27	17			
SO _π *	70a	-7.730	2	20			25	2	27	4	9	2			
Ru 4d _π	69a	-8.394	2	52		1	2			13	4		1		
Ru 4d _{π(nb)}	68a	-8.601	2	63		2				3			8		

Desc	Orbital	Energy (eV)	occ	Ru			SOR				ar	en	MeOH	Expt energy (eV)	Assignment
				4d	5s	5p	3p	3s	O	R					
MeOH	67a	-8.732	2	25					2				66		
Ru 4d _π	66a	-8.902	2	59			2		10		12	1	5		
SO _π (LP)	65a	-9.077	2	18			4		46	11	2		6		

(2b) MO description of complex **2b**.

Desc	orbital	energy (eV)	occ	Ru			SOR				ar	en	MeOH	Expt energy	Assignment
				4d	5s	5p	3p	3s	O	R					
en _σ *-SC _σ *	90a	-1.841	0		1		1			9	46	32			
CH _σ *-SC _σ *	89a	-1.959	0		-1		3			19	39	34	2		
CH _σ *-SC _σ *-SO _σ *	88a	-1.985	0		2		13	2	2	18	44	8		2476.0	SC _σ * ← S _{1s}
ar _π *-SC _σ *-SO _σ *	87a	-2.113	0			2	6	1	2	10	52	15			
ar _π *-SC _σ *-SO _σ *	86a	-2.283	0		2	2	4	1	2	8	63	6			
CH _σ *-SC _σ *	85a	-2.532	0	1	3		9	1		11	39	29			
CH _σ *-SO _σ *	84a	-2.653	0		5		2			9	40	37			
CH _σ *-SO _σ *	83a	-2.771	0		9		8		3	5	30	33		2474.8	SO _σ * ← S _{1s}
SO _σ *	82a	-3.309	0	5		3	40		4	9	13	17			
Ru-ar _π *	80a	-4.263	0	18		1	2				75	2			
Ru-ar _π *	79a	-4.284	0	17			1				79				
RU _{4dσ} *	78a	-4.952	0	48			18		4		20	5		2474.3	RU _{4dσ} * ← S _{1s}
RU _{4dσ} *	77a	-5.219	0	55							26	17			
SO _π *	76a	-7.625	2	17			27	3	3 2	4	5				
Ru 4d _π	75a	-8.001	2	55		2			4	5	15	1	5		
MeOH	74a	-8.113	2	4									91		
Ru 4d _π	73a	-8.308	2	67					4		15	2	1		
Ru 4d _π (nb)	72a	-8.496	2	76	1				7		5		1		
SO _π (LP)	71a	-8.884	2	17			5		4 9	10	2	2	7		

(3a) MO description of complex 3a.

Desc	orbital	energy (eV)	occ	Ru			SO ₂ R				ar	en	Expt energy	Assignment
				4d	5s	5p	3p	3s	O	R				
CH _σ * -SOC _σ *	95a	-0.860	0		3	-2	6	1	2	21	41	19		
CH _σ * -SC _σ *	94a	-1.005	0		6		6	3	3	27	30	22		
CH _σ * -SC _σ *	92a	-1.281	0				3	1		16	47	24		
CH _σ * -SC _σ *	91a	-1.345	0		8	3	3	1		7	55	14		
R _π * -SOC _σ *	88a	-1.689	0		5		5	2	2	37	31	7		
CH _σ *-SC _σ *+O _{2pπ}	87a	-1.883	0		2		4		1	12	64	8		
CH _σ *-SC _σ *+O _{2pπ}	86a	-1.952	0	-1	2	2	5		1	10	42	27		
ar _π *-SC _σ *+O _{2pπ}	83a	-2.421	0	3		2	27		7	5	13	34	2479.1	
ar _π * -SC _σ *+O _{2pπ}	82a	-2.495	0		1	-1	5		1	2	57	26		
CH _σ * -SOC _σ *	81a	-2.655	0		13	1	3			7	25	42		
CH _σ * -SO _σ *	80a	-3.041	0		2	4	12		5	6	18	34	2477.6	SO _σ *←S _{1s}
CH _σ * -SO _σ *	79a	-3.436	0	2			9		8	12	9	50		
R _π *-Ru _{4dσ} *-SO _σ *	76a	-4.283	0	8			2	5	7	39	22	7		R π* ← S _{1s}
Ru-ar _π *	75a	-4.443	0	16						5	75			
Ru-ar _π *	74a	-4.539	0	11			1		1	25	55			
Ru _{4dσ} *	73a	-5.163	0	35	4	1	4	3	9	10	14	16	2476.9	Ru _{4d(σ*)} ←S _{1s}
Ru _{4dσ} *	72a	-6.098	0	52	2		1	1	1		23	11		
Ru 4d _π	71a	-7.707	2	58		2	1	1	4		14	8		
O _{2pπ}	70a	-8.001	2	17	1		3	2	35	8	5	19		
Ru 4d _{π(NB)}	69a	-8.113	2	58					14	3	11	2		
Ru 4d	68a	-8.308	2	63					9	3	13	2		
R _π	66a	-8.496	2	10			1		8	68	4	2		
SO _π	65a	-8.884	2	23			8		31	21	6			

(3b) MO description of complex **3b**.

Desc	orbital	energy (eV)	occ	Ru			SO ₂ R				ar	en	Expt energy	Assignment
				4d	5s	5p	3p	3s	O	R				
en _σ *-SOC _σ *	107a	-0.523	0				3		3	19	38	24		
CH _σ *-SOC _σ *	106a	-0.560	0		1		2	1	1	3	79	4		
en _σ *-SOC _σ *	103a	-0.799	0			2	3	3	3	16	38	26		
CH _σ *-SC _σ *	102a	-0.848	0				1			9	52	22		
CH _σ *-SC _σ *	101a	-0.859	0				1			7	59	18		
CH _σ *-SOC _σ *	97a	-1.367	0				1		2	19	57	15		SC _σ * ← S _{1s} / SO _σ * ← S _{1s}
CH _σ *-SOC _σ *	96a	-1.464	0			3	11		2	8	54	12		
ar _π *-SOC _σ *	94a	-1.692	0	1		3	18		5	19	34	9	2479.2	
CH _σ *-SC _σ *-SO _π *	93a	-1.718	0		1	3	16	2	4	8	41	15		
CH _σ *-SOC _σ *	92a	-1.772	0		13		12		3	22	39	2	2478.3	
CH _σ *-SOC _σ *	91a	-1.845	0		4		7			8	47	22		
en _σ *-SC _σ *-SO _π *	89a	-2.139	0		1		4			18	21	47		SO _π * ← S _{1s}
ar _π *-SO _π *	88a	-2.316	0		3	1	2			4	77	3		
Π*-Ru _{4dσ} *	82a	-4.086	0	10				3	3	48	25			R _π * ← S _{1s}
Ru-ar _π *	81a	-4.191	0	19						4	71	3		
Ru-ar _π *	80a	-4.348	0	12						26	55	2		
Ru _{4dσ} *	79a	-5.226	0	45			7	3	4	10	21	5	2477.0	Ru _{4dσ} * ← S _{1s}
Ru _{4dσ} *	78a	-5.301	0	50							30	16		
Ru 4d _π	77a	-8.233	2	59					10		17	4		
SO _π *	76a	-8.332	2	44	2	2	3	1	17	4	17			
Ru 4d _π (NB)	75a	-8.676	2	73					4	13	2			
Ru _{4dπ} * O _{2pt}	74a	-8.870	2	39			2		27	13	8			

B.2: Selected Input files for each type of calculations:

ADF Input files for Chapter 3 can be found in the supplementary information of the related publication.⁹⁶

Selected ORCA files are given here.

1. Geometry optimization for scalar-relativistic effect of complex **2aZn**

```
! RKS OPT BP86 TZVP def2-TZVP/J ZORA Split-RI-J
      SlowConv SCFCONV6
! NormalSCF
! Normalprint
! Grid4 Nofinalgrid

% SCF MAXITER 500
end

% basis NewGTO 44 "TZVPP" end
      NewAuxGTO 44 "TZVPP/J" end
End

* xyz 3 1
C -0.605820  1.329045 -0.301372
C  0.019674  0.069592 -0.196767
C  1.433476 -0.048823  0.055612
C  2.162258  1.155241  0.240143
C  1.536400  2.438854  0.168769
C  0.142411  2.540092 -0.082346
Ru  0.468086  1.199897  1.686634
S  1.762016  1.908078  3.632934
O  1.417680  0.883062  4.797851
C  2.159066 -1.383199 -0.032845
C  1.504193 -2.535208  0.742545
C -0.528322  3.883224 -0.183230
N -1.090289  2.199998  2.852804
C -1.613983  1.329132  3.962912
C -1.514440 -0.119472  3.519908
N -0.118840 -0.343211  3.042678
C  2.325892 -1.746891 -1.525717
C  3.623538  1.669218  3.349676
C  4.338108  2.451960  4.452675
C  3.977504  0.190291  3.343505
H  3.229102  1.090916  0.457483
```

```
H  2.120542  3.343366  0.340535
H -1.679011  1.385798 -0.491970
H -0.584132 -0.831837 -0.311700
H -1.581702  3.847816  0.128937
H -0.006813  4.645377  0.410092
H -0.520639  4.217351 -1.233072
H  3.166643 -1.226974  0.386437
H  2.057732 -3.467320  0.563978
H  1.524990 -2.357394  1.827766
H  0.465988 -2.717409  0.425408
H  2.935735 -2.655660 -1.624808
H  2.820749 -0.942080 -2.086783
H  1.351778 -1.942375 -1.998841
H  3.801528  2.142309  2.371009
H  5.427048  2.369429  4.317169
H  4.088646  2.045752  5.442914
H  4.075079  3.518502  4.437719
H  5.066596  0.065236  3.250912
H  3.659284 -0.277184  4.285890
H  3.498026 -0.348775  2.514391
H -1.754667 -0.789507  4.360639
H -2.210888 -0.338654  2.696785
H -0.967860  1.487652  4.835820
H -2.646075  1.603663  4.223368
H -0.019277 -1.291126  2.669740
H  0.539883 -0.198907  3.867610
H -0.732076  3.076229  3.249739
H -1.853526  2.457501  2.220622
Zn  2.471942  1.140174  7.027167 newgto "TZVPP"
      end
*
```

2. COSMO solvation effect on complex **2aZn**

```
! RKS OPT BP86 TZVP def2-TZVP/J ZORA Split-RI-J
      SlowConv SCFCONV6 COSMO(water)
! NormalSCF
! Normalprint
! Finalgrid6

% SCF MAXITER 500
end

% basis NewGTO 44 "TZVPP" end
      NewAuxGTO 44 "TZVPP/J" end
End

* xyz 3 1
C -0.815221  0.805373 -0.064177
C  0.141608 -0.252559  0.111665
C  1.539574 -0.000794  0.125374
C  1.920556  1.381748  0.213344
C  0.976799  2.435036  0.104111
C -0.410444  2.157811 -0.164403
```

Ru	0.390831	1.144225	1.867884	H	1.943897	-2.293135	1.742295
S	1.891916	1.040909	3.583171	H	1.349123	-2.913512	0.176134
O	1.613767	0.023097	4.815817	H	3.666607	-2.011295	-1.626669
C	2.575115	-1.090831	0.012322	H	3.164973	-0.348972	-1.998652
C	2.195240	-2.420496	0.675975	H	1.967084	-1.672853	-2.028927
C	-1.371859	3.254640	-0.480778	H	3.903247	1.528220	2.388213
N	-0.639462	2.725643	2.957710	H	5.356932	2.431254	4.271321
C	-1.438486	2.184861	4.113919	H	4.104242	1.998063	5.452177
C	-2.072045	0.887133	3.662957	H	3.789032	3.250263	4.212248
N	-0.973982	0.015733	3.104618	H	5.566392	-0.033733	3.498769
C	2.853403	-1.281890	-1.509699	H	4.373849	-0.528231	4.666327
C	3.834337	1.198331	3.435300	H	4.146271	-0.914273	2.907161
C	4.272327	2.283825	4.404937	H	-2.582026	0.377308	4.493489
C	4.476626	-0.153164	3.627407	H	-2.810228	1.053037	2.865993
H	2.976908	1.636943	0.317125	H	-0.749251	2.023502	4.954224
H	1.324289	3.469642	0.134125	H	-2.194874	2.916553	4.433880
H	-1.873388	0.552928	-0.164056	H	-1.389708	-0.772754	2.595479
H	-0.215484	-1.283312	0.146594	H	-0.444348	-0.395572	3.886027
H	-2.414482	2.993154	-0.257953	H	0.004844	3.453062	3.290779
H	-1.104320	4.212879	-0.013218	H	-1.272399	3.199259	2.300555
H	-1.322520	3.432928	-1.572216	Zn	2.370864	-1.748915	5.347099
H	3.506399	-0.710597	0.465033	newgto "TZVPP" end			
H	3.040709	-3.117725	0.610513	*			

3. Single point calculation for TDDFT-XAS of **3aZn**

! UKS BP86 TZVP def2-TZVP/J ZORA Split-RI-J	C	4.568783	1.371525	13.813520			
SlowConv SCFCONV7 COSMO(water)	N	4.203214	2.745113	14.281800			
! TightSCF	C	8.140253	1.917042	16.954106			
! Normalprint	C	4.529954	6.587471	16.564607			
! Grid4 NoFinalgrid	C	5.384469	7.774593	17.066091			
	S	2.774881	2.854324	16.976043			
% basis NewGTO 44 "TZVPP" end	O	1.758478	2.880268	15.812230			
NewAuxGTO 44 "TZVPP/J" end	Zn	0.907298	0.625918	18.080575 newgto			
end	"TZVPP" end						
	O	-0.008059	1.182306	19.760741			
% method SpecialGridAtoms 44	C	2.124677	4.060163	18.186354			
SpecialGridIntAcc 7	C	1.238698	5.042609	17.737788			
end	C	0.731223	5.954252	18.670310			
	C	1.120727	5.881022	20.012126			
% tddft NRroots 200	C	2.013042	4.889128	20.438497			
MaxDim 2000	C	2.528275	3.967199	19.523033			
OrbWin[0]=6,6,-1,-1	O	2.649591	1.473898	17.777745			
OrbWin[1]=6,6,-1,-1	O	-0.143224	1.111441	16.464421			
DoQuad true	C	3.914778	6.886674	15.192387			
end	H	3.208735	3.181488	19.854202			
	H	2.310605	4.828650	21.486031			
* xyz 3 1	H	0.722055	6.596805	20.732317			
C	7.020763	3.749904	15.596716	H	0.030624	6.723216	18.341591
C	7.191419	3.068214	16.832147	H	0.934343	5.083149	16.692077
C	6.393494	3.480206	17.948840	H	3.709665	6.438023	17.286458
C	5.514838	4.584083	17.822126	H	9.105516	2.305255	17.317802
C	5.383511	5.334620	16.605635	H	8.327622	1.433753	15.986620
C	6.121912	4.860274	15.491661	H	7.796051	1.175458	17.686989
Ru	4.982315	3.099538	16.239431	H	3.175170	2.837666	14.326603
N	5.010056	0.959287	16.176530	H	4.533906	3.439964	13.605943
C	4.314594	0.420744	14.962081	H	5.629476	1.381768	13.532613

H	3.975610	1.097887	12.930188	H	3.241123	7.751032	15.271978
H	3.241821	0.366002	15.188428	H	3.328320	6.036765	14.812018
H	4.672229	-0.591985	14.737007	H	4.682919	7.138525	14.446440
H	5.978808	0.623565	16.195147	H	-1.098758	1.302686	16.502224
H	4.553532	0.592016	17.020731	H	0.324143	1.882773	16.031375
H	5.996440	5.335971	14.518586	H	0.447264	1.021561	20.608821
H	7.566724	3.416781	14.714507	H	-0.936018	0.911156	19.898052
H	6.458521	2.942783	18.893825	O	1.209998	-1.343644	18.063277
H	4.897865	4.860008	18.678550	H	1.616445	-1.757982	18.847861
H	5.795160	7.586028	18.068241	H	0.464502	-1.920422	17.808433
H	4.765025	8.681309	17.116228				
H	6.222565	7.966610	16.379888	*			

4. Single point calculation for UV-vis simulation of **5b**

! RKS SP B3LYP VDW10 def2-TZVP def2-TZVP/J ZORA
RIJCOSX SlowConv SCFCONV6 COSMO(Water)

! TightSCF
! Normalprint
! Grid4 Finalgrid6
% basis NewGTO 44 "def2-TZVPP" end
NewAuxGTO 44 "def2-TZVPP/J" end
end
% tddft NRoots 100
MaxDim 500
end
* xyz 1 1

C	4.138244	3.751845	15.344398
C	2.748812	3.624089	15.147494
C	2.010992	4.828880	14.955091
C	2.634128	6.086848	14.964961
C	4.028963	6.204797	15.244039
C	4.764392	5.024521	15.430748
Ru	3.630714	4.799121	13.492852
Cl	4.110517	6.488845	11.811755
C	2.074504	2.289004	15.109741
C	4.710897	7.544597	15.404748
C	3.997550	8.711357	14.722059
N	4.961735	3.611783	12.324986
N	4.327334	2.700637	11.485634
C	3.019543	2.744410	11.235192
S	2.053577	3.957406	11.936429
C	6.256636	3.499318	12.284715
C	7.268830	4.271146	12.947071
C	7.164940	5.621476	13.329483
C	8.206535	6.276743	13.943221
C	9.429186	5.613679	14.239581
C	9.551554	4.267416	13.804837
C	8.509172	3.635376	13.168072
N	10.439076	6.244635	14.889462
N	2.516624	1.797877	10.420967
C	1.121212	1.471261	10.395421
C	0.230840	2.227302	9.644740

C	-1.123296	1.905065	9.651448
C	-1.563808	0.819595	10.401349
C	-0.674572	0.050157	11.144522
C	0.674716	0.383729	11.138810
I	-3.631507	0.328260	10.424839
C	4.872410	7.820499	16.911236
H	6.644092	2.673288	11.689095
H	5.829945	5.080291	15.600563
H	4.746262	2.859571	15.417604
H	0.958587	4.768732	14.710567
H	2.043668	6.962960	14.746887
H	1.274396	2.275434	14.369997
H	1.634127	2.071405	16.086207
H	2.786638	1.499095	14.872619
H	5.708809	7.447088	14.971983
H	4.605506	9.611816	14.822385
H	3.033720	8.915479	15.194005
H	3.833683	8.513971	13.663462
H	5.422201	8.751299	17.062848
H	5.414517	7.016965	17.412093
H	3.894821	7.924399	17.387940
H	3.149035	1.081510	10.088835
H	4.914500	2.002510	11.043438
H	0.587905	3.067557	9.064924
H	-1.816118	2.498684	9.071837
H	-1.015890	-0.791266	11.730894
H	1.378338	-0.195034	11.723438
H	8.644825	2.610715	12.841252
H	10.470060	3.722406	13.960320
H	8.084662	7.321116	14.188785
H	6.265038	6.169443	13.097872
C	10.325738	7.653406	15.245862
C	11.705932	5.561709	15.126412
H	12.364061	6.220432	15.684912
H	11.560265	4.651695	15.713390
H	12.201036	5.290957	14.188912
H	11.216717	7.954221	15.788948
H	10.232243	8.286882	14.358561
H	9.462341	7.831963	15.891343
*			

NBO calculation of [Ru(p-cymene)(en)(SO-iPr)]⁺ in gas phase

5. NBO calculation of **2a**

! RKS BP86 SVP ZORA NORI
! TightSCF VerySlowConv

```

! Grid4 NoFinalgrid
! Normalprint
! NBO
% maxcore 1024
% scf maxiter 1000
  end
% pal nprocs 8
  end
* xyz 1 1
C   0.019674   0.069592  -0.196767
C   1.433476  -0.048823   0.055612
C   2.162258   1.155241   0.240143
C   1.536400   2.438854   0.168769
C   0.142411   2.540092  -0.082346
C  -0.605820   1.329045  -0.301372
Ru   0.468086   1.199897   1.686634
N  -1.090289   2.199998   2.852804
C  -1.613983   1.329132   3.962912
C  -1.514440  -0.119472   3.519908
N  -0.118840  -0.343211   3.042678
C   2.159066  -1.383199  -0.032845
C   2.325892  -1.746891  -1.525717
C  -0.528322   3.883224  -0.183230
S   1.762016   1.908078   3.632934
C   3.623538   1.669218   3.349676
C   3.977504   0.190291   3.343505
C   1.504193  -2.535208   0.742545
O   1.417680   0.883062   4.797851
C   4.338108   2.451960   4.452675
H   3.229102   1.090916   0.457483

H   2.120542   3.343366   0.340535
H  -1.679011   1.385798  -0.491970
H  -0.584132  -0.831837  -0.311700
H  -1.581702   3.847816   0.128937
H  -0.006813   4.645377   0.410092
H  -0.520639   4.217351  -1.233072
H   3.166643  -1.226974   0.386437
H   2.057732  -3.467320   0.563978
H   1.524990  -2.357394   1.827766
H   0.465988  -2.717409   0.425408
H   2.935735  -2.655660  -1.624808
H   2.820749  -0.942080  -2.086783
H   1.351778  -1.942375  -1.998841
H   3.801528   2.142309   2.371009
H   5.427048   2.369429   4.317169
H   4.088646   2.045752   5.442914
H   4.075079   3.518502   4.437719
H   5.066596   0.065236   3.250912
H   3.659284  -0.277184   4.285890
H   3.498026  -0.348775   2.514391
H  -1.754667  -0.789507   4.360638
H  -2.210888  -0.338654   2.696785
H  -0.967860   1.487652   4.835820
H  -2.646075   1.603663   4.223368
H  -0.019277  -1.291126   2.669740
H   0.539883  -0.198907   3.867610
H  -0.732076   3.076229   3.249739
H  -1.853526   2.457501   2.220622
*

```

APPENDIX C: XAS AND DFT ANALYSIS OF $\text{Ru}^{\text{II}}/\text{Os}^{\text{II}}$ -ARENE (η^6 -S-S) LIGATED COMPLEXES

C.1: Effect of Chelating Ligand Modification in Os-arene-dithiol Complexes

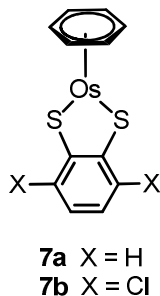


Figure C.1: Structures of novel five-coordinated $[(\eta^6\text{-Benzene})\text{Os}(\text{dithiol})]$ complexes (**7**)

Electronic structures of **7a**, $[(\eta^6\text{-Benzene})\text{Os}(1,2\text{-benzenedithiol})]$ and **7b**, $[(\eta^6\text{-Benzene})\text{Os}(3,6\text{-dichloro-1,2-benzenedithiol})]$ are examined using S K-edge XAS in concert with DFT, TDDFT and NBO calculations.

C.1.1: Sulfur K-edge X-ray Absorption Spectroscopy

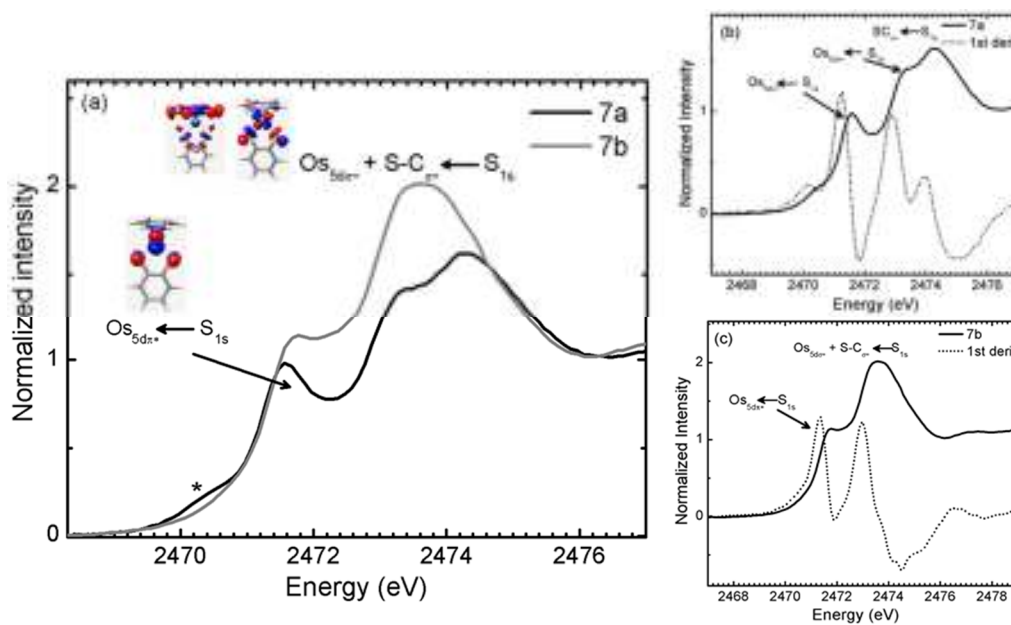


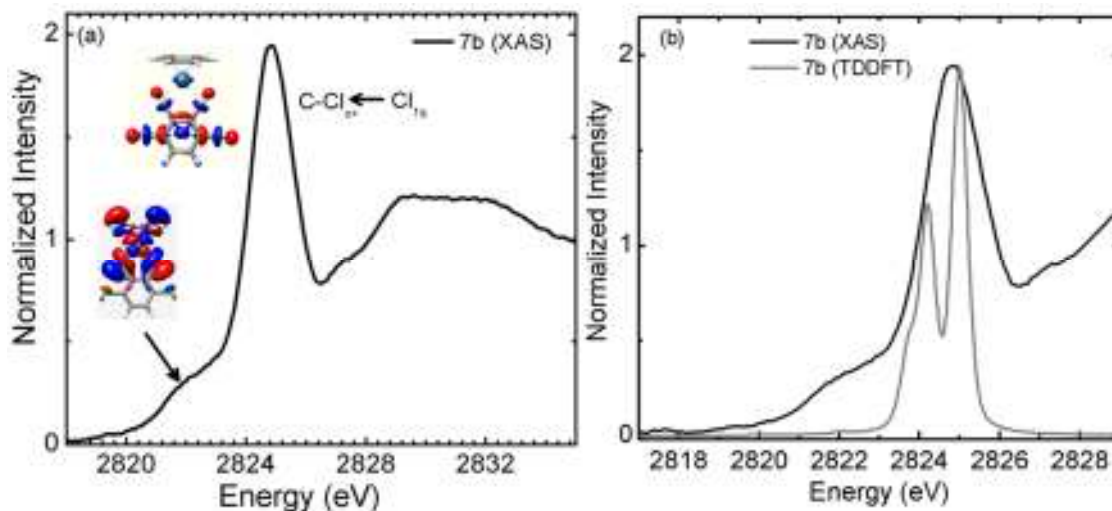
Figure C.2: (a) Normalized S K-edge XAS of complexes **7a** and **7b** with peak assignments, (b) XAS and 1st derivative spectrum of **7a**, (c) XAS and its 1st derivative spectrum of **7b**.

Table C.1: DFT calculated S_{3p} contribution to $Os-S_{\pi^*}$ and $Os-S_{\sigma^*}$ acceptor orbitals in **7a** and **7b**

Complex	% S_{3p} in $Os-S_{\pi^*}$	% S_{3p} in $Os-S_{\sigma^*}$	Total % S_{3p} in $Os-S$
7a	23.8	22.3	46.1
7b	22.4	21.7	44.1

Electronic structures of **7a**, [(η^6 -Benzene)Os(1,2-benzenedithiol)] and **7b**, [(η^6 -Benzene)Os(3,6-dichloro-1,2-benzenedithiol)] are examined using S and Cl K-edge XAS in concert with DFT and NBO calculations. As shown in Figure C.2, the S K-edge spectrum of **7a** shows three main features in the near edge region. The lower energy weak feature at 2471.6 eV is assigned to $Os_{5d\pi^*} \leftarrow S_{1s}$, a feature at 2473.2 eV is assigned to $Os_{5d\sigma^*} \leftarrow S_{1s}$ and the higher energy feature at ~ 2475.0 eV is assigned to $S-C_{\sigma^*} \leftarrow S_{1s}$. However, the last two features cannot be distinguished in **7b**. All the features are assigned based on literature and DFT calculations. The calculated S_{3p} character from DFT is shown in Table C.1. DFT results indicate that the halide substitution on the (S, S-) chelating ligand slightly reduce the S_{3p} character contribution to both orbitals. Therefore, the covalency of the $Os-S_{\pi}$ and $Os-S_{\sigma}$ is decreased.

C.1.2: Chlorine K-edge X-ray Absorption Spectroscopy

**Figure C.3:** (a) Chlorine K-edge XAS of complex **7b**. (b) XAS-TDDFT comparison for complex **7b**.

Somewhat surprisingly, the pre-edge region of the Cl K-edge XAS spectrum of **7b** (Figure C.3a) shows a weak shoulder at 2821.8 eV below the intense $C-Cl_{\sigma^*} \leftarrow Cl_{1s}$ transition. Based on TDDFT simulations, this weak low-energy feature may correspond to the presence of some Cl 3p character in the empty Os 5d orbitals; specifically overlap of a filled Cl 3p orbitals with the adjacent S 3p orbital

involved in σ -bonding with the metal centre (see Figure C.3, $\text{Os}_{5d\sigma^*}$ orbital). TDDFT simulations of the Cl K-edge XAS spectrum (Figure C.3b) is in good agreement with experimental XAS. Cl K-edge studies are consistent with the results obtained from S K-edge XAS.

C.1.3: Natural Bond Analysis

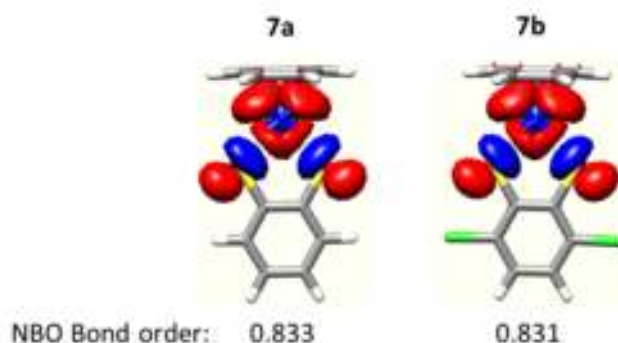
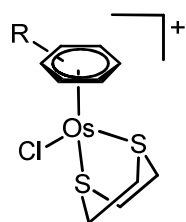


Figure C.4: Natural bond orbital pictures of $\text{Os-S}\sigma^*$ orbitals in complexes **7a** and **7b**.

The natural bond analysis of the Os-S bonds in **7a** and **7b** predicts that both Os-S bonds in each complex are equal and the bond order for **7a** (0.833) is slightly higher than **7b** (0.831) as shown in Figure C.4. XAS, DFT, TDDFT and NBO studies on these complexes suggest that the covalency of Os-S bond in **7a** is slightly greater than **7b**. Therefore, Os-S bond is weakened by the halide substitution on the chelating ligand.

C.2: Different Arene Substitution in Os-arene-dithiane Complexes



- 8a** R = bz
8b R = p-cym
8c R = bip

Figure C.5: Six-coordinated $[(\eta^6\text{-arene})\text{Os}(1,4\text{-dithiane})\text{Cl}]^+$ complexes (**8**).

Effect of arene (benzene, p-cymene and biphenyl) ligand substitution is investigated in a series of Os-arene-dithiane complexes, **8a-c** using S and Cl K-edges combined with DFT and NBO calculations.

C.2.1: Sulfur and Chlorine K-edge X-ray Absorption Spectroscopy

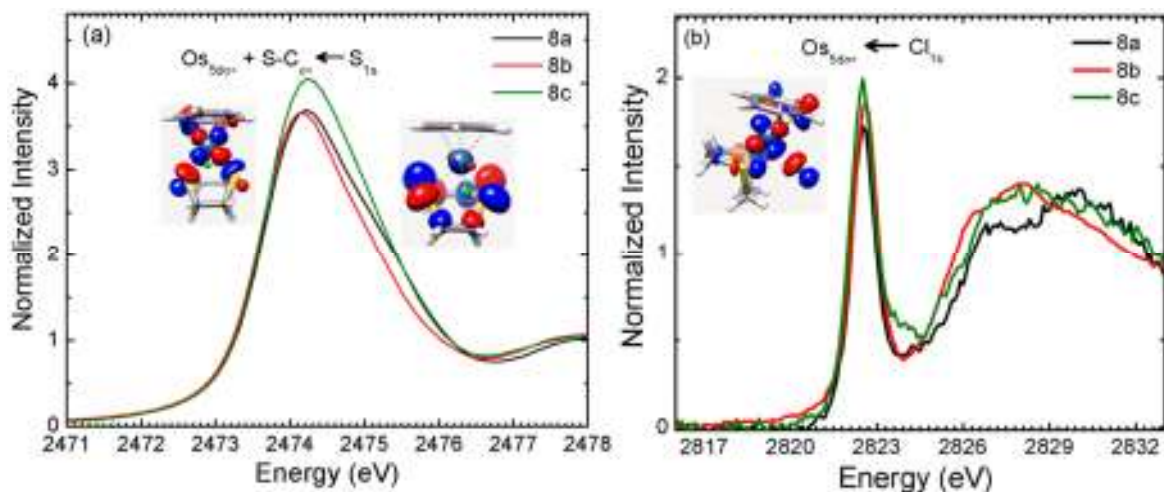


Figure C.6: (a) Sulfur and (b) Chlorine K-edge XAS of complexes **8a-c**.

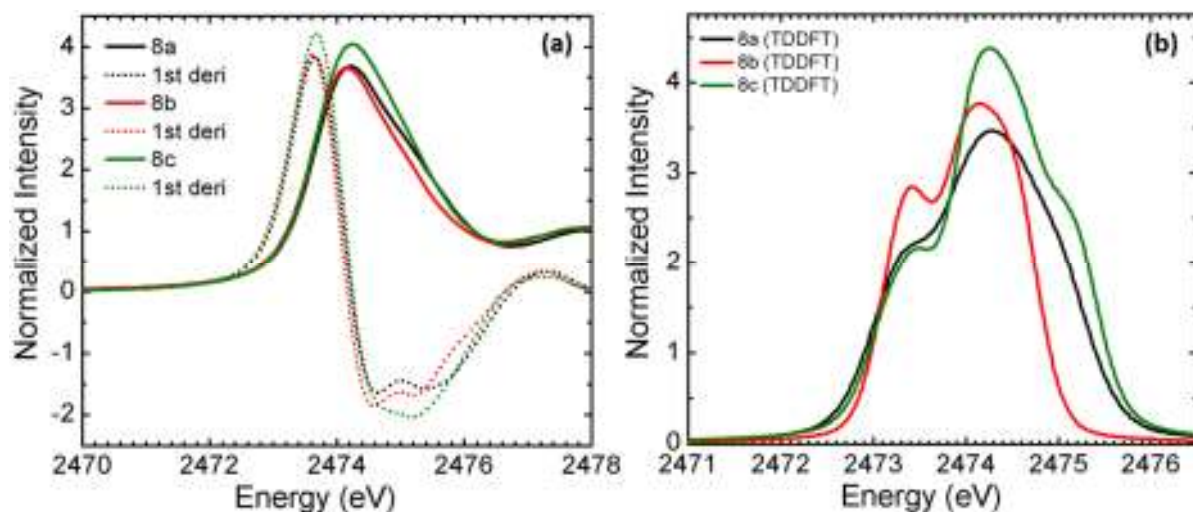


Figure C.7: (a) First derivative spectra of S K-edge XAS and (b) simulated TDDFT spectra of complexes **8a-c**.

S K-edge XAS of all these complexes show only a broad and intense feature at 2473.0 - 2476.0 eV, as shown in Figure C.6a. DFT calculation shows that this feature can be assigned to both $Os_{5d\sigma^*} \leftarrow S_{1s}$ and $S-C_{\sigma^*} \leftarrow S_{1s}$ transitions. Unlike in Ru-arene complexes, in Os-arene complexes the energy of $Os-S_{\sigma^*}$ and $S-C_{\sigma^*}$ are very close (a similar tendency is also observed in Os-arene thiosemicarbazone complexes in Chapter 5); hence they cannot be distinguished in the experimental spectra.

The first derivative spectra of the S K-edge XAS (Figure C.7a) also show that there are two features in each spectra. This is again supported by the simulated TDDFT spectra as shown in Figure C.7b. The S K-edge XAS combined with DFT calculations predicts that there is Os-S coordination

present in those complexes. However, the covalency of Os-S bond in those complexes cannot be extracted. Therefore, S K-edge XAS fails to investigate the effect of different arene substitution in those complexes.

Therefore, Cl K-edge XAS was attempted as a way to investigate the effect of different arene substitution in those complexes. A sharp and well separated feature appears at 2822.5 eV is assigned to $\text{Os}_{5d\sigma^*} \leftarrow \text{Cl}_{1s}$ transition as shown in Figure C.6b. The different arene ligand effect could, in principle, be investigated by quantifying the Os-Cl covalency. However, due to the poor quality of the data, such a comparison is not made here and we require better quality data for quantitative analysis.

C.2.1: Natural Bond Analysis

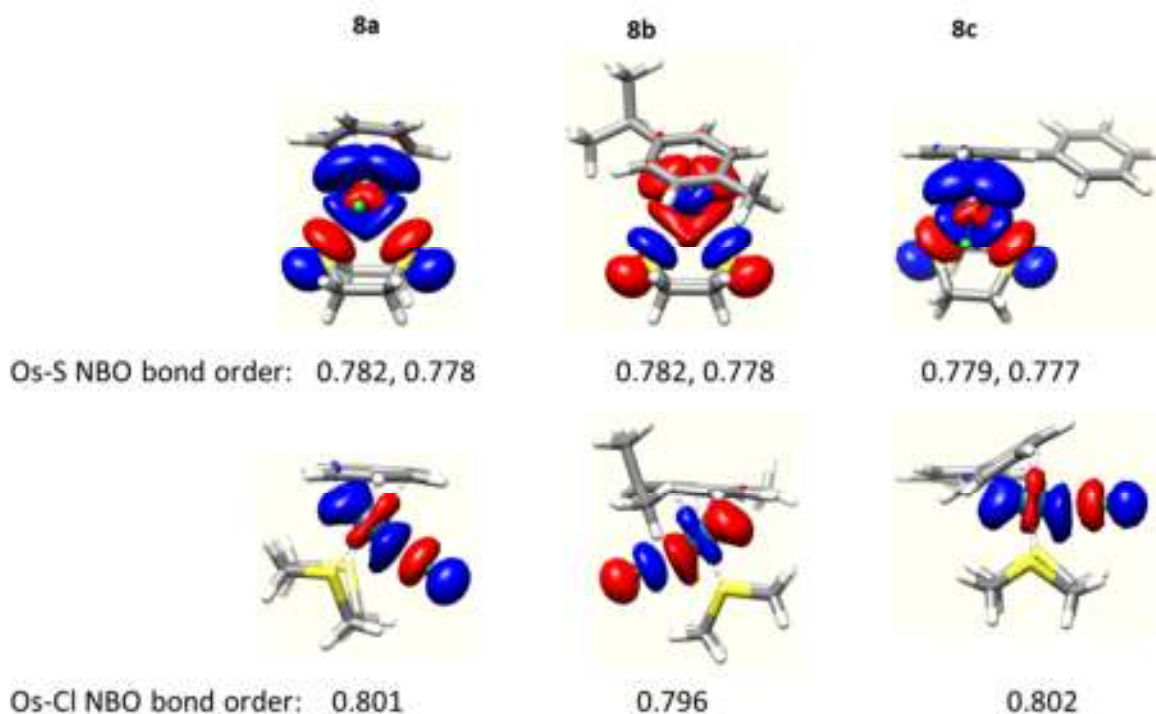


Figure C.8: Natural bond analysis of Os-S and Os-Cl orbitals of **8a-c**

NBO analysis indicates that the Os-S covalency and Os-Cl covalency in all the complexes are very close in nature. Each complex has two Os-S bonds, which are slightly different from each other in **8a-c**. The lowest covalency for Os-S bond is obtained in **8c**, [η^6 -bip)Os(dithiane)] whereas the lowest covalency for Os-Cl bond is obtained in **8b**, [η^6 -*p*-cym)Os(dithiane)].

C.3: Effect of geometry in Ru and Os Dodecarborane complexes

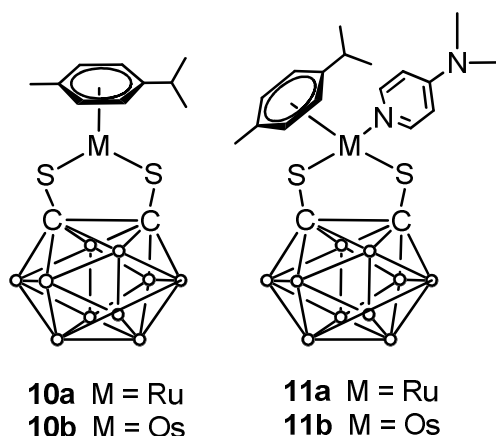


Figure C.9: Structures of five-coordinated, **10**, and six-coordinated, **11**, Ru^{II}/Os^{II} arene dodecarborane complexes

Ru^{II}-arene 16-electron (**10a**) and 18-electron (**11a**) complexes as well as Os^{II}-arene 16-electron (**10b**) and 18-electron complexes (**11b**) have been investigated through their electronic structure using S K-edge XAS, DFT, and TDDFT analysis

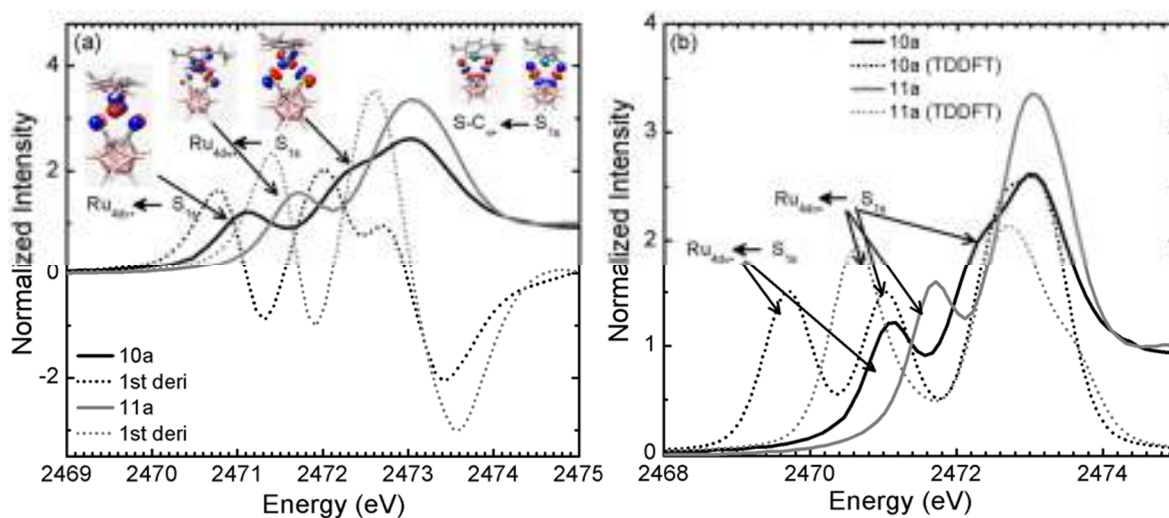


Figure C.10: (a) S K-edge XAS of **10a** and **11a** are compared with their 1st derivative spectra; (b) S K-edge XAS-TDDFT comparison of **10a** and **11a**.

Interestingly, as seen in Figure C.10a, there are 3 features appeared in the S K-edge XAS of **10a**, whereas only two features in **11a**. The simulated TDDFT spectra of complex **10a** also shows 3 main features and those features are assigned to Ru_{4dπ*} ← S₁₅, Ru_{4dσ*} ← S₁₅ and S-Cσ* ← S₁₅ transitions; whereas in the simulated spectrum of **11a**, there are two well separated features appeared and they can be assigned to Ru_{4dπ*} ← S₁₅ and S-Cσ* ← S₁₅ transitions. These features are further resolved in the 1st derivative spectra as shown in Figure C.10b.

Therefore, in the five-coordinated complex ligand is coordinated through Ru-S π and Ru-S σ interaction, however, in six-coordinated complex it is only coordinated through Ru-S σ interaction. This can be attributed that in 16-electron, five-coordinated complex **10a**, additional d-electron on the metal is coordinated through a π -interaction with S 3p lone pair in addition to σ -interaction. However, such interaction is not possible in 18-electron, six-coordinated complex **11a**.

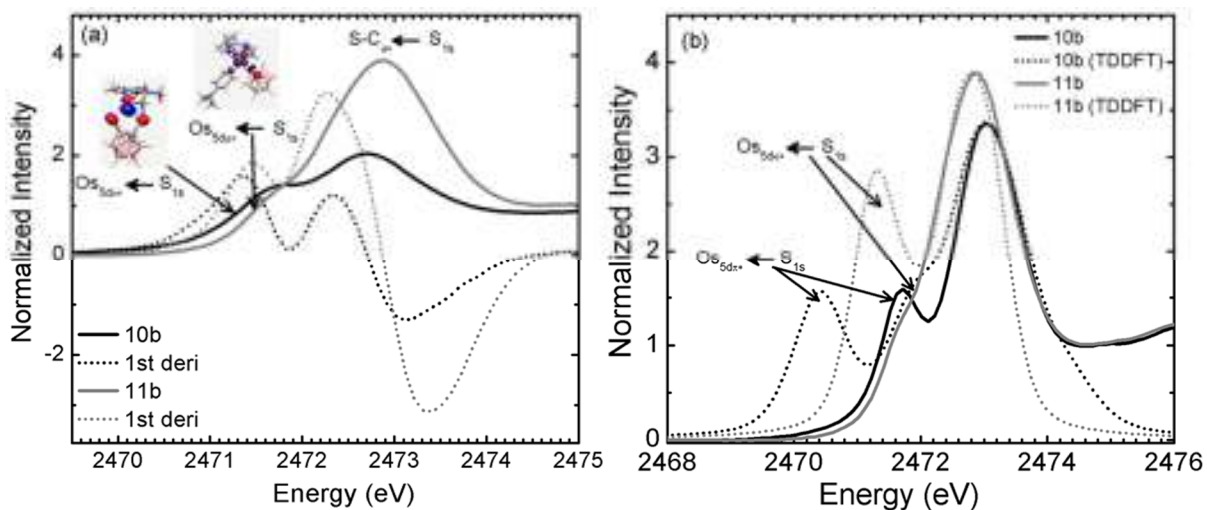


Figure C.11: (a) S K-edge XAS of Os^{II} complexes **10b** and **11b** are compared with their 1st derivative spectra; (b) XAS-TDDFT comparison of complexes **10b** and **11b**.

Table C.2: DFT calculated S_{3p} contribution to M_{ndπ*} and M_{ndσ*} acceptor orbitals in **10** and **11**

Complex	% S _{3p} in M _{ndπ*}	% S _{3p} in M _{ndσ*}
	DFT	DFT
10a	21.5	20.8
10b	21.0	16.0
11a	-	26.9
11b	-	26.4

Contrastingly, the S K-edge XAS of five- and six-coordinated Os^{II}-arene complexes, **10b** and **11b**, are dominated by two features, which is also consistent with the 1st derivative spectra of these complexes as shown in Figure C.11a. However, the simulated TDDFT spectrum of **10b** shows two main features and a shoulder on the second feature and the simulation of **11b** is very consistent with the experimental XAS results, Figure C.11b. The features are identified with the TDDFT simulation spectra, the Kohn-Sham molecular orbital picture and energy. Interestingly, the analysis indicates that in 16-electron, five-coordinated complex, all three interactions

such as $Os_{5d\pi^*} \leftarrow S_{1s}$, $Os_{5d\sigma^*} \leftarrow S_{1s}$ and $S-C_{\sigma^*} \leftarrow S_{1s}$ are present as it is observed in the Ru analogue. However, $Os_{5d\sigma^*} \leftarrow S_{1s}$ and $S-C_{\sigma^*} \leftarrow S_{1s}$ transitions are very close in energy, as a result they merge together and look like a single peak in XAS and shows a shoulder in the TDDFT spectra, Figure C.11b.

To investigate the strength of M-S bond in five-coordinated vs six-coordinated complexes as well as in the Ru vs Os complexes, DFT calculated S_{3p} -character involved in those orbitals are obtained as in Table C.2. DFT results suggest that the Ru-S $_{\sigma}$ bond in **11a** is more covalent than in **10a**; however, the overall Ru-S bond strength in **10a** is more covalent than in **11a** due to π - and σ - interactions. This trend is also supported by the Frontier MO diagram (Figure C.12) showing a down shift in energy of $Ru_{4d\sigma^*}$ orbital when it goes from **10a** to **11a**. Similarly, energy drop is also observed with Os^{II} complexes between **10b** and **11b** but in smaller extent compare to the Ru^{II} analogues. Therefore, this implies that the M-S bonds in six-coordinated complex are less covalent than the M-S bonds in five-coordinated complexes. In between the five-coordinated Ru^{II} and Os^{II} complexes (**10a** vs **10b**), the Os^{II} complex is less covalent compare to the Ru^{II} complex. However, the covalency of the M-S bond is almost equal in Ru^{II} and Os^{II} six-coordinated complexes (**11a** and **11b**). Systematic peak fitting should be performed to compare the DFT results with XAS.

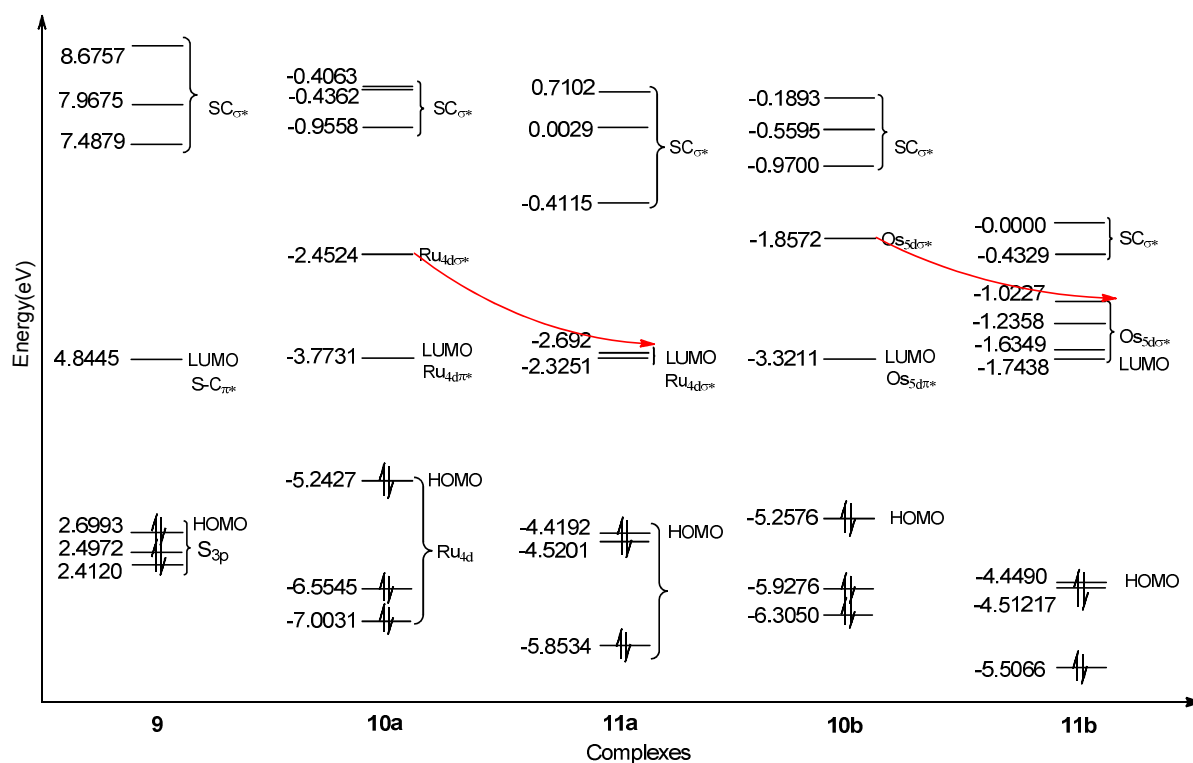


Figure C.12: Frontier MO diagram of complexes 9-11. Only α orbitals are shown (α and β are identical). Red arrow indicates the energy shift from $10a \rightarrow 11a$ and $10b \rightarrow 11b$. Orbitals are normalized to LUMO in each complex